Effects of Nanoparticles on Solid-Liquid Phase Change Heat Transfer Rate

By

© **Mohammad Parsazadeh**

A Thesis submitted to the School of Graduate Studies in partial fulfillment of the requirements for the degree of

Doctor of Philosophy

Faculty of Engineering and Applied Science

Memorial University of Newfoundland

May 2020

St. John's Newfoundland and Labrador

Abstract

Phase change materials (PCMs) have many engineering applications, such as thermal insulation, thermal management, and storing thermal energy. With a high latent heat of fusion, many organic PCMs such as paraffin are ideal for thermal energy storage, but their relatively low thermal conductivity makes the melting and solidification process lengthy. One way to improve this problem is the dispersion of highly conductive nanoparticles to the base PCM, making a mixture of so-called Nano-enhanced Phase Change Materials (NePCMs). However, adding nanoparticles changes many other properties of the mixture, such as viscosity, which may affect the total heat transfer rate in a complicated way. The literature on this topic shows some contradicting findings, with some studies reporting enhanced phase change heat transfer with nanoparticles, but some reporting reduced heat transfer rate. It is critically important to conduct a systematic study for a better understanding of the effects of nanoparticles on the solid-liquid phase change heat transfer rate.

This thesis aims to conduct such a study. It starts with a review of the analytical models for the phase change problems, the significant parameters on the phase change rate through scaling analysis, and reported effects of nanoparticles on the phase change rate. Then, a melting problem with Rayleigh-Benard convection is investigated in a rectangular enclosure both numerically and experimentally. It is found that the effect of nanoparticles on the total heat transfer rate during this melting process is highly dependent on the level of domination of natural convection (as compared to conduction) during the phase change process. Based on the scaling analysis and the experimental results, predictive correlations are developed for the viscosity and melting rate of the NePCMs. The effects of nanoparticles on the heat transfer and phase change rate are also numerically analyzed in shell-and-tube thermal energy storage units with and without fins. The different

behaviours of nanoparticles are investigated in terms of the significance and domination of natural convection in the melted regions. With a numerical and statistical approach, predictive correlations are developed for each case, and the potential interactions between the parameters in affecting the total heat transfer rate are identified.

Most previous researches came up with a critical concentration of nanoparticles for higher phase change rate in a particular energy storage case. The results are often not applicable to other cases. This research systematically analyzes the effects of nanoparticles on the phase change heat transfer rate, leading to better and more general understandings of these effects. It identified the key parameters (e.g., Rayleigh number) in the heat transfer process and developed predictive correlations for phase change rate. The new findings would be useful for designers of latent thermal energy storage systems as to whether and how nanoparticles could be potentially used in the design of latent thermal energy storage units.

Acknowledgements

I would like to thank my supervisor, Dr. Xili Duan, for his great guidance and valuable help with this thesis research. It has been a great opportunity to work with Dr. Duan, who consistently supported me during my Ph.D. study. This thesis would have not been possible without his valuable advice and the opportunities he has provided for me to learn and grow professionally. I would like to thank Dr. Yuri Muzychka and Dr. Kevin Pope on my supervisory committee for their support and advice regarding my research. Thank Dr. James and Mr. Dubey for their help in the viscosity measurements.

My Ph.D. study is financially supported by the Natural Sciences and Engineering Research Council of Canada (NSERC) and School of Graduate Studies (SGS) at Memorial University of Newfoundland. The generous financial support of these institutions is highly acknowledged. I am also grateful to work with many graduate students in the Thermofluid and Energy Group.

Last but not least, I want to thank my parents for their consistent support and encouragement, who helped me with every step of my life's journey, particularly during my doctoral program. Undoubtedly, who I am now, and who I will become, I owe to my parents.

Contents

Front Matter

List of Tables

List of Figures

List of Symbols

A_{Mushy} = Mushy zone constant [$kg / m^3 \cdot s$]

B = Boltzmann constant

$\ddot{B}$ = Regression coefficient

C_p = Specific heat [$J / kg \cdot K$]

d_{np} = Nanoparticle diameter [nm]

D = Diffusivity [m^2 / s]

Fo = Fourier number

g = Gravity acceleration [m / s^2]

Gr = Grashof number

h = Specific enthalpy [J / kg]

h_{ref} = Enthalpy at reference temperature [J / kg]

h_{conv} = Convective heat transfer coefficient [$W / m^2 \cdot K$]

H = Height [m]

k = Thermal conductivity [$W / m \cdot K$]

l = Length [m]

L = Specific latent heat [J / kg]

LF = Liquid fraction

Nu = Nusselt number

p = Pitch [mm]

P = Pressure [Pa]

Pr = Prandtl number

q'' = Heat flux [W/m^2]

R = A dependent parameter

Ra = Rayleigh number

s = Momentum source term [Pa/m]

S = Solid-liquid interface location [m]

Ste = Stefan number

t = Time [s]

T = Temperature [K]

T_m = Melting temperature [K]

T_{in} = Inlet temperature [K]

T_{ref} = Reference temperature [K]

$\vec{v}$ = Velocity vector [m/s]

W = Width [m]

x = x-direction [m]

y = y-direction [m]

z = z-direction [m]

Z = Brownian motion constant

Greek letters

α = Thermal diffusivity [m^2/s]

α_o = Fin angle [$\circ$]

β = Coefficient of thermal expansion [$1/K$]

γ = Local liquid fraction

$\ddot{\beta}$ = Regression coefficient

ρ = Density [kg/m^3]

ξ = Similarity variable

μ = Dynamic viscosity [$kg/m\cdot s$]

σ = Standard deviation

ϕ = Volume concentration [$vol.\%$]

Φ = An independent parameter

δ = Uncertainty

δR = Uncertainty of a dependent parameter

$\delta\Phi$ = Uncertainty of an independent parameter

δ_T = Thermal conduction layer [m]

υ = Kinematic viscosity [m^2/s]

ω = Weight concentration [$wt.\%$]

θ = Dimensionless temperature

τ = Dimensionless time

τ_o = Melting time variations [%]

Λ = Thermal conductivity enhancement [%]

Ω = Liquid fraction ratio

η = Grashof number reduction

Υ = Viscosity reduction [%]

Ψ_q = Fluid volume fraction [kg/m^3]

Subscripts

ave = Average

i = Initial

l = Liquid

NF = Nanofluid

r = Integer number, showing the sample number

s = Solid

w = Wall

List of Abbreviations

ADM = Adomian Decomposition Method

ANOVA = Analysis of Variance

CCF = Face-centered Central Composite design

DAQ = Data Acquisition Device

EG = Expanded Graphite nanoparticles

FVM = Finite Volume Method

HTF = Heat Transfer Fluid

LHTES = Latent Heat Thermal Energy Storage

M-TES = Mobilized Thermal Energy Storage

NePCM = Nano-enhanced Phase Change Material

OFAT = One-Factor-at-a-Time

PCM = Phase Change Material

RSM = Response Surface Method

SIMPLE = Semi-Implicit Method for Pressure Linked Equations

TAI = Thermocouple Analogue Input

VIM = Variational Iteration Method

VOF = Volume of Fluid

1-D = One-Dimension

Chapter 1 Introduction

1.1 Background

The solid-liquid phase change is a transformation from one thermodynamic state to another. During the phase change, thermal energy is released or stored latently at the solid-liquid interface, causing one boundary to move. This energy, called latent heat of fusion, is transferred from one phase to another through the heat conduction mechanism or the contribution of conduction and convection mechanisms. In pure materials, the temperature at which the substance's phase changes from solid to liquid or vice versa is called the melting (T_m) or freezing temperature (T_f). Also, if one point is defined as the melting temperature of the substance, the solid-liquid interface can be defined sharply. However, a range of temperatures is defined for an impure substance or alloy when the solid-liquid phase varies over this temperature range. This temperature range makes a third region called "mushy zone" which has an interface with the solid region at the solidus temperature (T_s) and an interface with the liquid region at the liquidus temperature (T_l) of the substance. The exact amount of latent heat released at each temperature in this region is rarely known, and these interfaces are hardly identifiable, but essentially a thickness is considered for this region, depending on the properties of the material.

The solid-liquid phase change has different engineering applications. One of the applications – thermal energy storage using solid-liquid phase change – has gained the attention of many researchers (Oro, De Garcia, Castell, Farid, & Cabeza, 2017). Moreover, solidification and melting of materials widely occur in other engineering applications, such as thermal management in space suits (Mondal, 2008), building materials (D. Zhou, Zhao, & Tian, 2012),

freezing of food or water (Tuan Pham, 2015), solidification of metals in casting (Stefanescu, 2009), to name a few.

Organic PCMs, such as paraffin wax, have high latent heat of fusion, making this type of PCMs suitable in different engineering applications, such as the design of compact thermal energy storage units with large capacity. Reviews on thermal energy storage with phase change material (PCMs) in building applications can be found in (Oro et al., 2017; H. Xu, Romagnoli, Sze, & Py, 2017; D. Zhou et al., 2012). But these PCMs usually have low thermal conductivity, resulting in a low heat transfer rate and long melting (charging) time (Oro et al., 2017). Numerous techniques, including adding fins, ribs, applying surface waviness or porous media, have been employed in order to enhance heat transfer rate of PCMs (Stritih, 2004; Y. Xu, Ren, Zheng, & He, 2017; Zauner et al., 2016; D. Zhou & Zhao, 2011). Another method of improving the heat transfer rate of PCM is by dispersion of highly conductive nanoparticles in it. The resulted mixture is often referred to as Nano-enhanced Phase Change Material (NePCM) (Arıcı, Tütüncü, Kan, & Karabay, 2017; Dhaidan, Khodadadi, Al-Hattab, & Al-Mashat, 2013; L. Fan et al., 2013; Ho & Gao, 2009; Nourani, Hamdami, Keramat, Moheb, & Shahedi, 2016; J. Wang, Xie, Li, & Xin, 2010; Zeng, FAN, Xiao, Yu, & Cen, 2013), which may render the heterogeneous mixture.

Unlike the calculation of the NePCM properties, such as density, specific heat and the latent heat using the thermodynamics rule of mixture, there is not a verified or scientific theory to derive the thermal conductivity and viscosity of the NePCM mixture based on the properties of their constituent materials due to complex behaviour of nanoparticles in the carrier fluid. Besides, the thermal conductivity enhancement in the solid region of the NePCM mixture would be easy to predict, different models were developed to predict the thermal conductivity of the NePCM mixture in the liquid region based on the effective medium theory, Brownian movement, or

interfacial layer and structure of nanoparticles (Michaelides, 2014). Despite developing some models, considering the Brownian motion in the model, the thermal conductivity prediction of the NePCM mixture in the liquid region is still questionable, and not a reliable universally valid model has been developed up to the date. However, it has mostly been accepted that the nanoparticles improve the thermal conductivity of the mixture (L. Fan et al., 2013; Nourani et al., 2016).

Adding nanoparticles in the PCMs can also have its downsides. Increasing the viscosity of the mixture is one negative aspect of adding nanoparticles in PCMs. Analytical and experimental models were used to predict the viscosity of the NePCM mixture. The analytical models are mostly limited to a specific geometry of particles, a small range of nanoparticle concentrations, and other parameters affecting the viscosity of the NePCM mixture, such as size of nanoparticles. These models usually underpredict the NePCM viscosity (Michaelides, 2014). Although the correlations based on the experimental data are capable of predicting the cases under the conditions by which the model is developed, they are incapable of predicting the other datasets.

As mentioned before, using nanoparticles and fins are two techniques that enhance the heat transfer rate of PCMs. Many studies proved that thermal conductivity enhancement causes heat transfer enhancement in nanoparticles-PCM mixtures even though the natural convection reduces.

Fins, regardless of improving heat conduction, may also form local vortexes and increase natural convection during the melting process. Also, adding nanoparticles suppresses the natural convection effect on the melting process. Most of the studies reviewed in the literature review chapter reported a total heat transfer enhancement in simple finless geometries. But does the total heat transfer always increase when nanoparticles are added? These studies reviewed in the literature did not pay attention to what occurs in a situation where natural convection is the dominant heat transfer mechanism. Most studies reported heat conduction enhancement with

nanoparticles compensating for the natural convection reduction, leading to total heat transfer enhancement. What if natural convection is the dominant heat transfer mechanism? What would be the effects of adding nanoparticles to the total heat transfer in that case?

1.2 Objectives and methodology

The main objective of this research is to systematically analyze the effects of nanoparticles on the heat transfer rate of NePCMs and to understand if the effects of nanoparticles are different in situations, causing different contributions between the conduction and convection mechanisms. Thus, analyzing the effects of nanoparticles on the heat transfer rate requires a criterion to be developed to better judge the effectiveness of the nanoparticles in the PCMs used in different applications, such as thermal energy storage, thermal insulation and cooling heat exchangers of electronic devices. Although the findings are obtained from different geometries in this thesis, the thesis first aim, the effects of nanoparticles on the phase change heat transfer rate, remains unified.

The research starts with solving a one-dimensional two-region melting problem and conducting some scaling analysis for a rectangular enclosure heated from the bottom to understand the heat transfer regimes, occurring during the melting problem as shown in **Fig. 1-1**. After better understanding the phase change problem, a rectangular enclosure heated from one side is designed and built to understand and study the melting problem in the presence of Rayleigh-Benard convection (Bejan, 2013). Designing a simple rectangular enclosure let us validate the experimental setup with an analytical solution in the absence of natural convection. To do this, the enclosure's walls are made of plexiglass with low thermal conductivity, to insulate the walls and, transparent, to visualize inside the enclosure. A data acquisition system will also be utilized for measurement purposes. At first, the enclosure will be filled with a pure PCM, and a hot plate is placed on top of the enclosure to provide a uniform temperature. It is worth noting that the hot

plate is a temperature controlling plate, and its duty is to keep the wall temperature at a certain temperature, which is above the PCM melting point used in this thesis. The temperature distribution of the enclosure will be recorded using the data acquisition system. To validate the results obtained from the enclosure, the results will be compared with the analytical solution. The results will be valid if a reasonable discrepancy is observed between these two different approaches (experimental and analytical approaches). In the case of the hot plate at the bottom, the Rayleigh-Benard convection is created, and then, a numerical simulation will be carried out. The numerical model will also be compared with the experimental results.

To analyze the effects of nanoparticles on the melting rate, the enclosure designed and built earlier is implemented for further experiments. This time, the enclosure is filled with the NePCM to systematically examine the effects of various nanoparticle concentrations on the heat transfer rate. During a series of experiments, it will be investigated whether a concentration of nanoparticles would have the same effect on the melting rate at different temperatures set at the boundary. If not, what are the reasons for these changes in the melting rate behaviour with the same nanoparticle concentration? The results of the experiment not only reveal the importance of nanoparticles in a rectangular enclosure heated from the bottom, but also indicate a significant fact about adding nanoparticles and increasing the heat transfer rate. This fact that will be discussed later may be one important reason to differentiate conclusions made about the melting rate after adding nanoparticles. The thermal conductivity and viscosity of the samples will be measured to understand how much the thermal conductivity, the Grashof and Rayleigh numbers change after adding nanoparticles. This will also help understand how much the thermal conductivity enhancement should be in the case of Grashof number reduction in a rectangular enclosure heated from the bottom.

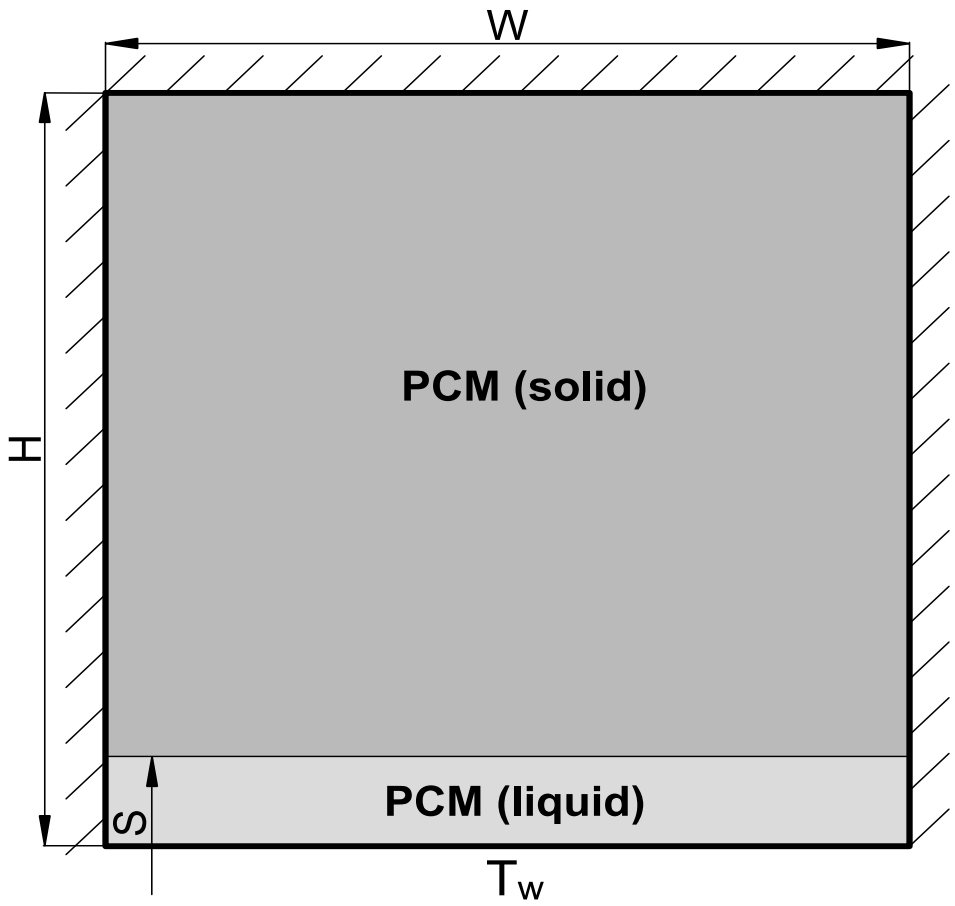

Fig. 1-1 Two-dimensional view of the melting problem in an enclosure heated from the bottom.

To evaluate the key findings obtained from studying the effects of nanoparticles on a rectangular enclosure heated from the bottom, this thesis will investigate similar problems in two commonly used latent heat thermal energy storages (LHTES) which are more realistic, such as shell-and-tube LHTES with and without fins.

First, the effects of nanoparticles will be evaluated on the heat transfer rate in a shell-and-tube LHTES unit (See **Fig. 1-2**), which is the simplest design and most commonly used, through a series of numerical and statistical analysis. The geometry orientation should be selected in a way that guarantees the creation of natural convection mechanism, which contributes to the total heat transfer. This is because the contribution of both conduction and convection is the issue studied

throughout this thesis in the presence of nanoparticles. The simplicity of the geometry will let us focus on the objective of the thesis. A numerical approach is implemented to simulate the NePCMs at different concentrations using the commonly used nanoparticles' thermal properties correlations. To analyze the data obtained numerically, a statistical approach will be employed to understand if there is any interaction between the selected parameters, affecting the heat transfer rate. This interaction means the distinct effect of a parameter, nanoparticle concentration for example, on the heat transfer rate, while other parameters are set at different values.

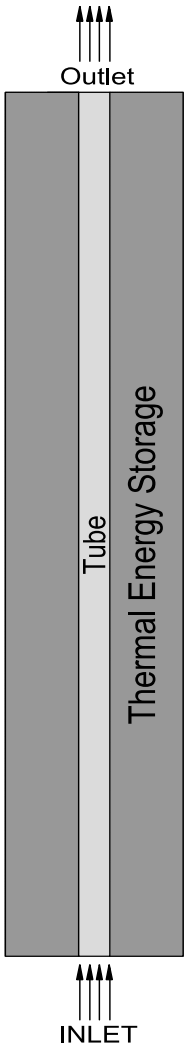

Fig. 1-2 Schematic diagram of a simple shell and tube thermal energy storage unit.

To study another realistic shell -and-tube LHTES, some fins are mounted to the outer wall of the tube and the new shell-and-tube is numerically simulated. The position and design of the fins will be chosen from a form that facilitates the local vortex formation, and subsequently the convective heat transfer mechanism. This design causes the natural convection mechanism of heat transfer to become dominant at the early stage of melting in a shell and tube unit mounted with fins. The importance of the vortex formation to enhance the heat transfer rate will later be seen in the results of the finless shell and tube unit explained above and an enclosure heated on one side (Bejan, 2013). In this research, the effects of nanoparticles and fins are numerically and statistically studied regarding the heat transfer rate in the presence of the fins. This helps analyze that whether the nanoparticles can still enhance the melting rate in a realistic shell-and-tube LHTES in which the convection mechanism becomes dominant at the early stage of melting.

1.3 Significance of this research

This research systematically analyzes the effects of nanoparticles on the phase change rate and to understand the reason for the many contradicting findings in the literature, regarding the melting rate after dispersing nanoparticles in PCMs. This research is important in two ways. One, the specific findings that are reached out after studying each case, which will provide useful information about the case under study. Two, the reasons that nanoparticles behave differently in terms of improving the phase change rate in different situations.

The research also provides useful scaling analysis for the melting problem in the presence of Rayleigh-Benard convection and nanoparticles for the first time. Afterwards, the melting process of a PCM will be analyzed experimentally and numerically, and a solid-liquid melting rate correlation will be developed, which has not been seen in the literature. For the first time, the effects of nanoparticles will be analyzed in a rectangular enclosure heated from the bottom

experimentally, and the research comes to a conclusion regarding the contradicting conclusions found in the literature.

This research further evaluates the key findings obtained experimentally in a more realistic LHTES and provides useful insight to design a shell-and-tube LHTES filled with PCM/NePCM. The possibility of existing interactions between different parameters will be studied, which is generally ignored in other studies.

In another commonly used and realistic LHTES, the shell-and-tube LHTES will be modified and mounted with fins to statistically and numerically study the effects of nanoparticles on the melting rate. Although a useful insight will be provided by arranging the position of the fins, the key findings obtained and evaluated earlier will be examined in this LHTES mounted with fins, and useful results will be obtained that can be applied to better design of LHTES.

1.4 Outline of the thesis

In chapter one (Introduction), the fundamental concepts of the topic were introduced along with some engineering applications in the field of study. The weakness of the phase change materials (PCMs) mainly used in these applications was also discussed. Then, some solutions to this PCMs weakness were briefly discussed. As one solution to the PCMs drawbacks, the pros and cons of adding highly conductive nanoparticles in PCMs were generally pointed out. The objectives of this research were also explained in chapter one. The objectives were accompanied by a research methodology to explain how the objectives will be met. The significance of this research was also discussed in this chapter.

In chapter two, a literature review is presented based on the solid-liquid phase change heat transfer, some commonly known and recently proposed ways to increase the solid-liquid phase

change heat transfer, and the advantage and disadvantage of these methods. The review will finally focus on the effect of nanoparticles on the melting rate to find the gap in this field of study.

In chapter three, the mathematical modelling of a melting problem is presented. At first, the solution for a one-dimensional two-region Stefan problem is introduced. This helps understand the concept of a melting experiment, design a rectangular enclosure in a proper size, and compare the experimental data with the analytical solution. Afterwards, a scaling analysis will be performed to understand the heat transfer regimes that may form in the case of heating the enclosure from the bottom, causing the Rayleigh-Benard convection. The governing equations and numerical approaches developed to simulate the melting problem will be described along with the correlations for nanofluids properties used to predict the thermal properties of the samples. Finally, the statistical approach used in this research will be introduced.

In chapter four, the enclosure and experimental setup will be designed and built; and then, the test procedure will be explained in this chapter along with the nano-enhanced phase change material sample preparation.

In chapter five, a numerical model will be developed to simulate a melting problem in a rectangular enclosure heated from the bottom. Afterwards, the enclosure designed and built earlier will be employed to conduct experiments for the case that the enclosure is heated from the bottom. The numerical and experimental results will provide complementary data about the heat transfer regimes created in this problem, and also be compared together. The experiments will be continued to analyze the effects of nanoparticles on the melting rate using the NePCMs with different nanoparticle concentrations. Finally, empirical correlations will be developed to predict the melting problem in this chapter.

In chapter six, the key finding obtained from the NePCM experiments will numerically and statistically be evaluated in a commonly used and simple shell-and-tube heat exchanger to gain further understanding of the problem.

In chapter seven, the shell-and-tube phase change heat exchanger studied in the previous chapter will be modified and some fins are mounted to the tube to evaluate the effect of nanoparticles on the solid-liquid phase change. This helps gain further understanding of the problem and the key findings obtained from the previous experimental and numerical results.

In chapter eight, the thesis will be summarized along with my conclusions and recommendations for future research trajectories.

Chapter 2 Literature review

This chapter presents a literature review on the existing analytical solutions of conduction driven phase change heat transfer problems and the effects of nanoparticles on the melting rate in the cases where both heat conduction and convection mechanisms affect the heat transfer rate.

2.1 Predictive models of solid-liquid phase change problems

Early analytical works modelled ice formation (Clapeyron & Lame, 1831; Stefan. J, 1891). The pioneers of moving boundary problems, also referred to as Stefan problems, were Clapeyron and Lame who studied them first in 1831(Clapeyron & Lame, 1831). The family of moving boundary problems are named Stefan problems due to early articles (Stefan. J, 1891; Stefan, 1889) written by Stefan. He indicated that melting and solidification rates are governed by a dimensionless number now called the Stefan number (Ste) which is defined by:

$$Ste = \frac{C_p(T_m - T_w)}{L} \tag{2-1}$$

where C_p is the specific heat of the substance, T_m is the substance melting temperature, T_w is the boundary or wall temperature and L is the latent heat of the substance.

To solve the Stefan problem, two functions need to be determined. One describes the temperature distribution $T(x,t)$ over the domain, and the other one explains the position of the solid-liquid interface $S(t)$. Solving solid-liquid phase change problems is analytically complicated and impossible in many situations. This is because of many factors affecting the phase change, such as the geometry complexities and multidimensionality, boundary conditions, impurity of the substance or formation of mushy zone, emergence of natural convection due to the density and gravity, changes in properties (conductivity, density and specific heat) with temperature, and surface tension at the free space etc.

To formulate the solid-liquid phase change and to provide an analytical solution, we simplify the solid-liquid phase change into a one-dimensional domain where a sharp interface separates solid and liquid phases, and the thermal properties of the substance do not change with temperature. The fundamental relations are to be satisfied with two conditions: (1) The temperature at the adjacent phases should be equal to a constant temperature called melting temperature, T_m , (2) an energy balance must be satisfied at the interface. The mathematical formulations, defining these requirements are derived in a two-region one-dimensional transient melting/solidification process. The term "two-region" is given to this problem, which was first studied by Neumann in a 1912 study (Neumann, 1912), due to the existing temperature distribution at both the solid and liquid phases, while one region remains at the melting temperature in a one-region Stefan problem. The domain is initially in a liquid state in a temperature lower than the substance melting temperature, then, the solidification process starts. Neumann found the exact solution for this problem in terms of a similarity variable, which is $\xi = \frac{x}{2\sqrt{\alpha_l}}$ (Neumann, 1912).

There is a mushy zone formed between the solid and liquid regions mainly in impure materials. To cover the mushy zone, Cho and Sunderland assumed that the solid fraction (f_s) varies linearly between solidus interfaces $(s_{sol}(t))$ and liquidus interfaces $(s_{sol}(t))$. They modified the phase change governing equations with some changes to cover the mushy zone, and found an exact solution for a three-region, one-dimensional, semi-infinite phase change problem (Cho & Sunderland, 1969).

The integral method, an approximate solution to the exact modelling equations, was used to solve a one-dimensional transient melting problem by Goodman (T. Goodman, 1961; T. R. Goodman, 1958), and by many other researchers (T. Myers, 2010; T. Myers, Mitchell, Muchatibva, & Myers, 2007; Yao & Cherney, 1981; Zhang & Faghri, 1996). The method is relatively simple and straightforward. An arbitrary function is chosen for the temperature profile, for example, a second-degree polynomial approximation, and then the coefficient of each term in the arbitrarily chosen function is defined based on the boundary conditions.

The integral method could also be combined with the exact solution to find the phase change solid-liquid time in a two-region problem. Tien and Geiger (Tien & Geiger, 1967) also considered the mushy zone in a phase change problem and combined the integral method with the exact solution to find the phase change time.

Using a moving heat source is another method to solve phase change problems and is based on the absorption of latent heat, which can be treated as a moving heat source or sink. This method was analytically used to solve one-dimensional transient phase-change problems and later numerically developed for other conditions (Devesse, Baere, & Guillaume, 2014; Leung, 2001; Lightfoot, 1929). In this method, the phase change problem is replaced by an equivalent transient heat-conduction problem with a moving-plane heat sink or source located at the solid-liquid interface.

The perturbation method, an approximate analytical solution was used by many researchers (Jiji & Weimbaum, 1974; Pedroso & Domoto, 1973; Rathjen & Jiji, 1970; Seniraj & Bose, 1982) for one-dimensional semi-infinite phase change problems. In this method, the temperature and the interface transition rate equations are expanded in the form of a power series about the perturbation parameter, Ste. Using the perturbation method, a sequence of solvable partial differential equations (PDEs) are obtained, which should be solved as the solution of the first PDE implemented to address the next PDE, and so on. After finding the solution for all terms, the sum of them forms a final resulting equation describing the variation of the interface position.

The heat-balance integral method introduced earlier is a particular form of the weighted residual method (T. R. Goodman, 1964). The integral method has been updated by some researchers (T. Myers, 2010) (Mitchell & Myers, 2010a) (Mitchell & Myers, 2010b; Wood, 2001) (T. G. Myers & Mitchell, 2011). The most updated heat balance integral method, the combined integral method, has a higher accuracy than other heat balance integral methods. The method can cover different boundary conditions, including the time-dependent boundary condition in both one-region and two-region Stefan problems.

The homotopy perturbation method (J.-H He, 1999a, 2000, 2004, 2005, 2006c, 2006a, 2006b, 2008, 2009), developed by He, is the combination of two methods, namely, the homotopy analysis method (Liao, 1998, 2003, 2004, 2009, 2012), developed by Liao, and the perturbation method (Ganji & Rajabi, 2006; Jiji & Weimbaum, 1974; Nayfeh, 1973; Pedroso & Domoto, 1973; Rathjen & Jiji, 1970; Seniraj & Bose, 1982). The procedure for the homotopy analysis method can be obtained in detail in (Liao, 1998). These methods can be used in nonlinear partial differential equations, and they were widely used to solve Stefan problems (Caldwell & Kwan, 2003; Singh, Gupta, & Rai, 2011b).

The Adomian decomposition method (ADM), developed by G. Adomian (Adomian, 1983), is based on the search for a solution in the form of a series, and involves decomposing the nonlinear operator into a series. The terms of the series are calculated recursively using Adomian polynomials (Adomian, 1994). The method was used in different applications, including nonlinear heat equations (Adomian, 1988; Pamuk, 2005; Wazwaz, 2001). This method was also used to solve Stefan problems (Radosław Grzymkowski & Słota, 2005). The variational iteration method (VIM), developed by He (J.-H He, 1998b, 1998a, 1999b, 2006c), is a modification of a general Lagrange multiplier method (Inokuti, Sekine, Mura, & Nemat-Nasser, 1978), and was implemented to determine the solution of non-linear differential equations in different applications (Abdou & Soliman, 2005; J-H He, 2000; J.-H He, 2007). The one-region and two-region Stefan problems were solved using VIM in some studies (Słota, 2007) (Słota & Zielonka, 2009) (Rajeev, Nath, & Subir, 2009) (E Hetmaniok, Słota, & Zielonka, 2009) (Singh, Gupta, & Rai, 2011a). The procedures of ADM and VIM are similar. A detailed comparison of these two methods can be found in a 2011 study (Edyta Hetmaniok, Słota, Witua, & Zielonka, 2011). By solving a one-region Stefan problem, it was concluded that VIM is fairly more effective than ADM in terms of accuracy for solving the Stefan problem.

Similarity transformation was widely used to convert the partial differential governing equations implemented to solve the Stefan problem into ordinary differential equations. In one attempt, the similarity transformation was used to solve the Stefan problem with varying diffusivity (Voller & Falcini, 2013). In another study (Kumar, Singh, & Rajeev, 2018), the similarity solution was used to transform the PDE of a

one-region Stefan problem into an ordinary differential equation. Then, a shifted Chebyshev tau method (Doha, Bhrawy, & Ezz-Eldien, 2011; Doha, Bhrawy, & Ezzeldeen, 2011; Ghoreishi & Yazdani, 2011) was used to solve the transformed system. The similarity solution was also used to solve a one-region Stefan problem with temperature-dependent thermal conductivity (Ceretani, Salva, & Tarzia, 2018; Natale & Tarzia, 2003), a two-region Stefan problem (Ceretani & Tarzia, 2016; Lombardi & Tarzia, 2001), a two-region Stefan problem with a time-dependent heat flux boundary condition and temperature-dependent physical properties (Briozzo & Tarzia, 2002), and a three-region Stefan problem (Evgeniy N. Kondrashov, 2006). The analytical methods reviewed above are listed in **Table 2-1**.

Table 2-1 Different analytical methods.

Method	Study	Approx./ Exact	Domain	Validation	Coordinate system	# of regions	Comment
Early Methods	(Neumann, 1912)	Ex	1D	-	Ca	2	-
	(Paterson, 1952)	Ex	1D	-	Cy	2	-
	(Cho & Sunderland, 1969)	Ex	1D	-	Ca	3	-
	(Lightfoot, 1929)	Ap/Ex	-	Ex	-	2	-
	(Seniraj & Bose, 1982)	Ap	-	Ex	-	2	Suitable for complicated geometries Robin condition
	(London & Seban, 1943)	Ap	1D	Ex	Ca	1	Robin condition
	(Foss & Fan, 1972)	Ap	1D	Ex	Ca	2	Constant slope at interface
Integral method	(T. Goodman, 1961)	Ap	1D	Ex	-	1	Could be off from the exact solution depending on the function chosen for temperature
	(Tien & Geiger, 1967),	Ap	1D	Ex	Ca	3	-

(T. Myers et al., 2007)	Ap	1D		Ca	2	Cubic heat balance integral method; Finite domain
(Sadoun, Si-Ahmed, & Colinet, 2006)	Ap	1D	Ap (Wood, 2001); Ap (Mennig & Ozisk, 1985); Ap (Caldwell & Kwan, 2003)	Ca	1	Time-dependent boundary condition
(T. Myers, 2010)	Ap	1D	Ap (T. Myers et al., 2007) Ap (Braga, 2004)	Ca	1	Time-dependent heat flux boundary condition
(Mitchell & Myers, 2010b)	Ap	1D	Ap (CIM/ RIM)	Ca	1	Time-dependent boundary condition
(Mitchell & Myers, 2010a)	Ap	1D		Ca	1	Dirichlet and Robin conditions. Quadratic, cubic and exponential approximating functions
(T. G. Myers & Mitchell, 2011)	Ap	1D	Ex/Ap/ N (Mitchell & Vynnycky, 2009) (FDM)	Ca	1/2	Dirichlet /Neumann/ time-dependent boundary conditions

	(Mitchell, 2015)	Ap	1D	Ap/ N (FDM)	Ca	2	Neumann/ Robin conditions Finite domain
	(Mitchell, 2012)	Ap	1D	Ex/ Ap (HBIM) / N (Mitchell & Vynnycky, 2009)	Ca	1	Finite domain
Eigenvalue Expansion	(Talati, Mosaffa, & Rosen, 2011)	Ap	2D	N (Carslaw & Jaeger, 1959) (Enth)	Ca	1	Neumann condition 2D domain was simplified to two 1D domains
	(Mosaffa, Talati, Rosen, & Tabrizi, 2012)	Ap	2D	N (Carslaw & Jaeger, 1959) (Enth)	Ca	1	2D domain was simplified to two 1D domains Robin condition
	(Khalid, Zubair, & Ali, 2017)	Ap	1D	Ex (Ozisk & Necati, 1993) (EIFM)	Cy	2	Dirichlet/ Robin conditions Finite domain
HPM	(Caldwell & Kwan, 2003)	Ap	1D	A (Mennig & Ozisk, 1985) N (Calwell & Ozisk, 2002) (Enth)	Ca / Cy/ Sph	1	Time-dependent boundary condition

	(Singh et al., 2011b)	Ap	1D	Ex	Ca	1	Dirichlet Condition Fractional diffusion solid-liquid modelling Finite slab
	(Rajeev & Kushwaha, 2013)	Ap	1D	Ex	Ca	1	Neumann condition Variable latent heat Fractional diffusion solid-liquid modelling Not suitable for long phase-change time
	(Rajeev, 2014)	Ap	1D	Ex	Ca	1	Neumann condition Variable latent heat
ADM	(Qin, Duan, & Yin, 2014)	Ap	1D	Ex	Ca	2	Finite domain Neumann and Robin conditions
	(Bougoffa, Rach, Wazwaz, & Duan, 2015)	Ap	1D	N (FDM)	Ca	1	Neumann boundary condition Variable latent heat
VIM	(Słota & Zielonka, 2009)	Ap	1D	Ex	Ca	1	Curvilinear domain converted to rectangular domain

	(Słota, 2007)	Ap/Ex	1D	Ex	Ca	1	Neumann condition
	(E Hetmaniok et al., 2009)	Ap	1D	Ex	Ca	1	Curvilinear domain converted to the rectangular domain
	(Rajeev et al., 2009)	Ap	1D	-	Ca	1	Time-dependent boundary condition
	(Singh et al., 2011a)	Ap	1D	Ex & Semi- Analytical	Ca	2	Temperature-dependent physical properties
	(Edyta Hetmaniok et al., 2011)	Ap	1D	Ex	Ca	1	-
	(Voller & Falcini, 2013)	Ex	1D	-	Ca	1	Variable diffusivity
Similarity Solution	(Y. Zhou, Wang, & Bu, 2014)	Ex	1D	-	Ca	1	Variable latent heat Neumann condition
	(Kumar et al., 2018)	Ap	1D	Ex	Ca	1	Temperature-dependent thermal conductivity Time-dependent boundary condition
	(Ceretani & Tarzia, 2016)	Ex	1D	-	Ca	2	Robin condition

(Evgeniy N. Kondrashov, 2006)	Ap	1D	-	Ca	3	Dirichlet condition Temperature dependent properties
(Briozzo & Tarzia, 2002)	Ex	1D	-	Ca	2	Time-dependent heat flux Nonlinear physical properties
(Lombardi & Tarzia, 2001)	Ex	1D	-	Ca	2	-
(Natale & Tarzia, 2003)	Ex	1D	-	Ca	1	Temperature-dependent thermal conductivity Time-dependent heat flux
(Ceretani et al., 2018)	Ex	1D	-	Ca	1	Temperature-dependent thermal conductivity Robin condition
(Radoslaw Grzymkowski, Hetmaniok, Pleszczynski, & Slota, 2013)	Ap	1D	N	Ca	1	Dirichlet condition

Other Methods	(Kartashov & Krotov, 2009)	Ex	1D	-	Ca	1	Dirichlet, Neumann and Robin conditions
	(Feltham & Garside, 2001)	Ap	1D	N	Ca / Sph	2	-
	(Alexandrov, Nizovtseva, Malygin, Huang, & Lee, 2008)	Ap	1D	Ex	Ca	3	-
	(E. N. Kondrashov, 2007)	Ex	1D	-	Ca	3	Finite slab Considering convective term
	(E N Kondrashov, 2009)	Ex	1D	-	Ca	3	Considering the relative movement of the phases
	(F. Li, Liu, & Yue, 2009)	Ex	3D	-	Ca	2	No analytical solution
	(Pan et al., 2017)	Ap	1D, 2D, 3D	Ex & N (FVM)	Ca	1	The semi-analytical solution failed

* Ex: Exact, * AP: Approximate, *Ca: Cartesian, *Cy: Cylindrical, *Sph: spherical, *HBIM: Heat Balance Integral Method, *HPM: Homotopy Perturbation Method, * Enth: Enthalpy method, *CIM: Combined Integral Method, *RIM: Refined Integral Method, * N: Numerical, * FDM: Finite Difference Method, * FVM: Finite Volume Method

2.2 Effects of nanoparticles on the melting rate

In this section, the effects of nanoparticles are reviewed in different geometries in three subsections. In the first subsection, the effects of nanoparticles on rectangular enclosures are reviewed, and the review will help build the experimental setup of this research. The next two subsections review the effects of nanoparticles on other simple and complex geometries that help find the gap in the numerical and statistical study of this research.

2.2.1 Rectangular enclosures

Judging from several different engineering applications of PCMs, PCMs in square enclosures that are heated from the side or bottom are very conventional. The former is representative of solar collectors and double-wall insulations, for example, while the latter refers to the thermal insulations oriented horizontally and cooling heat exchangers of electronic devices. For simplicity, enclosure means a square enclosure in this thesis unless another shape is specified.

The heat transfer process in the enclosures, which are heated from the side can be explained by defining four regimes. These regimes are the conduction regime, the mixed conduction and convection regime, the convection regime, and the shrinkage solid regime (Jany & Bejan, 1988). The heat transfer starts by means of conduction, up to a certain point, where the solid-liquid interface starts deforming from the top. This makes the rectangular shape of the liquid region deformed due to the advent of the natural convection mechanism of heat transfer. From this point, the mixed conduction and convection heat transfer is responsible for the melting rate until the thermal boundary layer formed in the lower extremity of the curved zone (upper zone) becomes the same order of the solid-liquid thickness of the lower (conduction) zone. Then, natural convection becomes the dominant heat transfer mechanism (third regime) until the solid-liquid

interface reaches to the right wall of the enclosure, which will soon be the beginning of the fourth regime. A detailed scaling analysis of this problem can be found in (Jany & Bejan, 1988).

From the above description, the contribution of conduction and convection heat transfer mechanisms is clearly seen on a phase change heat transfer problem in an enclosure heated from one side. This contribution between heat conduction and convection will be different if nanoparticles are added to the PCM. To study this, the ratio of height to width of the enclosure, the kind of boundary condition, the boundary condition at the remaining walls of the enclosure, the nanoparticle type and concentration, the thermal property variation of the mixture, the thermal conductivity enhancement, the Rayleigh number variation after dispersing nanoparticles, and the Stefan number may be necessary to be considered. In an enclosure with a Dirichlet boundary condition at one vertical wall, and an adiabatic condition at the remaining walls, for example, the rate of heat transfer and solid-liquid phase change increased with an increase of nanoparticle concentration (Kant, Shukla, Sharma, & Henry Biwole, 2017; Sebti et al., 2013). This enhancement is more pronounced if the temperature difference between the hot wall and the melting point of the NePCM increases (Sebti et al., 2013). This conclusion is rejected if the melting process occurs in an enclosure filled with copper oxide nanoparticles and cyclohexane at low Rayleigh numbers (Tasnim, Hossain, Mahmud, & Dutta, 2015). The reason for the discrepancy between the conclusions of these studies may lie on the ignored parameters listed above. None of these studies, for example, analyzed the problem in a wide range of Rayleigh numbers. The conclusion in (Kant et al., 2017) is, for example, based on one specific temperature difference between the hot wall temperature and the melting point. Also, the Rayleigh number and Stefan number ranges are not given in (Sebti et al., 2013), even though early analytical and experimental

works on the melting problems emphasized the importance of the Rayleigh number in an enclosure heated from the side (Jany & Bejan, 1988; Okada, 1984).

Previous studies mainly ignored to state the parameters, such as Ra and Ste numbers. However, more parameters are considered and studied in a melting heat transfer problem in an enclosure heated from one side by applying a Neumann boundary condition, while the remaining walls are insulated. In one attempt (Ho & Gao, 2013), it was found that the thermal conductivity enhancement is not able to compensate for the adverse effect of nanoparticles on natural convection in a range of Rayleigh numbers ($Ra = 1.71\times10^{6} - 5.67\times10^{7}$), leading to a degradation of heat transfer rate for a range of nanoparticles. However, dispersing nanoparticles in PCM led to an improved melting rate in a range of Rayleigh numbers ($Ra = 3.59\times10^{8} - 9.97\times10^{8}$) in another study (Al-Jethelah, Tasnim, Mahmud, & Dutta, 2018), even though nanoparticle concentration was fixed at one value. These studies performed better by specifying the range of Rayleigh and even Stefan numbers, but they did not conclude if the same conclusion would be obtained at a lower or higher Rayleigh number or a broader range of nanoparticles. Also, they did not measure the thermal properties of each NePCM sample. There might be a critical concentration of nanoparticles at which the heat transfer rate would behave differently from the behaviour reported in (Al-Jethelah et al., 2018; Ho & Gao, 2013). This critical concentration may be different at each Rayleigh number. There has not been a study conducted on an enclosure heated from one side, which found this point.

Similarly, the heat transfer process in an enclosure heated from the bottom forms Rayleigh-Benard convection and can be explained by defining two regimes, namely, conduction domination and convection domination regimes. In the conduction domination regime, the fluid is quiescent and the temperature changes linearly between the hot and cold boundaries, while the convection

mechanism starts dominating at a critical Rayleigh number on the order of 10^3 (Bejan, 2013). This is the classical Benard problem, in honour of H. Benard, who first studied this problem in 1900. By knowing these definitions, the nanoparticles may affect each of these regimes.

In contrast with the enclosures heated from one side, not many NePCM melting problems have seen studied in an enclosure heated from the bottom to the best of authors' knowledge. In one numerical study (Feng, Li, Li, Bu, & Wang, 2015), increasing the concentration of nanoparticles improved the melting rate at two different values of Grashof numbers even though the correlations for nanofluid properties listed in chapter 3 were used to find the NePCM properties, which may not be realistic (Bahiraei, Fartaj, & Nazri, 2017). Furthermore, the range of Rayleigh number is unclear, which may make the conclusion of the study only valid at the conditions of the research. This point can also be understood from the contradicting conclusions obtained from (Feng et al., 2015) and other studies (A. V. Arasu & Mujumdar, 2012; Ghalambaz, Doostani, Izadpanahi, & Chamkha, 2017), as the heat transfer rate decreased with an increase in nanoparticle concentration in the latter studies.

2.2.2 Other geometries

The effects of nanoparticles on the melting rate has been reviewed in other geometries. Many of these LHTES systems have been widely studied in other geometries other than rectangular enclosures (Al-Abidi, Mat, Sopian, Sulaiman, & Mohammad, 2016; Dutil, Rousse, Salah, Lassue, & Zalewski, 2011; Khodadadi & Hosseinizadeh, 2007; Nomura, Tsubota, Oya, Okinaka, & Akiyama, 2013; Zeng et al., 2013). In a two concentric cylinders geometry, the charging and discharging (solidification) times of thermal storage units with the dispersion of different mass fractions (2, 5, 10 wt.%) of CuO in paraffin wax was explored (Jesumathy, Udayakumar, & Suresh, 2012). Water with different flow rates was implemented as the heat

transfer fluid (HTF) into two concentric cylinders. Nano-enhanced phase change material was stabilized using the ultrasonic vibrator without surfactant. At the early stage of heating, energy was sensibly absorbed in the paraffin wax and the temperature of the paraffin wax gradually increased to its melting point, then, energy was latently stored. The total melting and solidification time reduction and linear increase of dynamic viscosity with higher nanoparticle mass fractions were also reported in this study. The thermal storage unit was also simulated to understand the effect of copper nanoparticles (Cu) dispersed in R50 fluid on melting time, liquid fraction, and penetration length into two concentric tubes filled with solid NePCM (S. M. J. Hosseini, Ranjbar, Sedighi, & Rahimi, 2013). It was found that that the thermal penetration depth of molten fluid accelerated with a higher concentration of the nanoparticles. As before, this conclusion may be different at different experimental conditions. In a similar geometry, for example, the thermal conductivity and melting time of paraffin wax with Al_2O_3 was evaluated in different volume fractions along with the melting rate in the presence of natural convection (A. valan Arasu, Sasmito, & Mujumdar, 2013). Regardless of a very high volume fraction of the nanoparticles under study, which may not be realistic, not a significant heat transfer rate enhancement was reported in the presence of both conduction and convection mechanisms of heat transfer. However, a Al_2O_3 volume fraction dispersed in pure water (as PCM) showed heat transfer improvement at different flow rates and temperatures in a thermal storage unit (Altohamy, Abd Rabbo, Sakr, & Attia, 2015), although the Rayleigh number range was not calculated. In another study, a finless thermal energy storage unit studied in (Aydin, Akgun, & Kaygusuz, 2007) was optimized (Sciacovelli, Colella, & Verda, 2013) by nanoparticles. The melting process of pristine paraffin wax with copper nanoparticles of different volume fractions in a vertical cylindrical shell and tube thermal storage unit was analyzed. It was concluded that the heat transfer rate increased with

additional nanoparticles in the Rayleigh number range under study, although it is not clear if the heat transfer rate shows a different trend in a larger nanoparticle concentration range. Improving the melting rate and expediting the charging time (melting time) were also reported in some studies (Dhaidan et al., 2013; Rabienataj Darzi, Jourabian, & Farhadi, 2016). However, some other studies (Bahiraei et al., 2017; Ho & Gao, 2009) reported unchanged or longer charging time when nanoparticles were added in PCMs. Some studies showed a critical nanoparticle concentration at which the trend of heat transfer rate will change with an increase in nanoparticles (Arıcı et al., 2017; Ebrahimi & Dadvand, 2015). It was found that the increased viscosity and reduction of natural convection in the melted PCMs leads to insignificant improvement or even a decrease of the total heat transfer rate in the LHTES units, even with a confirmed increase of thermal conductivity of the NePCMs (Ho & Gao, 2009). In other words, weakened natural convection mostly overweighed enhanced heat conduction and slowed the melting down in the complex geometries. These issues seem common for many different NePCMs, such as carbon nanotubes in 1-dodecanol (Zeng et al., 2013), aluminum oxide and copper oxide in paraffin (Ho & Gao, 2009). With nanoparticles, the reduction of natural convection was clear even in studies that showed improvement in total heat transfer and fast charging (A. valan Arasu et al., 2013; L. W. Fan, Zhu, Zeng, Lu, & Yu, 2014; Sciacovelli et al., 2013).

With these issues, researchers turned their interests to the traditional method of heat transfer enhancement with fins, with or without nanoparticles in PCMs. The effectiveness of fins in LHTES units has been demonstrated by many researchers (Tay, Bruno, & Belusko, 2013; Yang et al., 2017) and the effects of fin parameters, i.e., numbers, height and thickness, were analyzed on local natural convection and melting time. The melting performance of an LHTES unit with Y-shaped fins on the outer surface of an HTF tube and the same unit without fins, but with different

volume fractions (0.025 and 0.05) of nanoparticles in the PCM were analyzed (Lohrasbi, Sheikholeslami, & Ganji, 2016). It was found that the solidification rate in the LHTES unit with Y-shaped fins is significantly higher than that in the finless LHTES unit with nanoparticles. In a similar study (Sheikholeslami, Lohrasbi, & Ganji, 2016a), the Y-shaped fins were replaced by snowflake-shaped fins in LHTES units, and a similar conclusion was obtained. Although these authors did not mention any other basis in their comparison, they did report that the change of maximum energy capacity is negligible when fins or nanoparticles are added, and they ignored the effects of natural convection. Later on, a more systematic comparison was conducted to evaluate the heat transfer enhancement using nanoparticles and/or fins by considering triplex-tube LHTES units in three categories, i.e., nanoparticles alone, fins alone, and a fins-nanoparticles combination (Jasim M. Mahdi & Nsofor, 2017). The total volume fraction of nanoparticles and fins were set to 0.02, and it was demonstrated that the highest heat transfer rate (leading to a 59.2% faster charging time) was achieved when the fin volume fraction was 0.02 (no nanoparticles). These results indicate that finned LHTES might be a better solution than nanoparticle dispersion in terms of total heat transfer rate and charging/discharging time.

However, these studies missed one important aspect in the comparison of LHTES enhancement with fins or nanoparticles – the interactive effects between these two parameters. For example, will adding nanoparticles change the total heat transfer rate the same way with and without fins? Or how do the fins improve heat transfer in LHTES systems with or without nanoparticles? Many studies on heat transfer enhancement for LHTES indicated potentially important interactions between different parameters. For example, the dependency of nanoparticle enhancement on the porosity of a porous foam triplex-tube LHTES heat exchanger was demonstrated in a 2017 study (J. M. Mahdi & Nsofor, 2017). In studies on charging performance

of a mobilized thermal energy storage (M-TES) unit, the effects of flow rate, the geometry of flow channels, fins, expanded graphite (EG) nanoparticles, ways of wall heating, direct or indirect contact, etc. were analyzed (Shaopeng Guo, Li, Zhao, Li, & Yan, 2013; Shaopeng Guo et al., 2016; W. Wang et al., 2014, 2015). Their results indicate strong interactions between these parameters in determining the melting and solidification of PCM in the M-TES units. Similarly, the solidification and melting of PCM were enhanced by radial fins and nanoparticles in cylindrical annulus and analyzed. Both methods were found to be effective for heat transfer enhancement, but simultaneous effects of fins and nanoparticles were not studied. With potential interactions between multiple parameters in LHTES, it is desirable to simultaneously analyze the effects of fin and nanoparticle parameters, particularly to find the interactions between the two.

When multiple factors are involved in a study, efficient tools need to be used for analysis. The response surface method (RSM), a statistical technique for data analysis (Montgomery, 2012), seems suitable for this purpose. RSM analyzes the behaviours of different parameters (inputs) on the target response (output). RSM is able to identify the significant factors in a problem as well as possible interactions between the parameters. Eventually, a regression model can be generated. There are some studies (Lohrasbi, Sheikholeslami, & Ganji, 2017; Sheikholeslami, Lohrasbi, & Ganji, 2016b) that optimized the previous studies (Lohrasbi et al., 2016; Sciacovelli et al., 2013; Sheikholeslami et al., 2016a) to consider the interactions between different parameters using statistical methods.

2.3 Summary

In this chapter, different analytical methods to solve phase change problems were summarized. The methods can mostly be applied to predict one-dimensional solid-liquid phase change problems. The review also revealed that two mechanisms of heat transfer would form in

the case of heating an enclosure form the bottom. Namely, a conduction domination regime and a convection domination regime. In the conduction domination regime, the fluid is quiescent and the temperature changes linearly between the hot and cold boundaries, while the convection mechanism starts dominating at a critical Rayleigh number on the order of 10^3. These studies will help build the experimental setup of this research.

The solid-liquid phase change in an enclosure heated from the bottom is one simple enclosure with many engineering applications. The effects of nanoparticles on the phase change rate in an enclosure heated from the bottom was not experimentally studied previously. Also, many contradicting conclusions have been obtained regarding the effects of nanoparticles on the phase change rate. To understand these contradicting conclusions, the rectangular enclosure would be a decent geometry due to its simplicity and the high contribution of natural convection in the total heat transfer rate if heated from the bottom. This helps the formation of strong natural convection, which will be useful to evaluate the effects of nanoparticles on the total heat transfer rate. Also, the experimental data of conduction-driven phase change heat transfer obtained from the enclosure can be compared with the available analytical methods listed in the literature to validate the experimental setup.

Past studies have also shown that nanoparticles increase the thermal conductivity and the viscosity of the NePCM. As mentioned before, increasing both the thermal conductivity and viscosity of the NePCM mixture affects the heat transfer rate differently, as the heat transfer can be enhanced, remained unchanged, and even reduced with an increase in nanoparticles. This depends on the parameters under study and the factors affecting the thermal conductivity of the mixture and the Grashof number, which influence the Rayleigh number. This has not been systematically analyzed in previous studies. The geometry may also be important if both

conduction and convection exist in the melting problem, as the contribution of natural convection (advection) may be higher in the geometries, creating local vortexes (higher fluid motion).

The effects of nanoparticles on the phase change rate were also studied on other geometries. The review showed the effect of nanoparticles and fins on the heat transfer rate, but the natural convection and/or the interactions that may exist between nanoparticles and fins were not considered in these studies. More importantly, fins, besides improving the heat conduction mechanism of heat transfer, create local vortexes, which improve the heat transfer rate. There is a little to no information available on how adding nanoparticles suppresses the natural convection created due to the local vortexes, and how much the total heat transfer rate would change after adding nanoparticles. This thesis will also analyze these effects in shell-and-tube thermal energy storages with and without fins, both numerically and statistically.

Chapter 3 Analytical, numerical and statistical models

In this chapter, the exact solution for a one-dimensional solid-liquid phase change is introduced to verify the experimental setup. A scaling analysis is performed to identify the heat transfer regimes that form in an enclosure heated from the bottom. The appropriate dimensionless numbers and the relationships between these numbers and the melting process of NePCMs in each of these regimes are established. The governing equations and the numerical method that need to be used to simulate the phase change problem in different geometries will be introduced. Finally, the statistical method that is employed to analyze the data is described.

3.1 Analytical model

To compare the experimental results with the exact solution of the one-dimensional two-region Stefan problem, the following equations need to be solved. A schematic diagram of the problem is shown in **Fig. 3-1**. To solve this problem:

Heat conduction in the liquid region:

$$\frac{\partial T(x,t)}{\partial t} = \alpha_l \frac{\partial^2 T(x,t)}{\partial x^2} \quad 0 \le x \le S(t), t > 0 \tag{3-1}$$

Heat conduction in the solid region:

$$\frac{\partial T(x,t)}{\partial t} = \alpha_s \frac{\partial^2 T(x,t)}{\partial x^2} \quad S(t) < x, t > 0 \tag{3-2}$$

Interface temperature:

$$T(S(t),t) = T_m \tag{3-3}$$

Stefan condition:

$$q_s'' - q_l'' = \rho L \frac{dS}{dt} \tag{3-4}$$

where $q_s'' = k_s \frac{\partial T_s}{\partial y}$ and $q_l'' = k_l \frac{\partial T_l}{\partial y}$.

Initial condition:

$$T(x,0) = T_i < T_m \tag{3-5}$$

Boundary condition

$$T(0,t) = T_w > T_m \tag{3-6}$$

where T is the temperature, T_m is the melting temperature, T_i is the initial temperature, T_w is the wall temperature, S is the solid-liquid interface location, α is thermal diffusivity ($k / \rho \cdot C_p$), t is time, x is the location in x-direction, L is latent heat, k_s and k_l are PCM thermal conductivity in solid and liquid phases, and subscripts l and s represents liquid and solid, respectively.

The exact solution for a one-dimensional two-region phase change problem can be expressed as (Alexiades & Solomon, 1993; Hu & Argyropoulos, 1996):

$$\theta_l(x,t) = \frac{T_l(x,t) - T_w}{T_m - T_w} = \frac{erf\,(x / 2\sqrt{\alpha_l t})}{erf\,(\lambda)} \tag{3-7}$$

$$\theta_s(x,t) = \frac{T_s(x,t) - T_i}{T_m - T_i} = \frac{erfc(x / 2\sqrt{\alpha_s t})}{erfc(\lambda\sqrt{\alpha_l / \alpha_s})} \tag{3-8}$$

$$\frac{Ste_l}{\exp(\lambda^2) erf\,(\lambda)} - \frac{Ste_s \sqrt{\alpha_s}}{\sqrt{\alpha_l}\exp(\alpha_l \lambda^2 / \alpha_s) erfc(\lambda\sqrt{\alpha_l / \alpha_s})} = \lambda\sqrt{\pi} \tag{3-9}$$

Where $\theta_l(x,t)$ is the dimensionless temperature in the liquid region, $\theta_s(x,t)$ is the dimensionless temperature in the solid region, $Ste_l = C_{p,l}(T_w - T_m)/L$, $Ste_s = C_{p,s}(T_m - T_i)/L$, and λ is the solution to the transcendental equation. The relationship between S and λ can be written as follows:

$$S(t) = 2\lambda\sqrt{\alpha_l t} \tag{3-10}$$

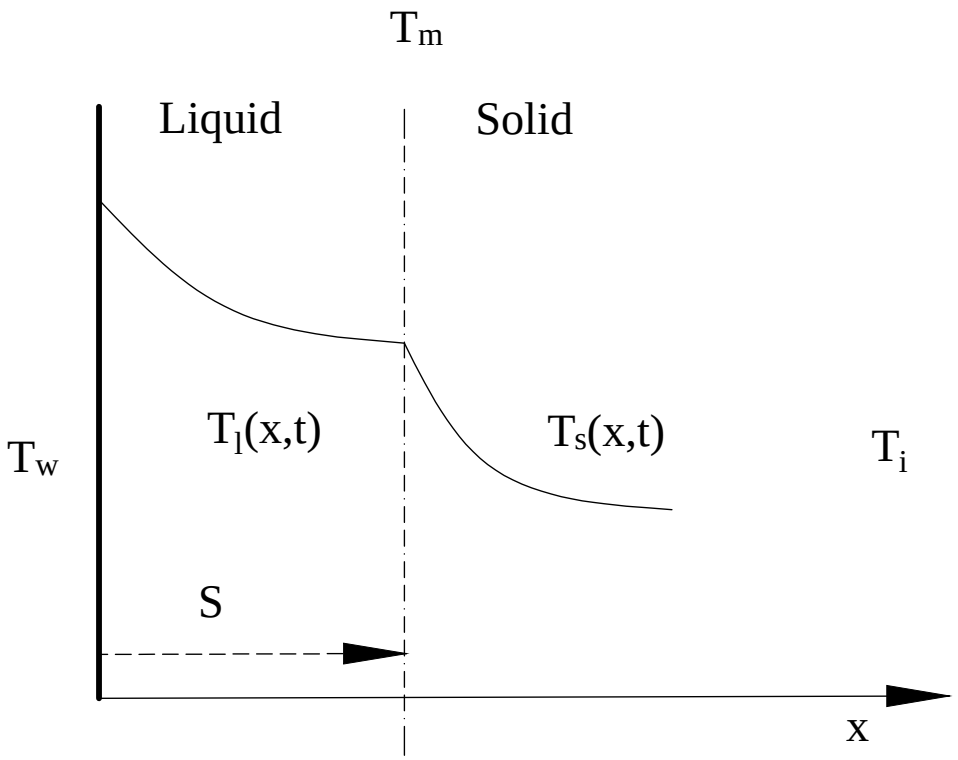

Fig. 3-1 Space-time diagram for the two-phase Stefan problem.

To compare the experimental results and the exact solution, some assumptions must be considered in addition to the sources of error. 1) The melting temperature is 24^oC (no mushy zone exist); 2) The PCM physical properties are temperature-independent; 3) Heat loss is zero; 4) No interface change is considered due to the PCM expansion (the density variation between the solid and liquid phases); and 5) The latent heat and specific heat were obtained at both solid and liquid

regions for coconut oil from a 2018 study (Al-Jethelah et al., 2018), which may not be exactly the same as the latent heat and specific heat of the coconut oil used in this study. However, the other physical properties measured in this study were nearly identical to that study (Al-Jethelah et al., 2018), which will be shown in the next section.

3.2 Scaling analysis

3.2.1 Conduction domination

The convection onset criterion, $Ra_H \sim 1708$, is valid for a sufficiently long enclosure in the horizontal direction. A similar criterion can be considered for other horizontal layers of fluid with critical Rayleigh numbers on the order of 10^3 (Bejan, 2013). The heat transfer in a bottom heated enclosure starts with a heat conduction mechanism, and the solid-liquid interface remains horizontal with no deformation during this regime. Thus, there is a balance between the heat flux in both solid and liquid regions and the heat of fusion absorbed at the solid-liquid interface. Using Eq. 3-4, this energy balance can be written in the form of (Faghri & Zhang, 2006):

$$k_{\phi,s}\frac{\Delta T_s}{S}, k_{\phi,l}\frac{\Delta T_l}{S} \sim \rho_\phi L_\phi \frac{S}{t} \tag{3-11}$$

where the first and second terms on the left-hand side represets the heat flux in solid and liquid regions at the interface, the first term on the right hand-side represents the rate of thermal energy that storead/released during the phase change, $\Delta T_s = (T_m - T_i)$ and $\Delta T_l = (T_w - T_m)$, T_m is the melting temperature, and subscript ϕ represents the physical properties of NePCM. After rearranging Eq. (3-11), this can be explained as:

$$S \sim H \cdot (Ste \cdot Fo)^{1/2} \left[\left(\frac{k_{\phi,s}}{k_{\phi,l}} \frac{\Delta T_s}{\Delta T_l}\right)^{1/2}, 1 \right] \tag{3-12}$$

$$Fo = \frac{\alpha_{\phi,l} t}{H^2} \tag{3-13}$$

$$Ste = \frac{C_{p,\phi,l}(T_w - T_m)}{L_\phi} \tag{3-14}$$

where H is the height of the enclosure, t is the time, $\alpha_{\phi,l}$, $C_{p,\phi,l}$ and L_ϕ are the thermal diffusivity, specific heat and latent heat of the NePCM.

The heat flux can be neglected in the solid region if $\Delta T_s \ll \Delta T_l$ (one-region Stefan problem is one example of this situation). If so, Eq. (3-12) reduces to:

$$S \sim H \cdot \left(Ste \cdot Fo\right)^{1/2} \tag{3-15}$$

This equation shows the solid-liquid interface relationship and/or the liquid fraction with Ste and Fo numbers at the early stage of melting. According to the terminology of phase change heat transfer, the product of Ste and Fo numbers is the dimensionless time. The nanoparticles volume fraction (ϕ) appears inside $Fo \cdot Ste$ as the physical properties of the NePCM changes with changing ϕ. Therefore, adding nanoparticles directly affects the NePCM mixture properties, and consequently the Fo and Ste numbers. The specific heat and latent heat, for instance, decrease with higher ϕ, while the thermal conductivity and density increase (Al-Jethelah et al., 2018). However, the latent heat of fusion reduction is greater than the reduction in the specific heat, causing an increase in the Ste number. Similarly, the thermal diffusivity increases by adding the nanoparticles leading to a rise in the Fo number (Al-Jethelah et al., 2018). It is concluded that adding nanoparticles leads to larger Ste and Fo numbers, and subsequently a thicker liquid region. This regime is shown in **Fig. 3-2**.

The heat flux can be written as:

$$q''_{\phi,l} \sim k_{\phi,l} \frac{\Delta T_l}{S} \tag{3-16}$$

There are two ways that Nu number may be defined in the case of nanoparticles and PCM. One, the effect of nanoparticles is embedded in the Nu number, and the Nu number is based on the NePCM thermal conductivity ($Nu_\phi = h_{conv} H / k_{\phi,l}$) (Tasnim et al., 2015). Two, the Nusselt number is based on the PCM thermal conductivity ($Nu_{\phi=0} = h_{conv} H / k_l$). The latter, which is more frequently employed in different NePCM studies (Al-Jethelah et al., 2018; Ho & Gao, 2013; M. Hosseini, Mustafa, Jafaryar, & Mohammadian, 2014), shows the Nu number increment due to the increase in the thermal conductivity of NePCM. However, both of these definitions will have the same result in the case of finding the convective heat transfer coefficient (h_{conv}). To avoid confusion, $Nu_{\phi=0} = Nu$, and is expressed as:

$$Nu = \frac{h_{conv} \cdot H}{k_l} \tag{3-17}$$

where k_l is the thermal conductivity of the pure PCM. The heat transfer coefficient is computed from:

$$h_{conv} = \frac{q''_{\phi,l}}{\Delta T} \tag{3-18}$$

Combining Eqs. (3-17) and (3-18), the Nu number is defined by:

$$Nu \sim \frac{k_{\phi,l}}{k_l} (Ste \cdot Fo)^{-1/2} \tag{3-19}$$

In this definition, the Nu number decreases by elapsing time and increases by enhancing the thermal conductivity of the Nano-PCM mixture.

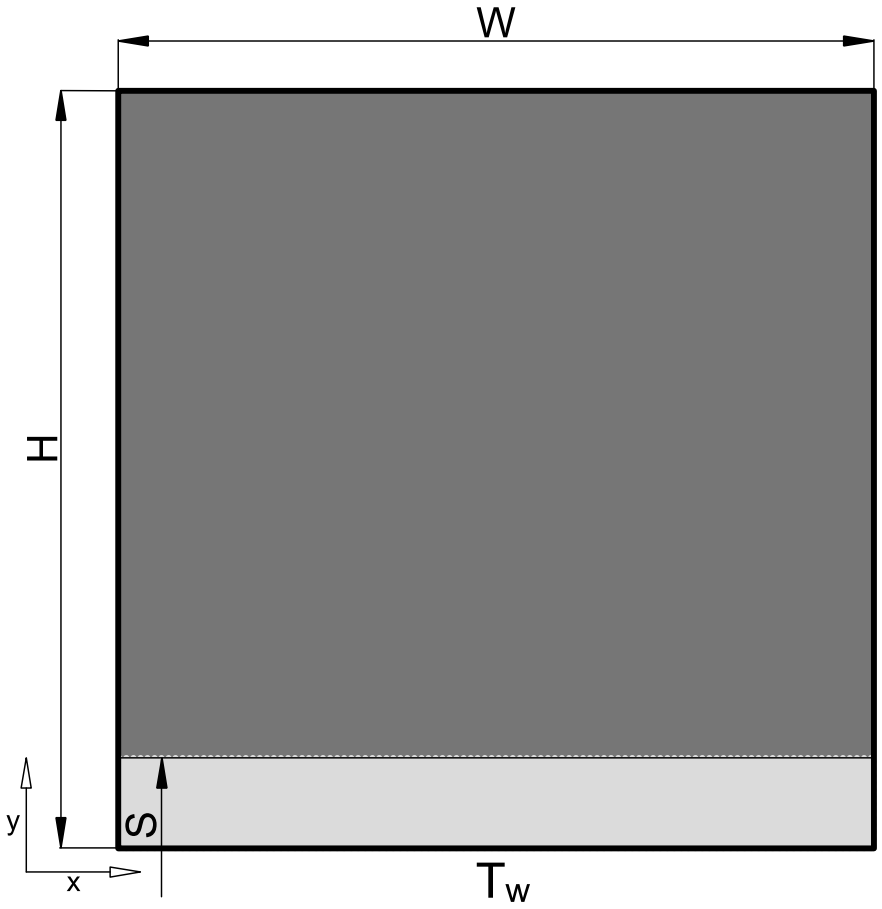

Fig. 3-2 Conduction regime.

3.2.2 Convection domination

This regime starts as soon as the Ra number becomes greater than the critical Ra number, which causes the formation of the rotating rolls of flow shown in **Fig. 3-3**(a). In this regime, three regions can be formed in terms of the temperature. Two conduction layers indicated with δ_T sandwich the third region, the core of the fluid layer. The temperature of the conduction layers

drops of size $\Delta T_l / 2 = (T_w - T_m)/2$ across δ_T while the core of the fluid layer remains at $T_{ave} = \frac{T_w + T_m}{2}$ (Bejan, 2013) shown in **Fig. 3-3**(b). These conduction layers become unstable when the Rayleigh number (Ra_{δ_T}) exceeds 10^3 (Bejan, 2013).

The thickness of these layers is proportional to:

$$\delta_T \sim 10S \cdot Ra_S^{-1/3} \tag{3-20}$$

where $Ra_S = Gr_S \cdot \Pr = \frac{g\beta\Delta TS^3}{\upsilon_\phi^2} \cdot \frac{\upsilon_\phi}{\alpha_\phi} = \frac{g\beta\Delta TS^3}{\upsilon_\phi \alpha_\phi}$.

The heat transfer between T_w and T_m is hindered by the thin conduction layers thickness. Therefore,

$$q''_{\phi,l} \sim k_{\phi,l} \frac{\Delta T_l}{\delta_T} \tag{3-21}$$

This is equivalent to writing:

$$q''_{\phi,l} \sim \frac{k_{\phi,l}}{10S} \Delta T_l \cdot Ra_S^{1/3} \tag{3-22}$$

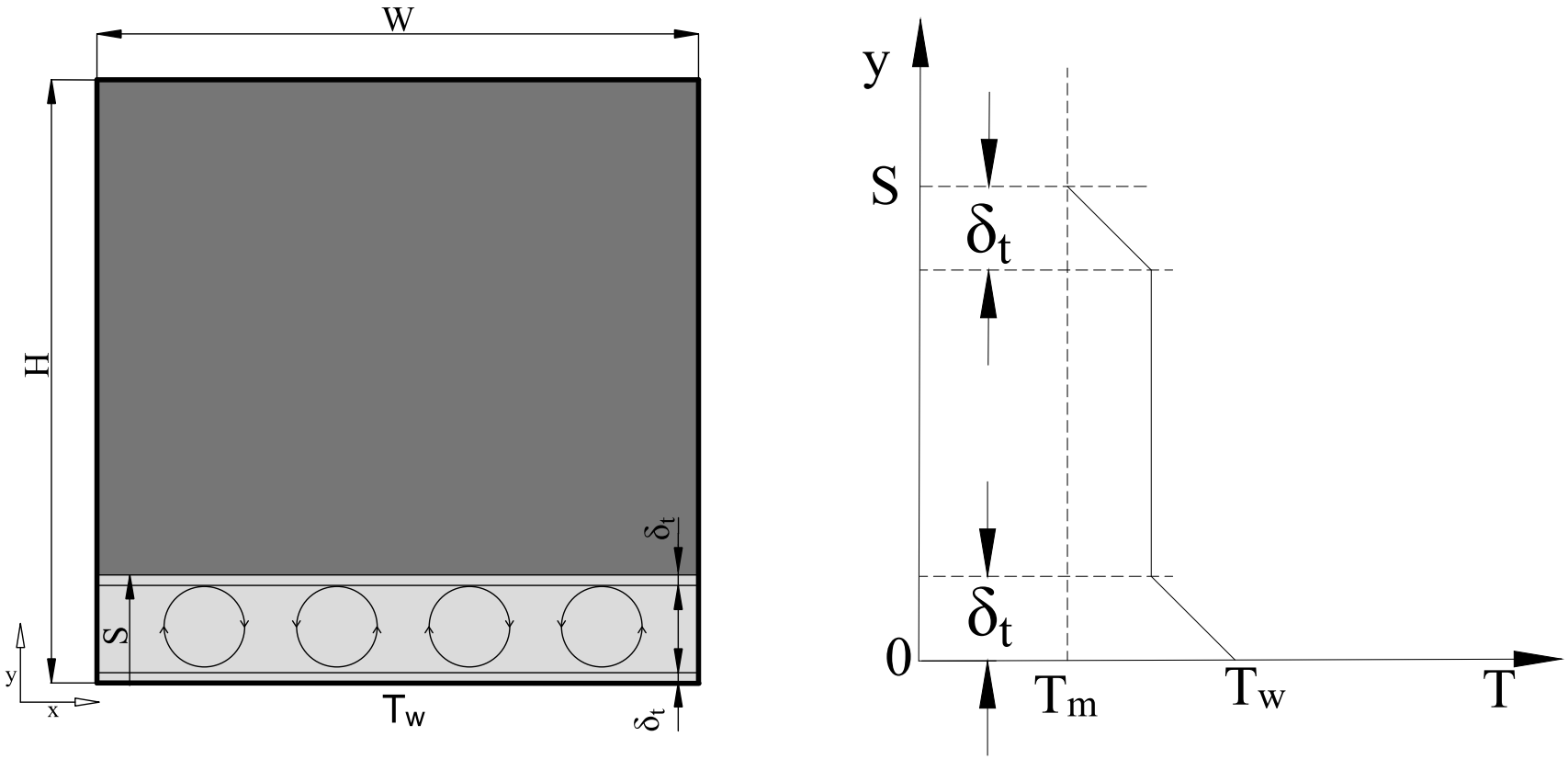

(a) (b)

Fig. 3-3 (a) Convection regime (b) Temperature vs. location in the liquid region in the convection regime.

Since in the convection regime the solid-liquid interface is always deformed, it would be more appropriate to explain the solid-liquid interface in terms of the average solid-liquid interface location (S_{ave}). Using Eqs. (3-4) and (3-22), the solid-liquid interface thickness is proportional to:

$$S_{ave} \sim H \cdot (Ste \cdot Fo)^{1/2} \left[\left(\frac{k_{\phi,s}}{k_{\phi,l}} \frac{\Delta T_s}{\Delta T_l} \right)^{1/2}, 10^{-1/2} Ra_S^{1/6} \right] \tag{3-23}$$

where the first term in the bracket represents the conduction heat transfer in the solid region, and the second term represents the convection heat transfer in the liquid region. Similar to conduction domination regime, it is found that the heat flux can be neglected in the solid phase if $\Delta T_s \ll \Delta T_l$, also the Ra number on the second term becomes comparatively large at this regime, making the second term on the right-hand side of Eq. (3-23) greater than the first term (one-region Stefan problem is one example of this situation). If so, Eq. (3-23) reduces to:

$$S_{ave} \sim 10^{-1/2} H \cdot (Ste \cdot Fo)^{1/2} Ra_S^{1/6} \tag{3-24}$$

By using a simple energy balance, the scale for the convective heat transfer coefficient can be obtained as follows in the second regime:

$$h_{conv} \sim \frac{k_{\phi,l}}{\delta_t} \tag{3-25}$$

Using Eqs. (3-17), (3-20), (3-24) and (3-25), the Nu number can be obtained in the convection regime as follows:

$$Nu \sim 10^{-1/2} \frac{k_{\phi,l}}{k_l} (Ste \cdot Fo)^{-1/2} Ra_S^{1/6} \tag{3-26}$$

At the end of melting $S \simeq H$. Therefore, from Eq. (3-24), it is found that:

$$Ra_{S\simeq H}^{1/6} \sim 10^{1/2}(Ste \cdot Fo)^{-1/2} \tag{3-27}$$

Combining Eqs. (3-26) and (3-27), it can be found that:

$$Nu \sim 10^{-1} \frac{k_\phi}{k_l} Ra_{S\simeq H}^{1/3} \tag{3-28}$$

This relationship between Nu number and Ra_H number is referenced for fluid $(k_{\phi,l} = k_l = k_{fluid})$ with no phase change in an enclosure heated from the bottom if the Ra_H number exceeds its critical value (Bejan, 2013).

The scaling analysis carried out in this section divided the NePCM melting problem in an enclosure into two distinct regimes. It is found that adding nanoparticles increases the heat transfer at the first regime where conduction is dominant while no conclusion can be made for the second regime because it depends on two factors, namely $k_{\phi,l}/k_l$ and Ra. One reason for the uncertainty regarding the effect of nanoparticles on the heat transfer rate can be attributed to the Ra number of the mixture, which is not considered in many studies.

3.3 Numerical model

To compare the experimental results with the numerical results, the melting problem needs to be simulated numerically. Also, the effects of nanoparticles on the heat transfer rate at the shell-and-tube geometries will be numerically analyzed.

To model phase change heat transfer with single and/or multi-phase fluids, air and NePCM for example, transient continuity, momentum, and energy equations are employed. The Volume of Fluid (VOF) method is based on the fact that two or more fluids are not interpenetrating. A variable is introduced for each additional fluid as the volume fraction of each fluid in the computational

domain. The fluids should sum to unity in each control volume. By knowing the volume fraction of each of the fluids, the fields of all variables and properties are shared by the fluids and represent volume-averaged values. Thus, the variables and properties in any given cell represent one of the fluids or the mixture of fluids, depending on the volume fraction values. In other words, if the q^{th} fluid's volume fraction in the cell is denoted by Ψ_q, the following conditions might happen as follow: $\Psi_q = 0$: The cell is empty of the q^{th} fluid; $\Psi_q = 1$: The cell is full of the q^{th} fluid; $0 < \Psi_q < 1$: The cell contains the interface between the q^{th} fluid and at least one more fluid. Appropriate variables or properties are assigned to each control volume based on the local value of Ψ_q. The volume fraction equation is not solved for the primary fluid. The primary-fluid volume fraction is computed based on the $\sum_{q=1}^{n} \Psi_q = 1$. The tracking of the interface is also accomplished by the solution of a continuity equation for the volume fraction of one or more fluids. For the q^{th} fluid, this equation can be written as (ANSYS FLUENT, 2013):

$$\frac{\partial}{\partial t}\left(\Psi_q \rho_q\right) + \nabla \cdot (\Psi_q \rho_q \vec{v}_q) = 0 \tag{3-29}$$

$$\frac{\partial}{\partial t}(\rho \vec{v}) + \nabla \cdot (\rho \vec{v}\vec{v}) = -\nabla P + \mu \nabla^2 \vec{v} + \rho \vec{g} + \vec{s} \tag{3-30}$$

$$\frac{\partial}{\partial t}(\rho h) + \nabla(\rho \vec{v} h) = \nabla(k \nabla T) \tag{3-31}$$

where $\vec{v}$ is velocity vector of fluid, P is pressure, μ is dynamic viscosity, $\vec{g}$ is the gravity vector, $\vec{s}$ is momentum source term, h is enthalpy.

To model the solid-liquid phase change, the enthalpy porosity technique is used in this study. This technique has been used in many previous studies (S. Guo et al., 161AD; Yang et al.,

2017). The advantage is that it does not require tracking of the solid-liquid interface. The enthalpy term, h in Eq. (3-31), is expressed as:

$$h = h_{ref} + \int_{T_{ref}}^{T} C_p dT + \gamma L \tag{3-32}$$

where h_{ref} is enthalpy at a reference temperature (T_{ref}), and L is latent heat of fusion, and γ stands for the local liquid fraction. The latter can be obtained as:

$$\begin{aligned} \gamma &= 0 && if \quad T < T_{solidus} \\ \gamma &= \frac{T - T_{solidus}}{T_{liquidus} - T_{solidus}} && if \quad T_{solidus} < T < T_{liquidus} \\ \gamma &= 1 && if \quad T_{liquidus} < T \end{aligned} \tag{3-33}$$

The enthalpy porosity technique treats both phases as porous media. Thus, the momentum source can be defined as:

$$\vec{s} = \frac{(1-\gamma)^2}{(\gamma^3 + \varepsilon)} A_{mushy} \vec{v} \tag{3-34}$$

where ε is a small number around 10^{-3} to avoid division by zero, and A_{mushy} represents the mushy zone, an area where velocity gradually decreases to zero between liquid and solid regions. A_{mushy} is usually a large coefficient between 10^4 $kg/m^3 \cdot s$ and 10^6 $kg/m^3 \cdot s$ (Abdollahzadeh & Esmaeilpour, 2015). In this thesis, a standard value of $A_{mushy} = 10^5$ $kg/m^3 \cdot s$ is employed.

Depending on the phase change heat transfer problem and the number of fluids that are simulated, Eqs. (3-29)-(3-31) need to be solved simultaneously. The modelling is conducted with a finite volume method (FVM).

The pressure field is desired to be computed as part of the solution, as its gradient is not normally known beforehand. In the case of simulating compressible flow, continuity equation may

be used as the transport equation for density in addition to (3-29)-(3-31). The energy equation is also the transport equation for temperature. Then, the equation of state $P = f(\rho, T)$ is employed to find the pressure. However, if the flow is incompressible, the density remains constant and not linked to the pressure. In this case, coupling between the velocity and pressure introduces a constraint in the solution of the flow field. In the case of introducing a correct pressure field in the momentum equations, the resulting velocity field should satisfy continuity. SIMPLE algorithm, an iterative solution strategy, can be employed to link the pressure-velocity. In this algorithm, the convective fluxes per unit mass through cell faces are evaluated from so-called guessed velocity components. Moreover, the pressure filed is guessed and employed to solve the momentum equations, and a pressure correction equation, deduced from the continuity equations, is solved to find a pressure correction field, which is employed to update the pressure and velocity fields. In other words, the velocity and pressure fields are guessed in the first iteration. The SIMPLE algorithm progressively improves these guessed fields. This process is iterated until the convergence of the pressure and velocity fields. The SIMPLE algorithm is indicated in **Fig. 3-4**. Time step is set to a certain value depending on the problem that is simulated, and an iterative time-advancement scheme is used for solving all equations in a segregated mode until convergence criteria for all variables are met.

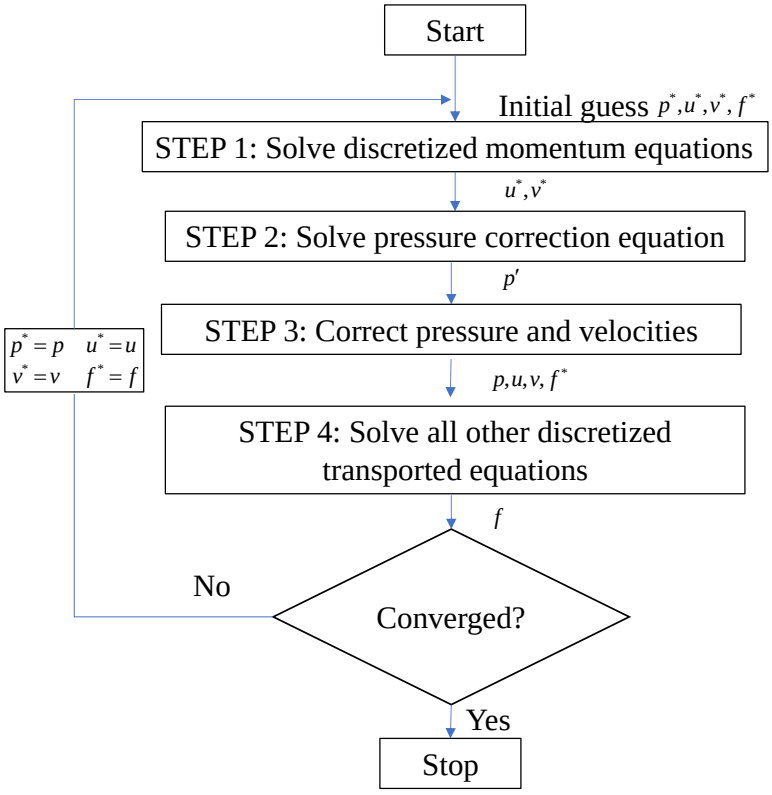

Fig. 3-4 The SIMPLE algorithm (Versteeg & Malalasekera, 2007).

In this thesis, two assumptions are employed to simulate different phase change problems, regarding the density change of the NePCM. The first assumption is the Boussinesq approximation (Shang, 2006), which ignores the density change where they appear except in the terms multiplied by gravity, and the second assumption is user-defined functions to consider the density change with temperature. The latter would be more realistic but makes the simulation computationally expensive, as the C-programming language needs to be implemented.

Among the turbulence models, the best known one is the $\kappa-\varepsilon$ model. The computing resources required for reasonably accurate flow computations are modest, and this approach has been mainly employed to simulate flow in many engineering applications. Thus, the $\kappa-\varepsilon$ model is adopted to simulate the turbulence may occur during the phase change or in the heat transfer fluid (HTF), transferring its thermal energy to the thermal storage unit filled with PCM. The

standard $\kappa-\varepsilon$ model has two model equations, namely κ and ε, based on our best understanding, the relevant turbulent process causes changes to these variables. κ and ε are used to define velocity scale (ϑ) and length scale (ℓ). If one velocity scale and one length scale suffice to describe the effects of turbulence, dimensional analysis yields (Versteeg & Malalasekera, 2007):

$$\nu_t = C\vartheta\ell \tag{3-35}$$

where C is a dimensionless constant of proportionality. The eddy viscosity can be obtained by applying dimensional analysis as follows:

$$\mu_t = C\rho\vartheta\ell = \rho C_\mu \frac{\kappa^2}{\varepsilon} \tag{3-36}$$

where C_μ is dimensionless constant.

The standard $\kappa-\varepsilon$ model uses the following transport equations for κ and ε:

$$\frac{\partial(\rho\kappa)}{\partial t} + \nabla\cdot(\rho\kappa\mathbf{v}) = \nabla\cdot\left[\frac{\mu_t}{\sigma_k}\nabla\kappa\right] + 2\mu_t S_{ij}\cdot S_{ij} - \rho\varepsilon \tag{3-37}$$

$$\frac{\partial(\rho\varepsilon)}{\partial t} + \nabla\cdot(\rho\varepsilon\mathbf{v}) = \nabla\cdot\left[\frac{\mu_t}{\sigma_\varepsilon}\nabla\varepsilon\right] + C_{1\varepsilon}\frac{\varepsilon}{\kappa}2\mu_t S_{ij}\cdot S_{ij} - C_{2\varepsilon}\rho\frac{\varepsilon^2}{\kappa} \tag{3-38}$$

In other words, these equations are:

Rate of change of κ or ε	+	Transport of κ or ε by convection	=	Transport of κ or ε by diffusion	+	Rate of production of κ or ε	-	Rate of destruction of κ or ε

where S_{ij} is the rate of deformation, C_{μ} , σ_{κ} , σ_{ε} , $C_{1\varepsilon}$ and $C_{2\varepsilon}$ are adjustable constants. A comprehensive data fitting was performed in a wide range of turbulent flows to find these constants for the $\kappa-\varepsilon$ models (Versteeg & Malalasekera, 2007). Further details can be found in (Versteeg & Malalasekera, 2007).

In this thesis, commercial ANSYS software will be employed to simulate the phase change problems. The governing equations, turbulent model, discretization method, the algorithm to couple pressure and velocity terms described in this section are used in the software. Also, the volume of fluid (VOF) model is applied to treat the multiphase fluid in the case of existing more than one fluid in the domain. To consider the physical properties of the NePCM dependent on the temperature, the C-programing language is used to write user-defined functions, which will be compiled to the FLUENT solver.

3.3.1 Correlations for nanofluid properties

The properties of PCMs change with the addition of nanoparticles. Density and specific heat of NePCM are obtained using the following equations (J. M. Mahdi & Nsofor, 2017):

$$\rho_{NePCM} = \phi\rho_{np} + (1-\phi)\rho_{PCM} \tag{3-39}$$

$$(\rho C_p)_{NePCM} = (1-\phi)(\rho C_p)_{PCM} + (\phi\rho C_p)_{np} \tag{3-40}$$

where ϕ is volume fraction, C_p is specific heat, and subscripts “np” and “PCM” stand for nanoparticle and PCM respectively.

Latent heat of NePCM is given as:

$$L_{NePCM} = \frac{(1-\phi)(\rho L)_{PCM}}{\rho_{NePCM}} \tag{3-41}$$

where L is the latent heat of pristine paraffin wax.

Viscosity and thermal conductivity of the NePCM are calculated with the following correlations (Sasmito, Kurnia, & Mujumdar, 2011):

$$\mu_{NePCM} = \mu_{PCM}(C_1 e^{C_2 \phi}) \tag{3-42}$$

$$k_{NePCM} = \frac{k_{np} + 2k_{PCM} - 2\phi(k_{PCM} - k_{np})}{k_{np} + 2k_{PCM} + \phi(k_{PCM} - k_{np})} k_{PCM} + \gamma \varsigma Z \phi \rho_{PCM} C_{p,PCM} \sqrt{\frac{BT}{\rho_{np} d_{np}}} f(T, \phi) \tag{3-43}$$

The first part of Eq. (3-43) is derived from the Maxwell model and the second part represents the Brownian motion, which is a reason for the dependency of thermal conductivity on temperature. Moreover, d_{np} stands for the nanoparticle diameter, Z is the Brownian motion constant, which equals to 5×10^4, B is the Boltzmann constant which equals to $1.381\times10^{-23}\ \frac{J}{K}$, γ is a correction factor, its value is defined from Eq. (3-33), and C_1 and C_2 are constants, which are listed in **Table 3-1**. In addition, ς is an empirical correlation in the Brownian motion term and is defined as:

$$\varsigma = \varsigma_1(100\phi^{\varsigma_2}) \tag{3-44}$$

where ς_1 and ς_2 are constants listed in **Table 3-1**. The other correction function $f(T, \phi)$ is defined as:

$$f(T, \phi) = 10^{-3}[28.217\phi + 3.917)T / T_{ref} - 30.669\phi - 3.91123] \tag{3-45}$$

where $T_{ref} = 319.15\ K$. Note that the latter part of Eq. (3-43) assumes that the Brownian motion of nanoparticles enhances the thermal conductivity of the NePCM. In actual thermal storage units, this may not be true since the melted PCM moves and would likely overwhelm the small fluctuations of the nanoparticles. Keeping this part in Eq. (3-43) makes sure that the highest

possible thermal conductivity is estimated for the NePCMs. For solid NePCMs, this part disappears due to lack of nanoparticle motion.

Table 3-1 The constants value for CuO and Al_2O_3 nanoparticles (Sasmito et al., 2011; Vajjha, Das, & Namburu, 2010).

Nanoparticle	Al_2O_3	CuO
C_1	0.983	0.9197
C_2	12.959	22.8539
ς_1	8.4407	9.881
ς_2	–1.07304	–0.9446

Also, ϕ is the volume fraction of nanoparticles, which can be found as follows (Azmi et al., 2013):

$$\phi = \frac{\omega \rho_{PCM}}{(1-\frac{\omega}{100})\rho_{np} + \frac{\omega}{100}\rho_{PCM}} \tag{3-46}$$

where ω is the weight concentration ($wt.\%$) of the nanoparticles.

3.4 Statistical approach

Traditionally the OFAT method has been extensively used for data analysis. This technique consists of selecting a set of levels for each parameter in a problem, then successively varying each parameter over its range while keeping other parameters unchanged. To analyze many parameters in a problem, this method requires many data and computational resources. Yet it often fails to identify the different levels of significance of the parameters and possible interactive effects between them. RSM, a collection of mathematical and statistical techniques for multiple data analysis, has these capabilities (Montgomery, 2012) and requires much smaller number of data.

The range of the parameters under study should be selected wisely, as very large parameter range affect the accuracy of the RSM analysis. To do this, a preliminary study is often required to find the vicinity of the stationary point where the response changes adversely (Montgomery, 2012).

Different independent parameters are selected in order to study their effects on the heat transfer and charging time of the thermal storage unit. Each parameter has three levels, namely, low, medium and high level. The level of each parameter intentionally changes by means of RSM. A center-point (medium level) of each parameter is added to detect possible nonlinearity of the model. The RSM method is able to cover the nonlinear behaviour of each parameter and develop a second-order regression model. Face-centered central composite design (CCF) (Montgomery, 2012) is used to predict the nonlinearity of the model. In this method, two parameters intentionally change to their medium level, and the response (i.e., charging time) is obtained and analyzed. If no nonlinearity is observed in the model, factorial design is employed to analyze different factors affecting the liquid fraction of NePCM. 2^k factorial design (Montgomery, 2012), for example, is implemented for the analysis of the impact of different parameters in the heat transfer rate. Two low and high levels are chosen for each of the selected main factors, in other words, "+" and "–"signs are assigned for high and low levels of each main factor respectively.

Analysis of Variance (ANOVA) test (Montgomery, 2012) is used to determine the adequacy of the model. Multiple regression analysis is developed as the predictor equation, which illustrates the role of each parameter and probable interactions between multiple parameters.

In the first step, a response equation is developed to represent the relationship between each independent parameter and the response (dependent parameter):

$$R = f(\Phi_1, \Phi_2, ...\Phi_n) \tag{3-47}$$

where R and Φ are the dependent and independent parameters, respectively.

A nonlinear regression model is approximated using a polynomial or higher-order model. In this research, a second-order model is used (Montgomery, 2012):

$$R = \ddot{B}_0 + \sum_{i=1}^{n} \ddot{B}_i \Phi_i + \sum_{i=1}^{n} \ddot{B}_{ii} \Phi_i^2 + \sum_{i=1}^{n} \sum_{j=1}^{n} \ddot{B}_{ij} \Phi_i \Phi_j + \varepsilon \quad (3\text{-}48)$$

where $\ddot{B}_0$ is the intercept term, $\ddot{B}$ is regression coefficient, and Φ_i and Φ_i^2 are the actual parameters and their squares, $\Phi_i \Phi_j$ is an interaction between the parameters, and ε is a random error.

Assumptions for ANOVA need to be met in case of using this method to verify the validity of the regression model. ANOVA assumptions are as follow (Montgomery, 2012): (1) $E(\varepsilon) = 0$; (2) $V(\in_i) = \sigma^2$, where σ^2 is the standard deviation of the data. This means all data groups or samples have equal variance; (3) departures from the group mean are normally distributed for all data groups; and (4) independency of the random error.

3.5 Summary

In this chapter, analytical solutions have been introduced along with the scaling analysis in an enclosure heated from below, creating a Rayleigh-Benard convection. Also, numerical and statistical approaches have been introduced for a phase change problem.

The problem and solution for one-dimensional conduction driven phase change heat transfer problem was explained. The solution will be compared with the experimental results obtained in the following chapters. Afterwards, scaling analysis has been employed to understand the regimes formed in a two-dimensional rectangular enclosure heated from the bottom and filled with PCM. It was found that the heat conduction is the dominant mechanism of heat transfer at small Rayleigh numbers (early stage of melting) up to a critical Rayleigh number. By moving the solid-liquid interface upward, the Rayleigh number becomes larger than the critical Rayleigh

number and convection heat transfer becomes the dominant heat transfer mechanism. By knowing these, it is expected that nanoparticles improve the melting rate at the early stage of melting when Rayleigh number is smaller than the critical Rayleigh number, meaning that the conduction mechanism is dominant based on the scaling analysis; however, no comment can be given regarding the total heat transfer rate at this stage.

The governing equations required to numerically simulate the solid-liquid phase change problem have been introduced. The discretization approach, the algorithm required to couple the pressure and velocity terms, the technique used to simulate the phase change, and the turbulent model used for simulations have been introduced. The approach will be implemented to simulate phase change problems with and without nanoparticles. To consider the effects of nanoparticles on the heat transfer rate, nanofluid correlations have been employed in the numerical simulations. A statistical approach has been introduced to analyze the data obtained from the numerical method. The statistical approach reveals if interactions exist between different parameters under study and provides a regression model for each case under study.

In the following chapters, the experimental, numerical and analytical models will be developed and compared to validate the results by achieving the same result with two different approaches. The experimental results will consider more realistic conditions that cannot be included in the analytical or numerical model, such as solid-liquid interface movement due to density change, temperature-dependent physical properties, and the real nanoparticles effects on the thermal conductivity, viscosity and heat transfer rate.

Chapter 4 Experimental setup and methodology

This chapter presents the design and setup of an experimental system to systematically study the effects of nanoparticles on the phase change rate. To do this, a particular nanoparticle needs to be dispersed into PCM at different concentrations to make different samples. The sample preparation will be discussed along with the experimental procedure.

After knowing the significant parameters, affecting the phase change rate in the enclosure described in the scaling analysis section discussed in the previous chapter, three scenarios may occur to the Ra number as one significant parameter after adding nanoparticles; 1) Ra increases 2) Ra number remains almost unchanged 3) Ra number decreases. As it was found from the scaling analysis in the previous chapter that the Ra number has a direct relation to the Nu number and the solid-liquid interface location, the first two scenarios do not have adverse effects on the heat transfer rate. However, the heat transfer rate might decrease if the third scenario occurs. This scenario would occur in reality. In this case, if $k_{\phi,s}/k_s$ and/or $k_{\phi,l}/k_l$ can compensate for the reduction in the Ra number, still the heat transfer rate increases. If not, the heat transfer rate may decrease. This is the main reason that the heat transfer rate decreases by adding nanoparticles. This has generally been ignored in previous studies, as many NePCM researches do not pay attention to the Ra, on which the experiment was conducted, or the Ra reduction after adding nanoparticles. This is because the contribution of natural convection is different at different Ra numbers. This chapter presents the sample preparation and experimental setup needed to study the above points.

4.1 Materials and equipment

The type of nanoparticles chosen for the experiment affects the Ra number differently. Adding single or multi-wall carbon nanotubes, for example, causes the Ra number to continually decrease with increasing the volume fraction (Eqs. 3-35 to 3-39 are employed to find a paraffin based mixture properties). This means that the third scenario described above occurs. Therefore, the $k_{\phi,l}/k_l$ value should be high enough to compensate for the Ra number reduction; otherwise, the heat transfer rate decreases as reported in (Zeng et al., 2013). On the other hand, some nanoparticles (mainly metallic nanoparticles) increase the Ra number with increasing ϕ based on the mixture properties obtained through the correlations for nanofluid properties. Thus, if copper nanoparticles, for example, are dispersed in a PCM at a wide range of concentration ($0-10$ vol.%), the melting rate should always be increasing as $k_{\phi,l}/k_l > 1$ and the Ra number is not reduced at this range. There are many numerical reports (Hosseinizadeh, Darzi, & Tan, 2012; Kashani, Ranjbar, Abdollahzadeh, & Sebti, 2012; Kashani, Ranjbar, Madani, Mastiani, & Jalaly, 2013; Sebti et al., 2013) that proved the melting rate enhancement from added copper nanoparticles. These reports also revealed that increasing ϕ improved the melting rate. However, the density of this type of nanoparticle is mainly high, making the dispersion and stability of the NePCM controversial. Thus, these nanoparticles dispersed in PCM can rarely be used at many charging and discharging cycles in the thermal storages or require a mechanism to guarantee the dispersion of nanoparticles in the PCM.

With the points described above in mind, we choose Al_2O_3 nanoparticles, as all three scenarios occur for this type of nanoparticle in a relatively small range of nanoparticles concentration. In a preliminary study, the correlations for nanofluid properties (See Eqs. (3-39)-

(3-43)) showed that the Ra number increases at first, and then decreases by increasing the concentration of Al_2O_3, meaning that all three scenarios occur, even though this trend may not be seen in the experiment. The results of this preliminary study are not shown, as the conclusion of this part of the research is based on the experimental results. The numerical properties of CuO were also used in the numerical studies. We also select coconut oil as the PCM for the experiment due to the high capacity of the coconut oil to keep the nanoparticles stable reported in a 2018 study (Al-Jethelah et al., 2018) and select paraffin properties in the numerical studies. The properties of the Al_2O_3 and CuO nanoparticles and coconut oil and paraffin are listed in **Table 4-1**.

After choosing the nanoparticles type, a range of nanoparticle concentrations along with a range of wall temperatures should be selected. To select the nanoparticles concentration range, the melting rate and the melting time of the pure PCM ($\omega_0 = 0$ $wt.\%$) is found through conducting the first experiment, then a concentration of nanoparticles (ω_1) is added to the PCM, and the melting time is obtained again through conducting the second experiment. Depending on the melting time reduction or addition compared to the pure PCM sample, another concentration of nanoparticles (ω_2), which is higher or lower than ω_1, is chosen to make the third NePCM sample. This process continues for a certain hot plate temperature (wall temperature) until a critical nanoparticle concentration, at which the highest melting rate occurs, is obtained. In the case of observing an adverse effect on the melting time (an addition to the melting time) for any concentration of nanoparticles compared to the pure PCM, the wall temperature is set to a lower temperature and the above procedure is repeated. Using this process to define the upper limit and lower limit of the nanoparticle concentration and the wall temperature, the nanoparticle concentration range is obtained.

Table 4-1 Physical properties of Al_2O_3 and CuO nanoparticles, aluminum, air, coconut oil, and paraffin.

Properties (units)	Al_2O_3 **nanoparticles** (Kandasamy, Wang, & Mujumdar, 2008)	CuO (Dhaidan et al., 2013)	**Al**	**Air**	**Coconut oil** (Al-Jethelah et al., 2018)		**Paraffin** (Dhaidan et al., 2013)	
					Solid (15^oC)	**Liquid (32^oC)**	**Solid**	**Liquid**
ρ **(kg/m^3)**	3600	6510	2719	1.225	920	915	-	-
μ **($Pa \cdot s$)**	N/A	N/A	N/A	1.7×10^{-5}	N/A	0.0326	N/A	-
C_p**($kJ/kg \cdot K$)**	0.765	0.54	0.871	1.006	3.75	2.01	2.89	
k **($W/m \cdot K$)**	36	18	202.4	0.024	0.228	0.166	0.21	0.12
β **($1/K$)**	N/A	N/A	N/A	N/A	N/A	7×10^{-4}	N/A	0.001
L **(kJ/kg)**	N/A	N/A	N/A	N/A	103	N/A	173.4	N/A
T_m **(ΔT_m)**	N/A				24 ($\pm2^{\circ}C$)		-	
Pr	N/A	N/A	N/A	N/A	394.73		-	

Thermal conductivity measurements are taken using KD2 PRO Thermal Conductivity Analyzer (Decagon Devices, USA) shown in **Fig. 4-1**. The measurement technique is based on transient-line-heat source theory. This theory is based on passing a certain amount of current through an infinitely long and very thin line which is buried in a semi-infinite medium. The line source acts as a heat dissipator and a temperature sensor. Depending on the thermal conductivity of the medium under study, the probe's temperature changes rapidly or slowly (the higher the

temperature increases, the lower the thermal conductivity of the medium is). The response to the temperature change is implemented to find the thermal conductivity of the medium.

Different sensors are designed to be used in different materials. In this research, the KS-1 sensor, which is 6.1 cm long, is implemented to measure the thermal conductivity of the medium in the liquid phase. The measurement scale of the probe ranges from 0.02 to 2 $W/m\cdot k$ with an accuracy of $\pm 5\%$. The sensor is not able to accurately measure the thermal conductivity of the liquid in the presence of natural convection, as natural convection is advection and conduction. A part of the thermal energy is transported by advection (fluid motion) if natural convection exists during the measurement, which causes the thermal conductivity is not properly measured. To address this problem, the sensor is used in a low power mode with a minimum measurement time (one minute). The thermal conductivity measurement condition should also be vibration-free. Any kind of vibrations due to fans, ventilation or movement should be avoided in the lab. The TR-1 sensor, which is 10 cm long, is used to measure the thermal conductivity of the medium in the solid phase. The sensor applied more heat during the measurement than KS-1 and the measurement time is also longer. The thermal conductivity measurement range is from 0.1 to 4 $W/m\cdot k$ in TR-1 sensor (Devices, 2011).

Fig. 4-1 KD2 PRO thermal conductivity analyzer.

The viscosity measurement of the samples is taken using a Cambridge Viscolab PVT viscometer shown in **Fig. 4-2**. The measurement is based on a simple and reliable electromagnetic concept. At a constant force, two coils magnetically move the piston back and forth and dedicated circuitry analyzes the piston's two-way travel time to measure the viscosity. The viscometer measuring range is from 0.1 to $10000\ cP$. A built-in temperature detector senses the temperature of the sample in the measuring chamber. The measuring chamber temperature is controlled through a thermal bath and a controller.

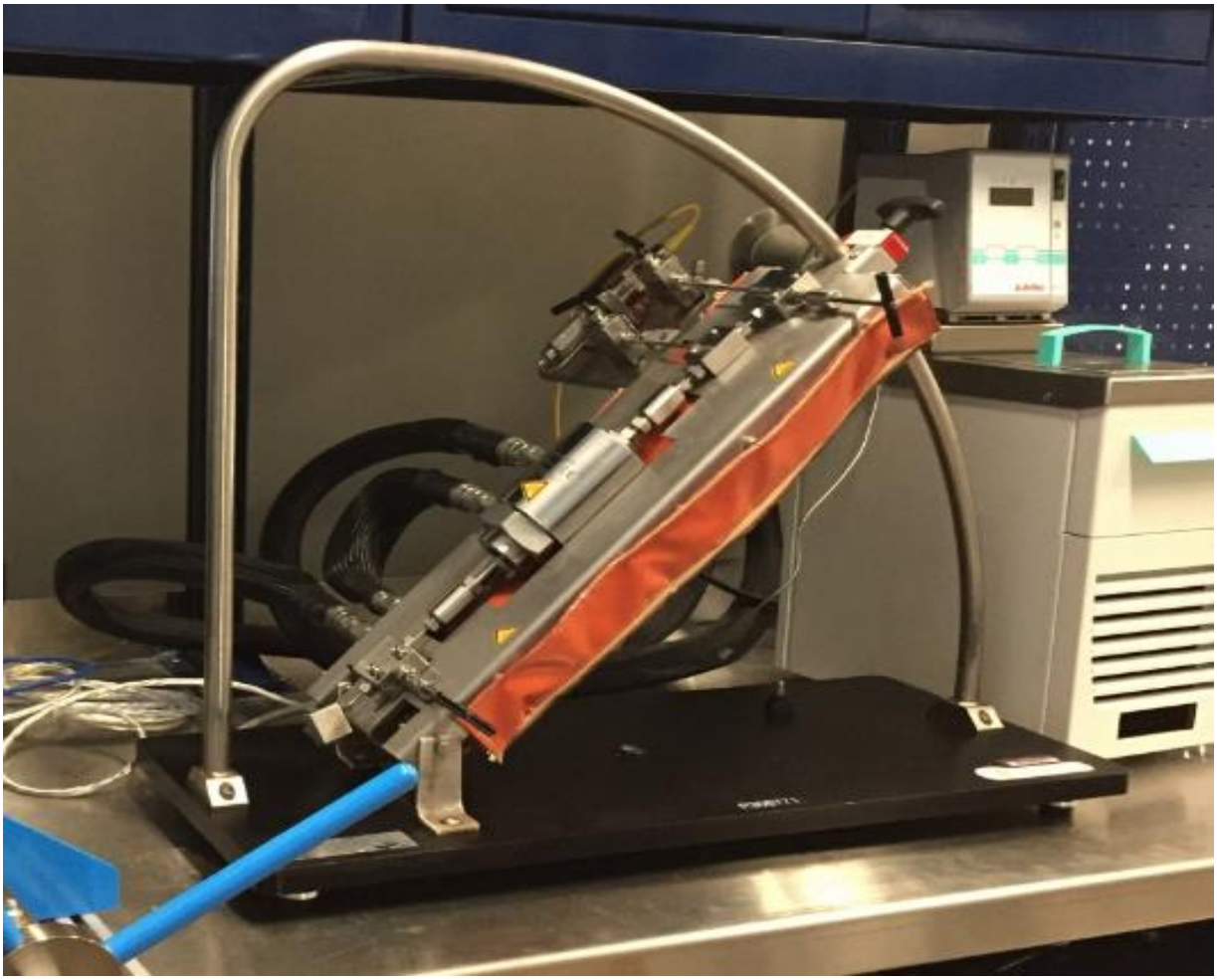

Fig. 4-2 Cambridge Viscolab PVT viscometer.

4.2 Sample preparation

To prepare the samples, Al_2O_3 nanoparticles (particle size $< 50\ nm$) is supplied by Sigma-Aldrich Co. St. Louis, Missouri, United States. As the nanoparticle size is fairly small, and also the nanoparticles are round, which help the stability of the mixture compared to other size and type of nanoparticles, such as nanowires, nanotubes and nanosheets. The nanoparticles weight is measured with a weigh scale, then dispersed into the desired amount of coconut oil, preheated to $70\ ^oC$ and stirred for an hour using a hot plate magnetic stirrer. Stirring the mixture at this high temperature facilitates the dispersion of nanoparticles due to the relatively low viscosity of the

molten PCM. To evaluate the stability of the mixture, the NePCM mixture is left motionless at $50\ ^{o}C$ for 5 hours. No sedimentation is seen at the low-nanoparticle concentrations, while small sedimentation is visualized at high-nanoparticle concentration, i.e. $\omega_3 = 1\ wt.\%$. To make sure the samples are well-dispersed, the samples are stirred inside the enclosure designed for the experiment after each experiment until the sample temperature reaches close to the solidifying temperature using a laboratory stand stirrer, as research on the stability of the samples is out of the scope of this research.

4.3 Experiment setup

The enclosure is designed using SOLIDWORKS ® software, and CNC machines are used to build the enclosure. A hot plate (temperature-controlling plate) is used on the bottom of the enclosure, although the location of the hot plate could be changed. The walls of the enclosure are one inch thick and made of a transparent plexiglass material, making an easy visualization during the phase change process, also providing a good insulation. A gasket is used to seal the walls in the case of leakage. Afterward, a leakage test is performed using water to make sure the fluid does not leak out. The enclosure and an exploded view of the cell and hot plate are depicted in **Fig. 4-3** (a),(b) (See Appendix 2 for more details). The hot plate (depicted in blue) is connected to a thermal bath, which keeps the hot plate temperature at a constant temperature, through circulating fluid in tubes. The enclosure's walls and tubes are covered with cryogel and polyurethane foam, respectively, to make sure the heat loss is minimum. The cryogel is detachable to provide easy access to the sample inside the enclosure. Eight T-type thermocouples are used at different locations in the enclosure to record the temperature, shown in Fig. **Fig. 4-3** (c). The thermocouples are connected to two Thermocouple Analogue Input (TAI) modules (NI-9211 from National Instruments) with a differential connection mode. The modules are connected to a USB chassis

which is connected to a computer. The whole device, called a data acquisition (DAQ) system, is a bridge between thermocouples (sensors) and the computer, basically converting analogue signals (voltage or current) to digital signals.

Also, a camera on a tripod is used to take pictures from the enclosure during the experiment. The third dimension of the enclosure, not shown in Fig. **Fig. 4-3** (c) is also $60\ mm$ and all the thermocouples are located in the middle of this dimension. The experiment schematic diagram and some parts of the experimental setup are shown in **Fig. 4-3** (d), (e). To avoid transient heat transfer, the thermal bath is connected to the enclosure using a three-way valve, not shown in **Fig. 4-3** (d), (e). This helps to have two loops: the first loop is used for warming the thermal bath up to a certain temperature set as the boundary condition without flowing the thermal bath fluid (water) inside the hot plate (transient state). The second loop is used to flow the thermal bath fluid into the test section (steady state) as soon as the temperature of the thermal batch reaches a uniform temperature set in the thermal bath. Before running the experiment, a benchmark test is conducted to make sure the thermocouples and other auxiliaries used in the experiment are working accurately. To obtain the interface location, the ImageJ and MATLAB® software are used. Then, the interface location is compared with the interface location found from the exact solution to verify the validity of the experiment. As mentioned earlier, if the interface location obtained by these two different approaches are reasonably coincided, the experimental results are valid. Also, the temperature distributions in both solid and liquid regions are recorded using the thermocouples and compared with the temperature distribution obtained from the exact solution.

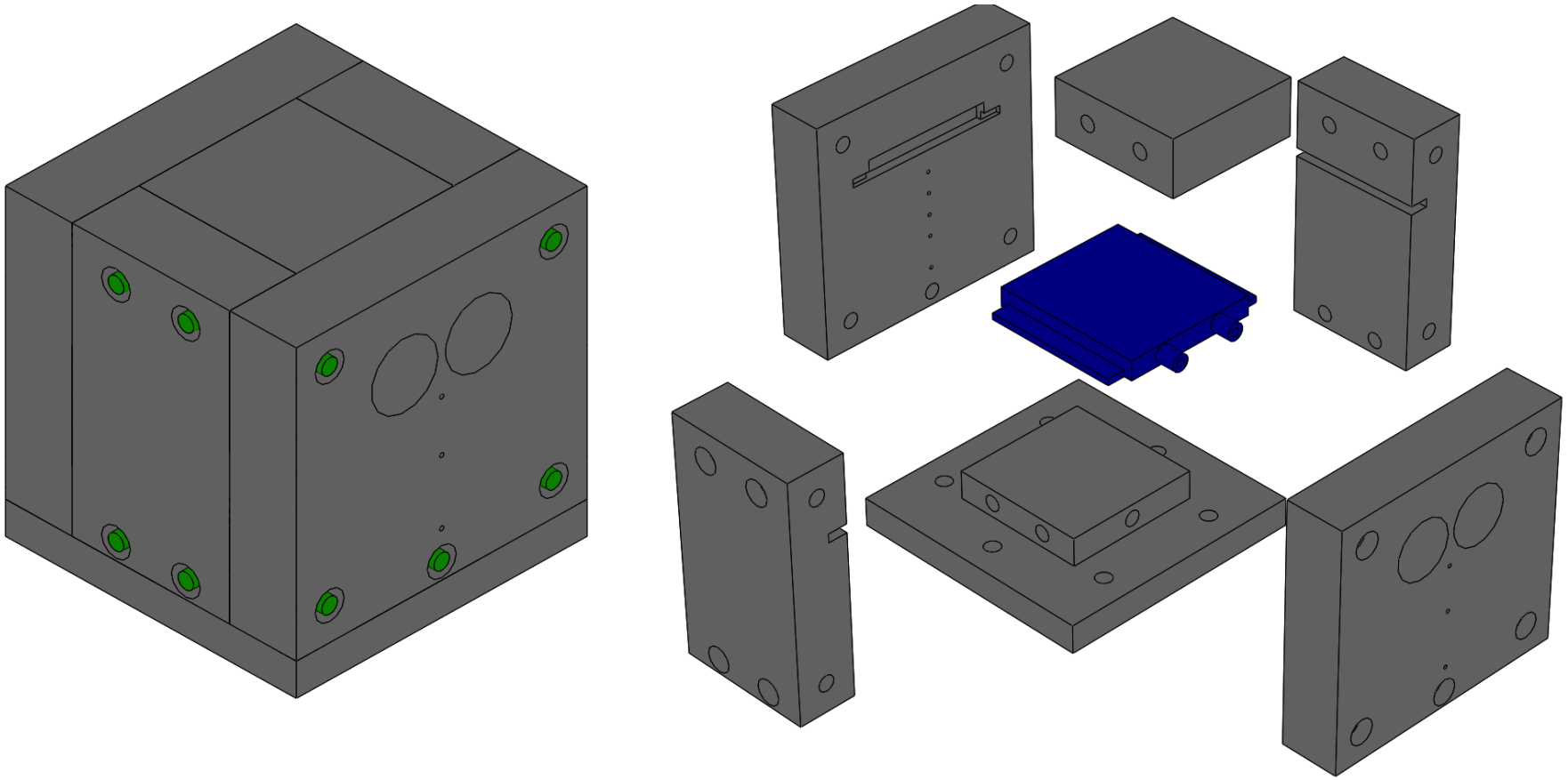

(a) (b)

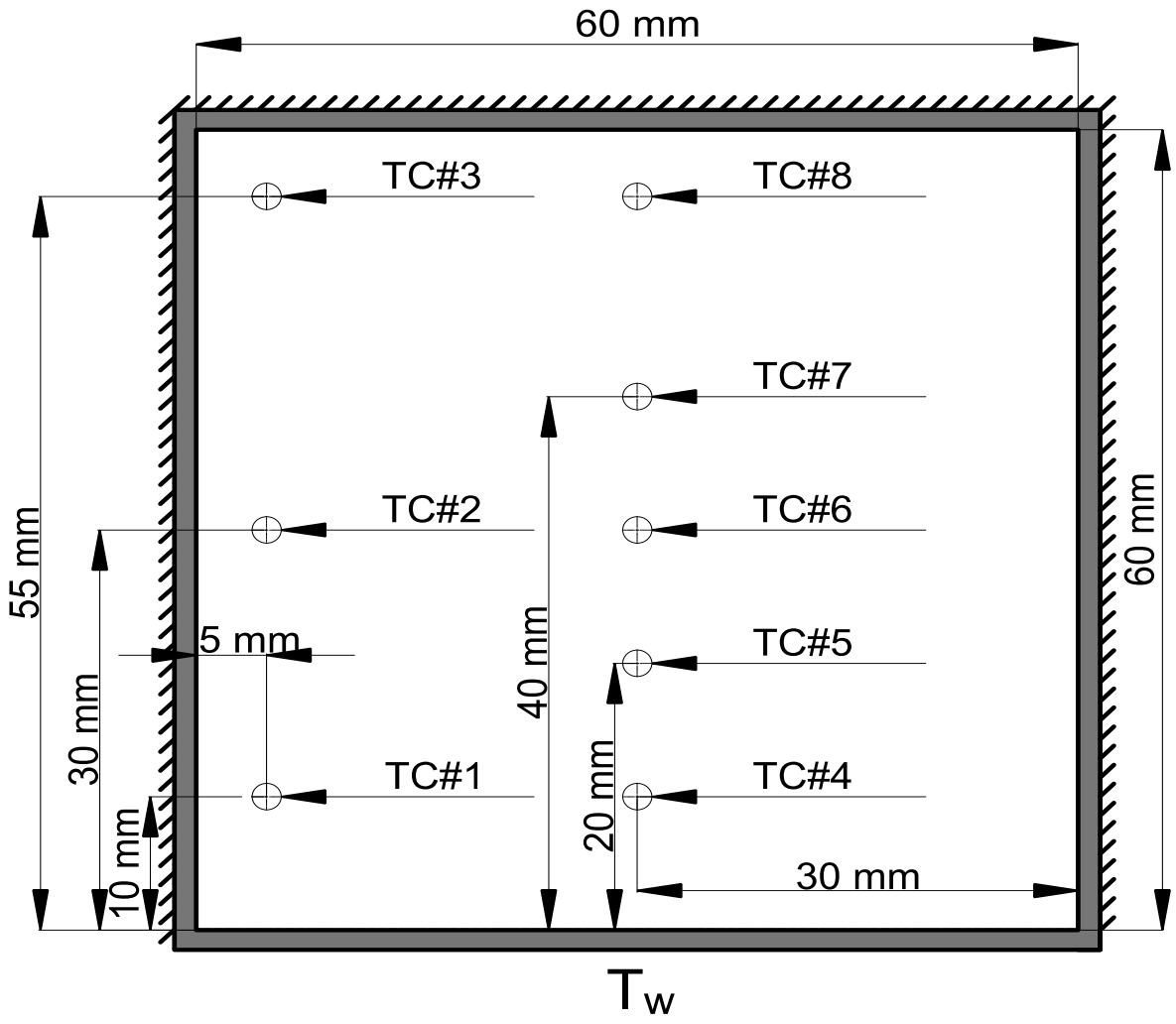
60 mm
TC#3
TC#8
TC#7
TC#2
TC#6
TC#5
TC#1
TC#4
55 mm
60 mm
40 mm
30 mm
5 mm
10 mm
20 mm
30 mm
T_w

(c)

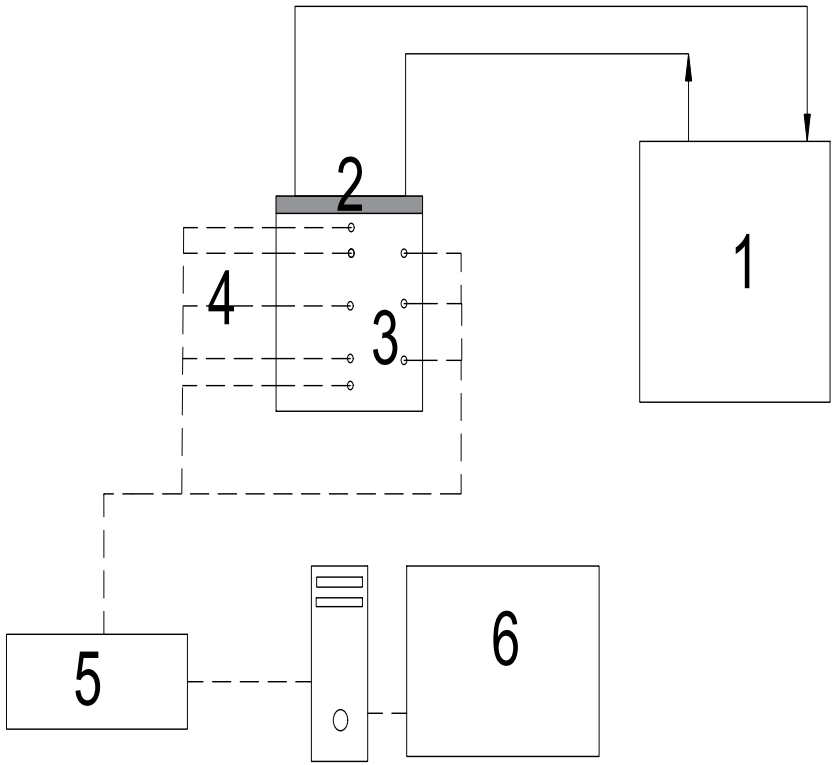

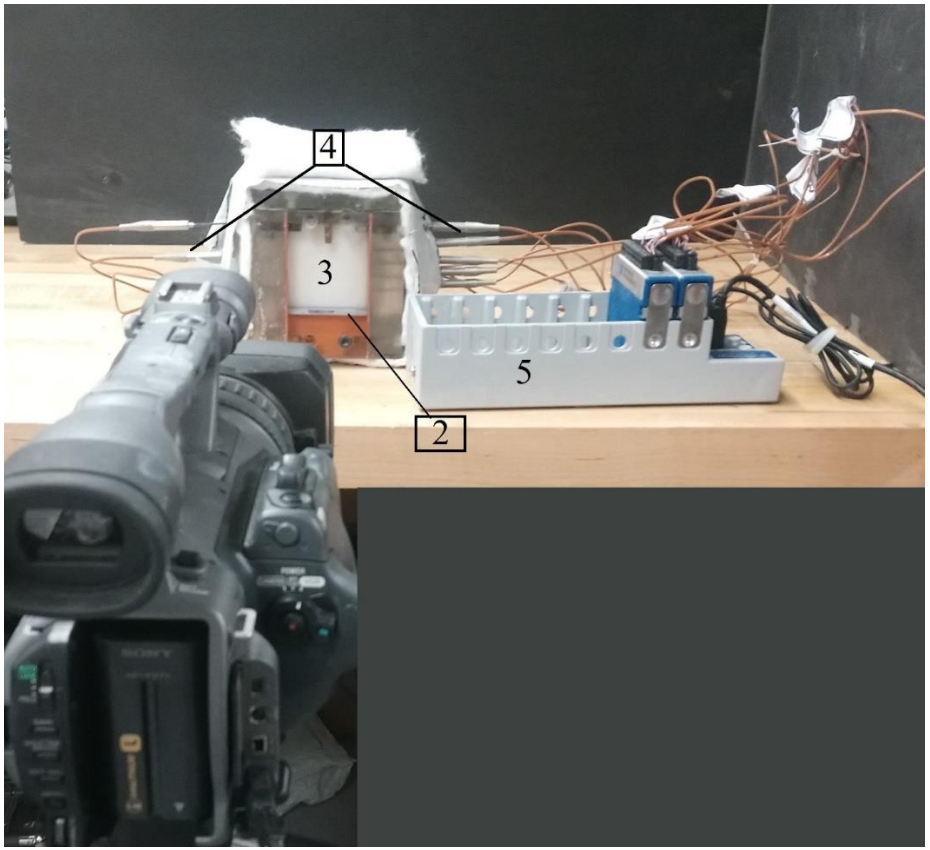

(d) (e)

Fig. 4-3 (a) Enclosure used in the experiment, (b) Exploded view of the enclosure, (c) The 2-D enclosure dimensions in millimetres and thermocouples location (d,e) experiment setup: 1: Thermal bath, 2: Hot plate, 3: Enclosure, 4: Thermocouple probes, 5: DAQ, 6: Computer.

4.4 Uncertainty analysis

The measurement uncertainty depends on the accuracy of measuring device. No measuring device is 100% accurate, so uncertainty exists. Random error, another source of error, causes the measuring values to deviate from the real value. Replication of the experiment is one way to find the best estimate of the real value which requires finding the average, standard deviation, and standard error. The measurements actual value falls within a range of values which is specified as follows:

$$\text{Measurement} = \text{Best estimate} \pm \text{Uncertainty} \tag{4-1}$$

The thermocouples that will be used in this study are the ungrounded T-type with the part number TJ36-CPIN-116G-2 purchased from a company called OMEGA. The uncertainty of the thermocouples, plexiglass thickness and other independent parameters are reported by the manufacturer and listed in **Table 4-2**, while the uncertainty of a dependent variable can be calculated as follows (Kline & Mcclintock, 1953):

$$\delta R = \left[\sum_{i=1}^{N} \left(\frac{\partial R}{\partial \Phi_i} \delta \Phi_i \right)^2 \right]^{1/2} \tag{4-2}$$

where $\delta \Phi$ is the uncertainty of the independent variables, affecting the dependent variable, for which the uncertainty is calculated. To find the Ra_S uncertainty, for example, the following propagation equation is employed, which extends Eq. (4-2):

$$\frac{\delta Ra_S}{Ra_S} = \left[\left(\frac{\partial Ra_S}{\partial S} \delta S \right)^2 + \left(\frac{\partial Ra_S}{\partial k} \delta k \right)^2 + \left(\frac{\partial Ra_S}{\partial \mu} \delta \mu \right)^2 \right]^{1/2} \tag{4-3}$$

Table 4-2 Uncertainty analysis.

Parameters	Uncertainty
T-type thermocouple	$\pm 0.5\ ^{o}C$
Enclosure volume	$\pm 5\ cm^{3}$
Nanoparticles weight	$\pm 10\ mg$
Thermocouples location (horizontal displacement)	$\pm 3\ mm$
Thermocouple location (vertical displacement)	$\pm 2\ mm$
Interface location	$\pm 1\ mm$
Thermal conductivity (solid material)	10%
Thermal conductivity (liquid material)	5%
Viscosity	1%
$Ra_{S\simeq H}$	16%
Gr_{H}	7%

Also, to find the overall uncertainty of the measured temperatures, the root sum square method (Abernethy, Benedict, & Dowdell, 1985) is employed to combine the location and thermocouple errors. Using this method the overall uncertainty of the measured temperature (combined uncertainties of both location and thermocouple errors), the overall nanoparticle concentration dispersed in the PCM (combined uncertainties of both nanoparticle concentration and the enclosure volume error), and the overall uncertainty of the interface location (combined

uncertainties of the interface location and the enclosure volume) are $6\,\%$, $4\,\%$, and $3\,\%$, respectively. The uncertainty of each parameter, including Ra_H are reported in **Table 4-2**.

4.5 Summary

In this chapter, an enclosure was designed and built along with the experimental setup to study the effects of nanoparticles on the phase change rate. Eight T-type thermocouples were inserted to an enclosure, which is heated from the bottom using a thermal bath. The thermocouples were also connected to a DAQ to measure and record the temperature variation inside the enclosure. The interface location changes were also visualized using a camera. The way the materials under study selected and the samples prepared was introduced in detail. The devices required to measure the thermal conductivity and viscosity of the samples were introduced and explained. In addition, the way that the uncertainty of the experiment is calculated was explained.

In the following chapter, the way the experiment is conducted, the thermophysical properties are taken, and the results of the experiment are obtained will be explained in detail.

Chapter 5 Effects of nanoparticles on the melting rate in an enclosure heated from the bottom

In this chapter, experimental studies are conducted to analyze the effects of nanoparticles on the phase change rate. One-dimensional conduction driven phase change heat transfer is investigated. The results are compared with the one-dimensional heat transfer exact solution (Eqs. (3-7)-(3-10)). Then, the melting of PCM is simulated in the presence of Rayleigh-Benard convection in the enclosure with the conditions explained in the previous chapter using Eqs. (3-29)-(3-31). The numerical simulation results are compared with the experimental results. The experiments are conducted to evaluate the effects of nanoparticles on the phase change rate, thermal conductivity, viscosity, instantaneous Rayleigh number, and the Grashof number.

5.1 Comparison between the analytical solution and experimental data

To verify the experimental setup in the next section, a pure heat conduction melting experiment (hot plate on the top, shown in **Fig. 4-3** (c)) is conducted twice to make sure the results are reproducible. The results discrepancy of the first and second iterations were not considerable. The thermocouples record the temperature at different locations, and a picture is taken to find the solid-liquid interface location in the enclosure at every 5 minutes. The pure PCM is initially at room temperature ($16\ ^{o}C$), which is lower than the melting temperature. The wall temperature is set to $70\ ^{o}C$. Once the experiment starts, a liquid region forms on the upper part of the enclosure. The solid-liquid interface is nearly planar as the only mechanism of heat transfer is heat conduction in this experiment. The solid-liquid interface for the pure conduction phase change experiment is indicated after 40 minutes in **Fig. 5-1**. A small mushy zone seems to be formed in this figure, which is considered as the solid region during the solid-liquid interface measurement. It is also observed that the thermocouples at the same distance from the hot plate (for example TC#1 and

TC#4) show nearly identical temperatures during the experiment, indicating a natural convection mechanism is not contributing to the heat transfer.

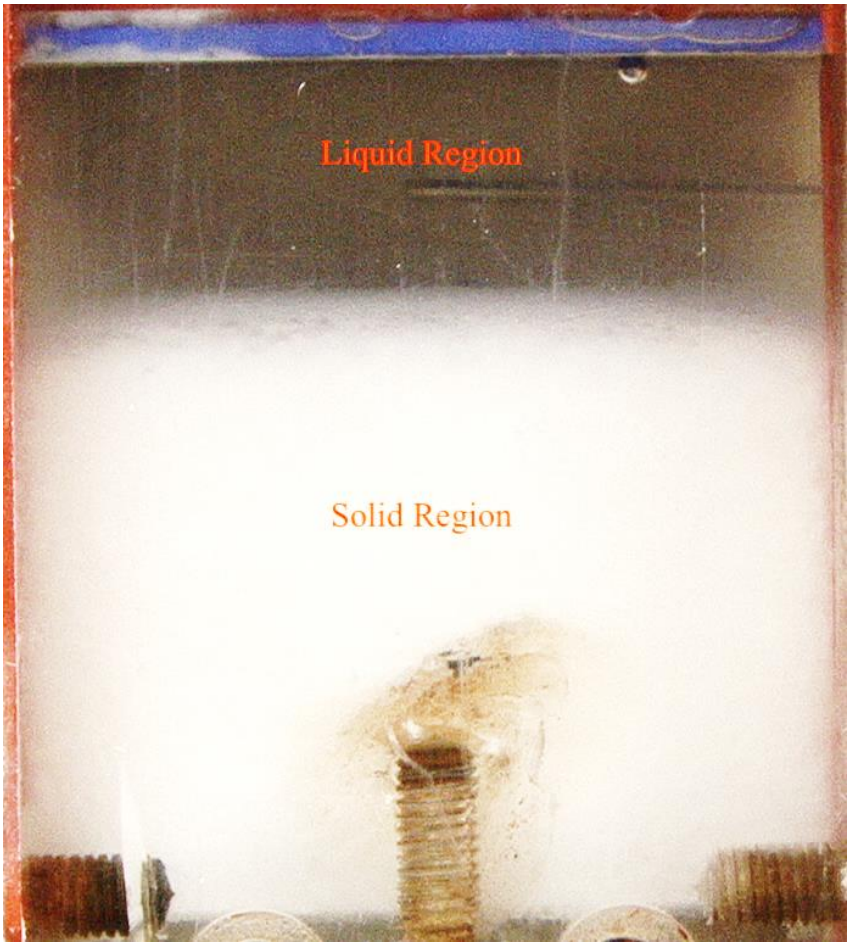

Fig. 5-1 The solid-liquid interface location after 40 minutes of melting from the top.

The interface location is obtained and compared with the exact solution for a one-dimensional two-region melting problem (Eqs. (3-9)-(3-10)) as shown in **Fig. 5-2** (a). Also, the temperature distribution is obtained in the solid region after 45 minutes and in the liquid region after 140 minutes using Eqs. (3-7)-(3-8). The temperature distribution is compared at both solid and liquid regions with the temperature at the same location measured using the thermocouples as

shown in **Fig. 5-2** (b-c). The maximum discrepancy of the interface and the temperature distribution between the experiment and the exact solution are 12 % and 9%, respectively, indicating a fairly good agreement. This deviation, however, can be attributed to the reasons mentioned in section 3.1.

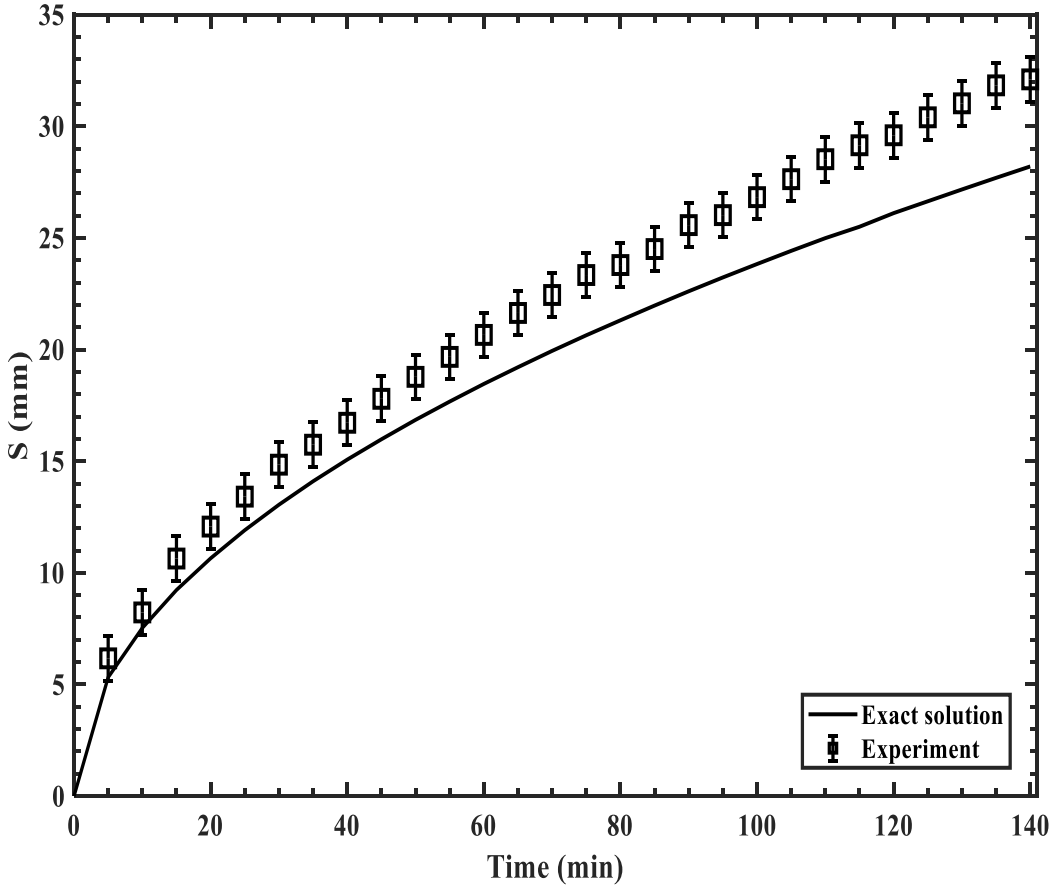

(a)

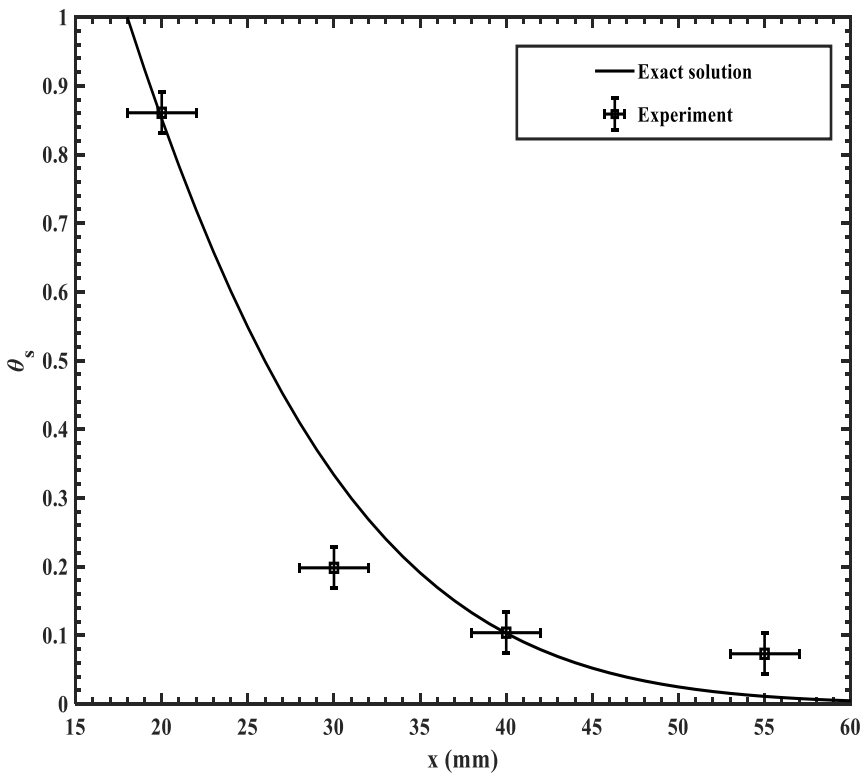

(b)

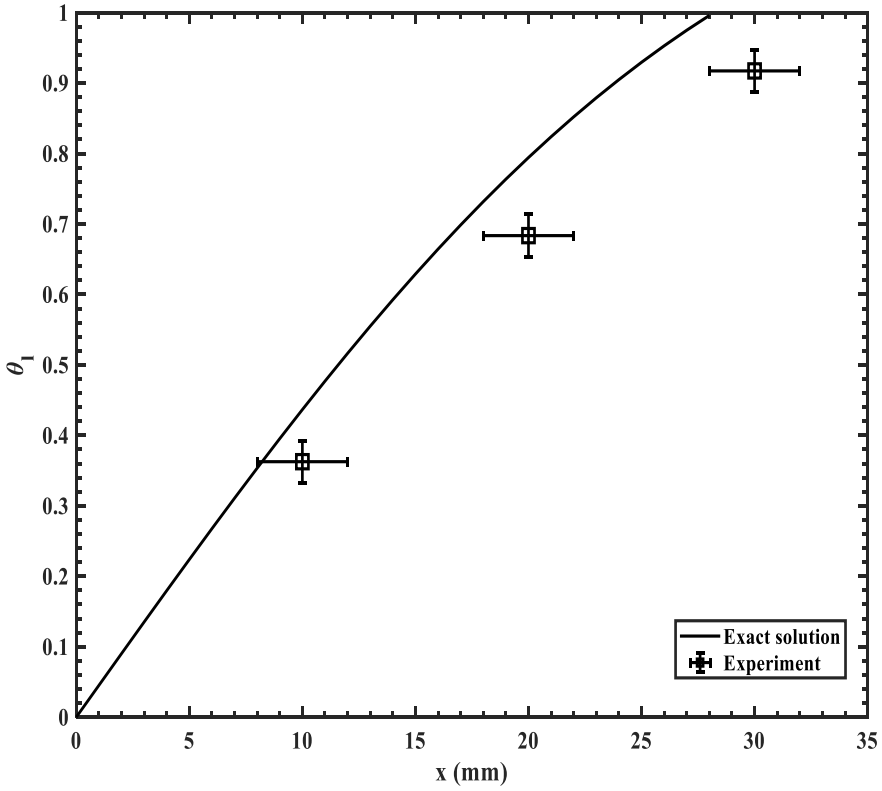

(c)

Fig. 5-2 (a) Solid-liquid interface location during the time obtained from the exact solution and the experiment, (b) Temperature distribution in the solid region after 45 minutes (c) temperature distribution in the liquid region after 140 minutes.

5.2 Comparison between the numerical predictions and experimental data

In this section, the numerical results are compared with the experimental results. The two conduction domination and convection domination regimes discussed in chapter 3 (scaling analysis section) are indicated and discussed along with the temperature and liquid fraction contours, hot-spots and streamlines of an enclosure heated from the bottom. To obtain grid-independent results in the numerical section, the time the wall temperature is set to $55\,^{o}C$ (lower than the wall temperature for the previous pure conduction experiment) and different grid sizes are implemented to find a grid-independent solution. The effect of grid size on the liquid fraction is evaluated in **Fig. 5-3**. It is found that the results are independent of the grid size of 200×200. This grid size is used for the comparison of numerical and experimental results in this study. In the experimental part, the enclosure is placed upside down to locate the hot plate on the bottom (See **Fig. 4-3** (e)). As mentioned earlier, this causes the Rayleigh-Benard convection heat transfer contributing to the total heat transfer to melt the PCM/NePCM faster. Similar to the numerical study, the wall temperature is set to $55\,^{o}C$ and a picture is taken to find the solid-liquid interface from the enclosure at every 150 seconds.

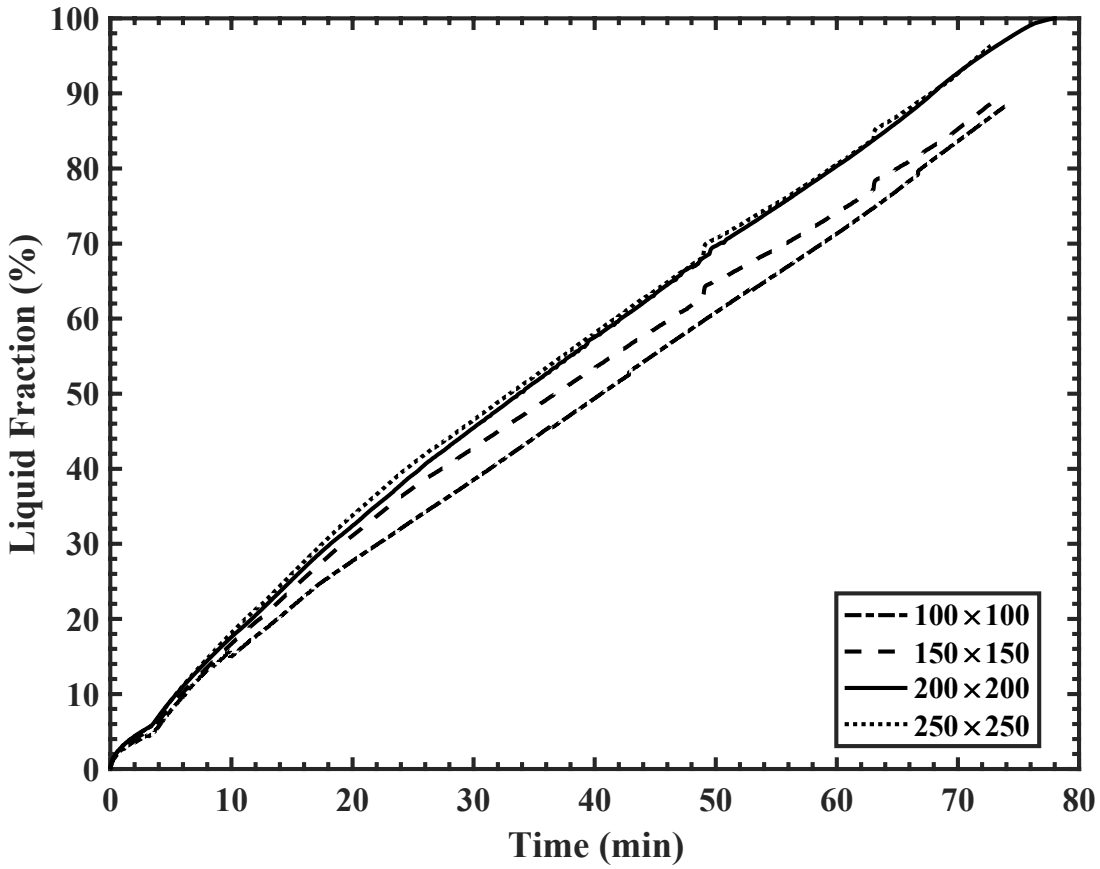

Fig. 5-3 Effect of grid size on the variation of the liquid fraction with time.

The liquid fraction obtained numerically and experimentally is shown in **Fig. 5-4**. It is found that the liquid fraction changes nearly linearly by elapsing time in the case of emerging Rayleigh-Benard in a melting problem, and there is a reasonably small deviation (maximum deviation: $\simeq 8\%$) which exists between the numerical and experimental liquid fraction. Also, the temperature variations are measured during this time at eight different locations (see **Fig. 4-3** (c)) in the enclosure and compared with the numerical results depicted in **Fig. 5-5** . A sharp temperature rise is seen at all locations at different times, depending on the thermocouple position. This phenomenon can be attributed to the passage of the melting directed toward the thermocouple. Regardless of the discrepancy found between the numerical and experimental values of TC#3 (see **Fig. 5-5** (c)), a reasonable agreement is seen between the temperature variation recorded with

TC#1 to TC#8 and the numerical model. In addition, the temperature fluctuates over time, particularly when the temperature reaches a nearly steady state at a certain point. This fluctuation is greater for numerical results than experimental results, as the thermocouples measure the temperature of a small region, while the temperature of a particular point is defined and measured in the numerical calculations, causing higher temperature variations. The fluctuations indicated in both numerical and experimental results can be attributed to the presence of Rayleigh-Benard convection, affecting the temperature variation with time, while these fluctuations were not observed in the temperature variations of the case heated from the top (pure heat conduction).

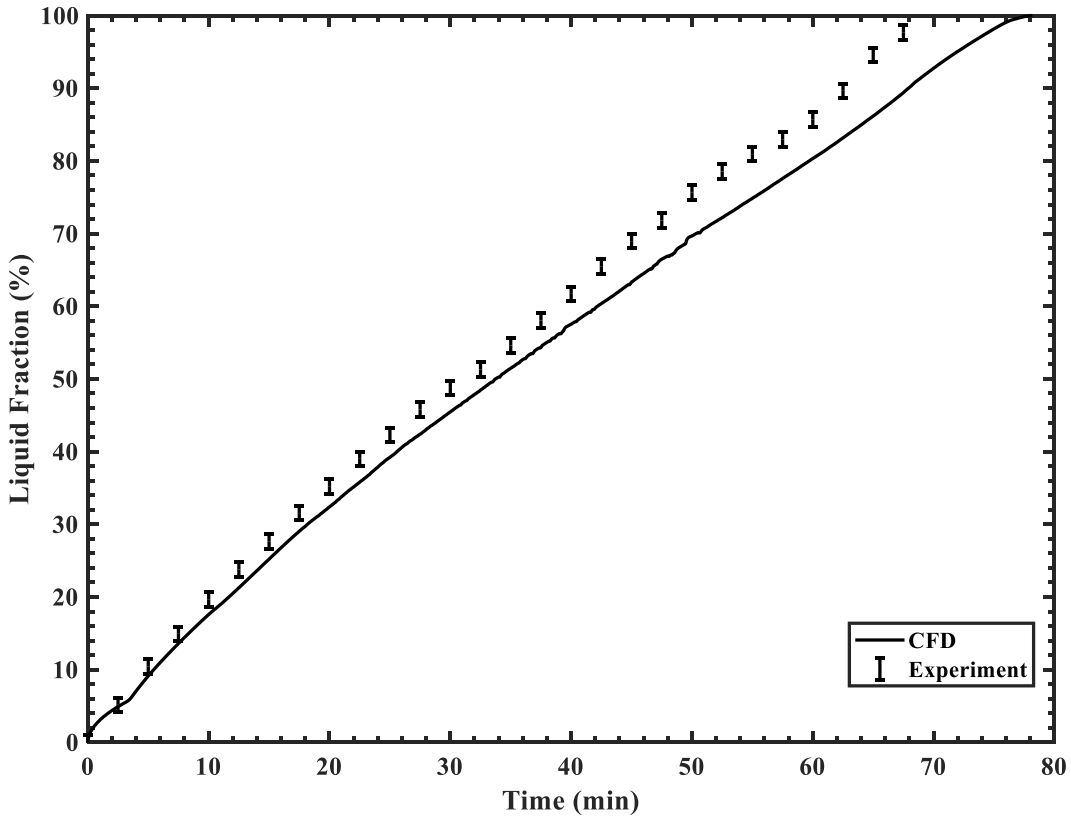

Fig. 5-4 Solid-liquid interface location over the time obtained from CFD and the experiment.

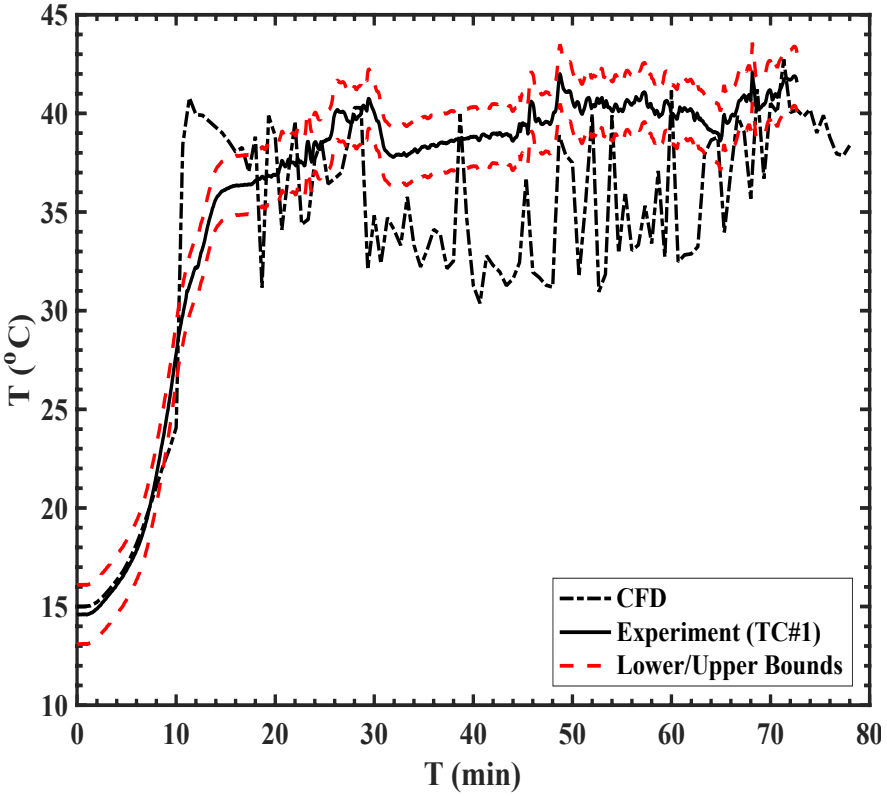
T (°C)
T (min)
CFD
Experiment (TC#1)
Lower/Upper Bounds

(a)

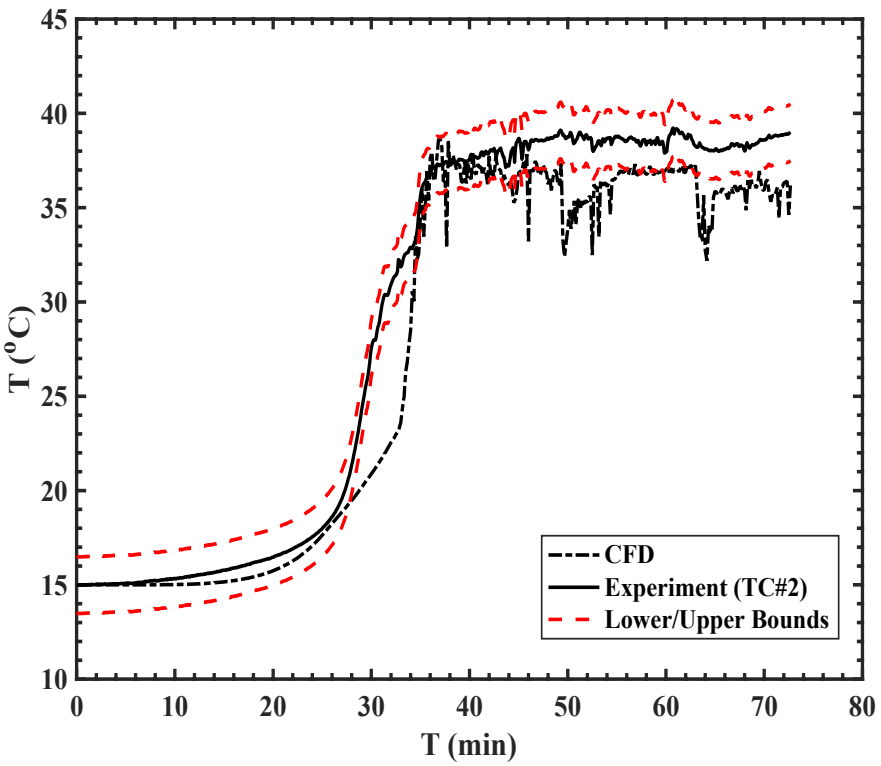
T (°C)
T (min)
CFD
Experiment (TC#2)
Lower/Upper Bounds

(b)

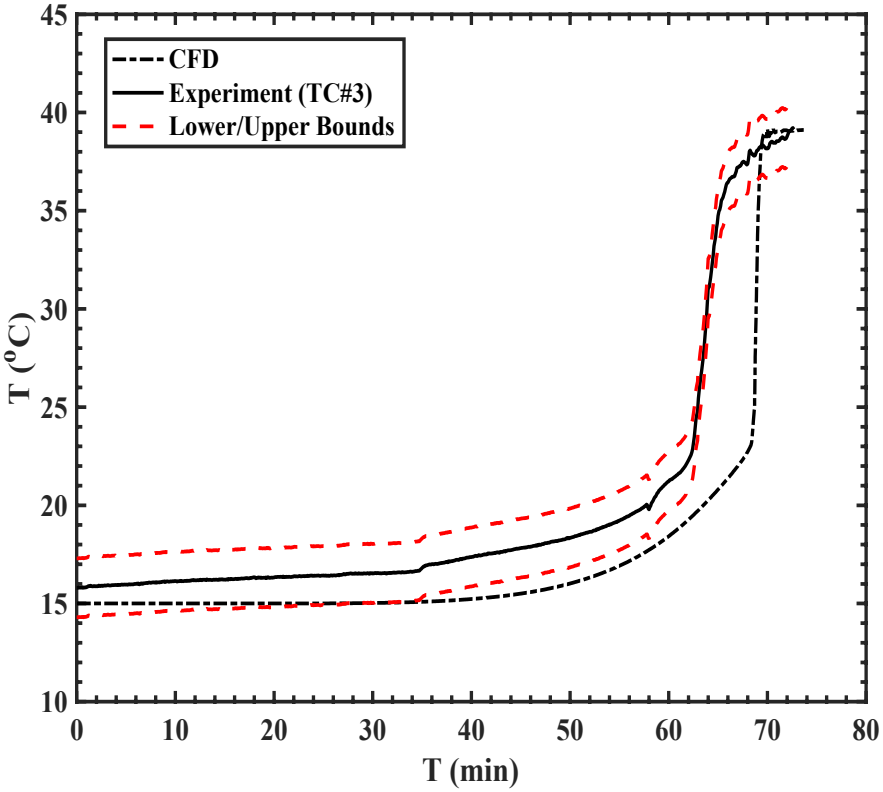
CFD
Experiment (TC#3)
Lower/Upper Bounds
T (°C)
T (min)
45
40
35
30
25
20
15
10
0
10
20
30
40
50
60
70
80

(c)

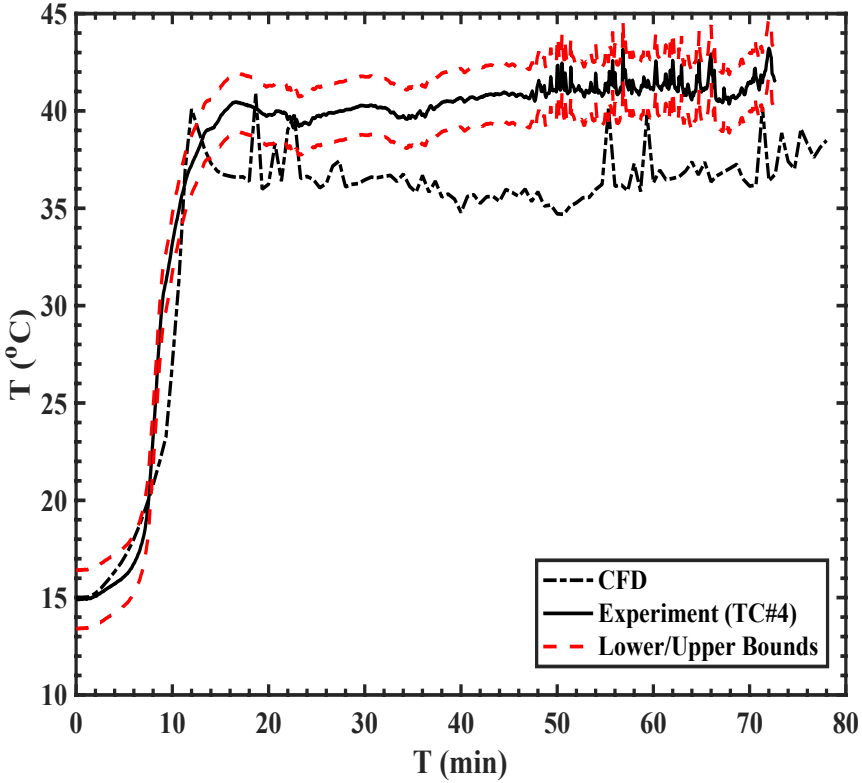
CFD
Experiment (TC#4)
Lower/Upper Bounds
T (°C)
T (min)
45
40
35
30
25
20
15
10
0
10
20
30
40
50
60
70
80

(d)

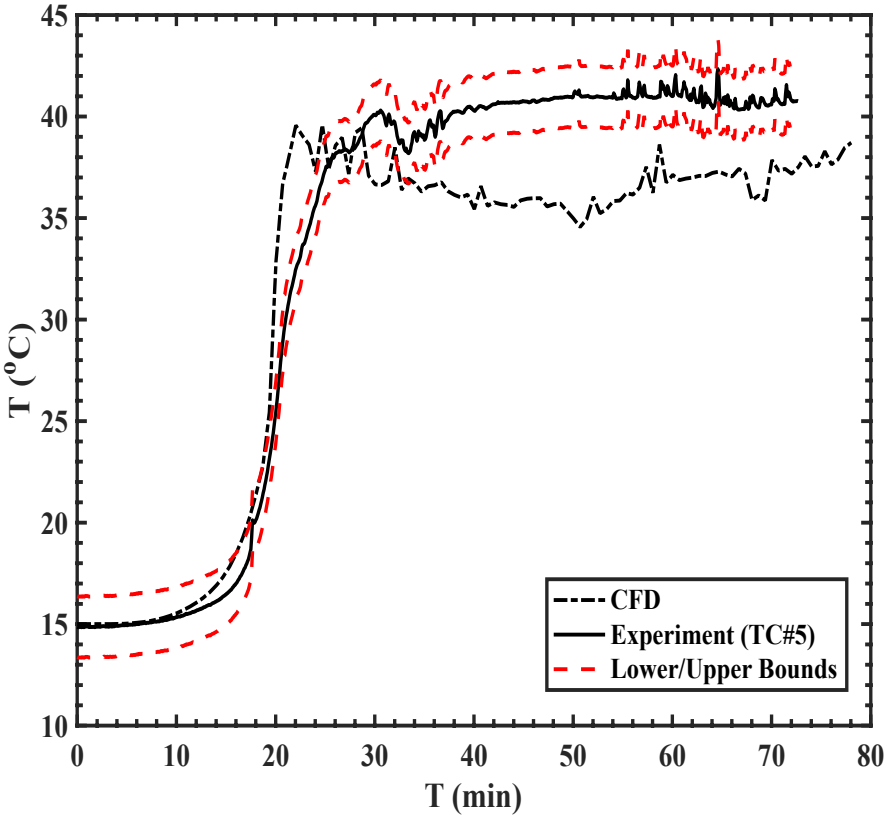
T (°C)
T (min)
CFD
Experiment (TC#5)
Lower/Upper Bounds

(e)

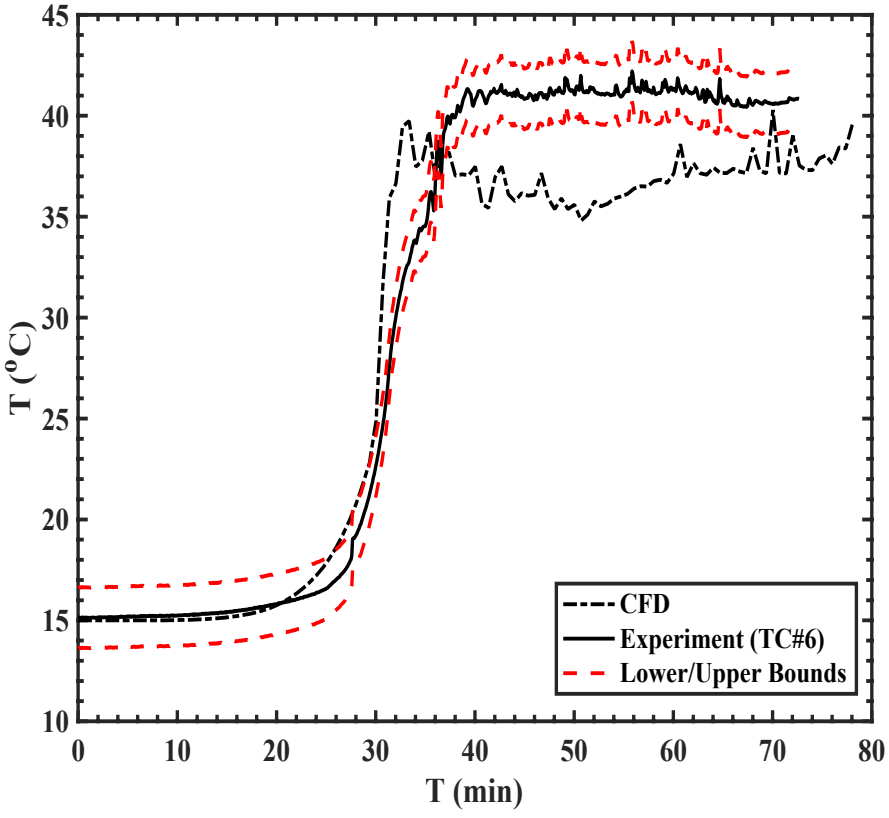
T (°C)
T (min)
CFD
Experiment (TC#6)
Lower/Upper Bounds

(f)

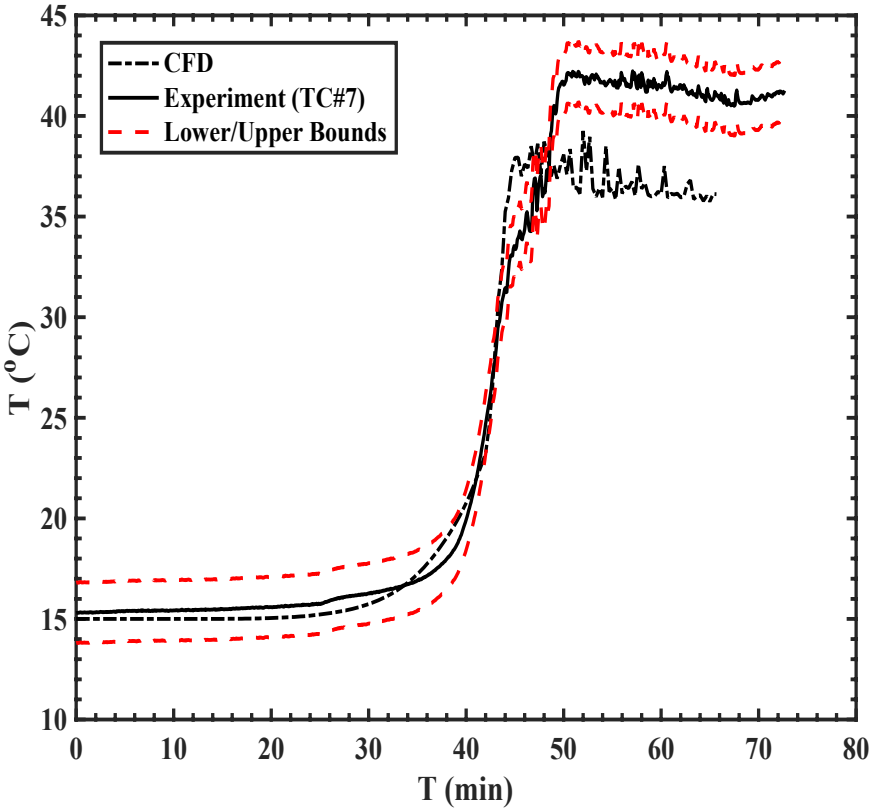

(g)

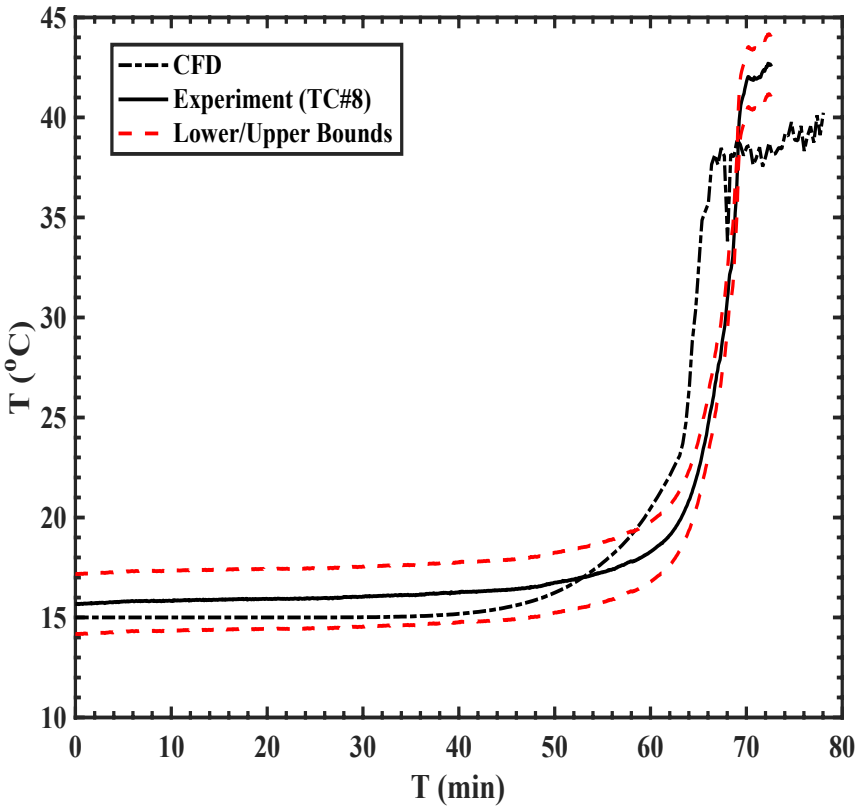

(h)

Fig. 5-5 Experimental and numerical temperature distribution at eight different locations in the enclosure (a) $x = 5\ mm,\ y = 10\ mm$ (b) $x = 5\ mm,\ y = 30\ mm$ (c) $x = 5\ mm,\ y = 55\ mm$, (d) $x = 30\ mm,\ y = 10\ mm$, (e) $x = 30\ mm,\ y = 20\ mm$, (f) $x = 30\ mm,\ y = 30\ mm$, (g) $x = 30\ mm,\ y = 40\ mm$, (h) $x = 30\ mm,\ y = 55\ mm$.

The melting process of the pure PCM heated from the bottom at a constant temperature of $55\,^{o}C$ is shown at seven different frames numerically **Fig. 5-6** (a-I) to (g-I), experimentally **Fig. 5-6** (a-II) to (g-II), and combined for a better presentation in **Fig. 5-6** (a-III) to (g-III). Two conduction domination and convection domination regimes discussed in the scaling analysis section are seen in the figures. Referring to Eq. 3-19, the conduction domination regime is the only mechanism of heat transfer at around the first three minutes of the melting process, shown in **Fig. 5-6** (a-I) and (a-II). The solid-liquid interface is planar, even though small rolls of flow start forming at the end of this regime. The rolls formed at the end of the conduction domination regime become larger and stronger by elapsing time, making the natural convection dominant (beginning of the natural convection domination regime), which causes the interface shape changes from planar to a periodic form (a series of waves) illustrated in **Fig. 5-6** (b-I) and (b-II). The number of waves formed at the solid-liquid interface is approximately proportional to the length of the enclosure divided by the length of the solid-liquid interface. A reason for this phenomenon is that the number of vortexes (rolls) created in the liquid region is dependent on the aspect ratio of the liquified region. Six waves are expected to be seen, for example, if the interface length is $1\,cm$ in this enclosure (the wavelength is small). The number of waves is more than six in **Fig. 5-6** (b-I) and (b-II) as the interface length is smaller than $1\,cm$ at this time. By elapsing time, the solid-liquid interface moves upward, and subsequently, the number of waves and rolls reduces, while they become larger and stronger, as indicated in **Fig. 5-6** (c-I) and (c-II). The natural convection also becomes stronger due to instantaneous enhancement in the Rayleigh number discussed in the scaling analysis section. With time, the solid-liquid interface moves upward and its length becomes approximately $1.5\,cm$, causing the number of waves to reduce to four as expected (the wavelength becomes larger), which are visible in **Fig. 5-6** (d-I) and (d-II). This trend continues as the number

of waves reduces to three when the solid-liquid interface length reaches approximately to $2\ cm$, as shown in **Fig. 5-6** (e-I) and (e-II), and the instantaneous Rayleigh number becomes larger. By moving the solid-liquid interface upward, the shape and number of the rolls become irregular at **Fig. 5-6** (f-I), while the solid-liquid interface shape is still similar in both numerical model and experiment, as shown in **Fig. 5-6** (f-I) and (f-II). This irregularity in the shape of the rolls may be attributed to the transition period from three waves to two waves as the number of waves again reduces when the solid-liquid interface length is approximately to $3\ cm$. The strength of the rolls of flow formed afterward becomes greater than before, as their pace in the streamlines is larger, shown in **Fig. 5-6** (g-I). Again, this is due to the increasing instantaneous Rayleigh number. Comparing the shape of the solid-liquid interface between the numerical and experimental results at these seven different time steps shows a good agreement between the numerical and experimental results.

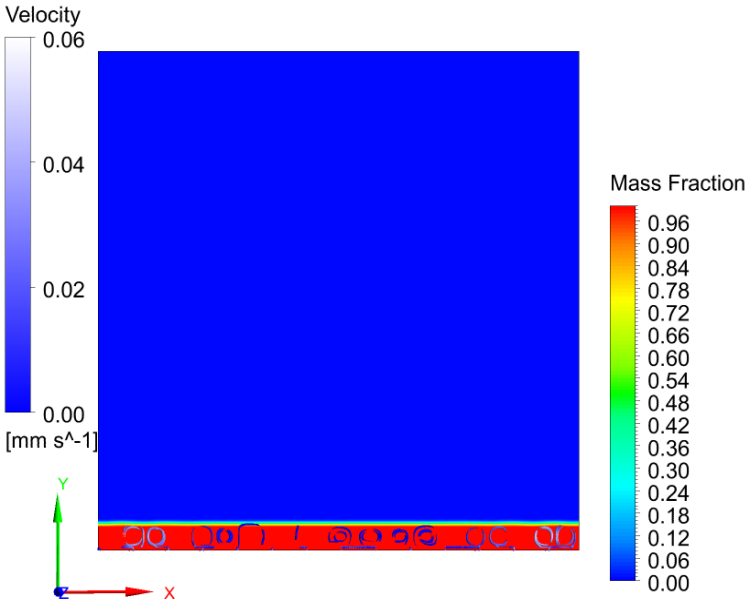
Velocity
0.06
0.04
0.02
0.00
[mm s^-1]
Y
X
Mass Fraction
0.96
0.90
0.84
0.78
0.72
0.66
0.60
0.54
0.48
0.42
0.36
0.30
0.24
0.18
0.12
0.06
0.00

(a-I)

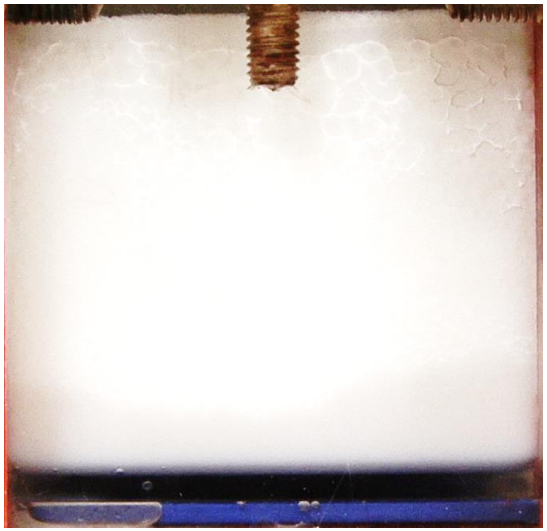

(a-II)

(a-III)

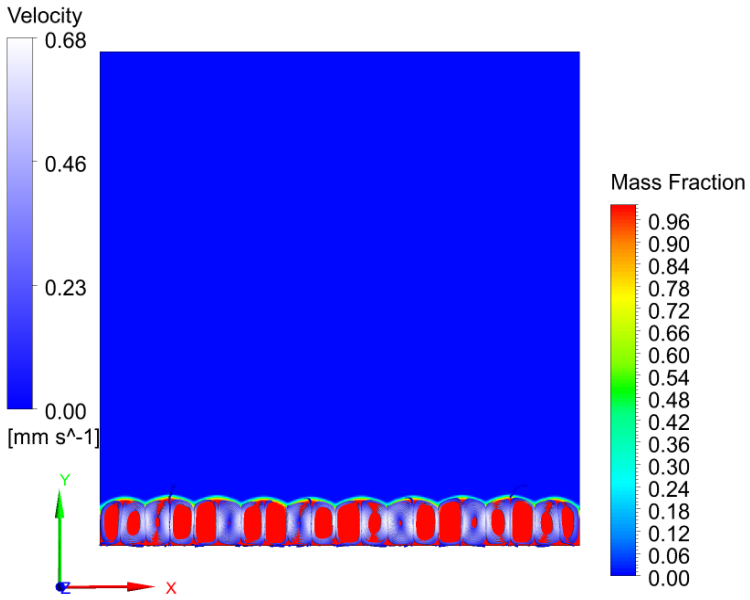
Velocity
0.68
0.46
0.23
0.00
[mm s^-1]
Y
X

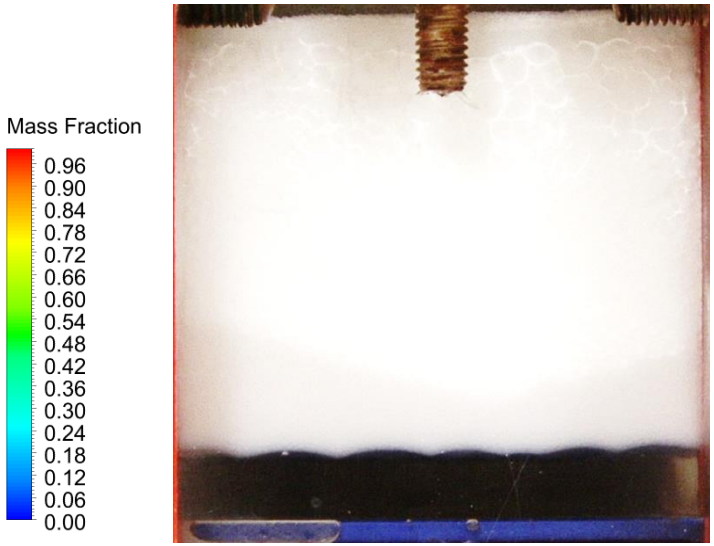
Mass Fraction
0.96
0.90
0.84
0.78
0.72
0.66
0.60
0.54
0.48
0.42
0.36
0.30
0.24
0.18
0.12
0.06
0.00

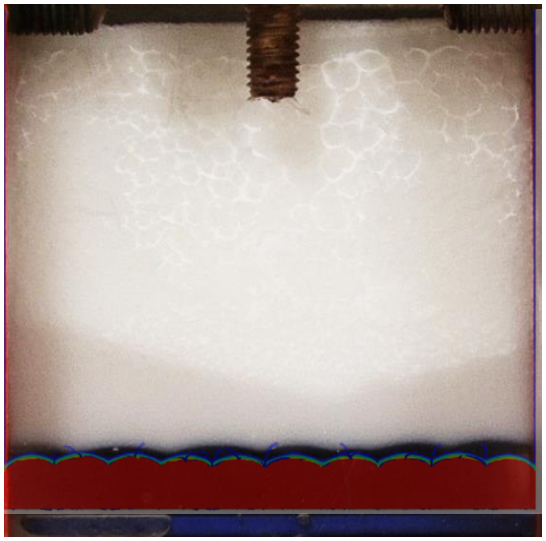

(b-I) (b-II) (b-III)

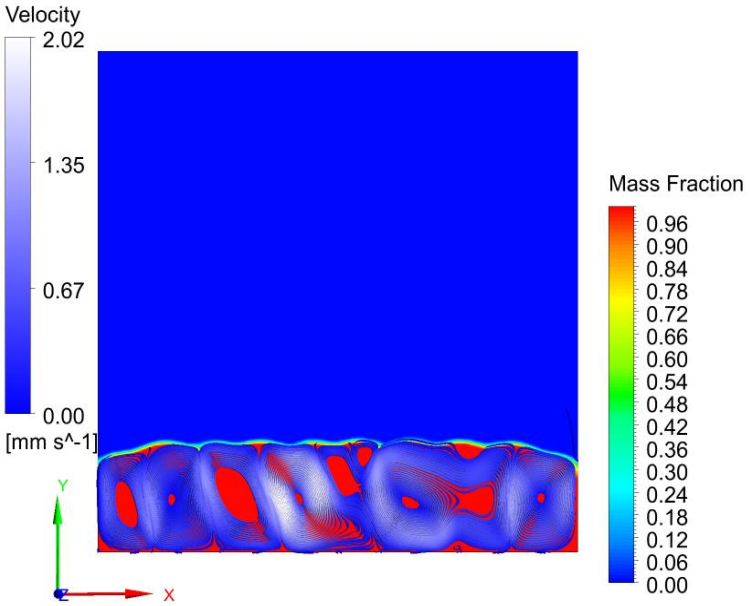
Velocity
2.02
1.35
0.67
0.00
[mm s^-1]
Y
X
Mass Fraction
0.96
0.90
0.84
0.78
0.72
0.66
0.60
0.54
0.48
0.42
0.36
0.30
0.24
0.18
0.12
0.06
0.00

(c-I)

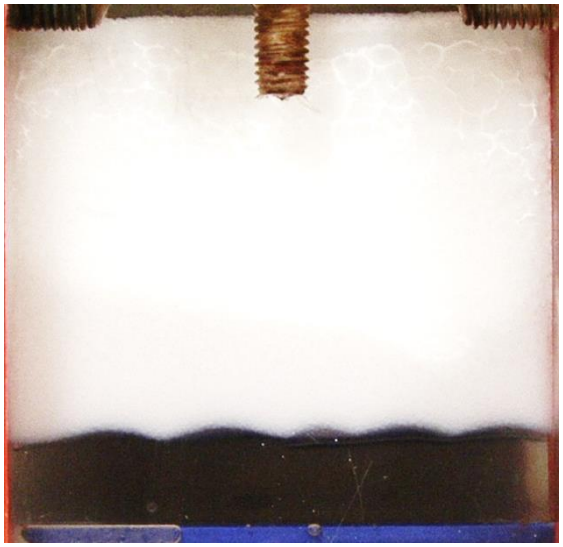

(c-II)

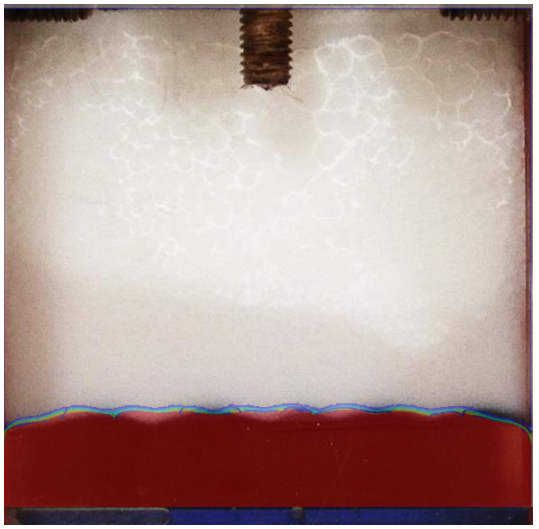

(c-III)

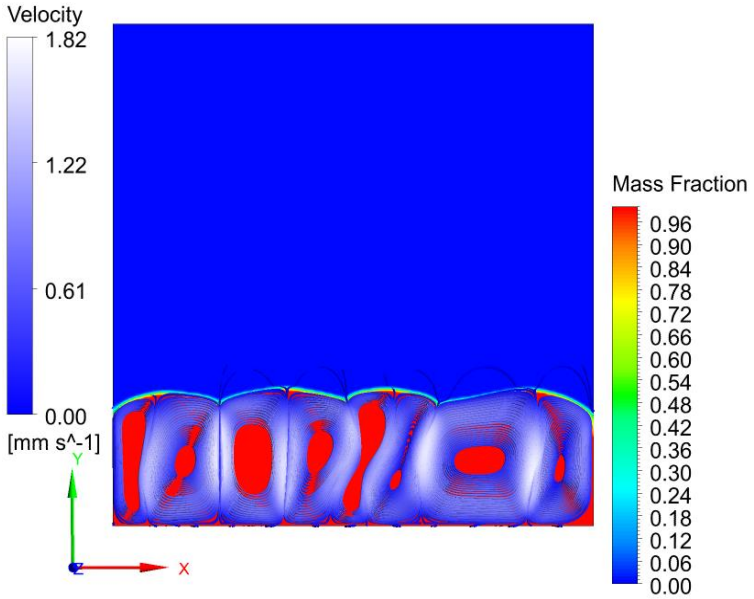
Velocity
1.82
1.22
0.61
0.00
[mm s^-1]
Y
X
Mass Fraction
0.96
0.90
0.84
0.78
0.72
0.66
0.60
0.54
0.48
0.42
0.36
0.30
0.24
0.18
0.12
0.06
0.00

(d-I)

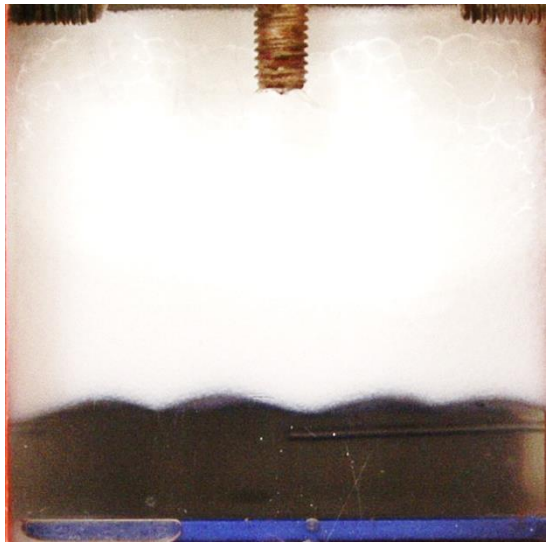

(d-II)

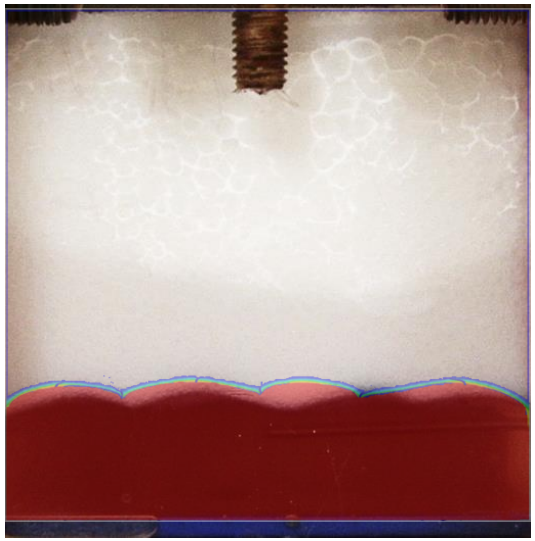

(d-III)

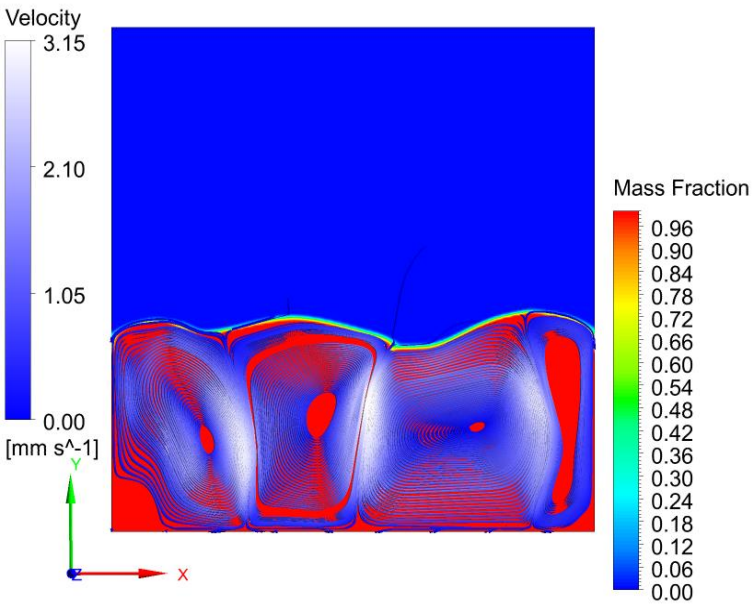
Velocity
3.15
2.10
1.05
0.00
[mm s^-1]
Y
X
Mass Fraction
0.96
0.90
0.84
0.78
0.72
0.66
0.60
0.54
0.48
0.42
0.36
0.30
0.24
0.18
0.12
0.06
0.00

(e-I)

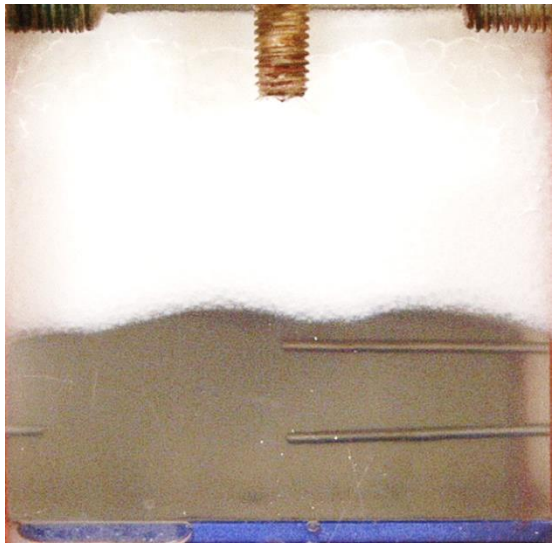

(e-II)

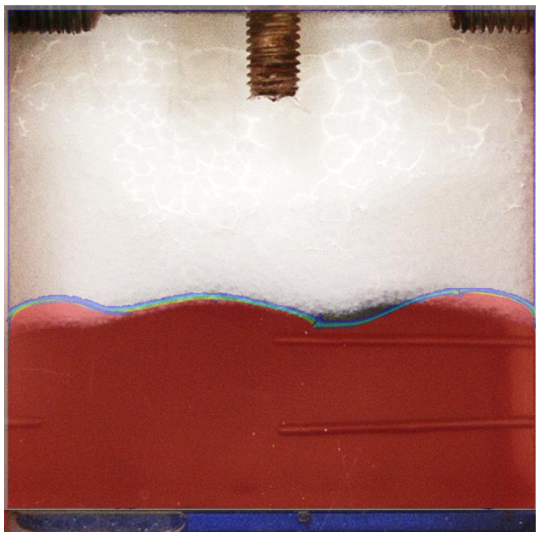

(e-III)

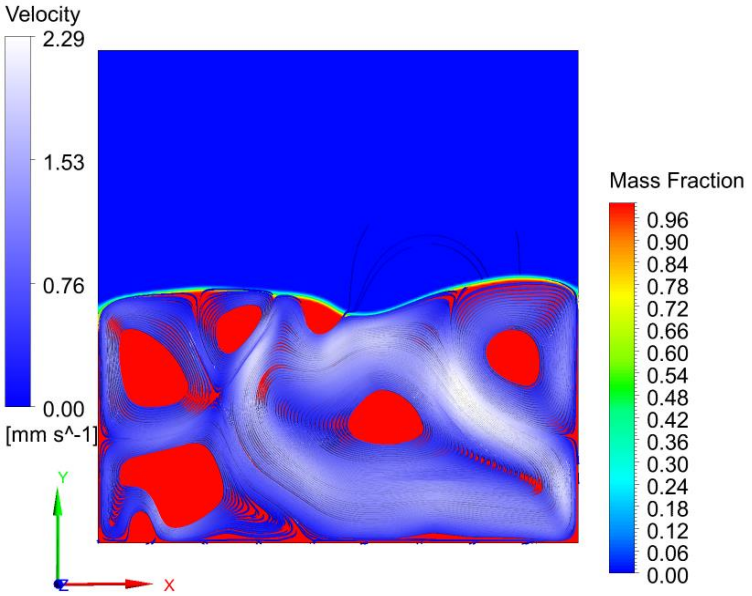
Velocity
2.29
1.53
0.76
0.00
[mm s^-1]
Y
X
Mass Fraction
0.96
0.90
0.84
0.78
0.72
0.66
0.60
0.54
0.48
0.42
0.36
0.30
0.24
0.18
0.12
0.06
0.00

(f-I)

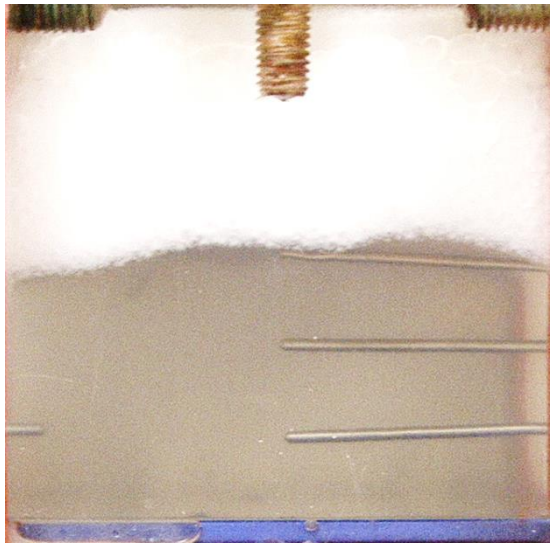

(f-II)

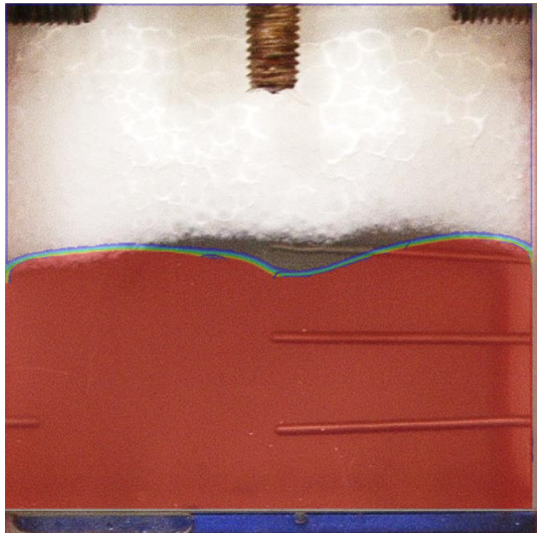

(f-III)

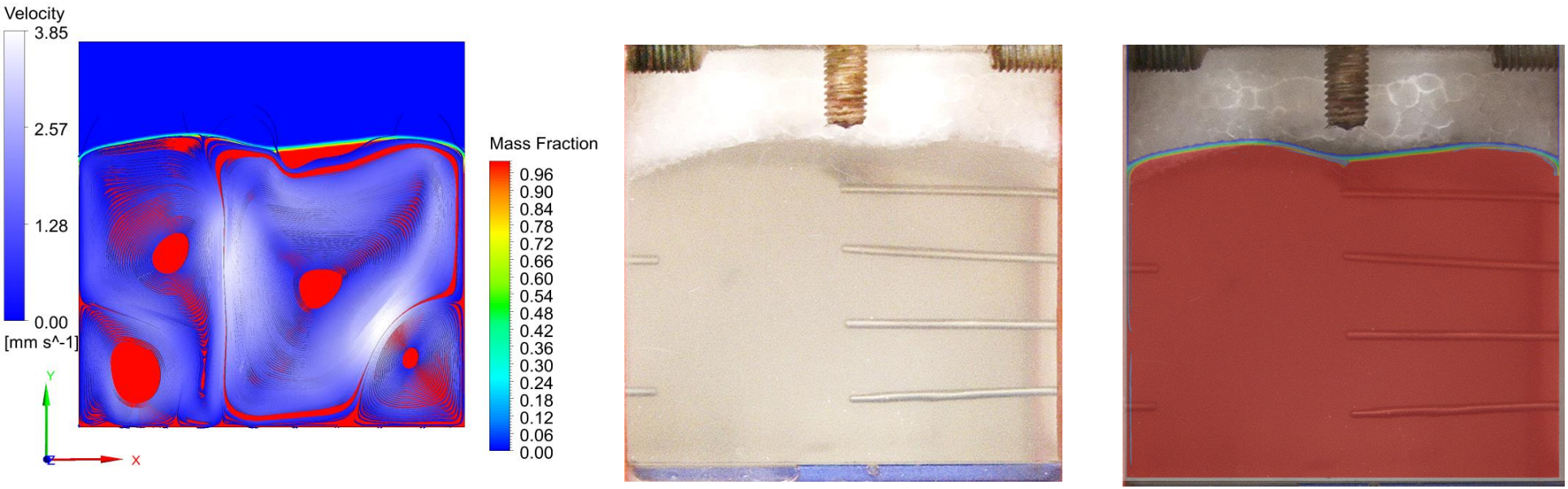

(g-I) (g-II) (g-III)

Fig. 5-6 Numerical (I), experimental (II), and a combination of numerical and experimental (III) melting process of the pure PCM at seven different time steps (a) 2.5 minutes (b) 5 minutes (c) 12.5 minutes (d) 15 minutes (e) 25 minutes (f) 35 minutes (g) 55 minutes.

To study the heat conduction domination and the Rayleigh-Benard convection domination regimes further, the bottom wall temperature is kept at $55\,^{o}C$ $(288.15\,K)$, and the temperature distribution of the pure PCM is shown in **Fig. 5-7** in Kelvin at four different time steps. The linear temperature distribution is observed for the first 2.5 minutes, as the heat conduction is dominant over this time shown in **Fig. 5-7** (a). However, the temperature distribution is not linear as soon as the convection starts dominating depicted in **Fig. 5-7** (b). More interestingly, some hot-spots form over the hot plate, which move from one place to another by elapsing time, shown in **Fig. 5-7** (b)-(d). The hot regions formation and their movement are only due to the rolls of flow formation and their displacement in the liquid region. The displacement between the hot and cold fluid is also observable in the form of plumes moving upward or downward, respectively (see **Fig. 5-7** (c)-(d)). This means that as soon as one warm stream moves upward, a cold stream moves downward to fill the space of the hot stream.

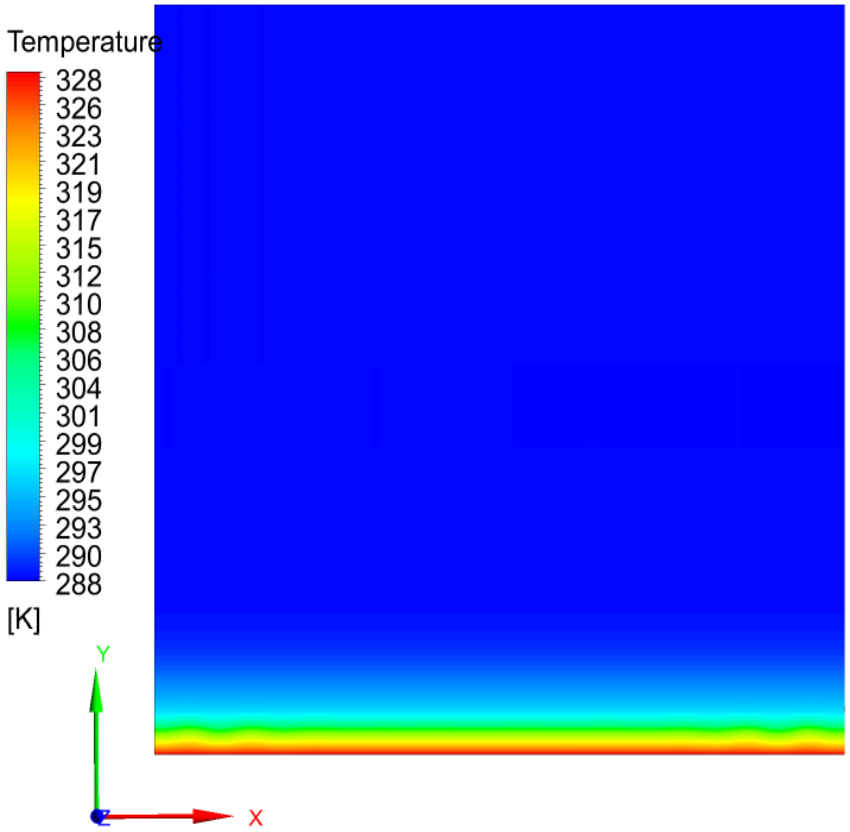
Temperature
328
326
323
321
319
317
315
312
310
308
306
304
301
299
297
295
293
290
288
[K]
Y
X

(a)

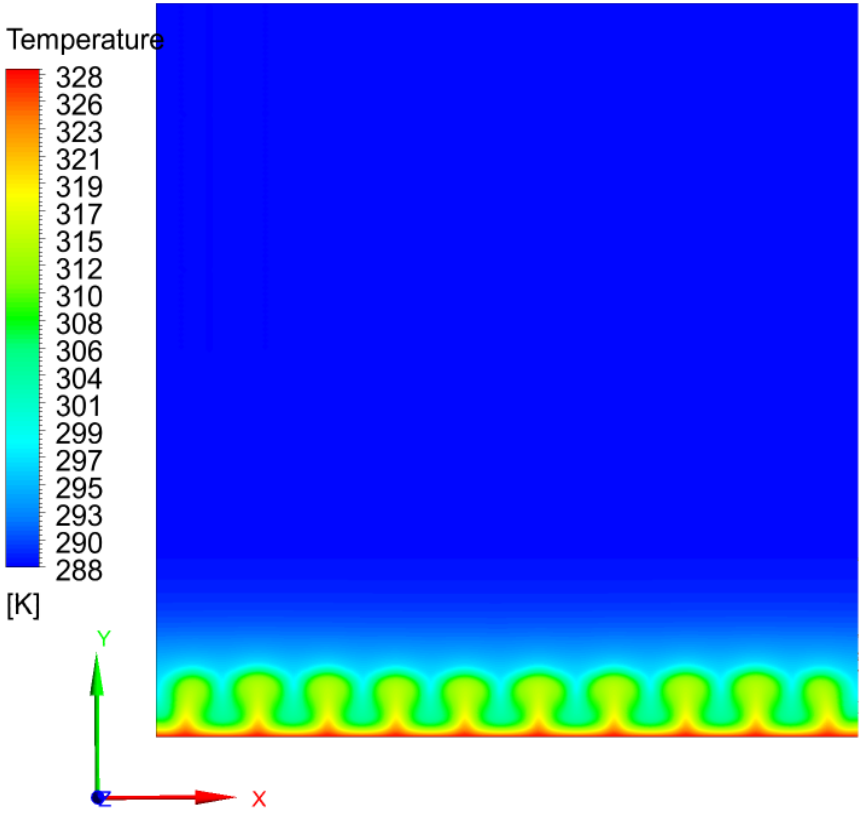
Temperature
328
326
323
321
319
317
315
312
310
308
306
304
301
299
297
295
293
290
288
[K]
Y
X

(b)

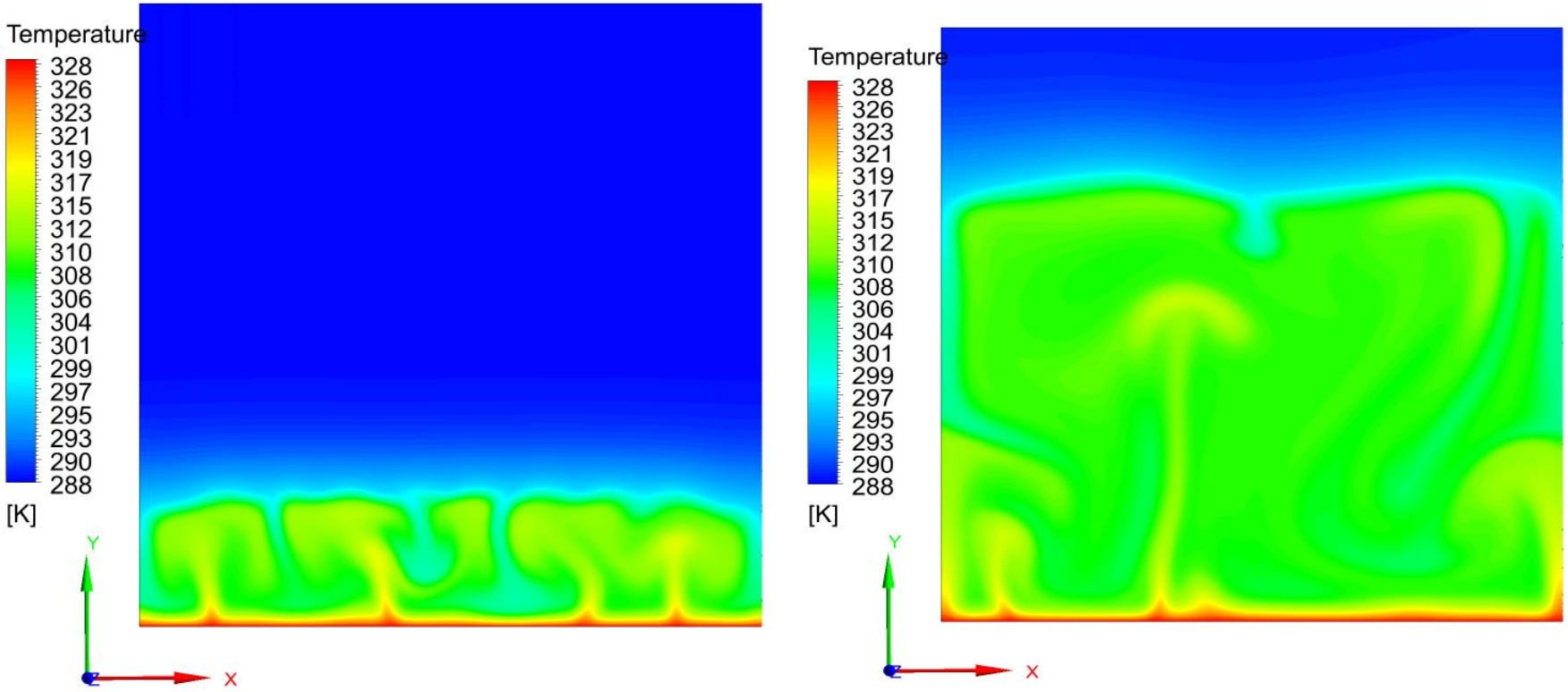

(c) (d)

Fig. 5-7 The temperature distribution of the pure PCM at four different time steps: (a) 2.5 minutes (b) 5 minutes (c) 12.5 minutes (d) 55 minutes.

5.3 Effects of nanoparticles

In this section, we study the problem statement explained at the end of the introduction to see whether the nanoparticles increase the total heat transfer rate or not.

The nanoparticle concentration effects on the heat transfer rate and melting time are studied through three groups of experiments ($T_w = 40$, 55, and $70\ ^oC$). Four NePCM samples with four different nanoparticle concentrations ($\omega_0 = 0\ wt.\%$, $\omega_1 = 0.12\ wt.\%$, $\omega_2 = 0.25\ wt.\%$, and $\omega_3 = 1\ wt.\%$) are prepared. The nanoparticle concentrations selection and the wall temperatures are selected in the way described in section 4.1. At each group of the experiments, the wall temperature is kept at a certain temperature above the melting temperature, and the melting time of each NePCM sample (different nanoparticle concentrations) is evaluated. Different nanoparticle concentrations of the samples let us study the effect of the nanoparticle concentration on the melting rate at a certain wall temperature. It is also important to know whether this effect does change at different wall temperatures which is why three groups of experiments are defined with different wall temperatures.

In the first group of experiments, the wall temperature is kept at $40\ ^oC$ and the solid-liquid interface location is monitored, then the liquid fraction changes are obtained through taking pictures at every 5 minutes shown in **Fig. 5-8** (a-I). According to Eqs. 3-19 and 3-26, the contribution of two parameters, thermal conductivity, and Rayleigh number, would affect the total heat transfer reduction or enhancement. A faster melting rate can be observed after adding nanoparticles up to $\omega_2 = 0.25\ wt.\%$. This is due to the thermal conductivity enhancement, which compensates for the possible Rayleigh number reduction, and improves the total heat transfer rate. However, adding nanoparticles beyond this value illustrated an adverse effect on the total heat

transfer rate, as the enhanced thermal conductivity could not compensate for the Rayleigh number reduction. Thus, the critical nanoparticle concentration is $\omega_2 = 0.25\ wt.\%$ if the wall temperature is kept at $40\ ^oC$. The thermocouples also record the temperature variations of the samples during the time. Although some of the thermocouples showed faster temperature change by adding nanoparticles up to $\omega_2 = 0.25\ wt.\%$, the other thermocouples showed an insignificant or slower temperature change. Judging the heat transfer enhancement through the data obtained through the thermocouples may not be possible, as they just provide the temperature at eight different locations of the enclosure. Due to this reason, these data are not shown. The effect of nanoparticles on the melting rate is also analyzed by defining a dimensionless variable called Ω ratio, which is the liquid fraction (LF) of the NePCM with a certain nanoparticle concentration divided by the liquid fraction obtained for the pure PCM ($\Omega_1 = LF_{\omega_1} / LF_{\omega_0}$, $\Omega_2 = LF_{\omega_2} / LF_{\omega_0}$, and $\Omega_3 = LF_{\omega_3} / LF_{\omega_0}$) during the dimensionless time (τ). The Ω ratio is obtained during a dimensionless time, which is time divided by the melting time of the NePCM sample that takes longer time to be fully melted in each Ω ratio. The Ω ratio larger than 1 shows heat transfer rate is improved by adding nanoparticles, while the ratio of one or smaller than one indicates no significant heat transfer or heat transfer reduction, respectively. The Ω ratio is defined for the first group of experiments and depicted in **Fig. 5-8** (a-II). It reveals that the heat transfer enhancement is relatively high for $\omega_1 = 0.12\ wt.\%$ and $\omega_2 = 0.25\ wt.\%$ at the early stages of melting where conduction mechanism may be dominant. However, a similar trend is not observed for $\omega_3 = 1\ wt.\%$. If a time step smaller than 5 minutes were chosen to find the liquid fraction, the chance of heat transfer enhancement for $\omega_3 = 1\ wt.\%$ would have been higher at the early stage of melting, as the natural convection is weak at this time. With time, the Ω ratio is reduced for all three nanoparticle concentrations

because adding nanoparticles probably reduces the Rayleigh number, even though the Ω_1 and Ω_2 ratios are still larger than 1 during the time, which can be attributed to the thermal conductivity enhancement term shown in Eq. 3-26. This means that the thermal conductivity enhancement can compensate for the Rayleigh number reduction at Ω_1 and Ω_2 but not Ω_3, as the Rayleigh number reduction may be smaller at two first ratios.

In the second group of experiments, the wall temperature is kept at $55\ ^oC$ and the liquid fraction is obtained at every 2.5 minutes. Surprisingly, the effect of nanoparticles in the PCM is different from the first group of experiments, as this time adding nanoparticles does not significantly change the melting rate. In contrast to the results shown in **Fig. 5-8** (a-I), the melting time for the samples with the nanoparticles concentration of ω_0 to ω_2 is similar as shown in **Fig. 5-8** (b-I). By taking pictures at smaller time steps than the first group of experiments, it is found that Ω is higher than 1 (heat transfer enhancement) for any concentration of nanoparticles at the early stage of melting shown in **Fig. 5-8** (b-II); however, a sharp reduction is observed after this time for Ω_2, Ω_3, which is again due to the possible Rayleigh number reduction. As the wall temperature is higher this time, the Rayleigh number and Rayleigh number reduction would also be higher compared with the first group of experiments. Thus, the natural convection contribution to the total heat transfer is more significant than the heat conduction contribution in the second group of experiments.

In the third group of experiments, the wall temperature is kept at $70\ ^oC$ and the liquid fraction is again obtained at every 2.5 minutes. A noticeable melting time difference is seen between the pure coconut oil and NePCM with $1\ wt.\%$ at the wall temperature of $40\ ^oC$ (See **Fig. 5-8** (a-I)), while this melting time difference is smaller at the wall temperature of $70\ ^oC$ (See **Fig.**

5-8 (c-I)). This reduction in the melting time may be due to the smaller viscosity difference that exists between the pure PCM and NePCM with $1\,wt.\%$ at higher temperatures than low temperatures (See **Fig. 5-10** (b)). More importantly, as shown in **Fig. 5-8** (c-I), adding nanoparticles has an adverse effect on the melting rate. This adverse effect can also be observed in **Fig. 5-8** (c-II), as the Ω ratio is mostly smaller than 1 for all three NePCM samples. This point is in contrast with the critical nanoparticle concentration reported in the two previous groups of experiments. Based on this, the key finding of this study is that adding nanoparticles improves the heat transfer rate and the melting time at low wall temperatures, leading to low Rayleigh numbers, but adding nanoparticles at high wall temperatures (high Rayleigh numbers) has an adverse effect on the heat transfer rate and decelerates the melting rate. The reason for this behaviour will be addressed in the next sections. Generally, the critical nanoparticle concentration, leading to a higher total heat transfer rate, strongly depends on many parameters; particularly the temperature difference between the melting point and the wall temperature. Thus, reporting a critical nanoparticle concentration may just be valid at the conditions on which the experiment is conducted, and does not necessarily illustrate a fact regarding the nanoparticles advantage or disadvantage. This conclusion may not be limited to the type of nanoparticles and the PCM used in this study, as the thermal conductivity enhancement and Rayleigh number change would both occur simultaneously if any other type of nanoparticles and/or PCM are used. This point is recommended to be examined using different nanoparticles and PCMs in another study. This may be one reason that different researches reviewed in chapter 2 ended up to various conclusions.

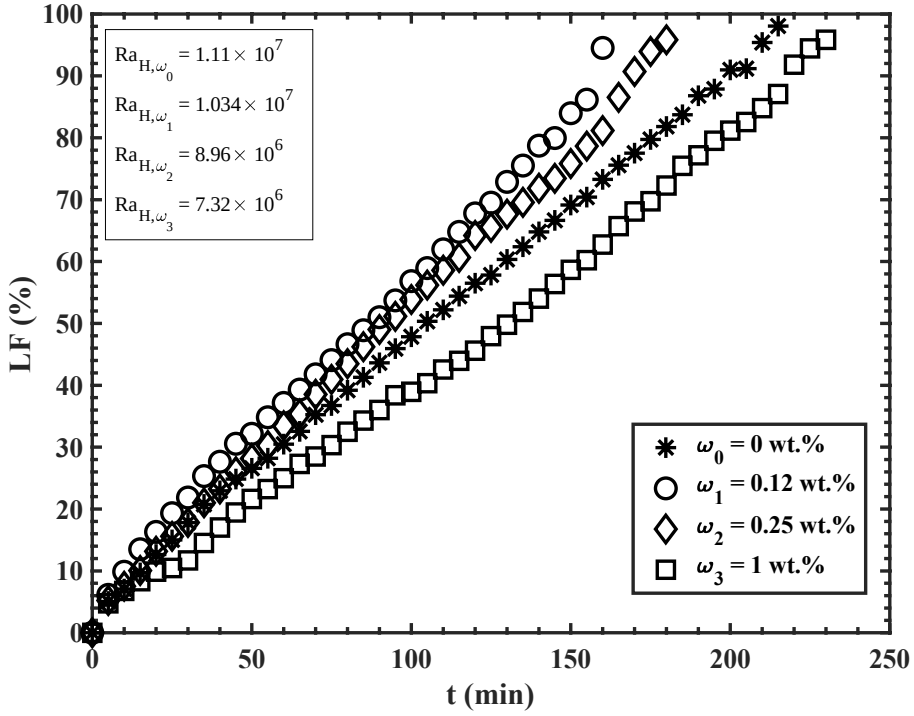
$Ra_{H,\omega_0} = 1.11\times 10^7$
$Ra_{H,\omega_1} = 1.034\times 10^7$
$Ra_{H,\omega_2} = 8.96\times 10^6$
$Ra_{H,\omega_3} = 7.32\times 10^6$
LF (%)
t (min)
ω_0 = 0 wt.%
ω_1 = 0.12 wt.%
ω_2 = 0.25 wt.%
ω_3 = 1 wt.%

(a-I)

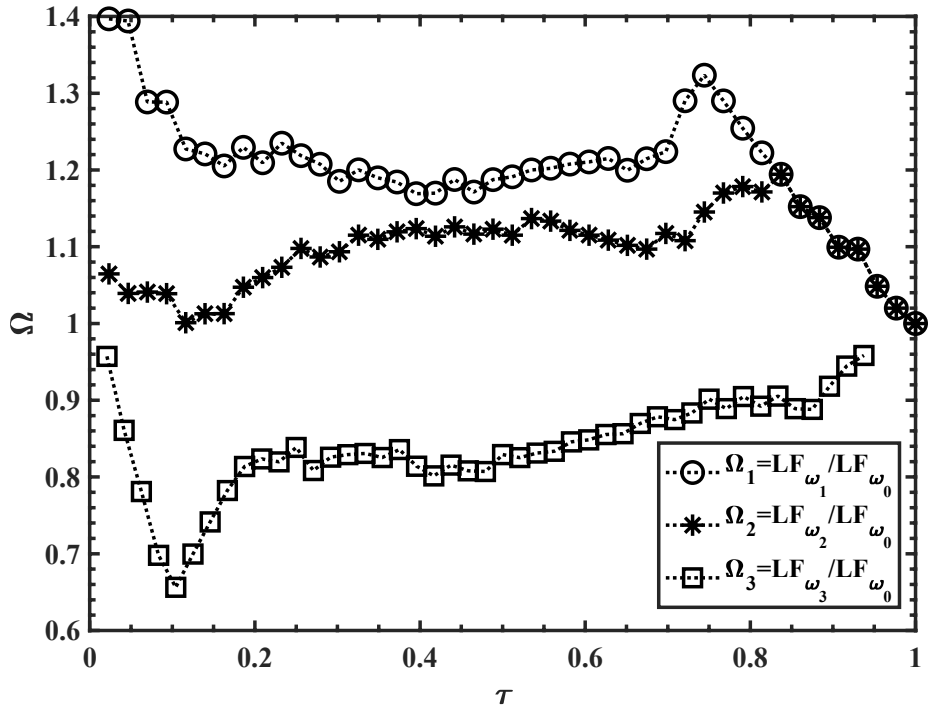
Ω
τ
Ω_1=LF$_{\omega_1}$/LF$_{\omega_0}$
Ω_2=LF$_{\omega_2}$/LF$_{\omega_0}$
Ω_3=LF$_{\omega_3}$/LF$_{\omega_0}$

(a-II)

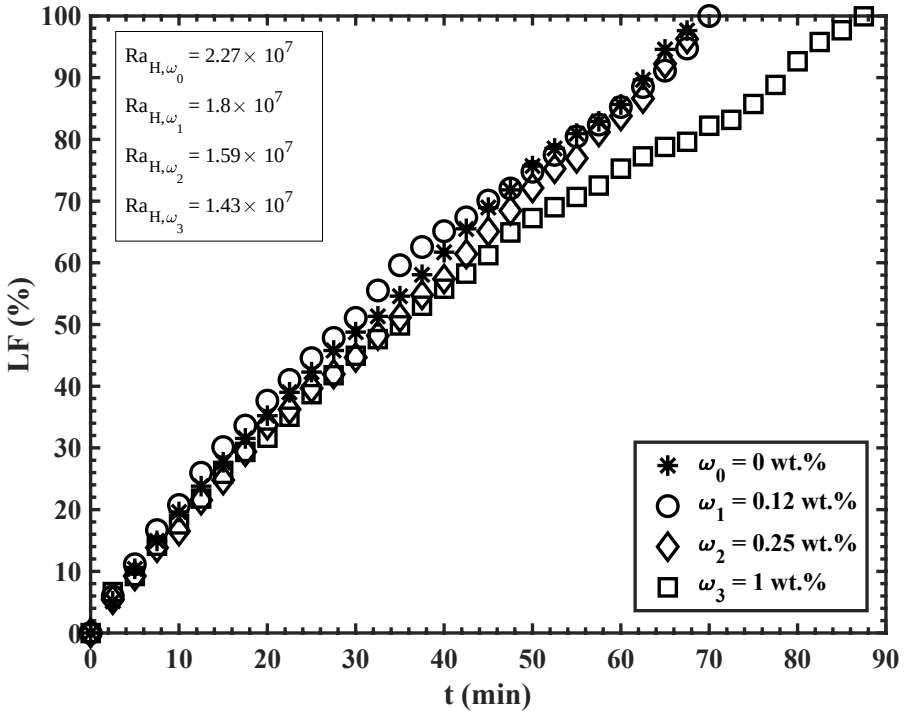
$Ra_{H,\omega_0} = 2.27 \times 10^7$
$Ra_{H,\omega_1} = 1.8 \times 10^7$
$Ra_{H,\omega_2} = 1.59 \times 10^7$
$Ra_{H,\omega_3} = 1.43 \times 10^7$
ω_0 = 0 wt.%
ω_1 = 0.12 wt.%
ω_2 = 0.25 wt.%
ω_3 = 1 wt.%
LF (%)
t (min)

(b-I)

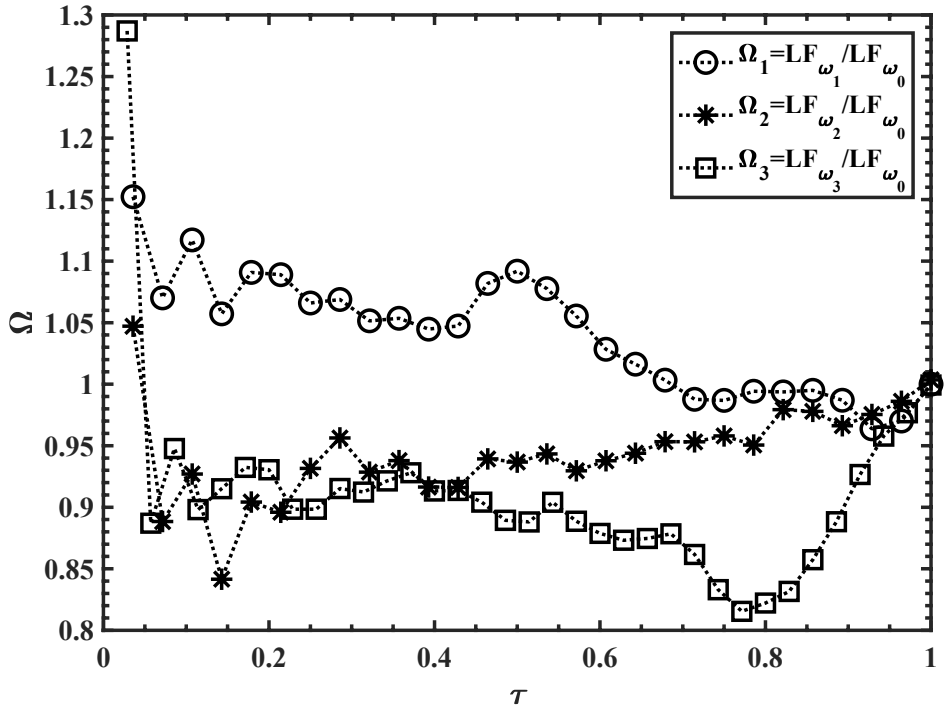
$\Omega_1 = LF_{\omega_1}/LF_{\omega_0}$
$\Omega_2 = LF_{\omega_2}/LF_{\omega_0}$
$\Omega_3 = LF_{\omega_3}/LF_{\omega_0}$
Ω
τ

(b-II)

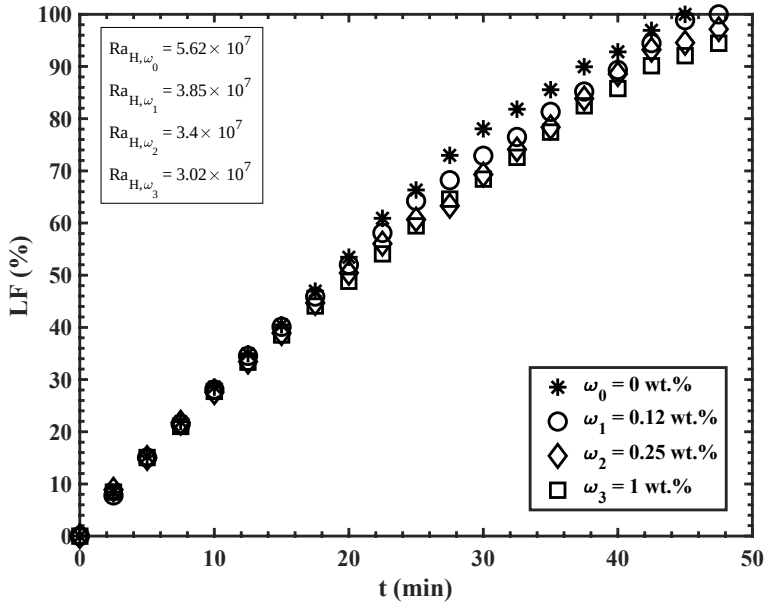

(c-I)

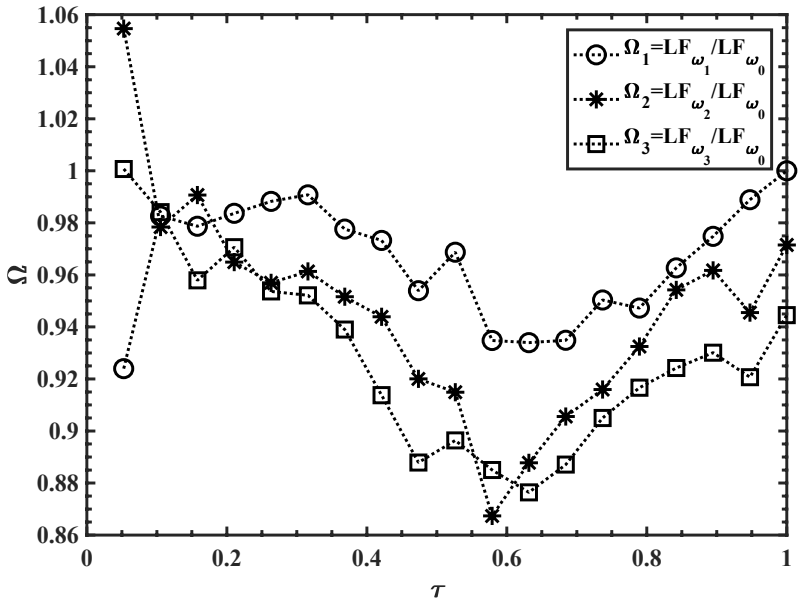

(c-II)

Fig. 5-8 Liquid fraction vs. time (I) and liquid fraction ratio vs. dimensionless time (II) of the NePCMs with four different nanoparticle concentrations at three different temperatures (a) $T_w = 40\ ^oC$, (b) $T_w = 55\ ^oC$, (c) $T_w = 70\ ^oC$.

5.4 Thermal conductivity and viscosity analysis of NePCM

To study the contribution of the thermal conductivity of the mixture and Rayleigh number in the total heat transfer rate, the thermal conductivity and viscosity of the samples are measured.

Thermal conductivity measurements are taken using a KD2 PRO Thermal Conductivity Analyzer (Decagon Devices, USA), of which a detailed description was given in chapter 4. The device is first calibrated by using the materials provided by the manufacturer. The samples are heated up to a certain temperature by placing them inside a thermal bath and leaving them to reach thermal equilibrium. Then, the thermal bath is shut down to avoid any vibration, and consequently natural convection. Then, the thermal conductivity is measured using the device, while the sample is inside the thermal bath. This process is repeated three times and the average value of the three measurements is calculated. The measurements are taken at elevated temperatures from $30\ ^{o}C$ to $70\ ^{o}C$ (liquid phase) and shown in **Fig. 5-9**, and at $17\ ^{o}C$ (solid phase) listed in **Table 5-1**. The thermal conductivity of the pure coconut oil in both solid and liquid phases is nearly the same as the thermal conductivity of the coconut oil measured at $15\ ^{o}C$ (solid) and $32\ ^{o}C$ (liquid) in a 2018 study (Al-Jethelah et al., 2018). It is found that adding any concentration of nanoparticles can improve the thermal conductivity of the coconut oil in the liquid phase shown in **Fig. 5-9** (a).

Also, the thermal conductivity enhancement (Λ) is shown in **Fig. 5-9** (b), where the minimum enhancement of the NePCMs in the liquid phase is approximately 10 % while the maximum enhancement is slightly over 40 %. It is worth mentioning that these maximum and minimum values may change due to the relatively large uncertainty of the device as shown in **Fig. 5-9** (b). As expected, the thermal conductivity of the pure coconut oil reduces by increasing the temperature; however, the thermal conductivity of the NePCMs at any nanoparticle concentration shows an increasing trend, up to a certain temperature (See **Fig. 5-9** (a)). Besides, if the thermal

conductivity enhancement compared with the pure PCM at a certain temperature is the matter, the thermal conductivity enhancement shows an increasing trend with increasing both temperature and nanoparticle concentration (See **Fig. 5-9** (b)). Regardless of the uncertainty of the measurement as one reason for this thermal conductivity enhancement with increasing the temperature, the Brownian motion could be the possible reason for the thermal conductivity enhancement, as the Brownian motion would be higher at lower viscosities (higher temperatures), leading to a slight enhancement in the thermal conductivity. At the solid phase, the thermal conductivity of the NePCMs is improved by increasing the nanoparticle concentration listed in **Table 5-1**, even though an insignificant enhancement is seen for the NePCM sample with ω_1 nanoparticle concentration. Enhancing the thermal conductivity of the NePCMs could be one reason for the total heat transfer enhancement of the NePCMs at both solid and liquid phases; however, the viscosity of the NePCMs, and subsequently the Rayleigh number's variations could be directly affecting the total heat transfer rate, which will be discussed in the next section.

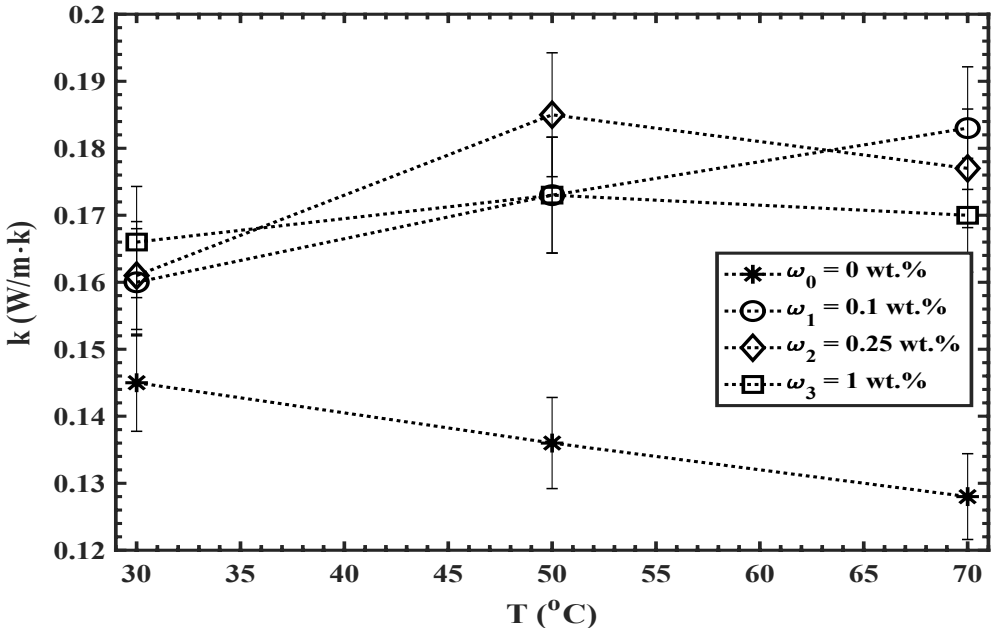

(a)

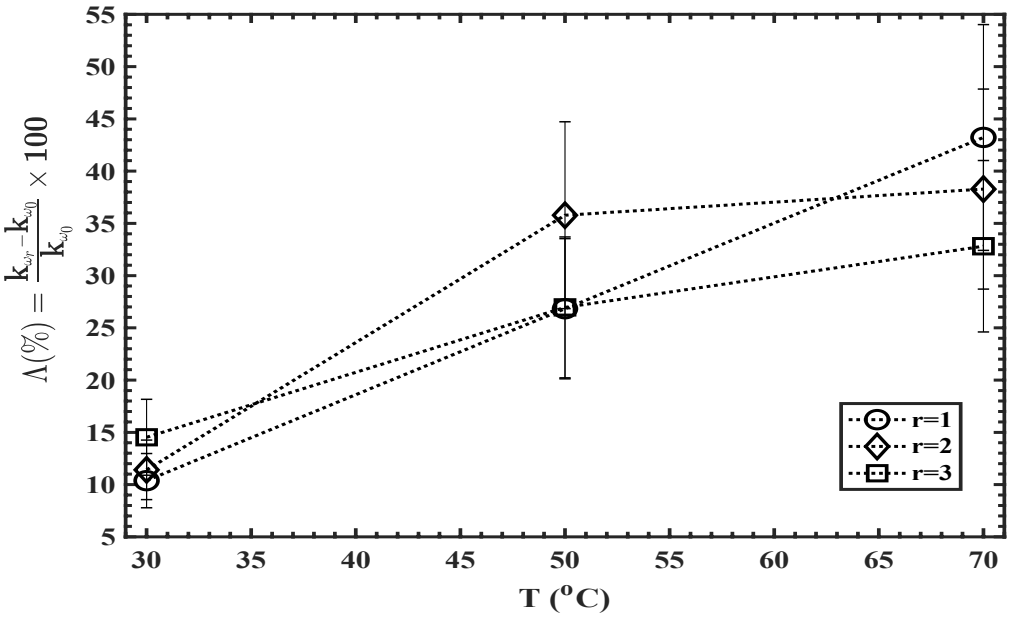

(b)

Fig. 5-9 Thermal conductivity values of the NePCM (a) with different nanoparticle concentrations at elevated temperature (b) Thermal conductivity enhancement.

Table 5-1 Thermal conductivity of the NePCM samples at the solid phase ($17\ ^{o}C$).

	$\omega_0 = 0\ wt.\%$	$\omega_1 = 0.12\ wt.\%$	$\omega_2 = 2.5\ wt.\%$	$\omega_3 = 1\ wt.\%$
$k(w/m\cdot K)$	0.23 ± 0.03	0.23 ± 0.03	0.25 ± 0.03	0.26 ± 0.03

The viscosity of the coconut oil is measured using a Cambridge viscolab viscometer. The viscometer is able to measure the viscosity of the sample at elevated temperatures with 1 % uncertainty. After calibrating the viscometer according to manufacturer instruction, the dynamic viscosity of the pure coconut oil used in this study is measured and compared with the viscosity of an overlay mature coconut oil found in a 2016 study (Patil, Benjakul, Prodpran, Senphan, & Cheetangdee, 2016) that fell within the temperature of $30\ ^{o}C$ to $70\ ^{o}C$. Although the kind of the coconut oil used in this research may be different, a good agreement is seen between our results and Patil et al. (Patil et al., 2016) study, as shown in **Fig. 5-10** (a). To measure the viscosity of the

samples, each sample is again melted and stirred for half an hour to guarantee the dispersion of nanoparticles using a hot plate stirrer. The samples' temperature is measured using a thermometer to make sure the samples' temperature is not above $30\ ^{o}C$ before placing them into the viscometer. The viscosity of the samples is then measured and shown in **Fig. 5-10** (b). As expected, increasing the nanoparticle concentration or decreasing the temperature of the sample increase the viscosity. The most and least viscous samples are the coconut oil with $1\ wt.\%$ dispersed nanoparticles and pure coconut oil. Although the viscosity of the NePCM with $0.12\ wt.\%$ is very close to the pure coconut oil viscosity, a slight difference is observed within the temperature range under study, making the NePCM sample with $0.12\ wt.\%$ nanoparticles more viscous than the pure coconut oil by comparing the average viscosity of the samples. The viscosity enhancement of the samples with different nanoparticle concentrations is calculated at two different temperatures using:

$$\Upsilon = 100 \times \frac{\mu_{\omega_r} - \mu_{\omega_0}}{\mu_{\omega_0}} \tag{5.1}$$

where Υ is the viscosity enhancement after adding nanoparticles in percent, and subscript r changes from 1 to 2 , showing the nanoparticle concentration of the NePCM sample.

The viscosity enhancement is listed in **Table 5-2** for two different temperatures. It is found that the viscosity enhancement is more pronounced at the initial temperature ($T = 30\ ^{o}C$) than final temperature ($70\ ^{o}C$). Interestingly, a small amount of nanoparticles increases the viscosity of the sample by $6.7\ \%$, which may negatively affect the heat transfer rate, while the viscosity increases approximately $41\ \%$ with $1\ wt.\%$ nanoparticle concentration. This amount of nanoparticle is still small and does take up approximately $0.03\ vol.\%$ by converting the

nanoparticles mass fraction to volume fraction using Eq. 3-42. The viscosity increase would be one main reason to increase the melting time.

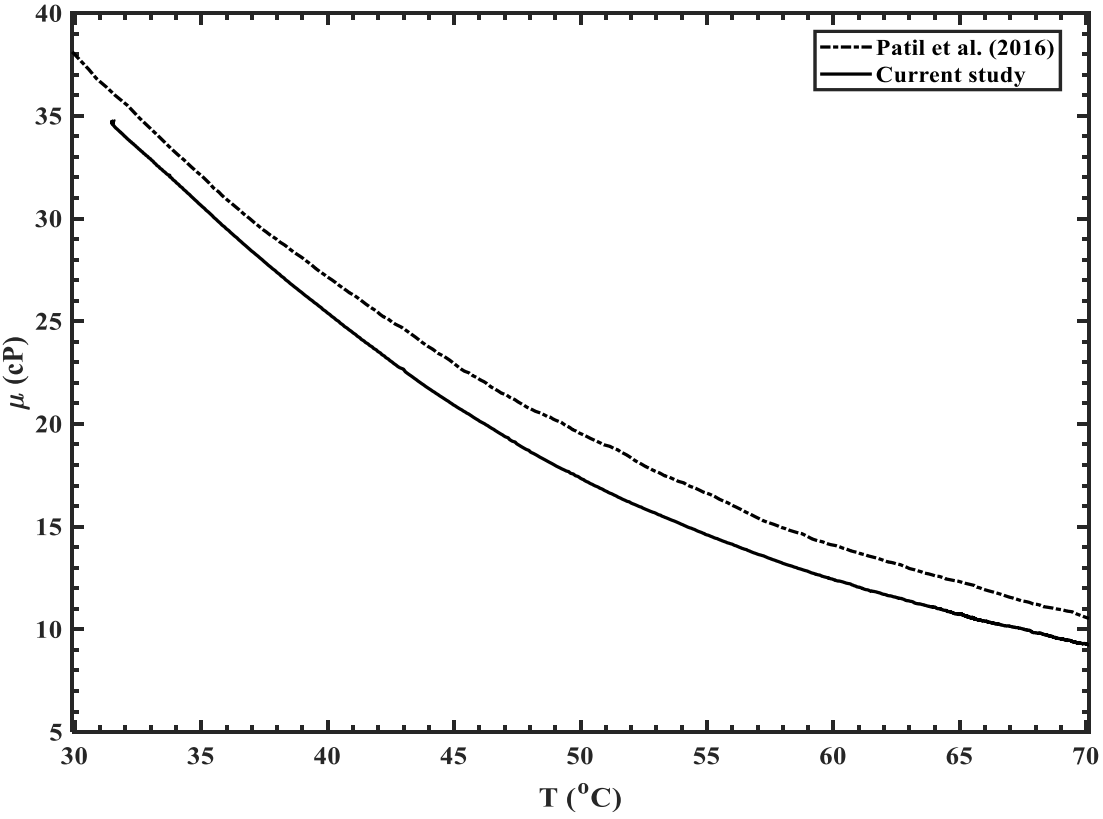

(a)

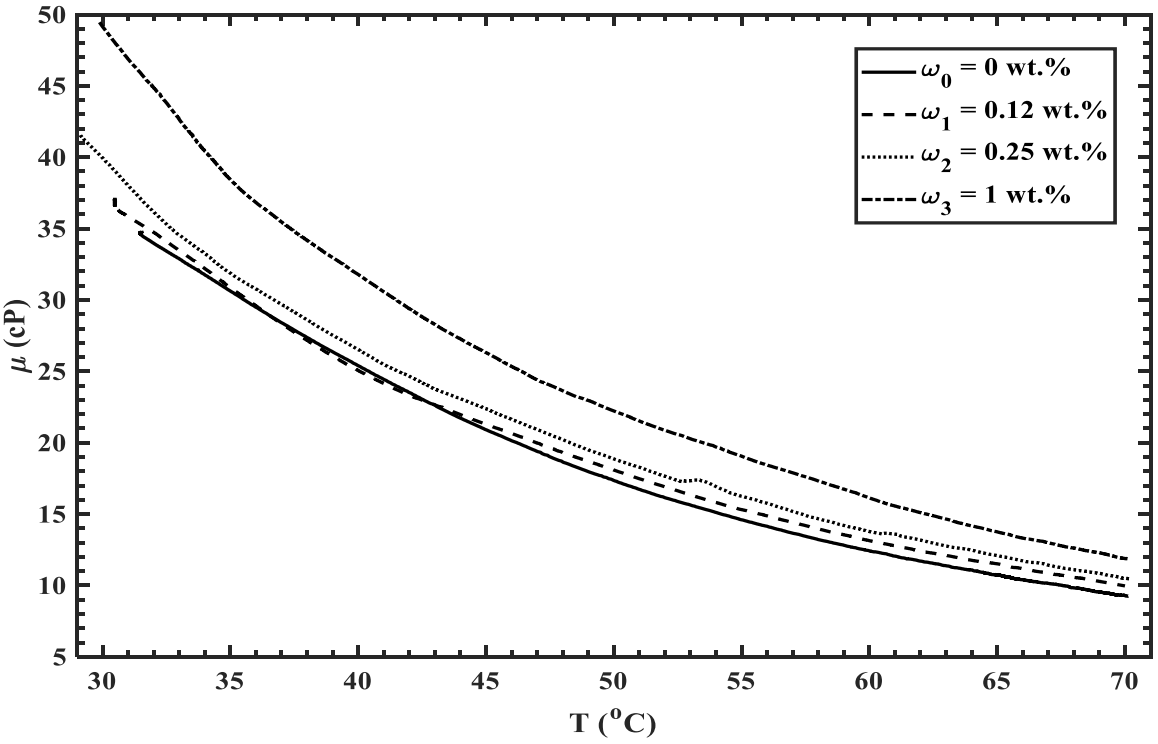

(b)

Fig. 5-10 (a) Comparison of the coconut oil viscosity between the current study and an overlay mature coconut oil (Patil et al., 2016), (b) The viscosity of the NePCMs with different nanoparticle concentrations.

Table 5-2 Viscosity enhancement with adding nanoparticles at different temperatures.

	ω_1	ω_2	ω_3
$\Upsilon_{@30^oC}$(%)	6.7	14.7	41.2
$\Upsilon_{@70^oC}$(%)	7.8	12.9	28.5

5.5 Melting time analysis

To understand the reason for the melting time variations with added nanoparticles, the Grashof number (Gr_H) and the instantaneous Rayleigh number (Ra_S) shown as one significant

term in the scaling analysis section, affecting the heat transfer rate are evaluated. The average solid-liquid interface location is used to find the instantaneous Rayleigh number for different nanoparticle concentrations at different temperatures set at the boundary. The Grashof and Rayleigh numbers are based on the properties of the samples measured in this study, including the mean thermal conductivity and viscosity, and the other properties reported in **Table 5-1**. To find the properties of the NePCMs, Eqs (3-35)-(3-37) are implemented. The maximum Rayleigh and Grashof numbers uncertainty calculated using Eq.4-2 are $16\,\%$ and $7\,\%$, respectively. The high Rayleigh number uncertainty can be attributed to the uncertainty of the KD2 PRO analyzer used to measure the thermal conductivity of the samples. In **Fig. 5-11**, the Rayleigh number variations for four NePCM samples are shown versus dimensionless average solid-liquid interface location ($\frac{S_{ave}}{H}$) at three wall temperatures ($T_w = 40$, 55 , and $70\ ^oC$). It is found that the Rayleigh number is reduced with higher nanoparticle concentration at all three wall temperatures. Although we indicated that the viscosity reduction is smaller at higher temperatures (See **Table 5-2**), the Rayleigh numbers reduction is more pronounced at the higher wall temperatures, which means a higher negative effect on the heat transfer rate.

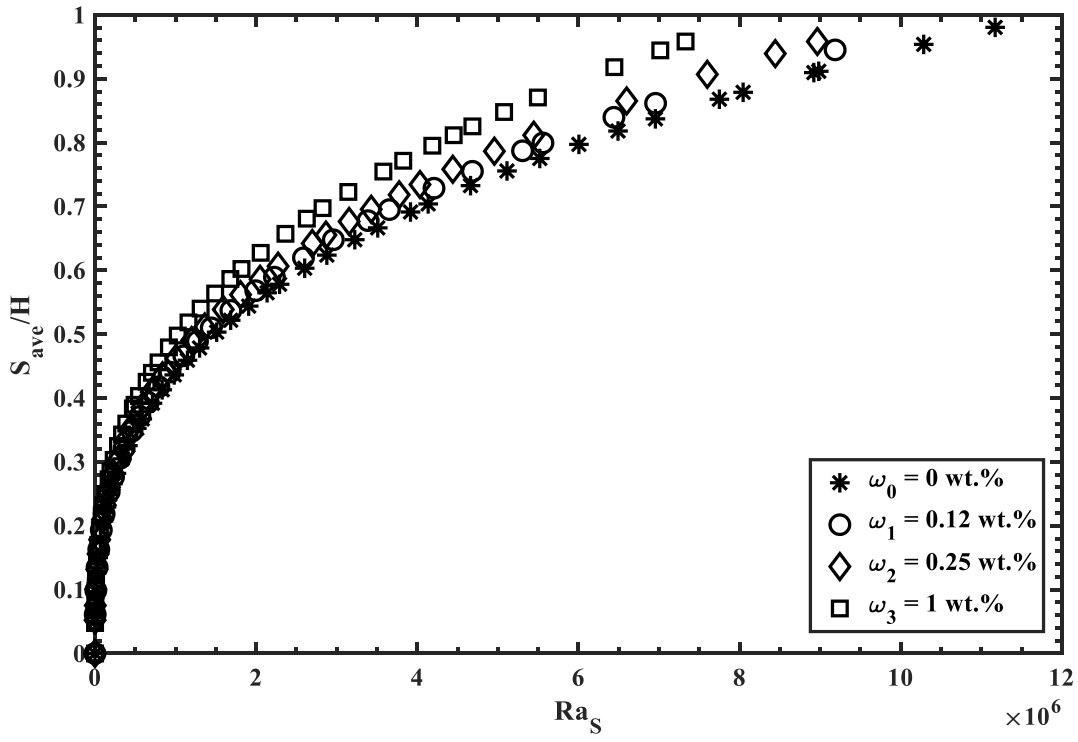
S_{ave}/H
Ra_S
$\times 10^6$
ω_0 = 0 wt.%
ω_1 = 0.12 wt.%
ω_2 = 0.25 wt.%
ω_3 = 1 wt.%

(a)

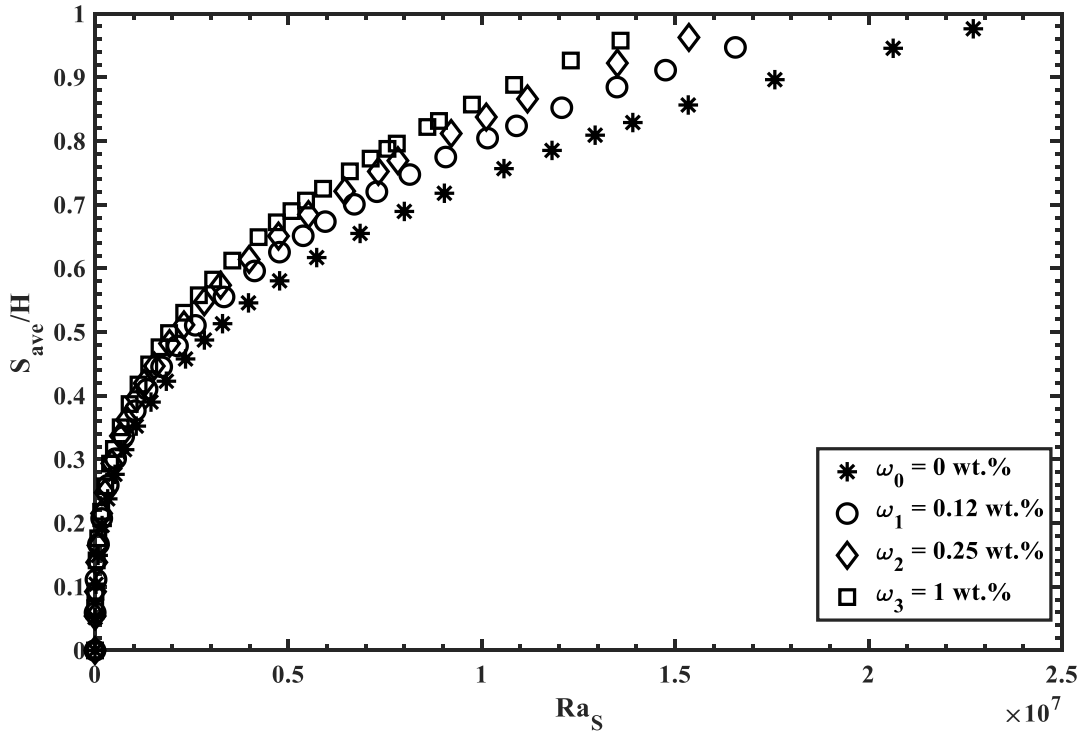
S_{ave}/H
Ra_S
$\times 10^7$
ω_0 = 0 wt.%
ω_1 = 0.12 wt.%
ω_2 = 0.25 wt.%
ω_3 = 1 wt.%

(b)

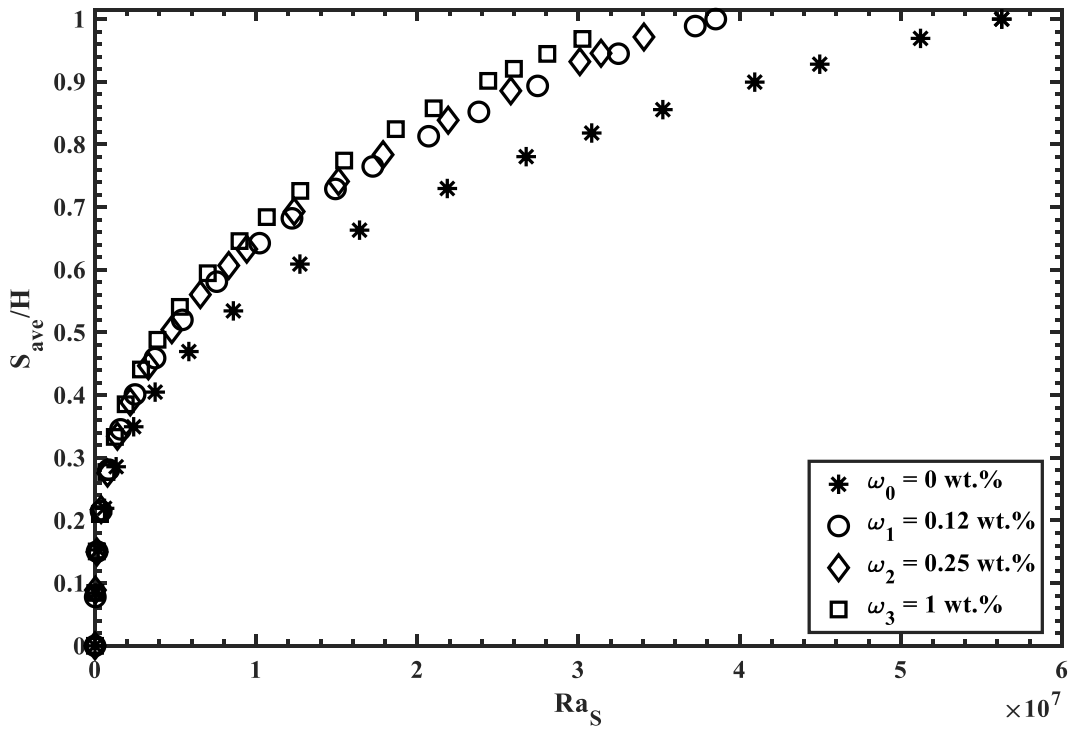

(c)

Fig. 5-11 The instantaneous Rayleigh number variations with the dimensionless average interface location at (a) $T_w = 40\ ^oC$ (b) $T_w = 55\ ^oC$ (d) $T_w = 70\ ^oC$.

The effects of nanoparticles on the melting time variations (τ_0) is calculated using Eq. (5-2) and listed in **Table 5-3** at different wall temperatures, along with the Grashof number reduction (η) calculated using Eq. (5-3), and the thermal conductivity enhancement in the liquid region (Λ) discussed earlier. The thermal conductivity enhancement with added nanoparticles is ignored in the solid region during this analysis, as an insignificant improvement was observed in the solid region with adding nanoparticles, and this insignificant improvement is similar for all the NePCM samples. The melting time variations of the NePCM samples are compared with that of the pure PCM ($\omega_0 = 0\ wt.\%$). The negative sign in the melting time variations shows that the melting completed a certain percentage of time faster compared to the pure PCM ($\omega_0 = 0\ wt.\%$), while the

positive sign indicates that the melting time took a certain percentage of time longer to be completed.

As expected, it is found that the thermal conductivity enhancement and Grashof number reduction have two contrary effects that determine if the melting time can be accelerated (See **Table 5-3**). It is also found that the Grashof number is reduced more with higher nanoparticle concentration and temperatures. However, a thermal conductivity improvement is observed with higher nanoparticle concentration and temperature up to a certain value. It is also observed that the thermal conductivity enhancement should be able to compensate for the Grashof number reduction to reduce the melting time. It is found from **Table 5-3** that around 11% thermal conductivity enhancement is able to compensate for approximately 1700 Grashof number reduction and in improving the melting time by approximately $16\ \%$. Similar to the Rayleigh number, the Grashof number reduction is higher at higher temperatures, leading to a greater negative effect on the buoyancy force, and consequently natural convection. Thus, adding nanoparticles at high Grashof numbers is not recommended. It can be concluded that if the addition of the nanoparticles reduces the Grashof number by approximately 4500, then the thermal conductivity enhancement should be over $35\ \%$ to improve the melting time with added nanoparticles (See **Table 5-3**). Generally, there is a relationship between these parameters that may help find out before an experiment is conducted whether or not adding nanoparticles reduces the melting time, which will be shown in the next section. This conclusion may not be limited to the type of nanoparticle and the PCM used in this research, however, it should be dependent on the geometry and boundary conditions on which the experiments conducted. This point is recommended to be studied in future research.

$$\tau_o(\%) = \frac{t_{\omega_r} - t_{\omega_0}}{t_{\omega_0}} \times 100 \tag{5-2}$$

$$\eta = Gr_{\omega_0,H} - Gr_{\omega_r,H} \tag{5-3}$$

Table 5-3 Variations of melting time of the NePCM samples with thermal conductivity enhancement and Grashof number reduction at different wall temperatures compared to the pure PCM.

T_w **(** ^oC **)**	ω_r **(** $wt.\%$ **)**	$\tau_0(\%)$	Λ **(** $\%$ **)**	η
	$\omega_1 = 0.1$	-25	10	434
40	$\omega_2 = 0.25$	-16	11	1728
	$\omega_3 = 1$	+6	14	8231
	$\omega_1 = 0.1$	+3	26	3254
55	$\omega_2 = 0.25$	0	35	4542
	$\omega_3 = 1$	+22	26	23080
	$\omega_1 = 0.1$	+5	43	15221
70	$\omega_2 = 0.25$	+11	38	34541
	$\omega_3 = 1$	+17	32	79359

5.6 Developing empirical correlations

In this section, we use the curve fitting approach, which is the process of constructing the best curve, fitting a series of data, to correlate one or more predictors (independent variables) with the response variable (dependent variable), using a series of data. To do this, the MATLAB® software is implemented. At first, the dynamic viscosity of the pure coconut oil is correlated with the temperature range (^oC) considered in this study using an exponential equation as follows:

$$\mu = 3.6\mu_{ref} e^{-1.1\frac{T}{T_{ref}}} \tag{5-4}$$

where μ is in $kg/m\cdot s$, T is in ^{o}C, μ_{ref} and T_{ref} are the reference viscosity and temperature that are 0.0348 $kg/m\cdot s$ and 31.5 ^{o}C, respectively.

As explained in section 3.2 (scaling analysis), the melting problem in an enclosure heated from the bottom (Rayleigh-Benard convection) is divided into two regimes based on the critical Rayleigh number ($Ra_{\delta_T} \sim 10^3$). In the first regime, The Rayleigh number is small ($Ra_S < Ra_{critical}$) and the heat conduction is dominant, while the Rayleigh number becomes larger ($Ra_{critical} < Ra_S$), and the natural convection becomes dominant in the second regime. Also, the Rayleigh number does not exceed its critical value at the short enclosures and/or the enclosures with small temperature difference at the bottom and the melting point of the substance inside the enclosure, meaning that the second regime (natural convection domination) may never form. Similarly, the Rayleigh number becomes very large in large enclosures with large temperature difference. In this situation, the first regime would be very short, which could be ignored, as the Rayleigh number quickly exceeds its critical value. To obtain an empirical correlation for the solid-liquid interface location and the parameters affecting the phase change in each of these situations, Eqs. (3-15) and (3-24) are employed, and the curve fitting approach is implemented. The solid-liquid interface can be found for two small and large Rayleigh numbers as follow:

$$S_{ave} = a_o H \cdot (Ste \cdot Fo)^m Ra_S^n \tag{5-5}$$

where a_o , m and n are constants that are listed in **Table 5-4**. The Pure PCM correlations are based on the data obtained from the pure PCM sample, while the NePCM correlation is based on the properties of all samples, including the pure PCM. The adjusted R^2 represents the strength of

the correlation to reproduce the response in the case of using the correlation, which is very high for the correlations developed. Interestingly, the m and n constants listed in **Table 5-4** are similar to the power of Eqs. (3-15) and (3-24).

Table 5-4 The constants for Eq. (5-5).

	a_o	m	n	Adjusted R^2
Pure PCM ($Ra_{critical} > Ra_S$)	0.93	1/2	0	0.93
Pure PCM ($Ra_{critical} < Ra_S$)	0.22	1/2	1/6	0.98
NePCM ($Ra_{critical} < Ra_S$)	0.66	1/2	2/25	0.93

As explained in the previous section, there is a relationship between the melting time variations, thermal conductivity enhancement and Grashof number reduction. The curve fitting approach is again implemented to correlate these parameters. The correlation can be written as follows:

$$\tau_o = 20590\eta^{-5.287} - 451.1\eta^{-0.4} - 0.00484\Lambda^2 + 4(\Lambda \cdot \eta)^{0.139} \quad (5\text{-}6)$$

The correlation is valid in the lower and upper limits of the parameters under study. This correlation may not be limited to the type of nanoparticle and the PCM used in this research, however, it should be dependent on the geometry and boundary conditions on which the experiments are conducted. This point is recommended to be studied in future research. The correlation developed above for the melting time variations with the Grashof number reduction and the thermal conductivity enhancement is also shown in **Fig. 5-12**. The logarithmic shape of

the figure clearly shows the importance of the Grashof number reduction compared to the thermal conductivity enhancement.

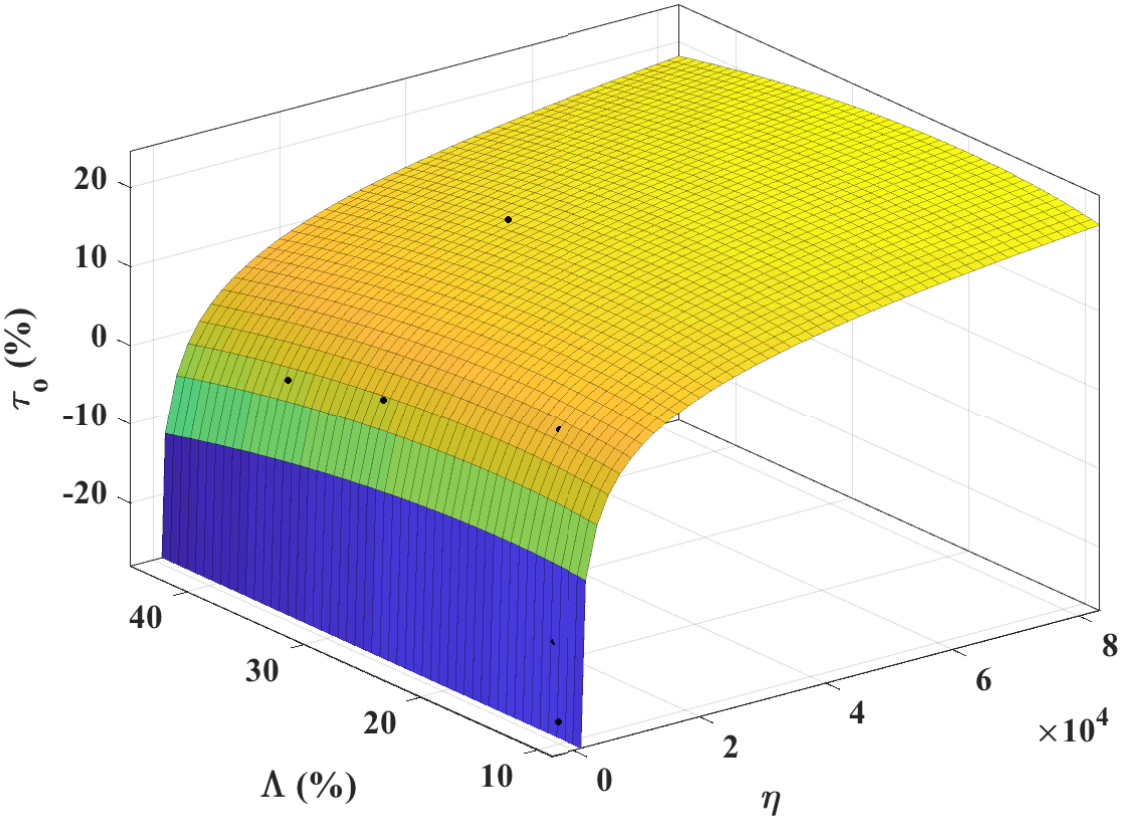

Fig. 5-12 Prediction of melting time variations (τ_0) vs. thermal conductivity enhancement (Λ) and Grashof number reduction (η).

5.7 Summary

In this chapter, the effect of adding nanoparticles on the melting rate was systematically studied using coconut oil as the base PCM and Al_2O_3 at different concentrations and temperatures at the boundary of an enclosure. To do this, an enclosure heated from the bottom, causing the creation of Rayleigh-Benard convection was designed and built. Through a systematic method, the nanoparticle concentration range and the wall temperature were selected. The analysis consisted

of three parts, namely scaling analysis, numerical parts, and experimental parts and led to the following findings:

Through the scaling analysis, it is found that:

- Two regimes were found to be forming during the melting process, namely conduction domination regime at the early stage of melting and the convection domination regime when the Rayleigh number reaches a critical value.
- The parameters that contribute to the total heat transfer are the thermal conductivity and Rayleigh number in the conduction and convection domination regimes.

Similarly, from the numerical part of the study, it was found that:

- Due to the Rayleigh-Benard convection, small rolls of flow are formed at the end of conduction domination regime, in which the solid-liquid interface remains planar, even though these rolls are weak and do not have a significant effect on the heat transfer rate in this region.
- Depending on the number of rolls, some hot-spots are formed over the hot plate. These hot-spots move over the hot plate by moving the solid-liquid interface upward.

And, from the experimental part of the study, it is concluded that:

- The number of waves formed at the solid-liquid interface has a relationship with the solid-liquid interface location and the width of the enclosure, meaning that the number of rolls is reduced by moving the solid-liquid interface upward (this point is also visible from the numerical simulations).

- The different behaviours of NePCMs at different temperatures can be attributed to the significant parameters reported in the scaling analysis, which are affecting the phase change rate.
- Adding nanoparticles showed an improvement in terms of melting rate at the very early stage of melting where the conduction mechanism is dominant (the first regime). In the case of short enclosures heated from the bottom, adding nanoparticles is a promising approach to enhance the heat transfer rate, as the heat conduction would be the only mechanism of heat transfer if the Rayleigh number does not reach its critical value.
- The nanoparticle concentration showed different behaviours at different wall temperatures. Although the melting time improved in the case of adding $0.12\ wt.\%$ and $0.25\ wt.\%$ nanoparticles at the wall temperature of $40\ ^{o}C$, no significant melting rate or melting time improvement was observed at the wall temperature of $55\ ^{o}C$. More interestingly, an adverse heat transfer effect was observed in the case of adding nanoparticles at the wall temperature of $70\ ^{o}C$.
- By considering the previous finding, reporting a critical nanoparticle concentration leading to a high heat transfer rate may just be valid at the condition on which the experiment conducted, and does not necessarily illustrate a fact regarding the nanoparticles' advantage or disadvantage.
- Adding nanoparticles improved the thermal conductivity of the NePCM mixture at both solid and liquid phases.
- The thermal conductivity of the NePCMs increased with increasing the temperature at the liquid phase that can be attributed to a stronger Brownian motion at a lower viscosity, while

the thermal conductivity of the pure PCM decreased with increasing temperature, as expected.

- The viscosity of the NePCMs increased with an increase in the nanoparticle concentration and with a decrease in the temperature.
- Adding nanoparticles is not recommended to reduce the melting time at high Grashof numbers.
- The addition of the nanoparticles reduced the Grashof number approximately by 4500. To compensate for this Grashof number reduction and to improve the melting time with adding nanoparticles, the thermal conductivity enhancement should be over $35\,\%$. This finding may not be limited to the type of nanoparticle and the PCM used in this research, however, this finding should be dependent on the geometry and boundary conditions on which the experiments conducted.
- An empirical correlation was developed to evaluate the relationship between the effect of nanoparticles on the melting time, the thermal conductivity enhancement, and the Grashof number reduction. This correlation may not be limited to the type of nanoparticle and the PCM used in this research, however, this point is recommended to be evaluated in future research.
- An empirical correlation was developed to predict the pure coconut oil viscosity.
- Empirical correlations were also developed to predict the average solid-liquid interface location for the PCM and NePCMs studied in an enclosure heated from the bottom.

In the next chapter, the effects of nanoparticles on the phase change and heat transfer rate will be examined numerically and statistically to understand better whether a concentration of

nanoparticles would have a same behaviour at different wall temperatures and conditions in a most common thermal storage unit.

Chapter 6 Effects of nanoparticles on the melting rate in a shell-and-tube thermal energy storage

From the previous chapter, it is found that there is an interaction between nanoparticle concentration and the wall temperature, meaning that the effect of the nanoparticles on the heat transfer rate changes at different wall temperatures. In this chapter, we aim to numerically and statistically evaluate this issue in a simple shell-and-tube thermal storage unit. The materials presented in this chapter has been published in a 2017 study (Parsazadeh & Duan, 2017).

In this part of the research, copper oxide nanoparticles (CuO) are dispersed in both water (HTF) and paraffin wax (PCM). The effects of the nanoparticles and another operational parameter, i.e., temperature investigated. The liquid fraction in the PCM is analyzed over 50 minutes of melting for different cases, as the effects of nanoparticles on the heat transfer rate and the possible interactions between the parameters under study are the main objectives of this part of the research, but not optimization of the thermal storage unit under study. A factorial design methodology is used to consider the probable interactions between the different parameters, for example considering the variation of NePCM properties at variable temperatures. This statistical method is used to find the effects of HTF inlet temperature and nanoparticle concentrations on the total heat transfer and the melting rate of the NePCM. Optimal concentrations of nanoparticles in both the HTF and the PCM are determined using this new approach, although these optimal concentrations would only be valid at the similar experimental conditions, as mentioned in chapter 5.

6.1 Theory

6.1.1 Physical model

The process begins when heated HTF from solar panels moves toward the tube inlet of the storage unit. A schematic solar thermal energy storage system is shown in **Fig. 6-1**, with the dimensions of the shell and tube configuration used in this study. The system consists of a vertically oriented shell and tube unit in which HTF moves upward in the tube. Thermal energy is transferred from the HTF in the tube to the PCM (paraffin wax) in the shell through a highly conductive wall. Physical properties of the paraffin wax in (Kandasamy et al., 2008) experimental study are used in the current numerical study. Copper oxide (CuO) nanoparticles with a particle diameter of 10nm are added into both the HTF and the PCM in order to study their impacts on heat transfer in the storage unit.

6.1.2 Assumptions and boundary conditions

To avoid the model computationally expensive, it is assumed that the nanofluid flow is uniform at the inlet of the tube. The thermal resistance of the wall between HTF and NePCM is assumed to be negligible. Also, the outer wall of the thermal energy storage unit (i.e., the shell) is assumed to be well insulated (i.e., adiabatic condition). Moreover, a symmetrical boundary condition is used for the shell and tube system. Reynolds number of HTF and initial temperature of NePCM are set to be 2000 (laminar numerical model is employed) and 322.15 K respectively. A pressure boundary (zero pressure) is considered for the HTF outlet.

NePCM properties are temperature-dependent while HTF properties do not change with temperature. In addition, density variation due to phase change is neglected. Copper oxide volume concentration range in HTF and NePCM varies between 0-4 vol.% and 0-7 vol.% respectively.

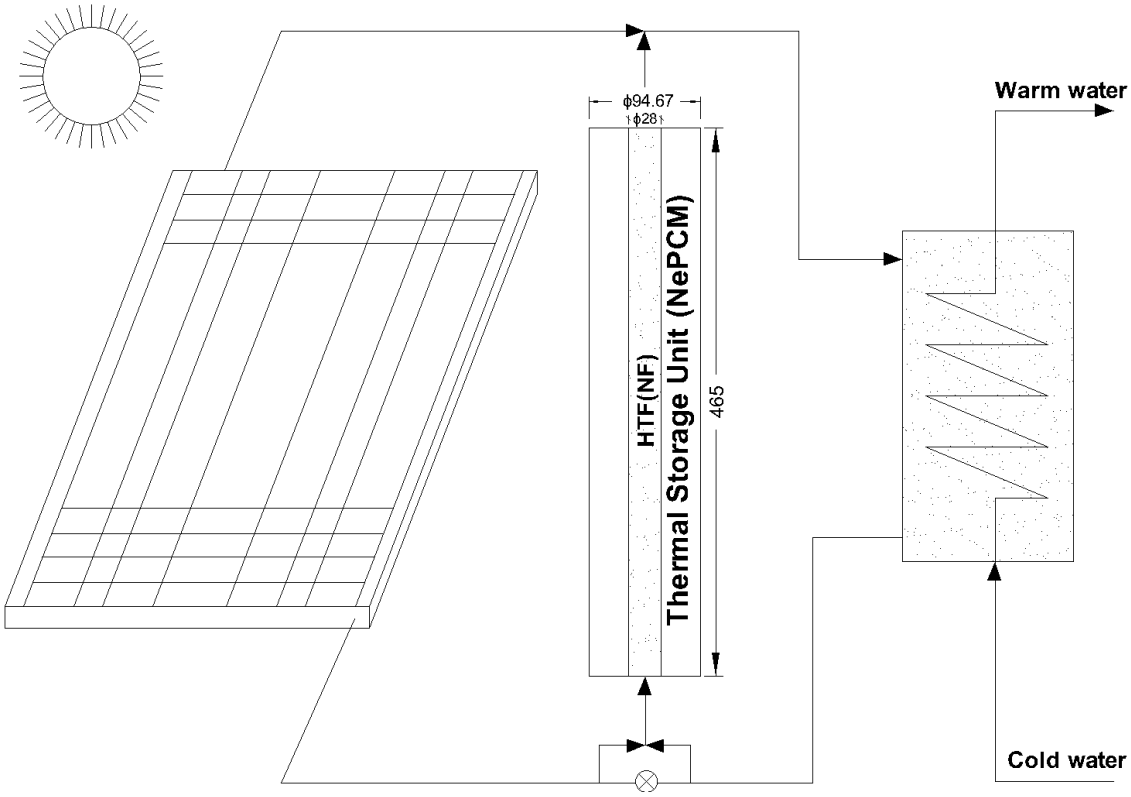

Fig. 6-1 Schematic of a shell and tube thermal energy storage unit for a domestic solar system.

Temperature-dependent paraffin wax ($T_m = 326.15 - 321.15K$) density and viscosity can be obtained in a 2008 study (Kandasamy et al., 2008) as follows:

$$\rho_{PCM} = \frac{800}{\beta(T - T_{liquidus}) + 1} \tag{6-1}$$

and dynamic viscosity of liquid PCM is given by:

$$\mu = 0.001 \times \exp(A_1 + \frac{A_2}{T}) \tag{6-2}$$

where A_1 and A_2 in Eqs. (6-1) and (6-2) are listed in **Table 6-1**. Other properties of paraffin wax and CuO are also listed in **Table 4-1**.

Table 6-1 Paraffin wax properties and variables.

Variable	**Value** (Reid, Prausnitz, & Poling, 1987)
A_1	-4.25
A_2	1790

6.2 Numerical approach and validation

The numerical approach described in section 3.3 is implemented for the simulation. Time step is set to 0.05, and the iterative time-advancement scheme is used for solving all of the equations iteratively in a segregated mode until convergence criteria for all variables, which is 10^{-6}, are met. Different mesh designs are implemented to obtain a mesh-independent solution. As shown in **Fig. 6-2**, two parameters are used for this mesh dependency test. One is the liquid fraction of the thermal storage unit over time and the other is the temperature variation in a fixed point, $x = 28\ mm$ and $y = 300\ mm$. It is found that variation of the results is negligible for the grid size of 22×222 and after. Thus, this grid size is used for the comparison of the current study with the numerical study of (Sciacovelli et al., 2013) and the experimental study of (Aydin et al., 2007) at a given point ($x = 28\ mm$ and $y = 300\ mm$). The details of these comparisons are shown in **Fig. 6-3**. Eventually, the average deviations of the current study with Sciacovelli et al. (Sciacovelli et al., 2013) and Aydin et al. (Aydin et al., 2007) studies are 13.9 % and 7.2 % respectively. This serves as a good validation of the current model against previous experimental and numerical results.

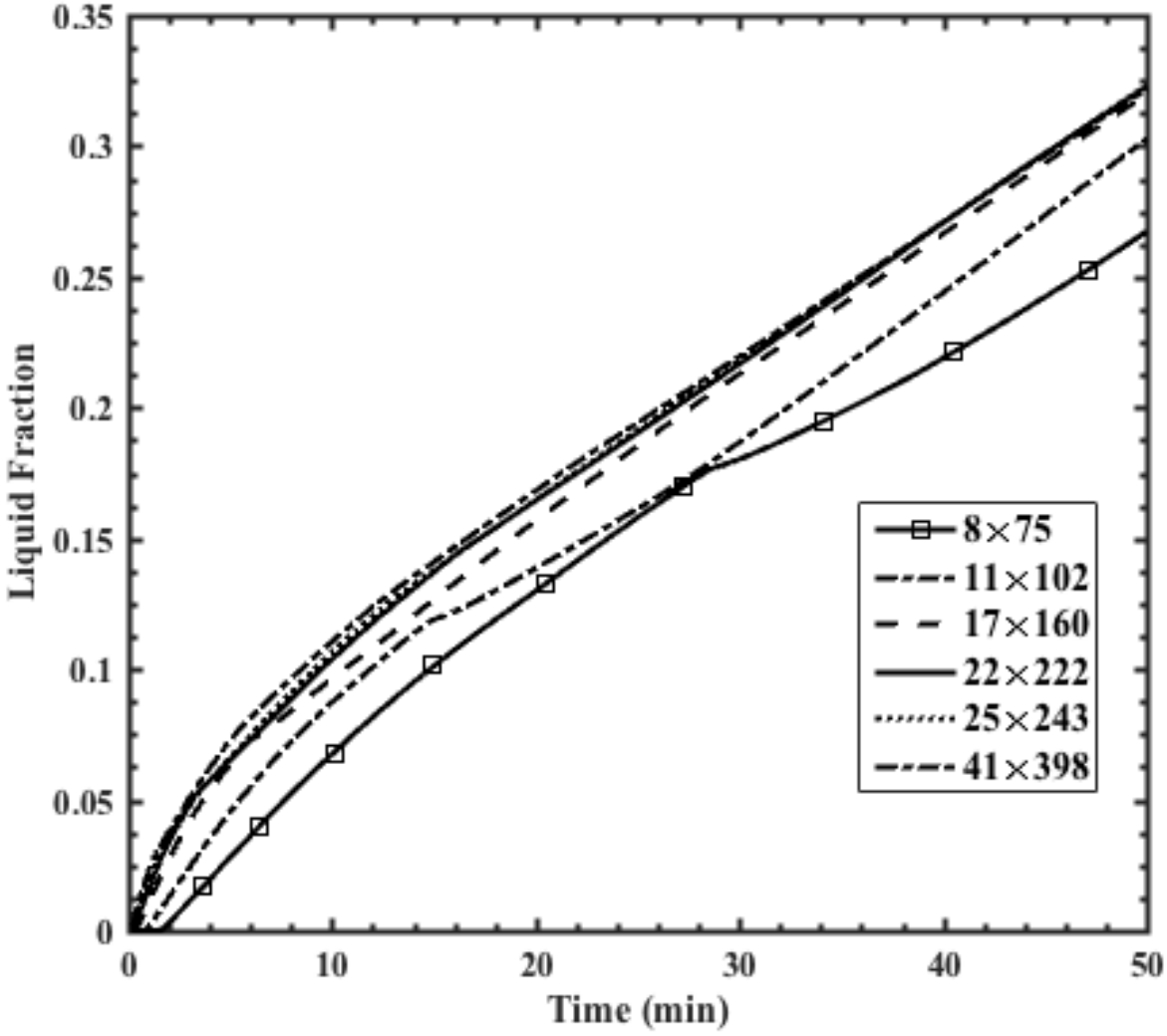
Liquid Fraction
Time (min)
0
0.05
0.1
0.15
0.2
0.25
0.3
0.35
0
10
20
30
40
50
8×75
11×102
17×160
22×222
25×243
41×398

(a)

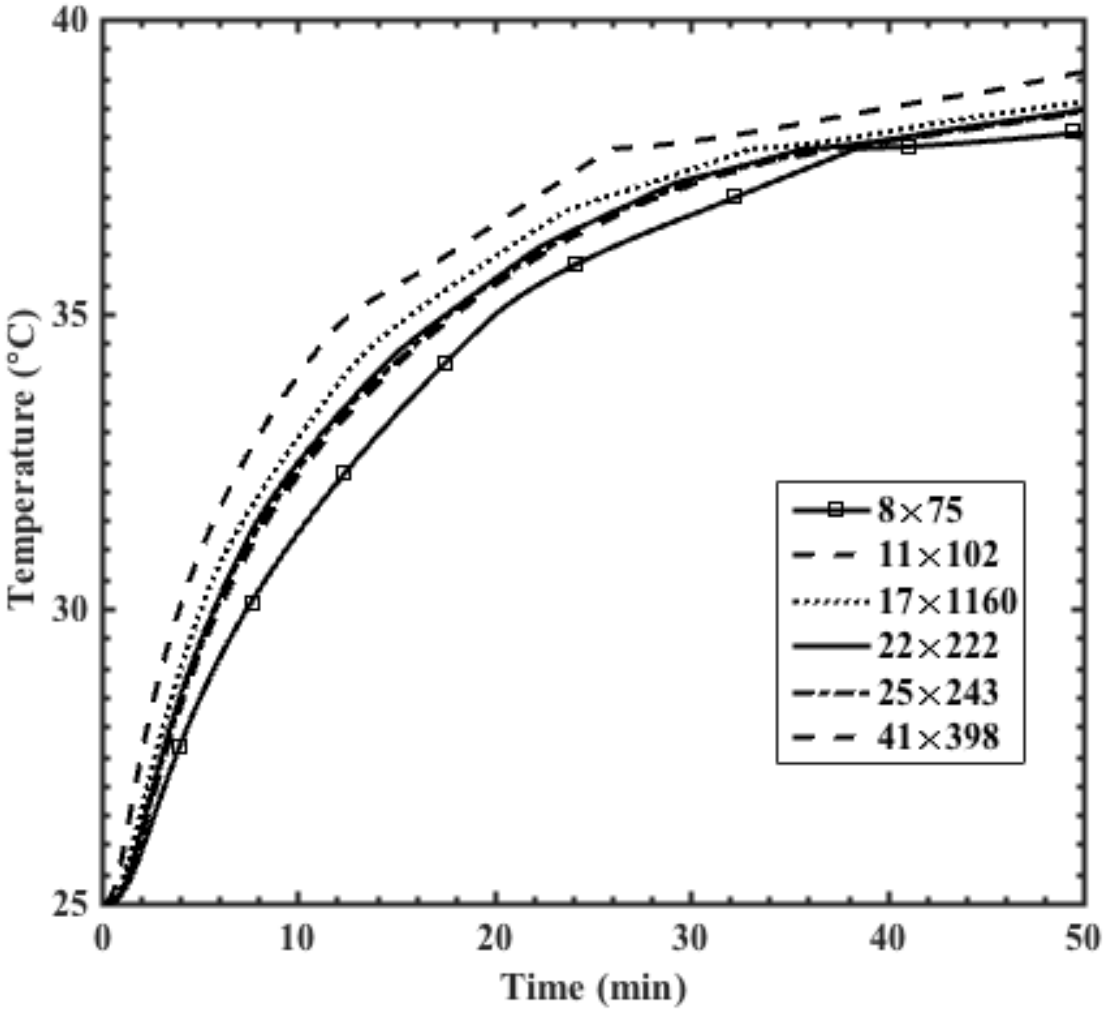

(b)

Fig. 6-2 Mesh independency test, (a) liquid fraction, and (b) temperature at $x = 28\ mm$, $y = 300\ mm$.

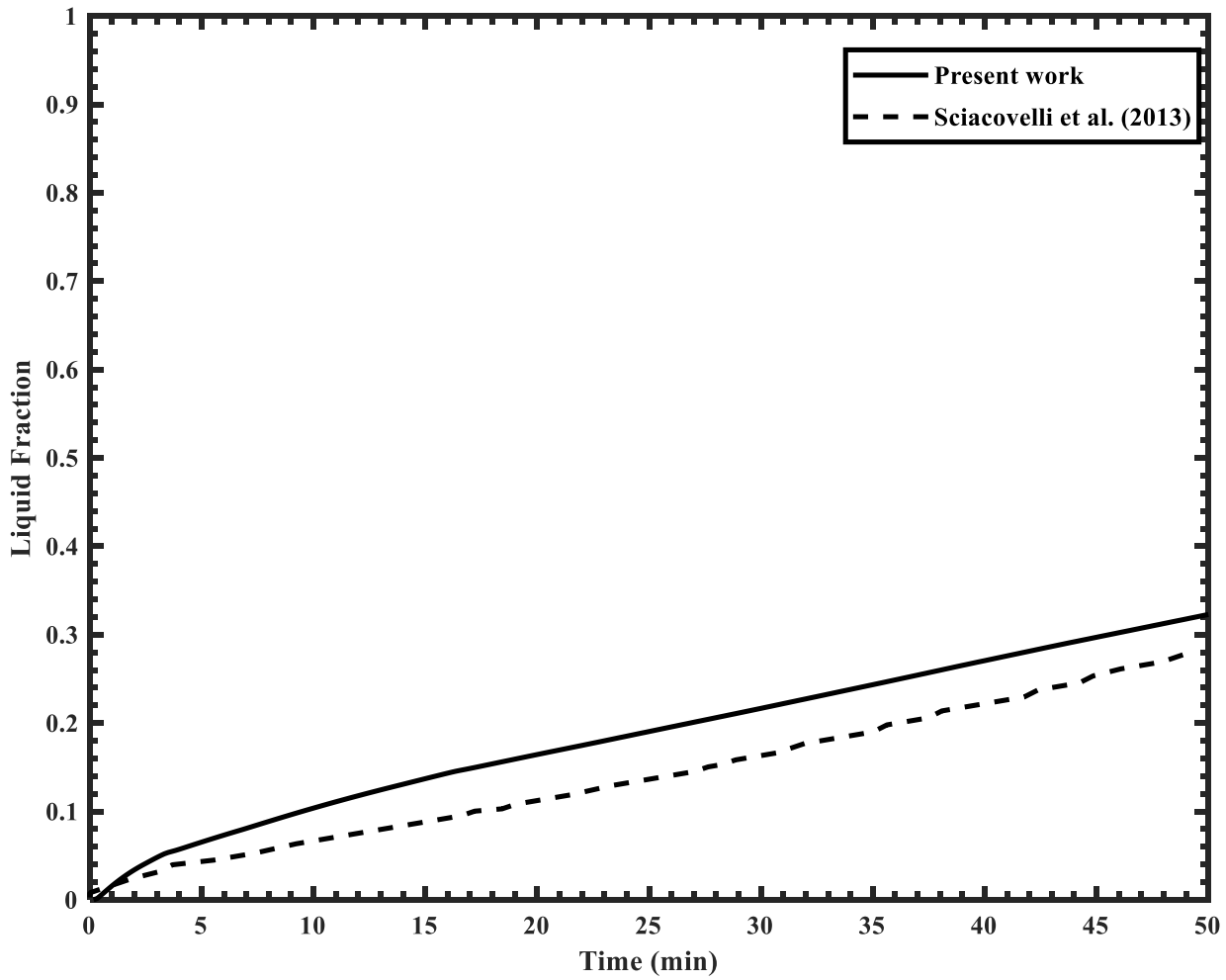
Present work
Sciacovelli et al. (2013)
Liquid Fraction
Time (min)
0
0.1
0.2
0.3
0.4
0.5
0.6
0.7
0.8
0.9
1
0
5
10
15
20
25
30
35
40
45
50

(a)

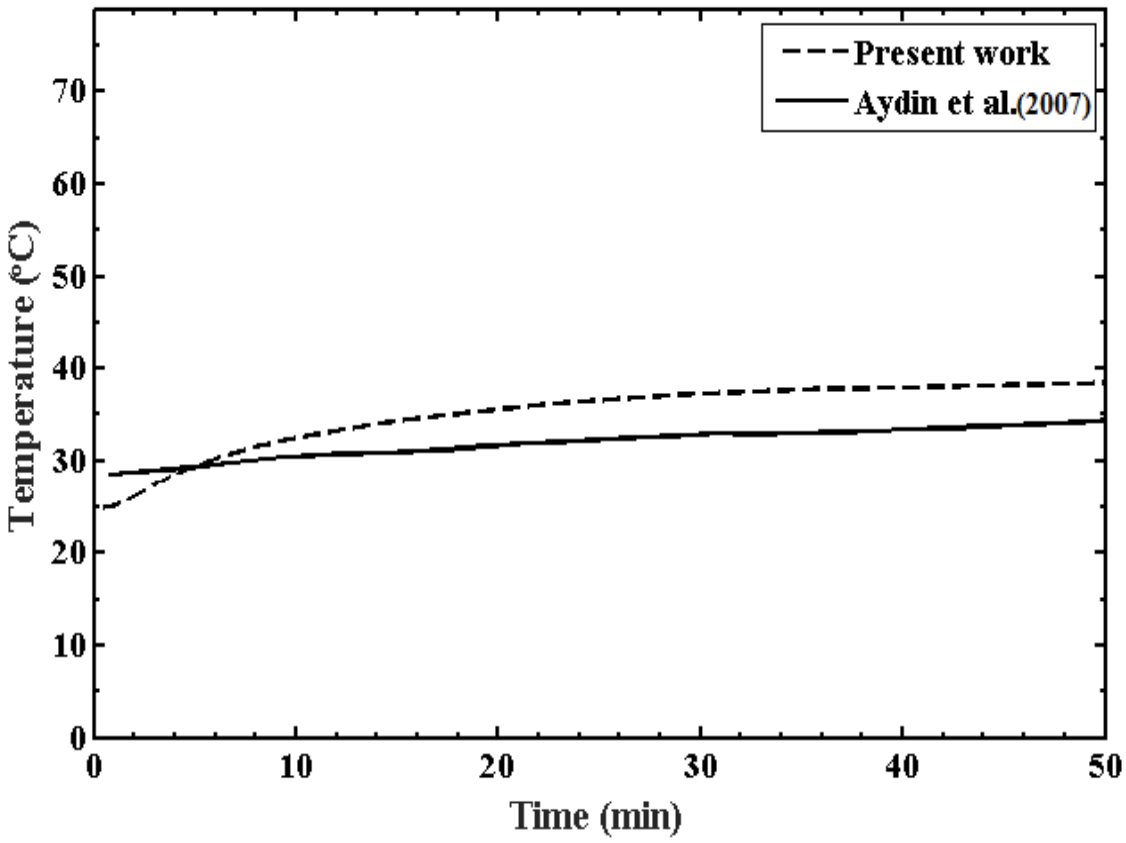

(b)

Fig. 6-3 Comparison between the present study and previous studies, (a) liquid fraction versus time from (Sciacovelli et al., 2013), and (b) temperature at $x = 28\ mm$, $y = 300\ mm$ versus time from (Aydin et al., 2007).

6.3 Statistical approach

A factorial design is employed to analyze three different factors affecting the liquid fraction of NePCM. 2^k factorial design (Montgomery, 2012) is implemented for the analysis of the impact of HTF inlet temperature, particle concentrations in both HTF and PCM as three main factors and their probable interactions. Two low and high levels are chosen for each of the selected main factors, in other words, "+" and "–"signs are assigned for high and low levels of each main factor respectively. As long as replication of the numerical computation under the same condition always

gives the same result, one replication is considered for each case. In the first step, eight cases are conducted with intentionally changed levels of the factors. Then, three more runs at the center-point of the factors, which are called “neutral”, are conducted to check the linearity of the response. For simplicity, nanoparticle volume fraction in the HTF and the PCM are assigned to be factor “A” and “B” respectively, and the temperature is named factor “C”. All selected factors are independent. The level-set for the case under study is shown in **Table 6-2**.

Table 6-2 Factors and levels for factorial design.

Case	A	B	C	Run label
1	–	–	–	(1)
2	+	–	–	a
3	–	+	–	b
4	+	+	–	ab
5	–	–	+	c
6	+	–	+	ac
7	–	+	+	bc
8	+	+	+	abc

ANOVA test (Montgomery, 2012) is used to determine the adequacy of the model. Multiple regression analysis is developed as the predictor equation, which illustrates the role of each factor and their probable interactions. In addition, in the case of curvature existence in the proposed model, the model needs improvements using RSM to cover the curvature or nonlinearity. The CCF design is used to predict the nonlinearity of the model. In this method, two factors intentionally change to their neutral level in order to observe their effect on the liquid fraction.

In the first statistical step, a response equation emerges to illustrate the relationship between each factor and the liquid fraction:

$$LF = f(\phi_{NF}, \phi_{PCM}, T) \tag{6-3}$$

where LF is liquid fraction after 50 minutes. In the case of the nonlinearity of the model, this function is approximated using a polynomial or higher degree model (See Eq. 3-44).

6.4 Results and discussions

Based on the factorial design in **Table 6-2**, different cases are assigned as depicted in **Table 6-3**. Nanoparticle concentrations in the HTF and the PCM vary in a range of 0-4 vol.% and 0-7 vol.% respectively, and temperature range is 350.15 - 370.15 K. The nanoparticle concentration ranges are chosen to study the interactions that may exist between the parameters under study, but not in a way to find the optimum condition. The In the first step, 8 runs are conducted based on the factorial design configuration with 3 center-points to check the linearity of the regression model.

Table 6-3 Liquid fraction after 50 minutes for different cases.

Case	ϕ_{NF} ($vol.\%$)	ϕ_{NePCM} ($vol.\%$)	Temperature (K)	Liquid Fraction (%)
1	0	0	350.15	56.40
2	4	0	350.15	56.83
3	0	7	350.15	59.54
4	4	7	350.15	60.02
5	0	0	370.15	88.12
6	4	0	370.15	88.55
7	0	7	370.15	89.32
8	4	7	370.15	89.83
9	2	3.5	350.15	63.55
10	2	3.5	370.15	93.28
11	2	3.5	360.15	82.41

6.4.1 Simulation results

In order to investigate the role of nanoparticles in the HTF and their effects on the melting rate, Reynolds number is kept unchanged. Moreover, the physical properties of NePCM are temperature-dependent and sensitive to volume fraction. C-programming language is employed to write user-defined functions to calculate all of the NePCM properties.

The contour of liquid fraction for case 6 is shown in **Fig. 6-4** at different times. At the onset of heat transfer, the melting process is controlled by heat conduction between the heat exchanger wall and the solid PCM. With time, a small melted region is formed in the upper side of the shell. This is the starting point for natural convection due to the buoyancy force as shown in **Fig. 6-4** (a). The melted region in the upper part of the thermal storage unit increases over time, which shows the contribution of heat conduction and convection on the heat transfer and melting rate as shown in **Fig. 6-4** (b). In other words, heat conduction is mainly responsible for the melting of the lower part, while natural convection is dominating on the upper part of the thermal storage unit. Heat conduction is weakened over time and replaced with convection as shown in **Fig. 6-4** (c). In the last stage, heat convection predominates on the heat transfer and PCM melting as shown in **Fig. 6-4** (d). Figure 6-5 shows the temperature distribution of the same case. It is seen that the temperature has a nearly axial symmetrical profile for the part where heat conduction dominates. In addition, thermal stratification can be seen when the buoyancy force appears. Eventually, thermal energy is stored in the form of sensible heat in the upper part of the shell until the temperature of PCM there equals the HTF temperature. The melting process continues to move downward in the storage unit.

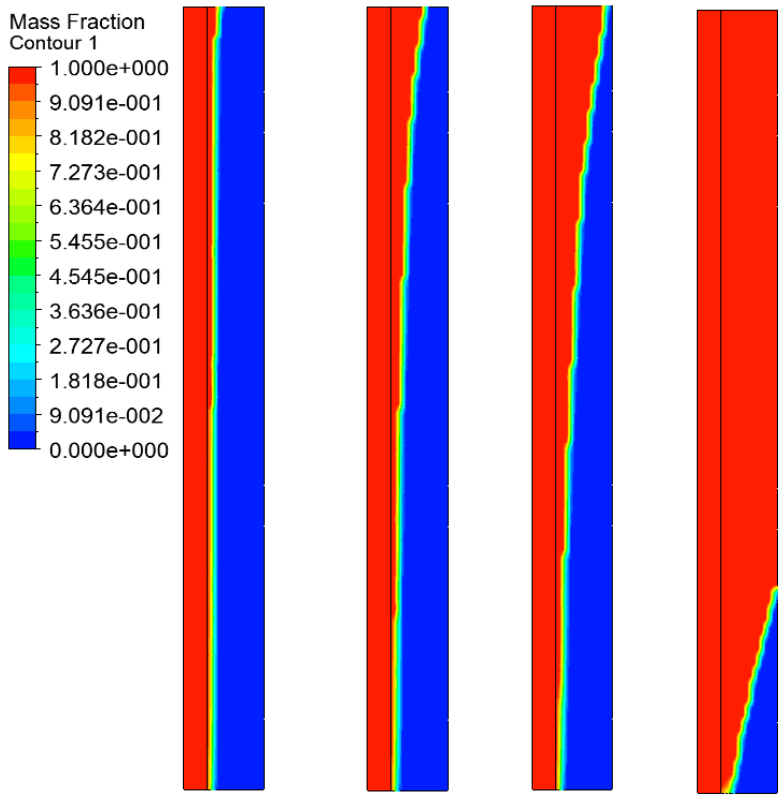

(a) *(b)* *(c)* *(d)*

Fig. 6-4 Liquid fraction for case 6, (a) 5 mins, (b) 10 mins, (c) 15 mins, (d) 50 mins.

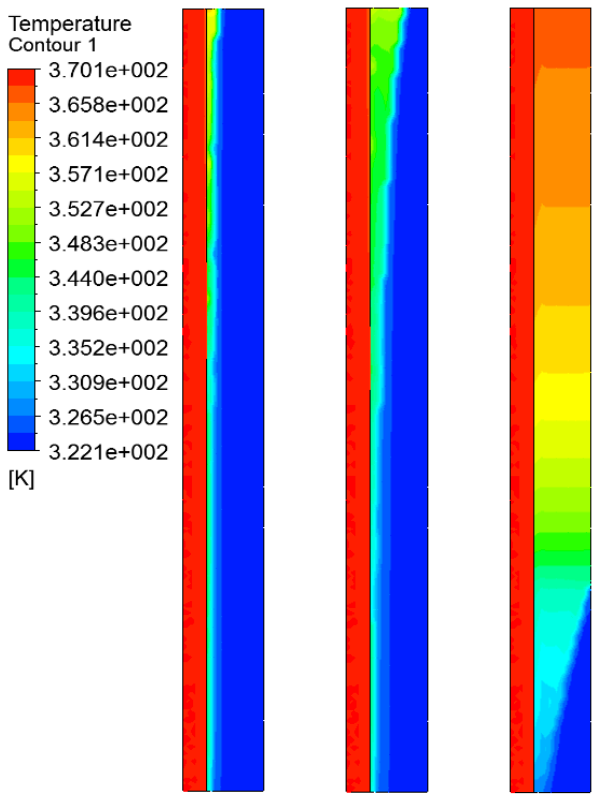

(a) *(b)* *(c)*

Fig. 6-5 Temperature contour for case 6, (a) 5mins, (b) 10 mins, (c) 50 mins.

As shown in **Table 6-3**, liquid fraction in the PCM increases when nanoparticle concentration in the HTF increases from 0 to 4 *vol*.%. With more nanoparticles, the viscosity and density of the nanofluid HTF increases, while the velocity might be reduced to keep the Re unchanged. However, the nanofluid thermal conductivity enhancement is large enough to compensate for the other adverse changes to heat transfer. This eventually leads to the increased heat transfer rate and liquid fraction enhancement in the PCM. On the other hand, the same behaviour is not seen in the NePCM. Nanoparticle loading from 0 to 7 *vol*.%increases the melting rate as shown in **Fig. 6-6**, for both HTF inlet temperatures of 350.15 and 370.15 K. However, more NePCM is melted with a nanoparticle concentration of 3.5 *vol*.% as shown in **Table 6-3**. Although

thermal conductivity of the NePCM increases with more nanoparticles, changes in the other properties such as density, viscosity and heat capacity may slow down the melting rate in the NePCM.

To investigate this, the effects of the HTF inlet temperature and particle concentration on heat flux to the PCM are depicted in **Fig. 6-7**. The heat flux fluctuations represent different heat transfer regimes, contributing during melting, namely pure conduction regime, start of convection regime, which improves the heat flux, and convection and conduction regimes on the top and bottom of the storage unit. It is evident that higher HTF inlet temperature leads to higher initial average heat flux. The average heat flux decreases dramatically for all cases at an early stage of the melting process, when heat conduction dominates. As discussed earlier, nanoparticles in the PCM lead to better total heat transfer due to stronger heat conduction. Therefore, in the first 5 minutes of the melting process, the cases with nanoparticles show a higher average heat flux than those without nanoparticles in the PCM. Subsequently, a combination of heat conduction and convection leads to a fairly constant average heat flux. However, total heat transfer decreases after a while, which leads to the reduction of average heat flux for cases 6 and 8. Heat flux reduction for case 8 is more pronounced than case 6 because of the weaker natural convection in case 8.

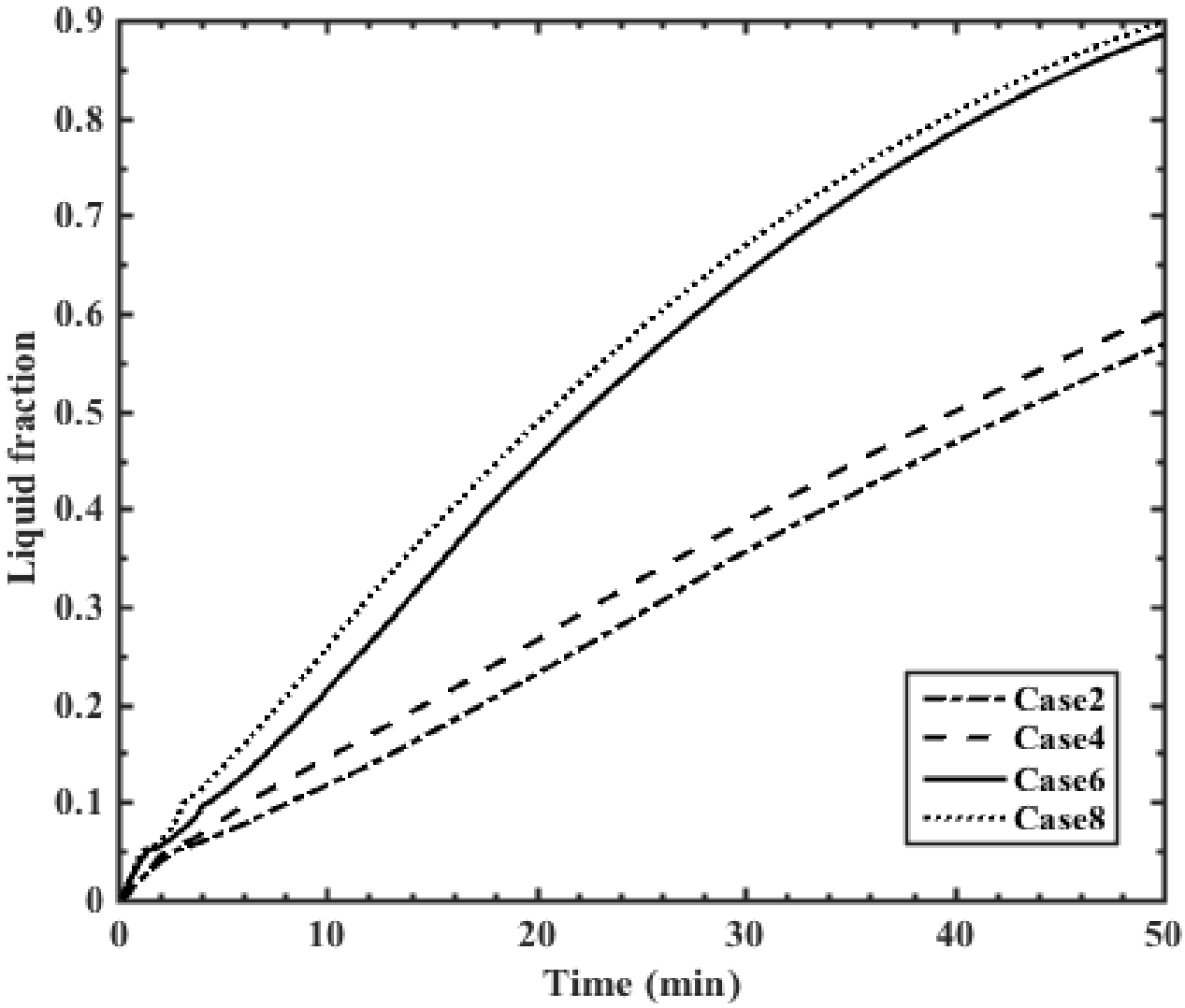

Fig. 6-6 Liquid fraction over the time, case 2 ($\phi_{NF} = 4\ vol.\%,\ \phi_{NePCM} = 0,\ T = 350.15\ K$), case 4 ($\phi_{NF} = 4\ vol.\%,\ \phi_{NePCM} = 7\ vol.\%,\ T = 350.15\ K$), case 6 ($\phi_{NF} = 4\ vol.\%,\ \phi_{NePCM} = 0,\ T = 370.15\ K$), case 8 ($\phi_{NF} = 4\ vol.\%,\ \phi_{NePCM} = 7\ vol.\%,\ T = 370.15\ K$).

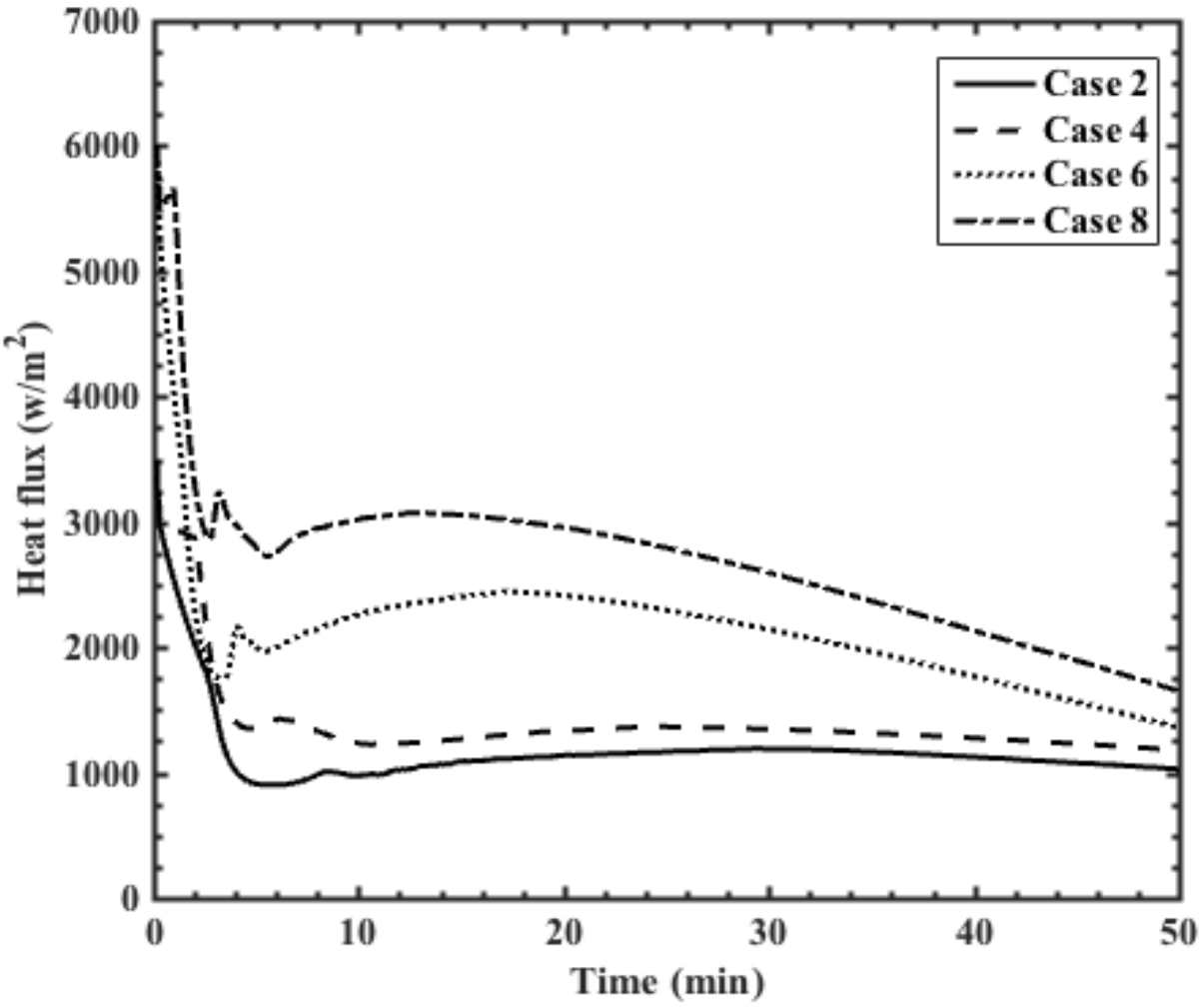

Fig. 6-7 Effect of HTF inlet temperature on average heat flux to the PCM storage unit for case 2 ($\phi_{NF} = 4\ vol.\%,\ \phi_{NePCM} = 0,\ T = 350.15\ K$), case 4 ($\phi_{NF} = 4\ vol.\%,\ \phi_{NePCM} = 7\ vol.\%,\ T = 350.15\ K$), case 6 ($\phi_{NF} = 4\ vol.\%,\ \phi_{NePCM} = 0,\ T = 370.15\ K$), *case 8* ($\phi_{NF} = 4\ vol.\%,\ \phi_{NePCM} = 7\ vol.\%,\ T = 370.15\ K$).

6.4.2 Statistical analysis

Multiple regression analysis (Montgomery, 2012) is used to develop a regression model, or predictive equation, from the above numerical results considering the significant factors and their probable interactions in affecting the liquid fraction variation rate in the PCM. The 2^k factorial design is used here with α-value set to 0.1, i.e., probability of 10 % for selection of insignificant

factors. In this work, the null hypothesis is that none of the selected factors are significant on the liquid fraction variation rate. Subsequently, the alternate hypothesis signifies that at least one factor is significant on the liquid fraction. In this step, the null hypothesis is rejected in favour of the alternate hypothesis. The only significant factor in this model is temperature as its p-value is much less than α-value as indicated in **Table 6-4**. In other words, F-value of the temperature is much larger than the critical F-value in the Fisher distribution table (Montgomery, 2012). Then, three more cases are intentionally set in the center-points of each factor in order to evaluate the model linearity. It is found that the model is nonlinear due to the existing curvature, as depicted in **Table 6-4**. In other words, at least one factor does not have linear behaviour on the liquid fraction changes. Thus, the model needs to be improved to a polynomial model using CCF.

Table 6-4 ANOVA table (Linear model).

Source	Sum of Square	df	Mean Square	F-Value	P-value	
Model	2345.54	4	586.39	77.39	<0.0001	Significant
T **(C)**	2333.56	1	2333.56	374.35	<0.0001	
Curvature	56.25	1	56.25	9.02	<0.017	Significant
Residual	49.87	8	6.23			
Cor Total	2439.68	10				

In the next step, four more cases are added based on CCF level requirements to improve the model and obtain a predictive equation that follows the nonlinear behaviour of the liquid fraction as depicted in **Table 6-5**. Null and alternate hypotheses are evaluated for the nonlinear model based on p-value obtained for each factor as shown in **Table 6-6**. In order to determine whether the obtained p-value of a certain factor is significant, its p-value is compared with α-value, which gives the probability of rejecting the null hypothesis when the hypothesis is true. Thus, if the p-value of a certain factor is smaller than the selected α-value, it means that the

contribution of that factor or variable is statistically significant in the model. Since p-value of ϕ_{NF} , ϕ_{NePCM} and temperature factors are less than the α-value, the null hypothesis is rejected in favour of alternate hypothesis with 90 % confident interval, and all insignificant factors are rejected as shown in **Table 6-6**. It is found that all the main factors have a significant effect on the liquid fraction as their p-values are much smaller than the selected α-value (0.1). Moreover, there is an interaction between ϕ_{NePCM} and temperature, which is statistically significant.

Table 6-5 Liquid fraction after 50 minutes for different cases (Augmented design).

Case	ϕ_{NF} (*vol*.%)	ϕ_{NePCM} (*vol*.%)	Temperature (K)	Liquid Fraction (%)
12	0	3.5	360.15	82.15
13	4	3.5	360.15	82.72
14	2	0	360.15	75.59
15	2	7	360.15	78.01

Table 6-6 ANOVA table (CCF model).

Source	Sum of Square	df	Mean Square	F-Value	P-value	
Model	2529.7	7	361.39	4623.09	<0.0001	Significant
ϕ_{NF} **(A)**	0.59	1	0.59	7.49	0.029	
ϕ_{NePCM} **(B)**	12.61	1	12.61	161.33	<0.0001	
T **(C)**	2333.56	1	2333.56	29852.53	<0.0001	
$\phi_{NePCM}T$ **(BC)**	1.85	1	1.85	23.7	0.0018	
ϕ_{NF}^2 **(A^2)**	0.33	1	0.33	4.18	0.08	
ϕ_{NePCM}^2 **(B^2)**	71.64	1	71.64	916.49	<0.0001	
T^2 **(C^2)**	34.51	1	34.51	441.46	<0.0001	
Residual	0.55	7	0.078			
Cor Total	2530.24	14				

In order to verify the accuracy of the predictive model, ANOVA assumptions need to be checked. For this purpose, the residuals of the model are evaluated. If the residuals of the model do not meet the ANOVA assumptions, a transformational term must be added to the model. Figure 6-8 (a) shows that the points are well distributed along the inclined line (well distribution of residuals) with no pattern. Also, **Fig. 6-8** (b) shows that the residual points are randomly scattered, with no outlier, and the residuals have constant variance. Figure 6-8 (c) reveals that the predicted and actual values agree well. Moreover, all of the factors are independent from each other. Thus, ANOVA assumptions are well met and no transformational term is required. In addition, R^2 of the model is 0.9998 in the current model indicating that A^2, B and C are responsible for 99.98 % of the model variation. The Adjusted R^2 is 0.9996, which means no insignificant or unnecessary term. The Predicted R^2 is 0.9990, showing the adequacy of the model for prediction.

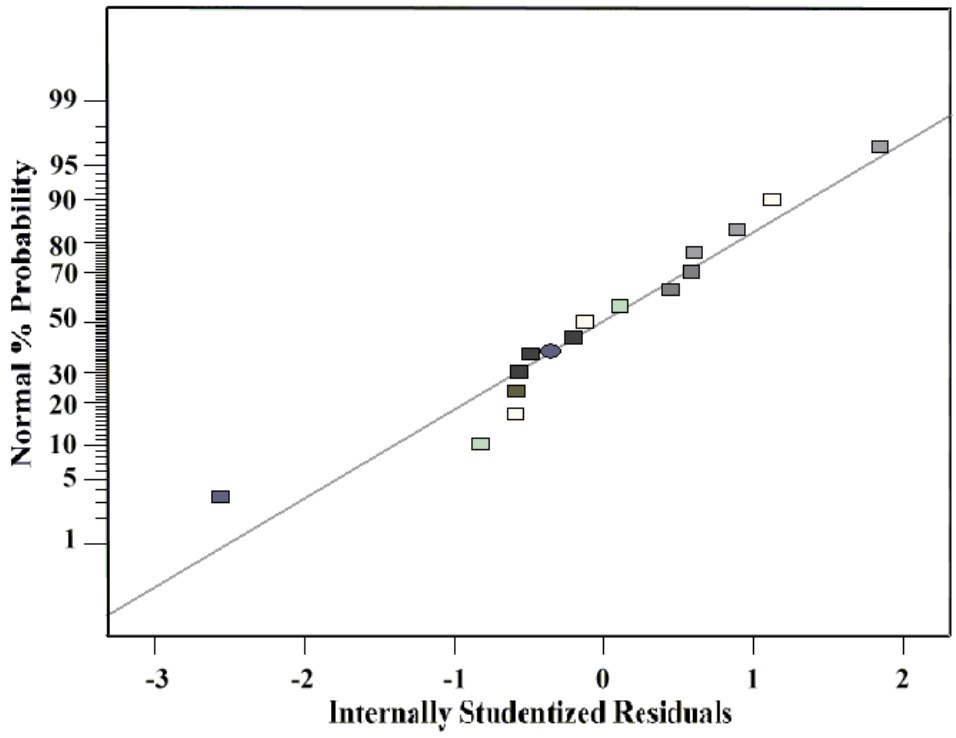

(a)

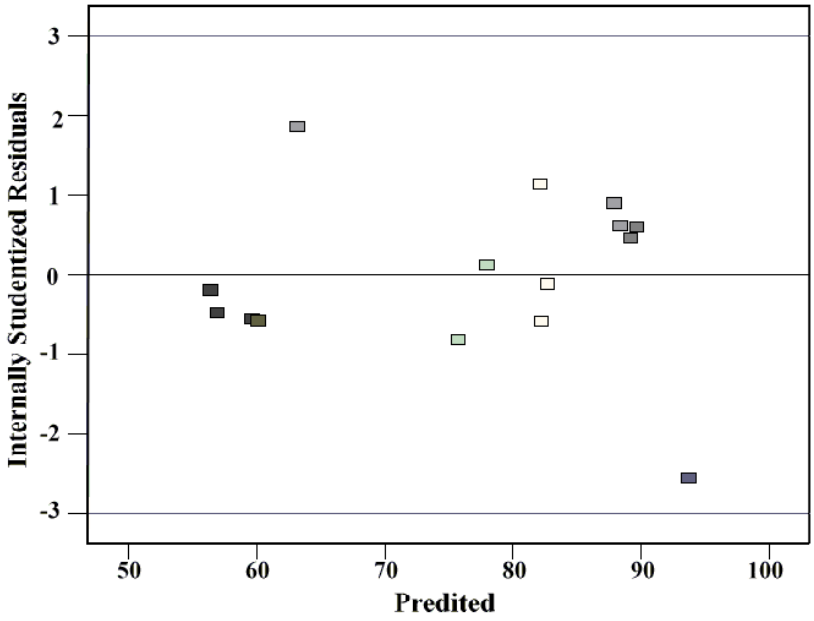

(b)

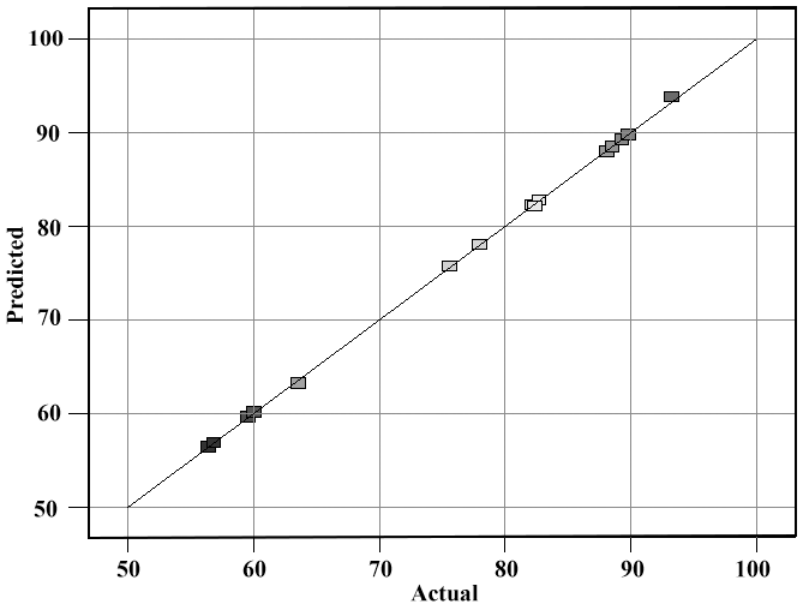

(c)

Fig. 6-8 Regression analysis of the model, (a) Normal plot of Residuals, (b) Residuals vs. predicted, (c) Predicted vs. Actual.

With all these considerations, the predictive equation (regression model) can be shown as follows:

$$LF = -5243.27658 - 23.56667\phi_{NF} + 828.91101\phi_{NePCM} + 27.96272T - 1.375T\phi_{NePCM}$$

$$+891.66667\phi_{NF}^2 - 4308.84354\phi_{NePCM}^2 - 0.036633T^2 \quad (6\text{-}4)$$

The above correlation covers liquid fraction value for ϕ_{NF} between 0-0.04, ϕ_{NePCM} between 0-0.07 and temperature between 350.15-370.15 K. It is found that all three factors have a nonlinear parabolic impact on liquid fraction variation, and interaction of temperature and ϕ_{NePCM} reduces the liquid fraction in case of ϕ_{NePCM} and temperature increase.

In order to show the contribution of each factor to the liquid fraction changes, coded range of each factor is indicated in **Fig. 6-9**. It is seen that temperature has a maximum impact on liquid fraction and this contribution increases for higher temperatures. Similarly, nanoparticle concentration in HTF slightly increases liquid fraction but this trend is not seen on NePCM. The liquid fraction decreases with nanoparticle concentration over 4 vol.%. It means that heat conduction enhancement cannot make up for the reduction in natural convection, which leads to a reduction of the total heat transfer rate. Figure 6-10 represents the interaction between ϕ_{NePCM} and temperature. It is found that growth of melted NePCM with $\phi_{NePCM} = 7$ vol.% is less than that of $\phi_{NePCM} = 0$ at higher temperatures. In other words, despite a remarkable liquid fraction difference between the pristine paraffin and NePCM with 7 vol.% nanoparticles at 350.15 K, the impact of the nanoparticles is less pronounced when the temperature increases. One possible reason is that lower viscosity at higher temperatures leads to higher buoyancy force and enhanced natural convection for the pristine paraffin wax. At higher HTF inlet temperatures (e.g., 370.15 K), fluid

motion heat transfer becomes stronger than that at lower HTF inlet temperatures (e.g., 350.15 K) and has more contribution to the total heat transfer than thermal conductivity. However, adding nanoparticle suppresses the fluid motion more at higher HTF inlet temperature which reduces the total heat transfer. One possible explanation is the more Grashof number reduction at high HTF inlet temperature (e.g., 370.15 K) than low HTF inlet temperature (e.g., 350.15 K) for a NePCM sample with a certain nanoparticle concentration. In Fig. **Fig. 6-11** (a), liquid fraction variation is shown for different temperatures and ϕ_{NePCM}. As discussed earlier, the maximum melting is obtained at the maximum temperature, but not the maximum ϕ_{NePCM}. Similarly, **Fig. 6-11** (b) shows liquid fraction variation for different nanoparticle concentrations in the HTF and the PCM, where the maximum melting is seen when nanoparticle concentration is maximum in the HTF.

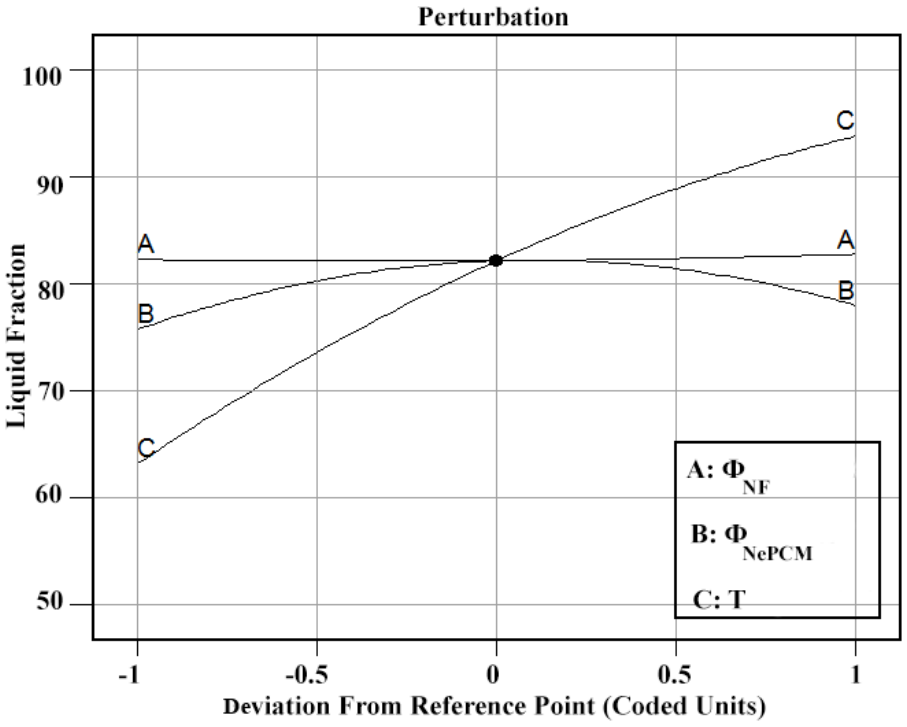

Fig. 6-9 Impact of factor **A** (ϕ_{NF}), factor **B** (ϕ_{NePCM}), and factor **C** (T) variation in a coded range on the liquid fraction.

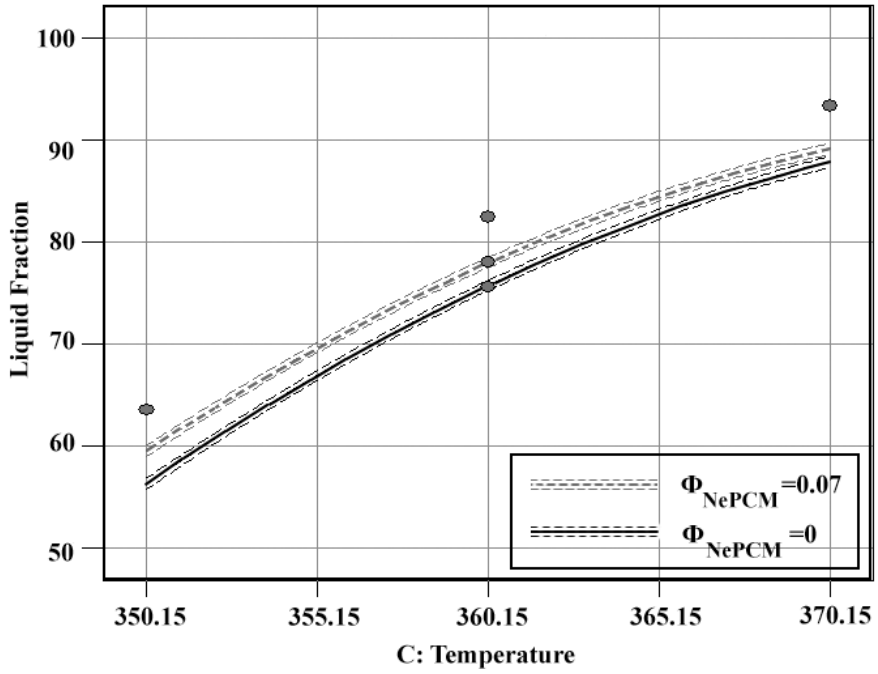

Fig. 6-10 Interaction of ϕ_{NePCM} and temperature on the liquid fraction.

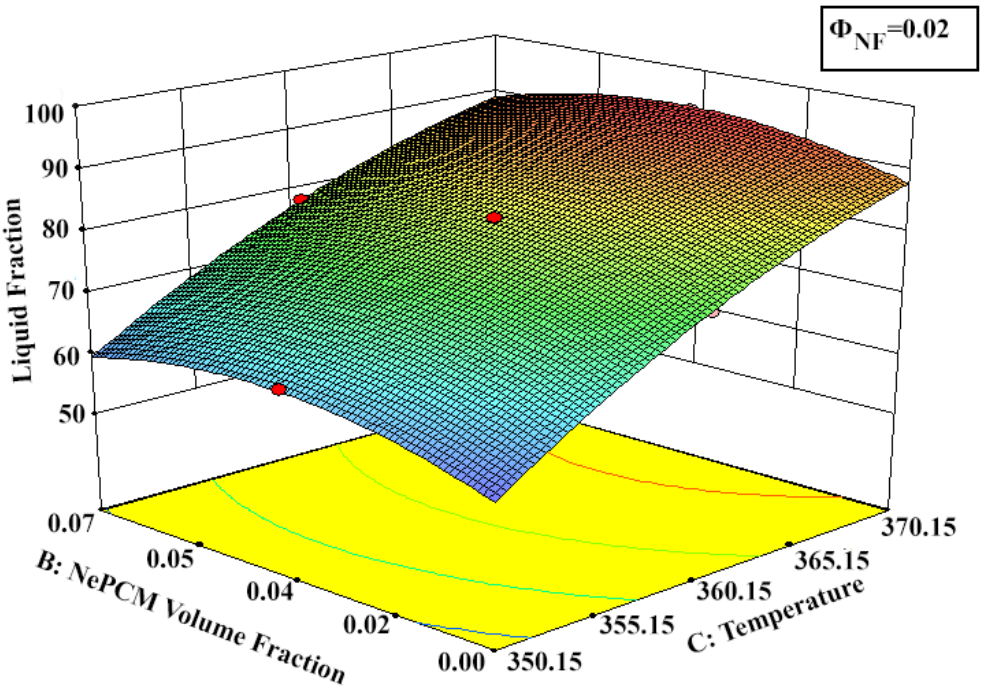

(a)

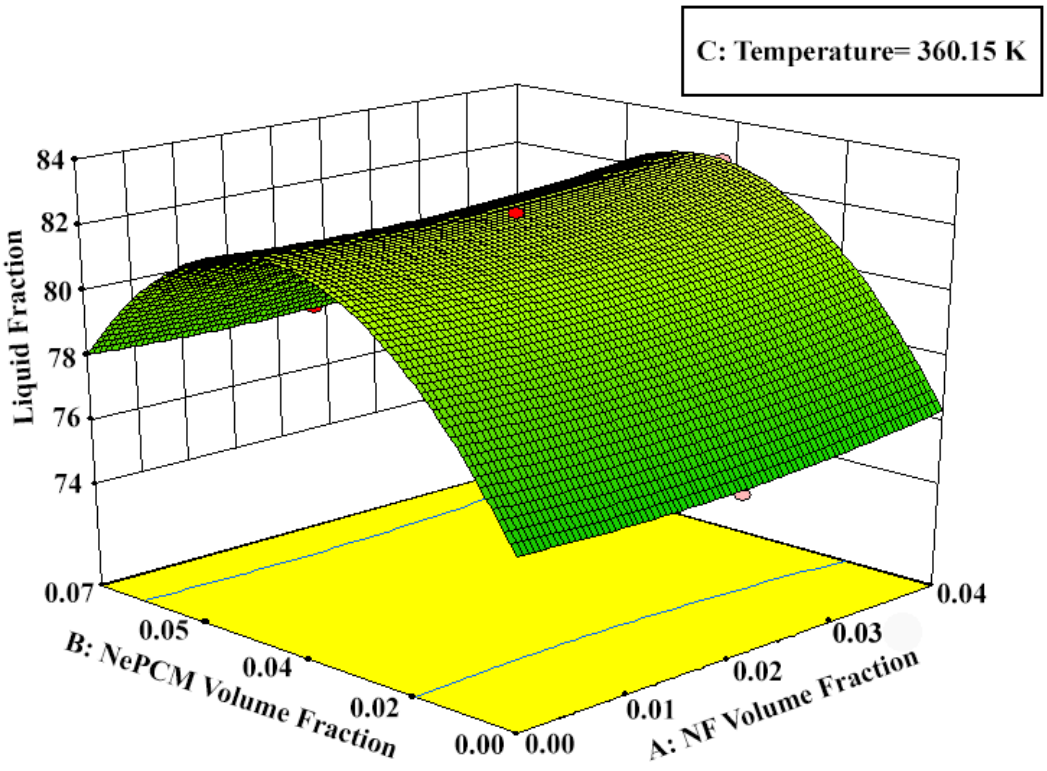

(b)

Fig. 6-11 Liquid fraction 3-D plot (a) ϕ_{NePCM} and Temperature (b) ϕ_{NF} and ϕ_{NePCM}.

6.5 Summary

This case study presents a numerical and statistical analysis of melting of paraffin wax enhanced with CuO nanoparticles in a latent thermal energy storage unit with water-CuO nanofluid as heat transfer fluid (HTF). The nanoparticle diameter is 10nm with a concentration range of 0-7 vol.% for the NePCM and 0-4 vol.% for the nanofluid. The effects of nanoparticle concentration in both of the HTF and the PCM, as well as the inlet temperature of the HTF were numerically investigated. The simulation results were analyzed statistically with a face-centered central composite design methodology. The following main conclusions can be drawn from this study:

- Adding nanoparticles into the HTF increased the total heat transfer rate between the HTF and the PCM. Consequently, the PCM melting process was expedited during charging of the thermal energy storage unit.
- Adding nanoparticles to the PCM, if below a critical concentration, can also enhance the total heat transfer and PCM melting. However, more nanoparticles in PCM beyond the critical concentration can lead to poor total heat transfer and decreased melting rate. One possible reason is that more nanoparticles increase the viscosity of the PCM, leading to a reduction in convective heat transfer.
- The obtained regression model for melting of NePCM is nonlinear. The three independent factors, i.e., HTF inlet temperature (T), nanoparticle concentration in the HFT (ϕ_{NF}), and nanoparticle concentration in the PCM (ϕ_{NePCM}), all showed parabolic effects on the liquid fraction rate during PCM melting. HTF inlet temperature is the most significant factor and ϕ_{NF} is the least significant factor.
- A significant interaction was seen between temperature and ϕ_{NePCM}. It was found that the effect of nanoparticles on NePCM is less pronounced at higher HTF inlet temperatures. This point has experimentally been indicated in an enclosure heated from the bottom.

In the following chapter, the effect of nanoparticles will be evaluated in a similar geometry mounted with fins to understand the importance of nanoparticles in geometry that natural convection mechanism of heat transfer would be the dominant heat transfer mechanism.

Chapter 7 Effects of fins and nanoparticles on the melting rate in a shell-and-tube thermal energy storage

From the previous chapter, it is found that the higher the wall temperature or natural convection, the less the nanoparticles are effective in a thermal storage unit. In this chapter, the effects of nanoparticles are evaluated in a geometry, promoting the natural convection with fins in a shell-and-tube thermal storage unit. Multiscale heat transfer enhancement with both fins and nanoparticles is investigated in a shell and tube LHTES unit. The materials presented in this chapter has been published in a 2018 study (Parsazadeh & Duan, 2018).

To do this, a common organic PCM, paraffin wax, is used with aluminum oxide nanoparticles as NePCM. This metal oxide nanoparticle is selected due to its good stability compared to metallic nanoparticles [33]. Horizontal circular plate fins are used on the outer surface of the HTF tube with the aim to promote natural convection with local circulations of melted PCM/NePCM. Numerical studies are conducted to find out the effects of fin parameters, i.e., pitch, angle, on heat conduction, natural convection, total heat transfer rate and charging time in the presence of nanoparticles at different concentrations. With RSM explained in chapter 3, we aim to identify the most significant parameters for the total heat transfer rate and charging time of the storage unit, as well as the interactions between these significant factors.

7.1 Theory

7.1.1 Physical model

Schematic of a solar thermal system can be seen in **Fig. 6-1** with a shell and tube heat exchanger for latent heat thermal energy storage. Figure 7-1 shows a schematic of the finned heat exchanger. It consists of a vertically oriented shell and a tube, with 7 aluminum fins around the

tube. The annulus is filled with a mixture of paraffin wax and Al_2O_3 nanoparticles (nominal diameter of 59 nm), with air occupying a small portion at the top. In this study, circular plate fins with a fixed length of 9 mm and thickness of 1 mm are considered.

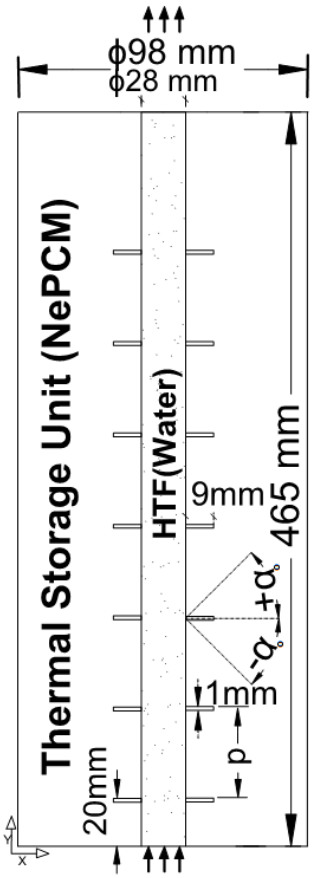

Fig. 7-1 Schematic of a shell and tube thermal energy storage unit.

The design with straight HTF tube and circular plate fins has low pressure loss and reasonable heat transfer rate, making it popular in both research and industry. It is clear that larger heat transfer surface area, i.e., longer and thicker fins, or a larger number of fins, increase the heat transfer rate. But in this part of the study, we aim to investigate the effects of other fin parameters (pitch, p, and angle, α_o) with a fixed surface area.

The heat transfer process begins when warm HTF moves upward in the tube. Over this process, thermal energy is transferred into the NePCM, which eventually melts. Thermal energy is stored in the NePCM sensibly and latently. Physical properties of these materials are listed in **Table 4-1**.

The range of each parameter to be studied needs be selected wisely, as very large range of the parameters might reduce the accuracy of RSM analysis, but very small range of the parameters might make it impossible to demonstrate their effects. In this study, the Al_2O_3 concentration (ϕ) varies from 0 (pure PCM) to 4 vol.% since higher nanoparticle concentration would not improve the total heat transfer rate indicated in the previous chapter (chapter 6) and could make the model inaccurate. For fin angle (α_o), the range of -45^o to 45^o is selected since we wish to find out the effects of fins on natural convection when the fin points to different directions relative to the flow direction of the melted PCM, i.e., in-flow, counter-flow, or in perpendicular. An angle that is too big may have insignificant effects on natural convection; the middle value of 45^o seems a good choice for this purpose. Pitch (p) of the fins has a range of 45 mm to 65 mm. With a fixed number of fins, the larger pitch (p=65 mm) allows more uniform distribution of the fins along the whole HTF tube, while the smaller pitch (p=45 mm) allows the investigation of concentrated fins in the bottom part of the annulus to compensate for weaker natural convection in that region.

7.1.2 Assumptions and boundary conditions

It is assumed that the HTF is a uniform flow at the inlet of the tube. The HTF tube was assumed to be thin Aluminum with high thermal conductivity therefore negligible thermal resistance. The fins are also made of aluminum. It is further assumed that air occupies 4 % of the thermal storage unit on the top portion. The outer surface of the thermal energy storage unit is perfectly insulated (i.e., adiabatic condition). The HTF is set to have an inlet temperature (T_{in}) of

363.15 K, with a Reynolds number of 4500. The NePCM initial temperature is set to be 300.15 K, and Al_2O_3 nanoparticles of spherical shape are homogeneously mixed with paraffin. It is assumed that the properties of the HTF and NePCM are independent of temperature, and density variation due to phase change is neglected. Finally, an axisymmetric boundary is assigned in the simulation (see **Fig. 7-1** and **Fig. 7-2**).

7.2 Numerical approach and validation

The modelling is conducted with a finite volume method (FVM). In this particular application, a segregated solver is adopted for the problem, and SIMPLE algorithm is used to solve the pressure-velocity coupling. A second-order upwind scheme is adopted for computation of convective fluxes, and second-order implicit time integration is employed. The Boussinesq approximation is applied to simulate buoyancy force and natural convection. Time step is set to 0.03, and an iterative time-advancement scheme is used for solving all equations in a segregated mode until convergence criteria for all variables, which is 10^{-6} in this study, are met. Figure 7-2 shows the grids and computational domain, where a grid size of 50×465 is implemented. To validate the numerical model, calculated liquid fraction variation over time is compared with the results of Sciacovelli et al. (Sciacovelli et al., 2013) as shown in **Fig. 7-3**. Additional validation is conducted by comparing average temperature and local temperature at a particular location (radius = 28 mm, height = 421 mm) simulated with the current model and experimental results in a thermal storage unit measured in a 2007 study (Akgün, Aydin, & Kaygusuz, 2007). The details of these comparisons are shown in **Fig. 7-4**. The average deviations of the current model from the reference studies ((Sciacovelli et al., 2013) and (Akgün et al., 2007)) are 7.8 % and 1.8 % respectively, indicating good validations of this model against both numerical and experimental data in previous studies.

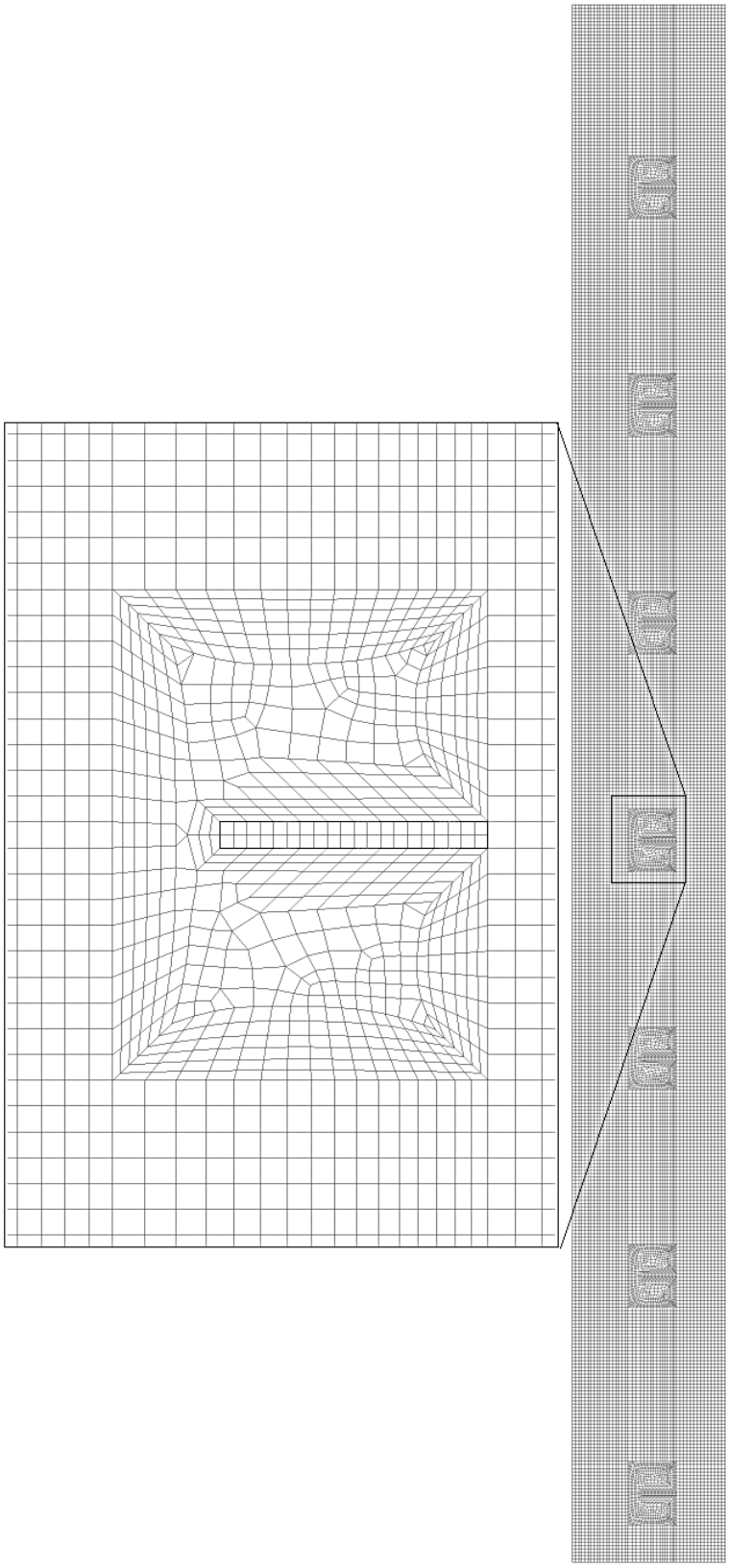

Fig. 7-2 Mesh and computational domain of the thermal storage unit.

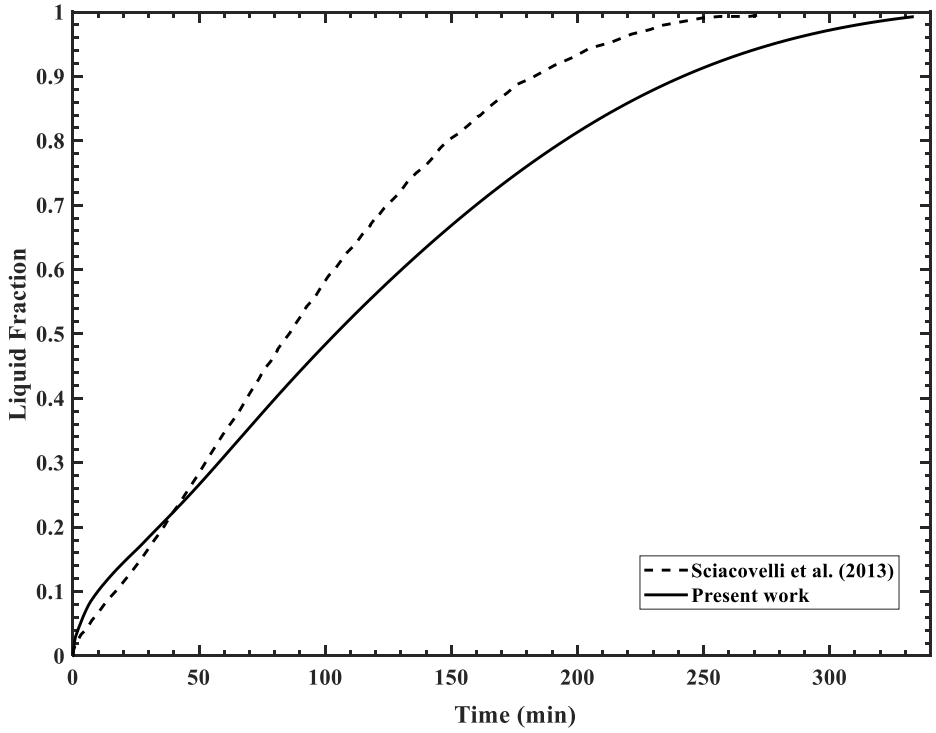

Fig. 7-3 Comparison between the liquid fraction of the present study and Sciacovelli et al. numerical study (Sciacovelli et al., 2013).

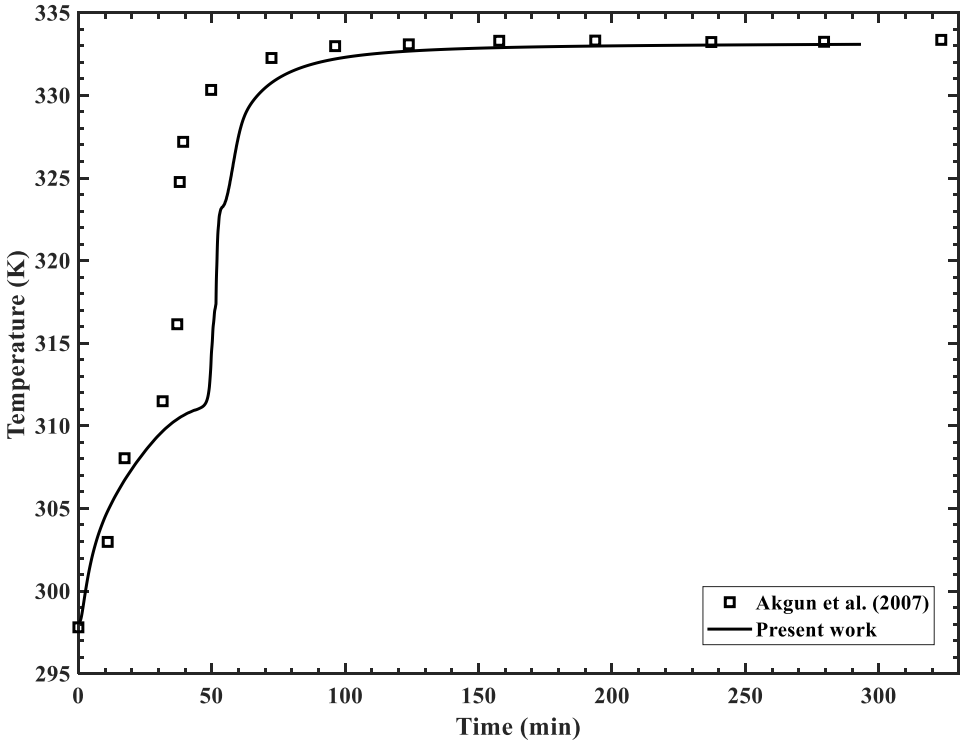

(a)

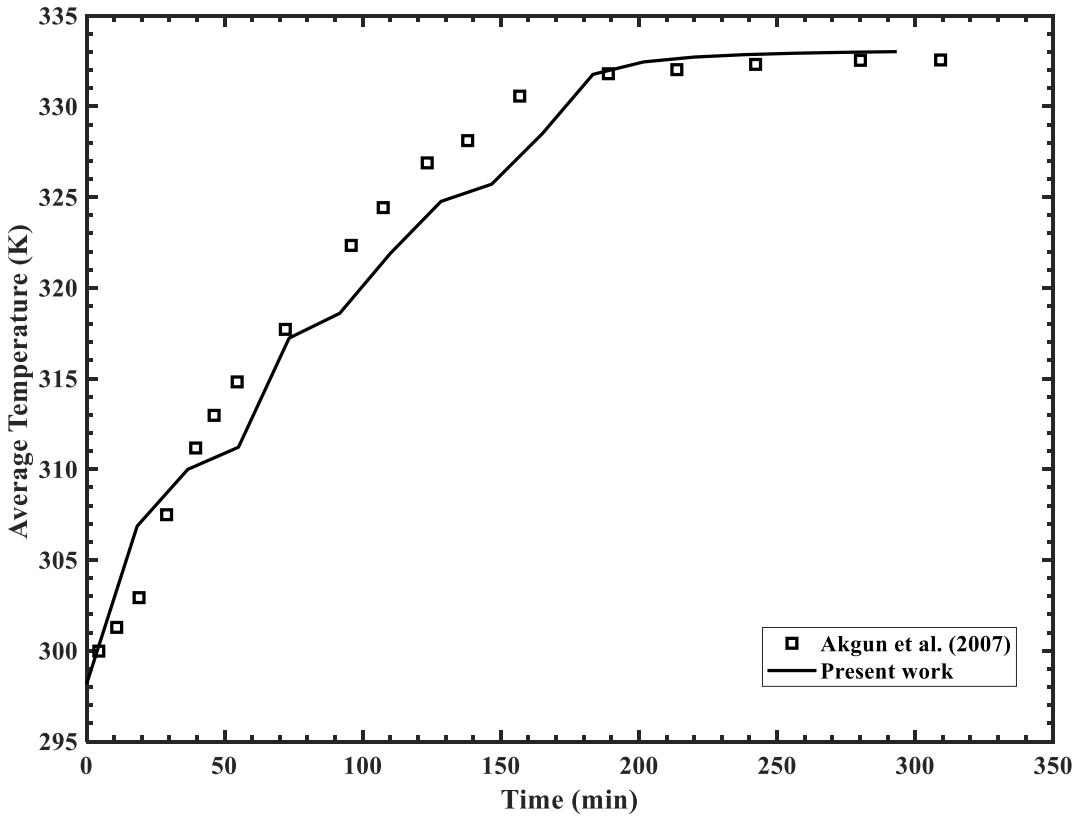

(b)

Fig. 7-4 Comparison between the present model and experimental study (Akgün et al., 2007): (a) local temperature at a point ($r = 28mm$, $z = 421mm$), and (b) average temperature.

7.3 Statistical approach

Three independent parameters, i.e., nanoparticle concentration (ϕ_{NePCM}), fins' angle (α_o) and pitch (p), are selected in order to study their effects on the heat transfer and charging time of the thermal storage unit. Each parameter has three levels, namely, low, medium and high level. The level of each parameter intentionally changes by means of RSM, making 15 different cases shown in **Table 7-1**. The range of each parameter has been discussed in section 7.1.1. A center-point (medium level) of each parameter is added to detect possible nonlinearity of the model. The variations of the charging time of the thermal storage unit are analyzed with RSM method under two different liquid fraction (LF) values. The RSM method is able to cover the nonlinear behaviour

of each parameter and develop a second-order regression model. The CCF design (Montgomery, 2012) is used to predict the nonlinearity of the model. In this method, two parameters intentionally change to their medium level and the response (i.e., charging time) is obtained and analyzed.

ANOVA test is used to determine the adequacy of the model. Multiple regression analysis is developed as the predictor equation, which illustrates the role of each parameter and probable interactions between multiple parameters.

In the first step, a response equation is developed to represent the relationship between each parameter and the charging (melting) time:

$$t_{melting} = f(\phi_{NePCM}, \alpha_o, p) \tag{7-1}$$

where ϕ_{NePCM} is NePCM volume fraction, and α and p represent fin angle and pitch respectively. A nonlinear regression model is approximated using Eq. 3-44 to cover the possible nonlinearty of the results.

7.4 Results and discussions

7.4.1 Simulation cases

Figure 7-5 shows different sections of the simulation domain with different fluids of various densities. Air occupies a top portion of the shell due to its lower density while PCM/NePCM occupies the bottom portion of the shell. HTF (water) enters the storage unit through the tube and moves upward.

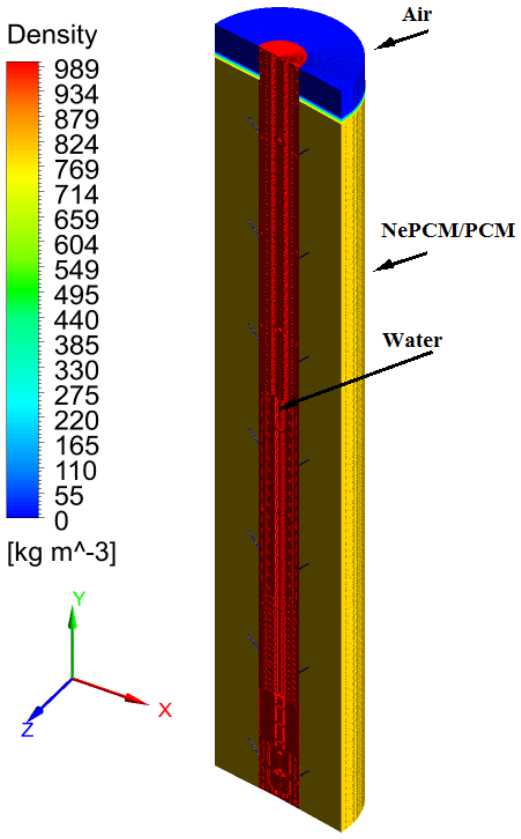

Fig. 7-5 Simulation model/domain and fluids densities.

The charging time of the NePCM is evaluated for different cases shown in **Table 7-1**, which was based on the CCF experiment design. The results in chapter 6 confirmed that the melting process is dominated by pure heat conduction at the early stage of melting, followed by mixed conduction and convection, and eventually heat convection becomes the main mechanism of heat transfer in the later stage of melting. A preliminary study on different cases revealed that the parameters under study have no effect on the charging time until 25 % of the PCM/NePCM is melted (LF = 0.25), and natural convection is mostly dominant in all cases under study when 70% of the PCM/NePCM is melted (LF = 0.7). The effects of the parameters become less pronounced afterwards (these results will be shown later). These two representative LF values (0.25 and 0.7) are selected for further investigations.

Table 7-1 Charging time of the thermal storage unit at two liquid fraction values for different cases.

Case	ϕ_{NePCM} (*vol*.%)	α_o (degree)	p (mm)	Charging time at LF= 0.25 (sec.)	Charging time at LF= 0.70 (sec.)
1	4	0	55	228	1176.6
2	0	45	45	218.4	1156.8
3	0	-45	45	273.6	1565.4
4	2	0	45	235.8	1215.6
5	0	45	65	183	1128.6
6	2	0	65	227.4	1153.8
7	0	-45	65	273.6	1675.2
8	2	45	55	213.6	1125
9	2	-45	55	241.2	1879.8
10	4	-45	65	269.4	1926
11	2	0	55	212.4	1156.2
12	4	45	65	210.6	1206
13	0	0	55	237	1175.4
14	4	-45	45	270.6	1912.8
15	4	45	45	216	1220.4

7.4.2 Effects of fin parameters on melting of PCM

Liquid fraction contour of pristine PCM at different time steps of cases 2 ($\alpha_o = 45^o$) and 3 ($\alpha_o = -45^o$) where p = 45 mm and cases 5 ($\alpha_o = 45^o$) and 7 ($\alpha_o = -45^o$) where p = 65 mm are shown in **Fig. 7-6** to demonstrate the effects of fin angle and pitch. At the early stage of melting (e.g., 90 seconds, **Fig. 7-6** (a)), there is no noticeable difference between different cases. The thickness of the melted region (around the HTF tube) varies along the entire length of the storage unit. This is due to the effects of heat conduction through the fins as well as some initial effects of convective heat transfer in the melted region around the fins. At charging time of 180 seconds (**Fig. 7-6** (b)),

small liquefied regions appear around the fins for cases 2 (p = 45 mm) and 5 (p = 65 mm) where $\alpha_o = 45^o$ and below the fins for cases 3 (p = 45 mm) and 7 (p = 65) where the fins' angle is -45^o. At this time, the buoyancy force starts to show its effects on the melting process. Also, a fairly uniform melted region is seen for cases 5 ($\alpha_o = 45^o$) and 7 ($\alpha_o = -45^o$) where p = 65 mm whereas the melting interface remains almost unchanged in the upper un-finned section for cases 2 ($\alpha_o = 45^o$) and 3 ($\alpha_o = -45^o$) where p = 45 mm, as the fins are concentrated in the bottom section of the thermal storage unit. Then, this behaviour continues with time elapsing. After 450 seconds (**Fig. 7-6** (c)), the melting rate in the un-finned section of cases 2 ($\alpha_o = 45^o$) and 3 ($\alpha_o = -45^o$) accelerates. Also larger liquefied PCM regions appear around the fins for cases 2 ($\alpha_o = 45^o$, p = 45 mm) and 5 ($\alpha_o = 45^o$, p = 65 mm) than cases 3 ($\alpha_o = -45^o$, p = 45 mm) and 7 ($\alpha_o = -45^o$, p = 65 mm), indicating higher rate of melting with fin angle of 45^o than that of -45^o. Hot-spots and changes in the vorticities created by the fins can be the reasons of different melting rates with different fin angles. This will be discussed with more details in the following sections. After 1080 seconds of melting, two observations can be made: (1) melting rate in the un-finned section is highly accelerated due to natural convection in the melted PCM (since warmer PCM moves upward); and (2) the fin angle of 45^o seems to accelerate the melting rate more than the other angles. At this last stage, liquid fraction results in **Fig. 7-6** (d) show that for all cases more PCM is melted on the upper portion of the storage unit than the lower portion. To quantify this, melting at 2500 seconds is analyzed. The PCM part of the thermal storage unit is split in half and the liquid fraction of the bottom half is compared with that of the full PCM portion, as shown in **Table 7-2**. It is clear that in all cases liquid fraction in the bottom portion is lower than that of the full storage unit. This trend is also obvious with temperature distributions shown in **Fig. 7-7**.

Table 7-2 Liquid fraction at the bottom half and full storage after 2500 sec.

Case	LF (Bottom part)	LF (Full storage)
Case 2 ($\alpha_o = 45^o$, $p = 45\ mm$, $\phi_{NePCM} = 0\ vol.\%$)	0.908	0.949
Case 3 ($\alpha_o = -45^o$, $p = 45\ mm$, $\phi_{NePCM} = 0\ vol.\%$)	0.689	0.833
Case 5 ($\alpha_o = 45^o$, $p = 65\ mm$, $\phi_{NePCM} = 0\ vol.\%$)	0.895	0.947
Case 7 ($\alpha_o = -45^o$, $p = 65\ mm$, $\phi_{NePCM} = 0\ vol.\%$)	0.627	0.811

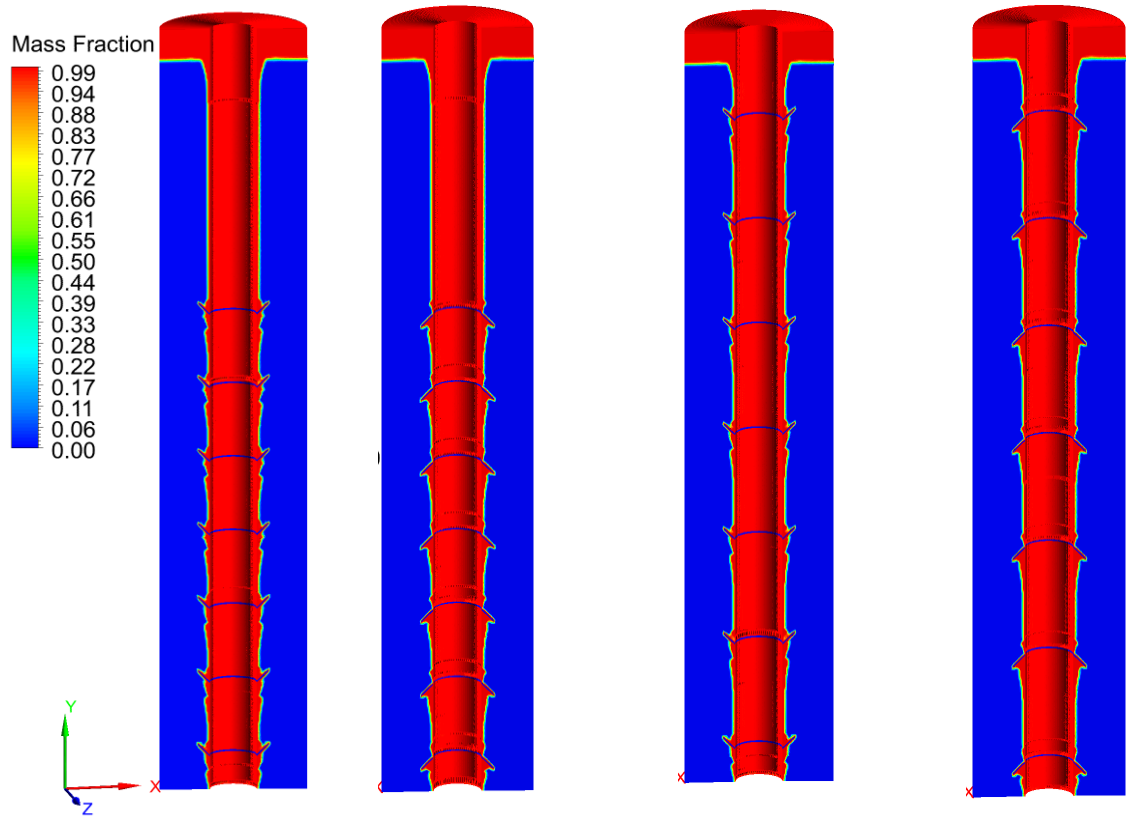

Case II Case III Case V Case VII

(a) Melting after 90 Seconds

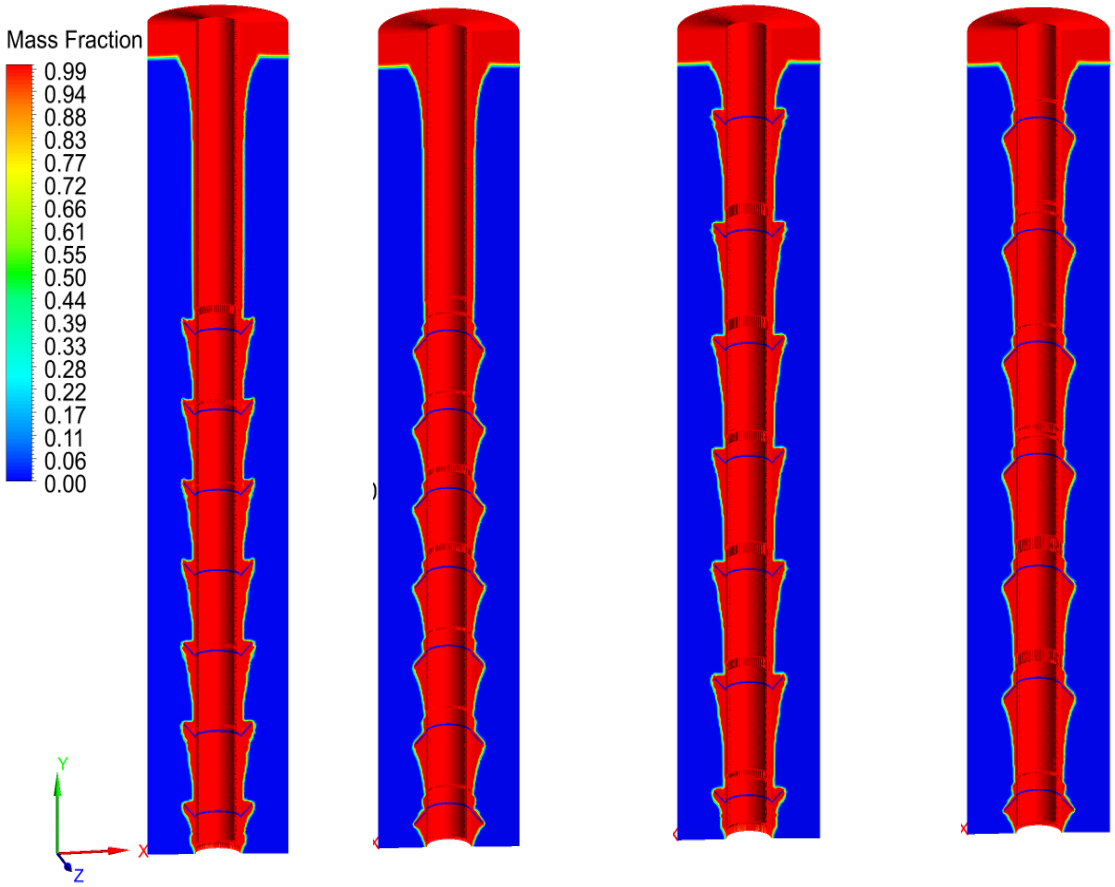

Case II Case III Case V Case VII

(b) Melting after 180 Seconds

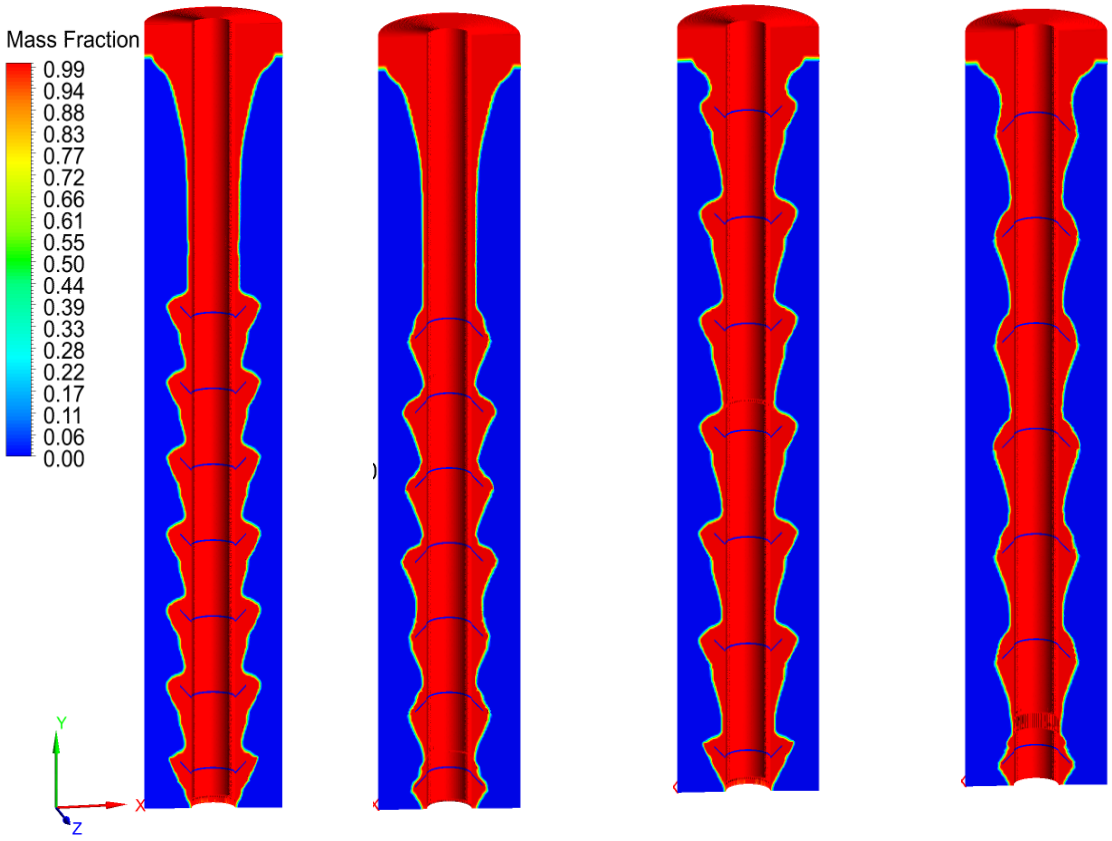

Case II Case III Case V Case VII

(c) Melting after 450 Seconds

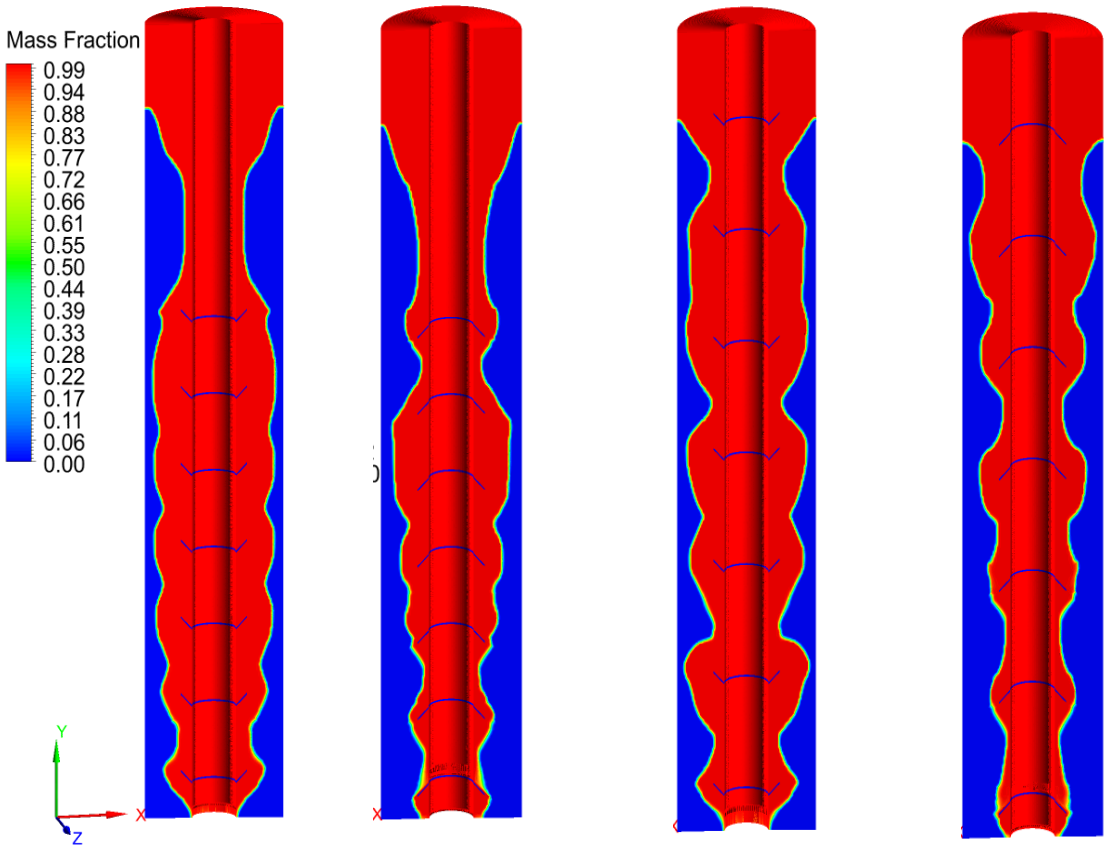

Case II Case III Case V Case VII

(d) Melting after 1080 Seconds

Fig. 7-6 Liquid fraction contours for different cases at different times during melting.

To investigate the effects of fin angle, temperature distributions of cases 5 (α_o = 45°, p = 65 mm) and 7 (α_o = -45°, p = 65 mm) at different time steps are analyzed and shown in **Fig. 7-7**. After 90 seconds of heating, a small temperature gradient can be found in PCM close to the HTF tube for both cases. This gradient becomes larger in the upper section of the shell where air exists. At 450 seconds of heating, the temperature distribution shows a skewed triangle shape when the fin angle is 45° and an equilateral triangle shape when the fin angle is -45°. More interestingly, a hot region is formed at the inner corner below the -45° fins since the liquefied PCM is stuck there. With 45° fins, the temperature distribution is more uniform with no hot region near the fins. The

hot regions near the -45^o fins remain over the whole charging time. These hot regions can slow down the total heat transfer rate. Better temperature distribution in case 5 (α_o = 45^o) is more obvious after 1080 seconds of heating than that in case 7 (α_o = - 45^o). From these results, it seems that a positive fin angle is desirable for LHTES. In addition, the temperature distributions in both cases are similar in the upper section of the storage unit after 2500 seconds since all PCM is fully melted in these sections. However, there is still a small portion of the un-melted PCM at the bottom of the tank. As discussed earlier, natural convection effects lead to fast melting in the upper portions. This provides an idea of designing longer fins at the bottom to achieve more uniform and fast melting. Future studies will address this along with optimization design of the heat exchanger.

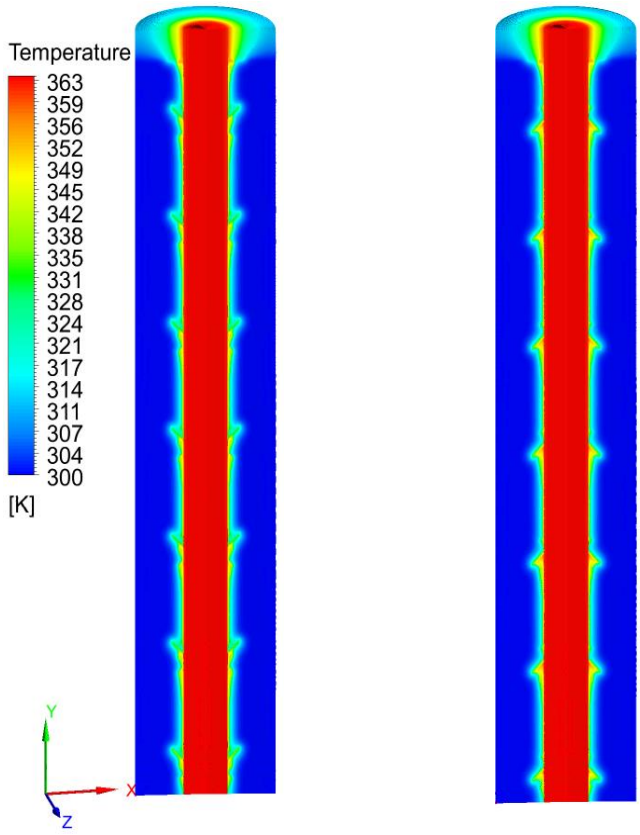

Case V Case VII

(a) Melting after 90 Seconds

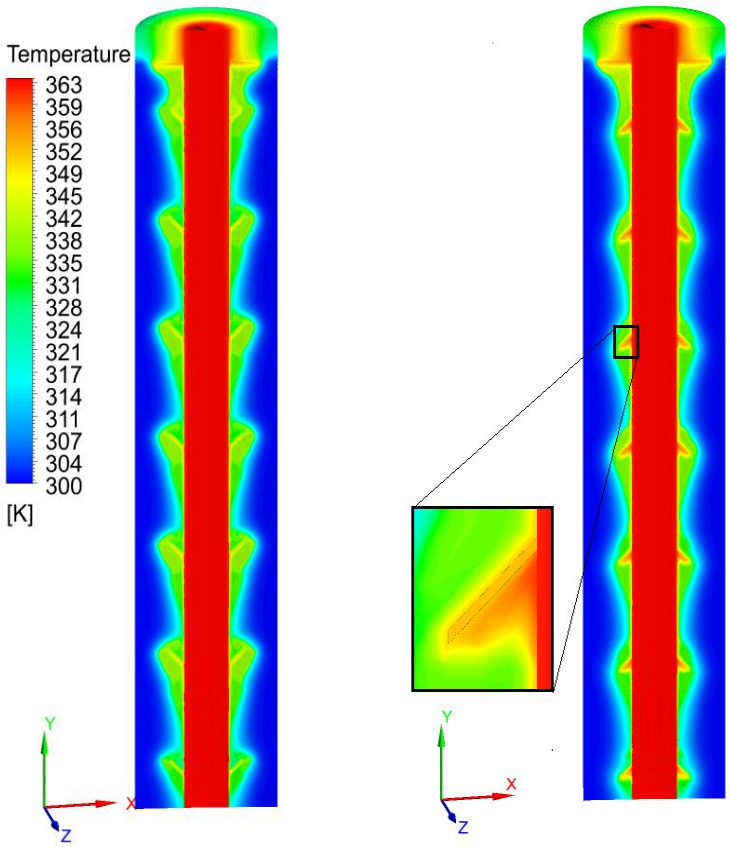

Case V Case VII

(b) Melting after 450 Seconds

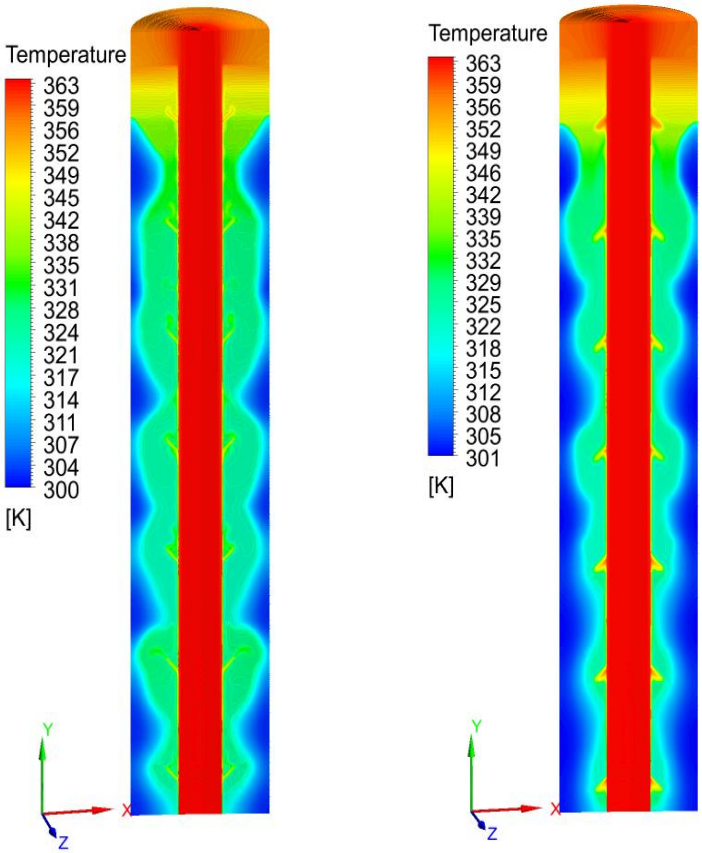

Case V Case VII

(c) Melting after 1080 Seconds

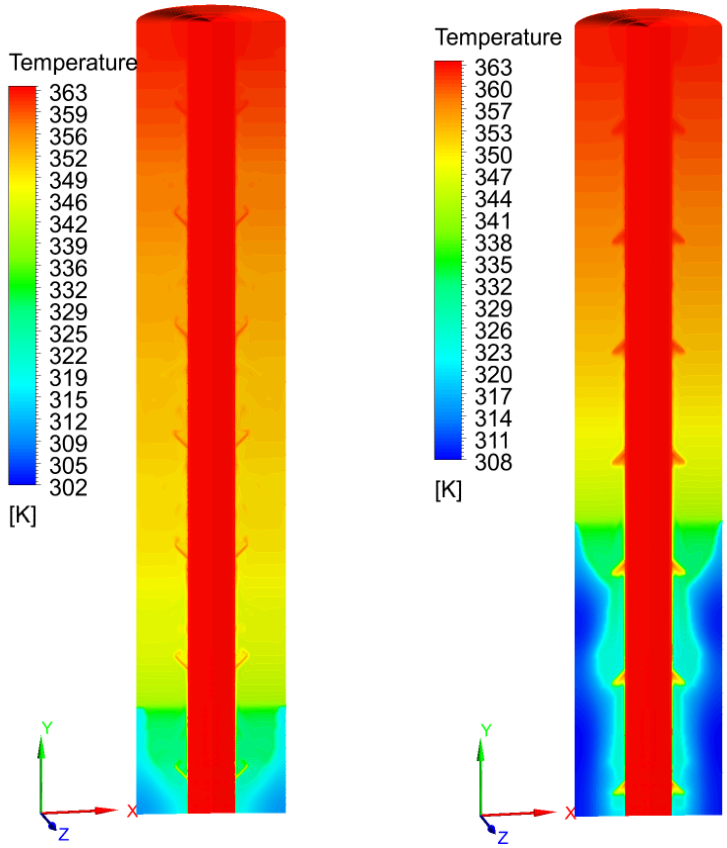

Case V Case VII

(d) Melting after 2500 Seconds

Fig. 7-7 Temperature contour for different cases over different time steps.

Figure 7-8 shows streamlines of the liquefied PCM between the sixth and seventh fins (from bottom of tank) in cases 2 (α_o = 45°, p = 45 mm), 3 (α_o = -45°, p = 45 mm), 5 (α_o = 45°, p = 65 mm), and 7 (α_o = -45°, p = 65 mm), at different time steps. These results demonstrate the effects of the fin angle and pitch on the fluid streamlines, which could help explain the differences in melting and charging time. It can be seen that after 90 seconds of heating, the buoyancy force starts to affect the melting process. Local vorticities develop below and above the fins when the fin angle is 45°, but just small vorticity is formed below the -45° fins. These local vorticities intensify after 180 seconds in all of the cases, but their magnitudes are larger when the fin angle is 45° and the

strongest one is seen in case 5 with a larger pitch of the fins. After 450 seconds, when natural convection becomes the main mechanism of PCM melting, case 2 (α_o = 45^o, p = 45 mm) is the only case with two large and strong vorticities below the fins and a smaller one on the back of the fin. The local vorticities for the cases with -45^o fins are much weaker, with smaller vorticities formed at the back of the fins. After 1080 seconds, it is clearer that the liquefied PCM is confined in a region below the fins forming a quite large vorticity in the cases of -45^o fins. At this stage, the fins behave like foils directing/disturbing the liquefied PCM flow. The results show that design in case 5 (α_o = 45^o, p = 65 mm) might be able to expedite the charging time more than the other cases due to the large number and magnitude of local vorticities formed by the fins which lead to prevention of hot-spot, better temperature distribution, and eventually stronger natural convection.

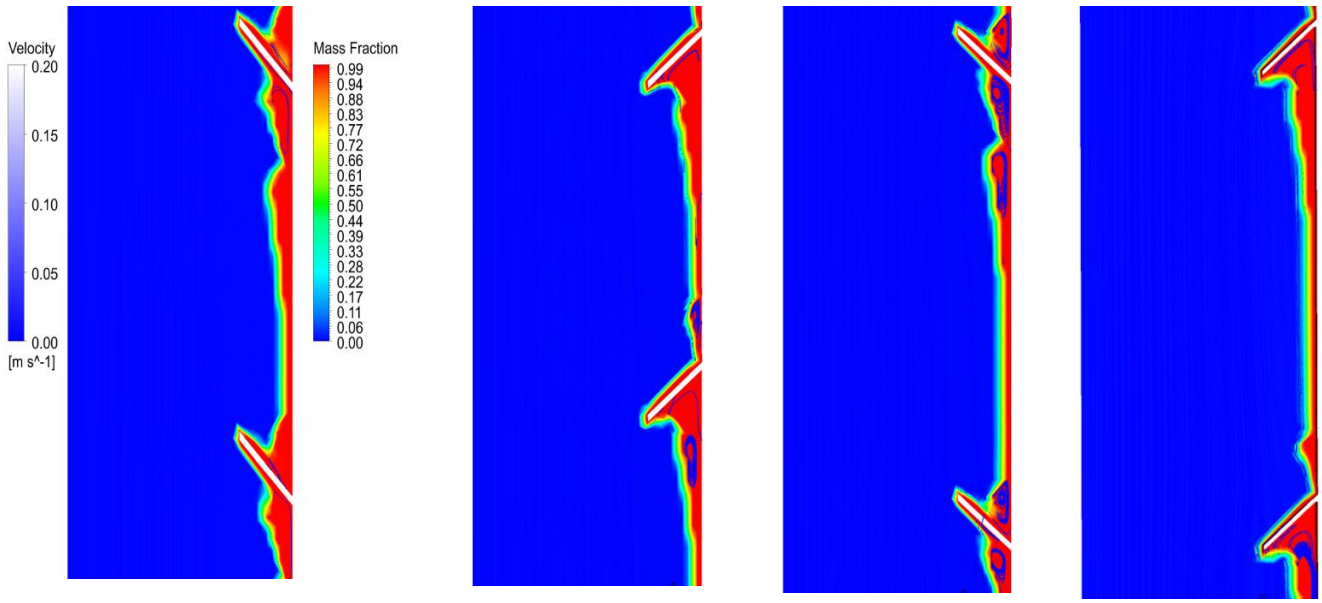

Case II Case III Case V Case VII

(a) After 90 Sec.

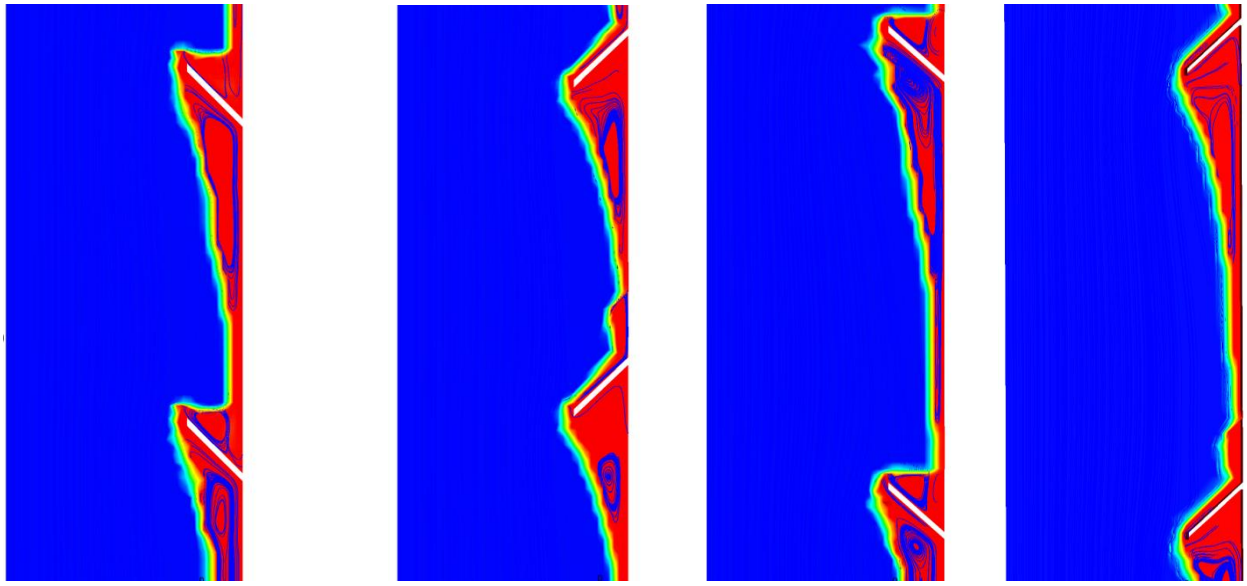

Case II Case III Case V Case VII

(b) After 180 Sec.

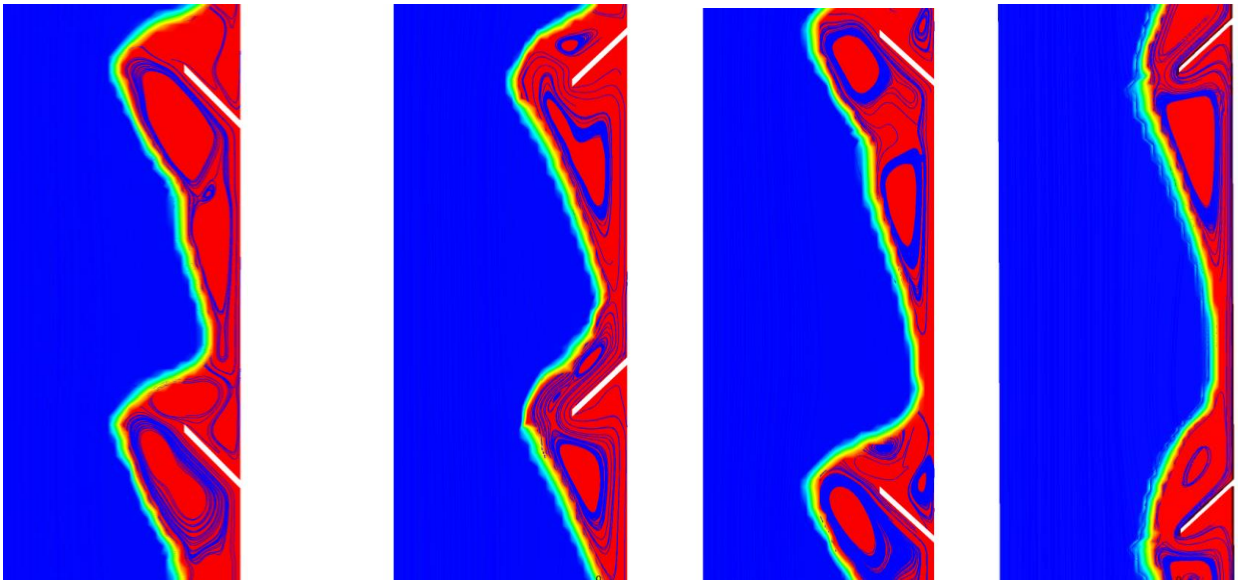

Case II Case III Case V Case VII

(c) After 450 Sec.

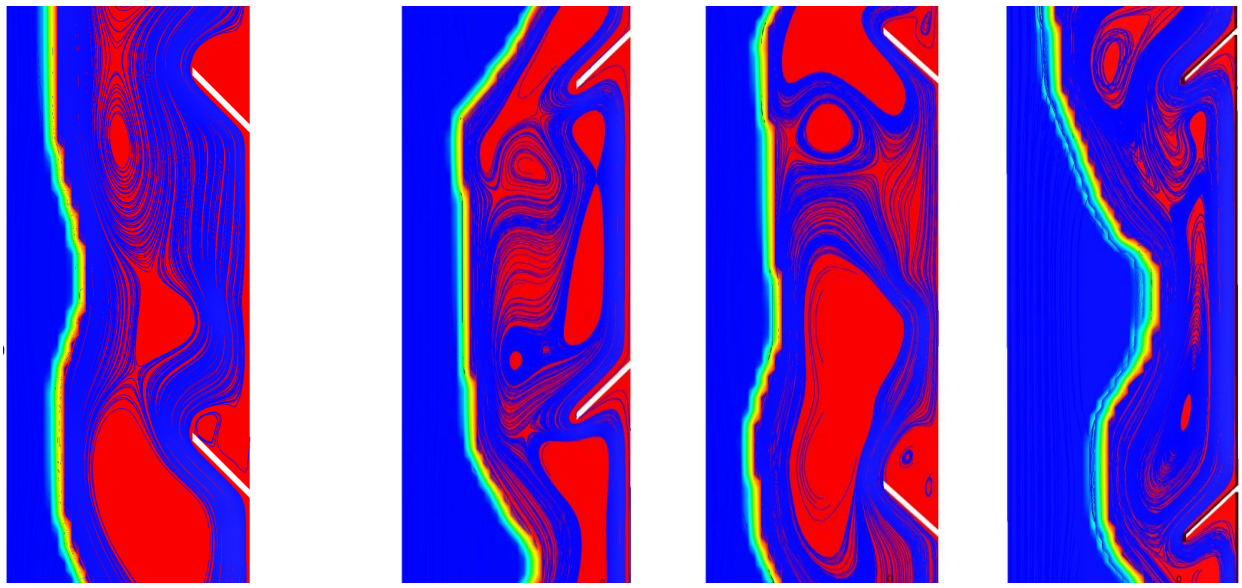

Case II Case III Case V Case VII

(d) After 1080 Sec.

Fig. 7-8 Streamlines of Case 2 **(**$\alpha_o = 45^o$, $p = 45\ mm$, $\phi_{NePCM} = 0\ vol.\%$**),** Case 3 **(**$\alpha_o = -45^o$, $p = 45\ mm$, $\phi_{NePCM} = 0\ vol.\%$), Case 5 ($\alpha_o = 45^o$, $p = 65\ mm$, $\phi_{NePCM} = 0\ vol.\%$) and Case 7 ($\alpha_o = -45^o$, $p = 65\ mm$, $\phi_{NePCM} = 0\ vol.\%$) at different times, namely.

7.4.3 Effects of fin parameters and nanoparticle concentration on melting of NePCM

Liquid fraction variations over time for different cases are shown in **Fig. 7-9**. As discussed earlier, no considerable difference can be found between different cases until LF=0.25. At LF = 0.25 and after, depending on the fin angle, effects of natural convection differentiate the charging time in different cases. Natural convection is mainly attributed to fin angle but not the pitch since there is no noticeable variation between cases of different pitches. Melting rates in cases with 45^o fin angle are considerably lower than those with -45^o fins, particularly after 1500 seconds of heating. Nanoparticles clearly show an adverse effect on total heat transfer and the charging rate. The results show that the charging time increases when nanoparticles are added. This agrees with

previous studies and demonstrates that thermal conductivity enhancement with nanoparticles in the PCM is not able to compensate for the natural convection reduction.

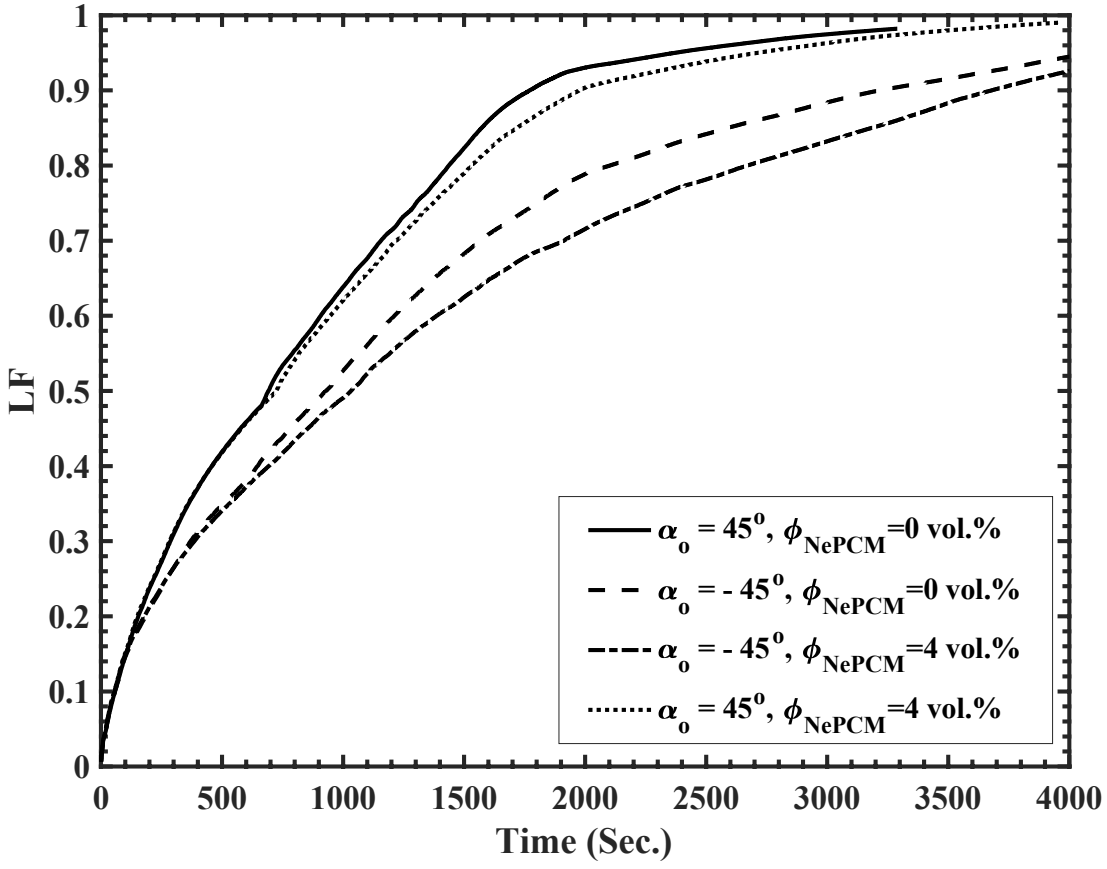

(a)

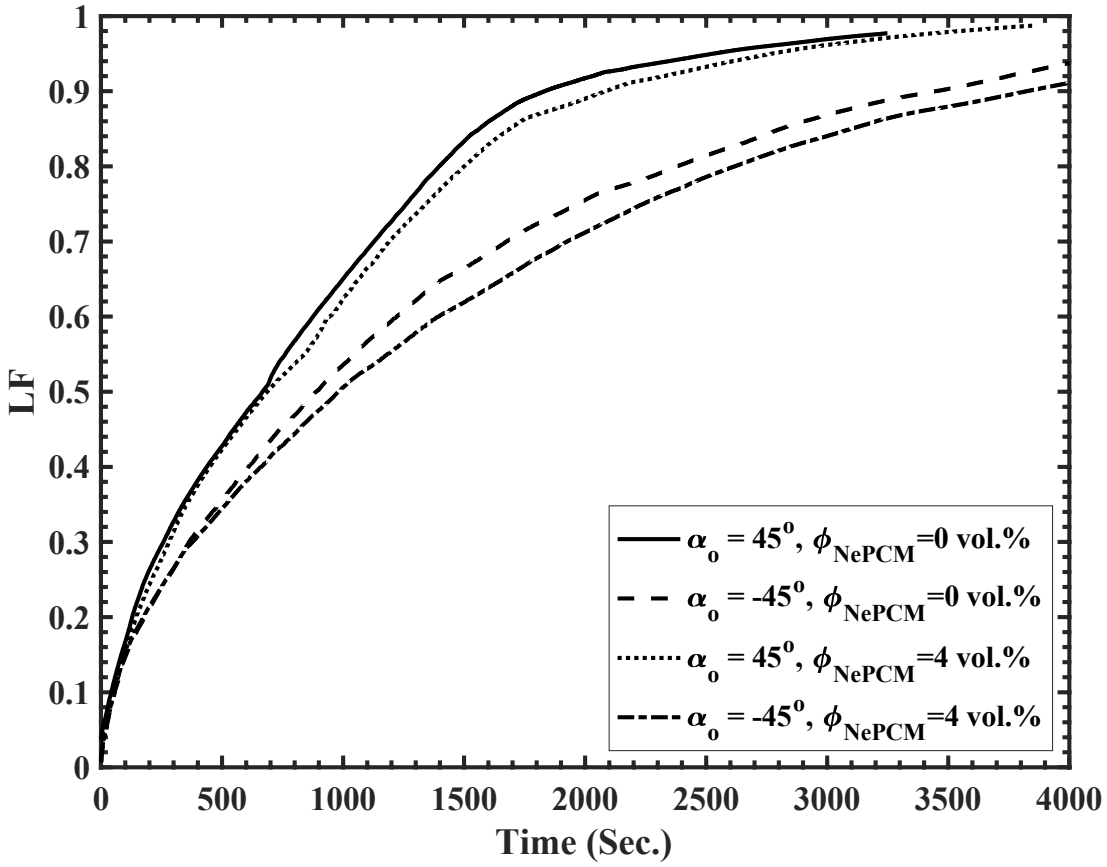

(b)

Fig. 7-9 Liquid fraction over the time (a) p=45mm (b) p=65 mm.

To the investigate heat transfer rate, we examined the instantaneous heat flux at different time instants, as depicted in **Fig. 7-10**. After a considerable reduction of heat flux at the early stage of melting in all of the cases, heat flux reduces even more for cases with fins angle of -45°. Also, the heat flux reduces further when nanoparticles are added. During the melting process, there is a period of time when heat flux increases and reaches its second maximum before decrease again. When heat flux is high (in the period of 700~1600 seconds), natural convection and total heat transfer rate reach to their maximum values. The total heat transfer rate is lower for α_o = -45° and/or $\phi_{NePCM} = 4\ vol.\%$. In this period of time, the local vorticities merge (See **Fig. 7-8**) and the

fins disturb/redirect the liquefied NePCM flow. Eventually, heat flux decreases towards a minimum when the NePCM temperature approaches the HTF temperature at the end of the charging time in all of the cases. Comparing the results in **Fig. 7-10** (a) and (b), one can find that the fin pitch does not show significant effects on melting of the NePCM.

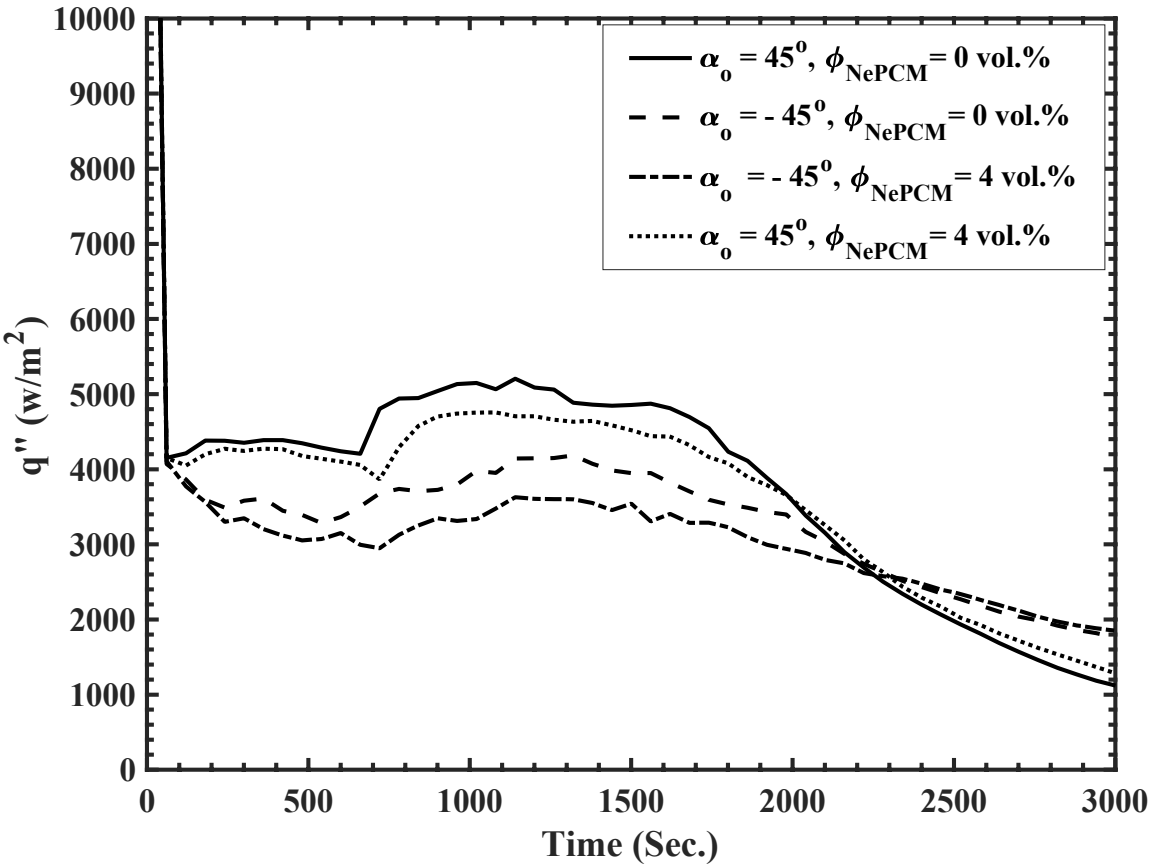

(a)

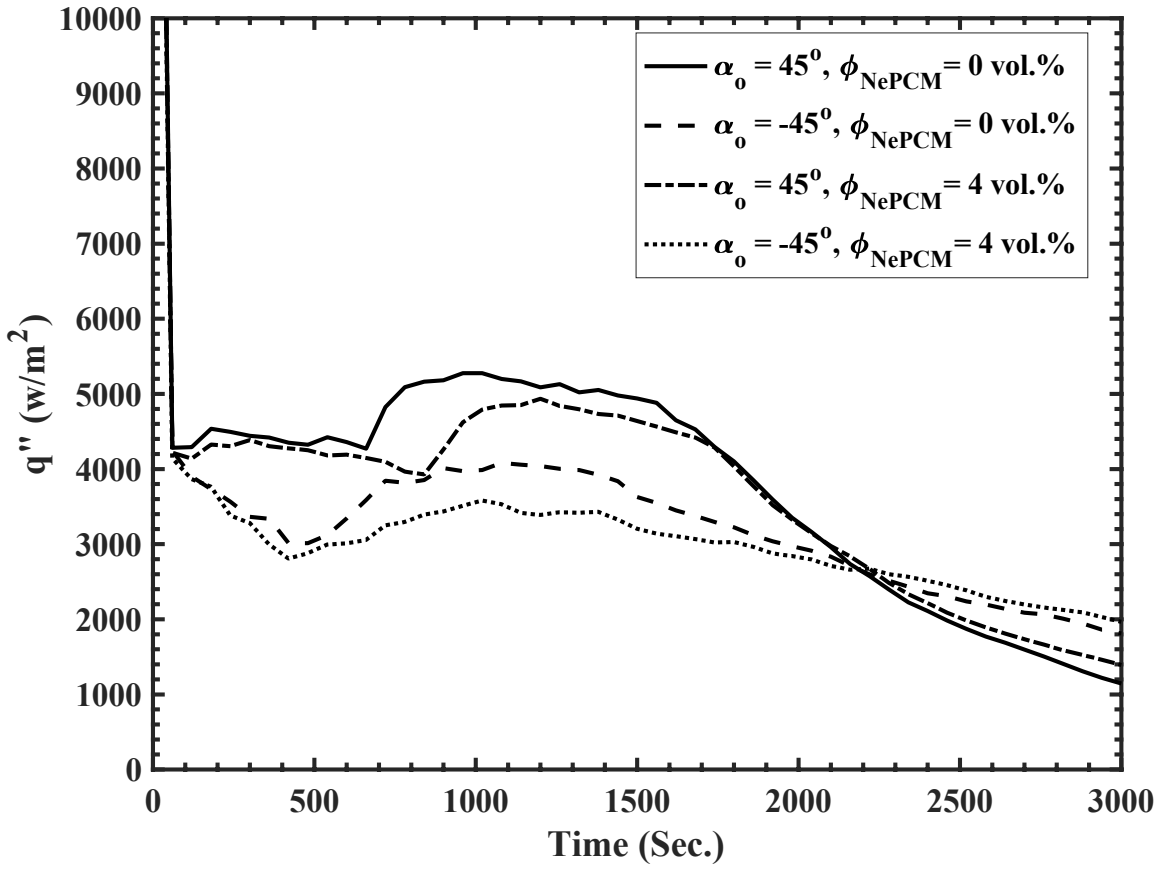

(b)

Fig. 7-10 Heat flux over time, (a) p=45mm (b) p=65 mm.

7.4.4 Statistical analysis with RSM

Significant parameters are identified with probable interactions between them in affecting the charging time using data listed in **Table 7-1**. Multiple regression analysis (Montgomery, 2012) is used to develop a regression model. The CCF design is employed with $\alpha_{statistical}$-value (significance level) (Montgomery, 2012) set to 0.1, i.e., probability of 10 % for selection of insignificant parameters. In this work, the null hypothesis is that none of the selected parameters are significant on the liquid fraction variation rate. Subsequently, the alternate hypothesis requires that at least one parameter is significant. In this step, the null hypothesis is rejected in favour of

the alternate hypothesis. In order to determine whether a parameter is significant, its p-value (calculated probability) is compared with the $\alpha_{statistical}$-value. If the p-value of a parameter is smaller than the selected $\alpha_{statistical}$-value, that parameter is statistically significant.

Since the melting process starts with heat conduction shown in the previous chapter, nanoparticle concentration affects the thermal conductivity of the mixture more in the early stage than in the later periods of time. It was found from previous sections that heat conduction might not be dominant even at the early stage of melting, and adding nanoparticles might even have an adverse effect on the total heat transfer rate. It would be interesting to know the effects of different parameters (nanoparticle concentration ϕ_{NePCM}, fin angle α and pitch p) on the NePCM melting process. This is done by examining these parameters with the RSM analysis (detailed above) on the two typical melting stages, i.e., at the early stage of melting (LF = 0.25) where heat conduction might be dominant, and near the end of the melting (LF = 0.7) where natural convection is dominant. The ANOVA results in **Table 7-3** and **Table 7-4** give the level of significance of these parameters.

Table 7-3 ANOVA table (LF=25%).

Source	F-Value	P-value
Model	48.51	<0.0001
Angle (α_o)	48.51	<0.0001

When LF = 0.25 (**Table 7-3**), p-value of the fin angle is much less than the $\alpha_{statistical}$-value 0.1, and all of the insignificant parameters (nanoparticle concentration ϕ_{NePCM}, fin pitch p) are rejected. Thus, the only significant parameter is fin angle α_o. This result indicates that ϕ_{NePCM} is not a significant parameter at the early stage of NePCM melting. This is a new finding different than earlier reports that heat conduction is dominant in finless LHTES shown in chapter 6 at the

early stage of melting. One possible reason is that once melting starts, the fins disturb the liquefied NePCM flow. Local vorticities and natural convection start to play a role in heat transfer along with heat conduction (mixed conduction and convection regime).

At LF = 0.7, similar ANOVA (**Table 7-4**) show that both nanoparticle concentration ϕ_{NePCM} and fin angle α_o become significant parameters in the late stage of melting. Interestingly an interaction between ϕ_{NePCM} and the fin angle (α_o) is also detected, which will be discussed later.

Table 7-4 ANOVA table (LF = 70 %).

Source	F-Value	P-value
Model	9.85	<0.0001
ϕ_{NePCM}	16.18	0.0024
α_o	287.79	<0.0001
$\phi_{NePCM} \times \alpha_o$	7.71	0.00995
ϕ_{NePCM}^2	87.71	<0.0001

After making sure that the ANOVA assumptions are met, R^2 of the model is 0.9756 in the current model indicating that ϕ_{NePCM} and α are responsible for 97.56 % of the model variation. The Adjusted R^2 is 0.9658, which means no insignificant or unnecessary term was selected in the model. The Predicted R^2 is 0.9458, showing high adequacy of the model for prediction. The regression model from this RSM analysis is shown as follow:

$$t_{charging} = 1107 + 37.02\phi_{NePCM} - 5.66867\alpha_o - 0.635\alpha \times \phi_{NePCM} + 0.14744\alpha_o^2 \qquad (7\text{-}2)$$

Here charging time is in "seconds", and the fin angle is in degrees to predict the time needed to melt 70% of the NePCM. Fin angle has a nonlinear parabolic impact on the charging time. It is

found to be the most significant parameter as indicated by the larger coefficient in the predictive model and larger F-value in **Table 7-4**.

In order to show contributions of the significant parameters on the melting/charging time, coded range of each parameter is illustrated in **Fig. 7-11**. In the coded range, -1 represents the lowest level, which is 0 vol.% for nanoparticle concentration and -45^o for the fin angle, and 1 represents the highest level which is 4 vol.% for nanoparticle concentration and 45^o for the fin angle. It is found that the charging time varies dramatically when the fin angle changes. Adding nanoparticles will increase the charging time. It means that heat conduction enhancement is not able to make up the natural convection reduction due to increased viscosity and decrease of buoyancy force, leading to the reduction of total heat transfer rate.

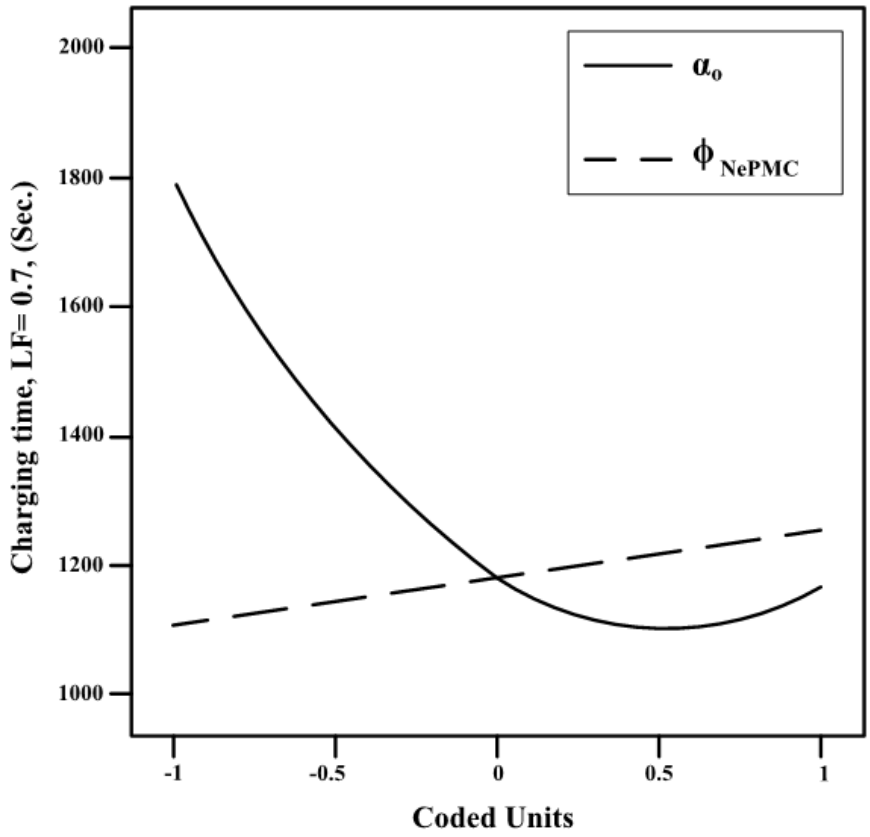

Fig. 7-11 Impact of ϕ_{NePCM} and α_o variation in a coded range on charging time.

The interaction between nanoparticle concentration ϕ_{NePCM} and fin angle α is analyzed and shown in **Fig. 7-12**. One can find that the charging time remarkably increases when ϕ_{NePCM} is increased with fin angle of -45°, while this charging time growth is less noticeable when the fin angle is 45°. This behavior could be due to the effects of nanoparticles on the local vortexes formed below and behind of the fins that the fin angle effect on them. This interactive effect is yet to be confirmed with other types of nanoparticles and PCMs, but an optimum fin angle is expected to improve the total heat transfer rate.

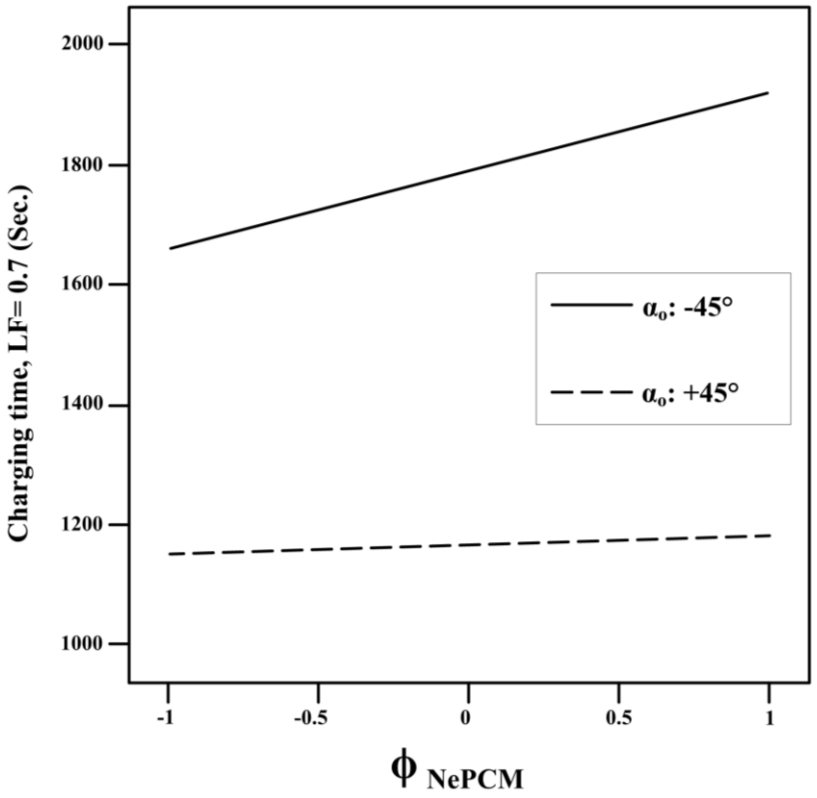

Fig. 7-12 Interaction between ϕ_{NePCM} and α_o on charging time.

A 3-D plot of the charging time is shown in **Fig. 7-13**. It is predicted that if $\phi_{NePCM} = 0$ *vol*.% and α_o in the range of 5° to 40°, one will expect shorter charging time than the other cases

analyzed. Although the figure shows an optimal fin angle of 25°, it is only true for the cases studied so far. Note that the predicted R^2 value indicates that the predicted charging time might deviate up to 6 % from the actual charging time. In the next section, a new case will be evaluated with new values of these parameters to achieve shorter charging time.

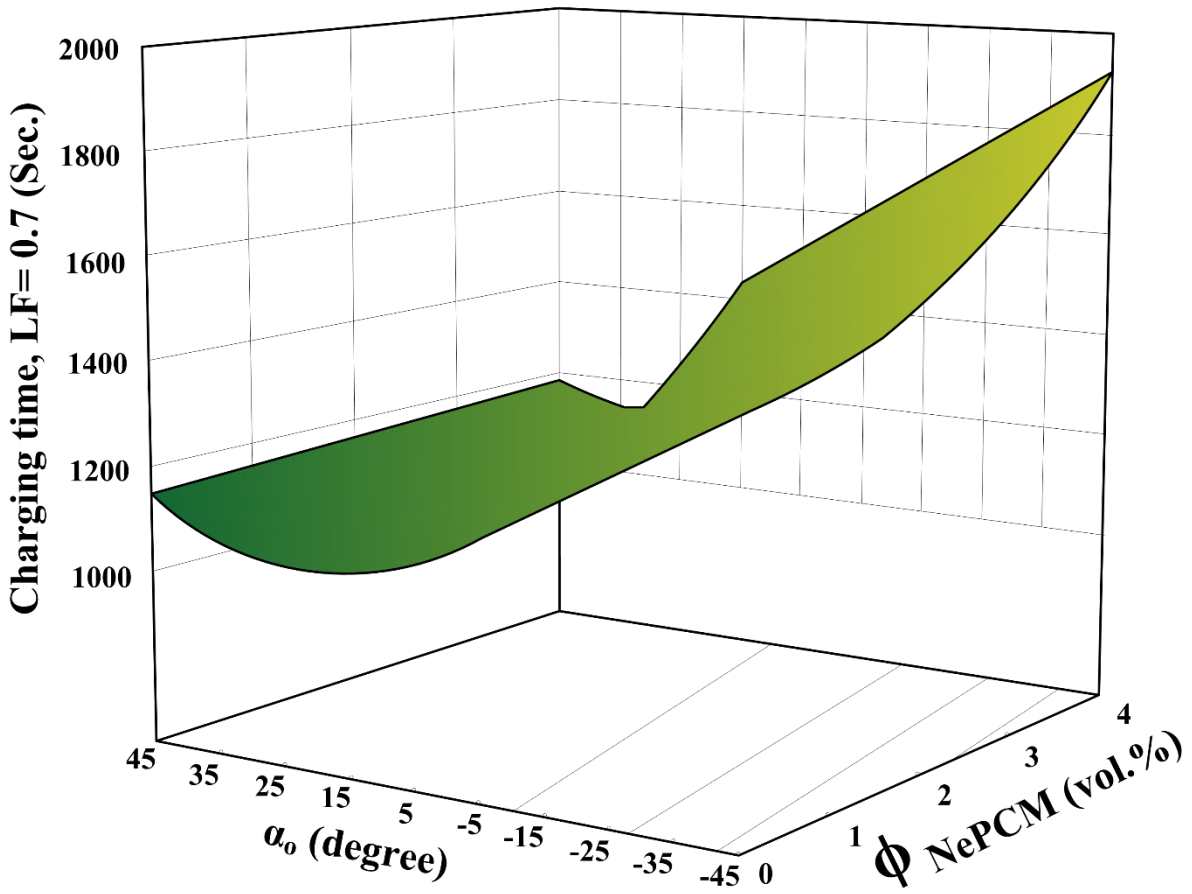

Fig. 7-13 Charging time 3-D plot.

7.4.5 Evaluation for shorter charging time

The statistical model predicts that if $\phi_{NePCM} = 0$ *vol*.% and the fin angle α_o is between 5° to 40°, the charging time would be lower than the other 15 cases listed in **Table 7-1**. To evaluate this prediction, a new case (16) is set up using the statistical data. ϕ_{NePCM} is set to be 0 *vol*.% and the

fin angle and pitch are set to be 35° and 65mm respectively. It is found that it takes 1119 seconds for 70 % of the NePCM to be melted in case 16, which is the shortest charging time for LF = 0.7 among all 16 cases. Comparison between the statistically predicted charging time (using Eq.7-2) and the numerically calculated one shows a small relative error of 2.6 %.

Figure 7-14 presents an instantaneous variation of LF when α_o = 35° and compared to different α_o and ϕ_{NePCM} combinations. It is found that except for the early stage of melting, the LF is improved over 20 % when α_o and ϕ_{NePCM} are 35° and 0 vol. % respectively compared to cases with α_o = -45°. However, this LF rate improvement is less pronounced when α_o = 45°. Figure 7-15 shows similar comparisons on an instantaneous variation of heat flux (q'') in the storage unit. The fluctuations seen in this figure is due to the sudden changes of the heat flux with α_o = 35° divided by the sudden changes of the heat flux of other cases. Overall, heat flux is improved with the favourable fin angle of α_o = 35° and $\phi_{NePCM} = 0\ vol.\%$. For each case, the variation of heat flux with time agrees with the variation of natural convection discussed earlier. Note that there is a dramatic heat flux reduction at the late stage of melting (after 2200 seconds) because most of the PCM is melted and its temperature approaches the HTF temperature. In case 16 (α_o = 35°), melting is faster than the other cases; so the temperature of the melted PCM approaches to HTF temperature faster than the other cases.

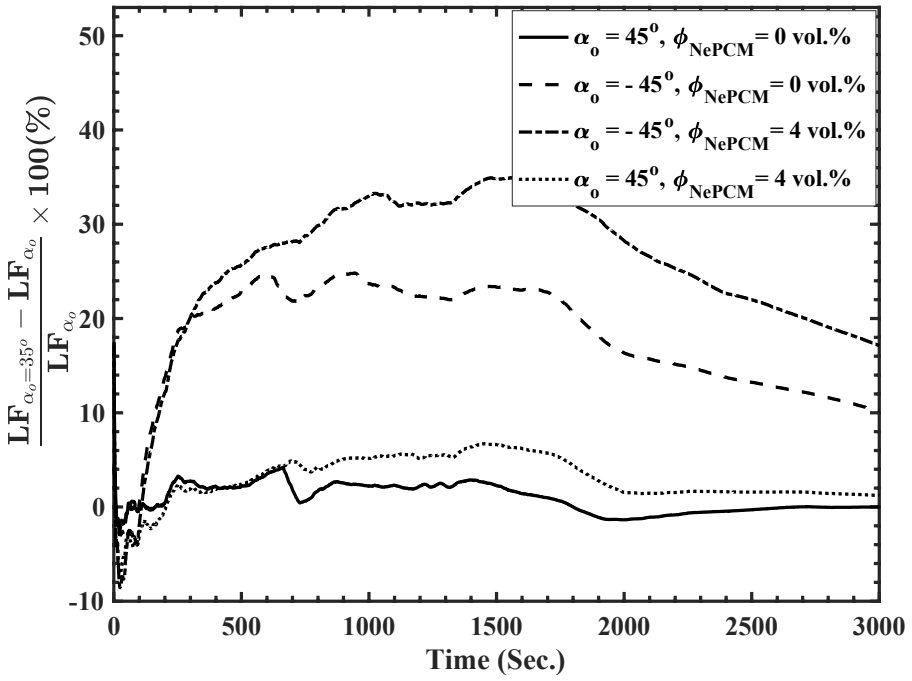

(a)

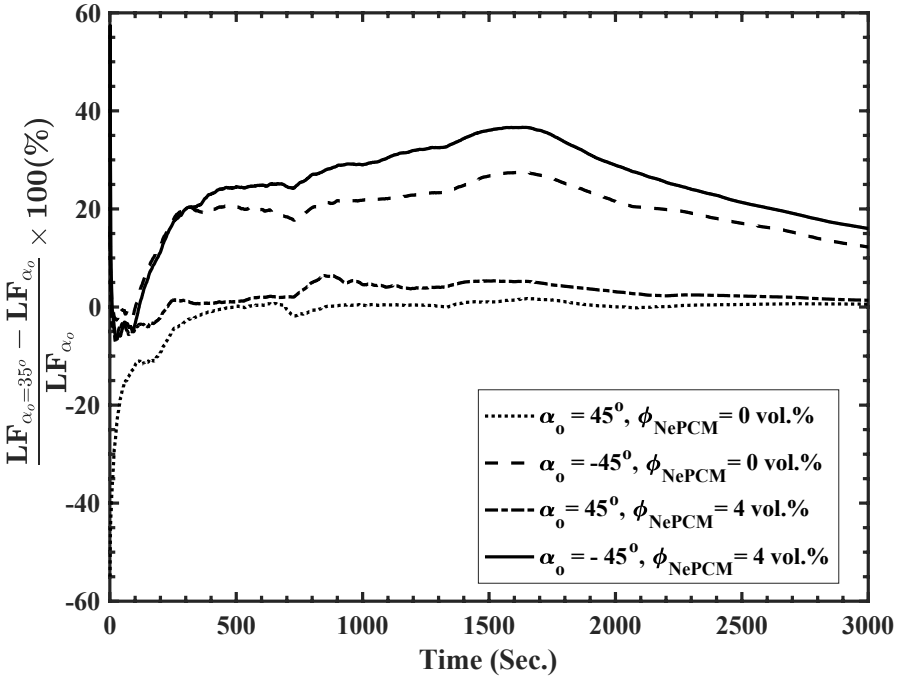

(b)

Fig. 7-14 Liquid fraction enhancement over time, (a) $p = 45\,mm$ (b) $p = 65\,mm$.

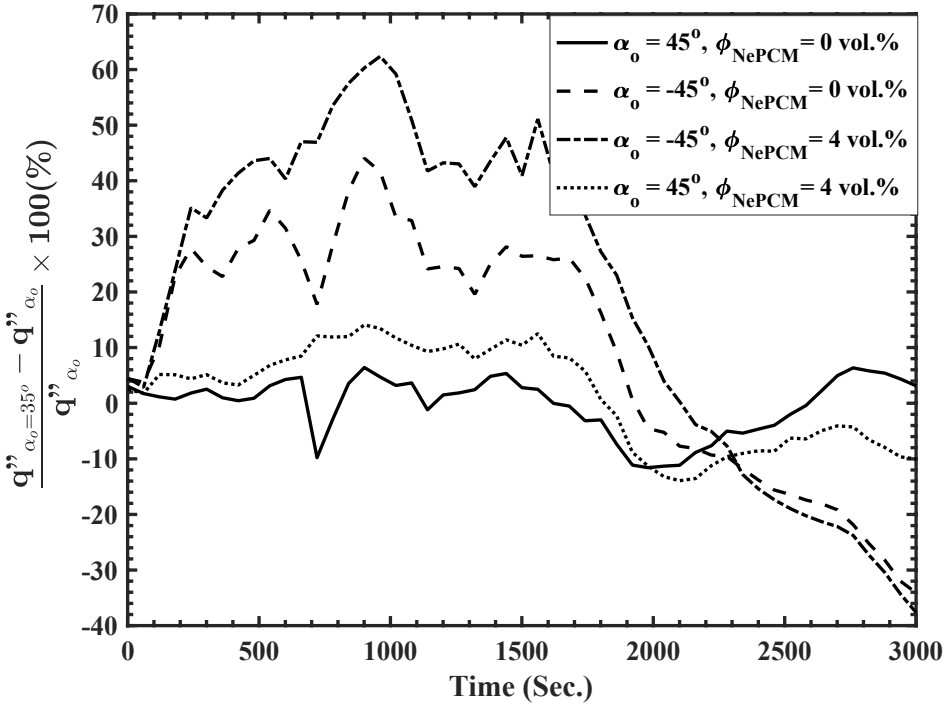

(a)

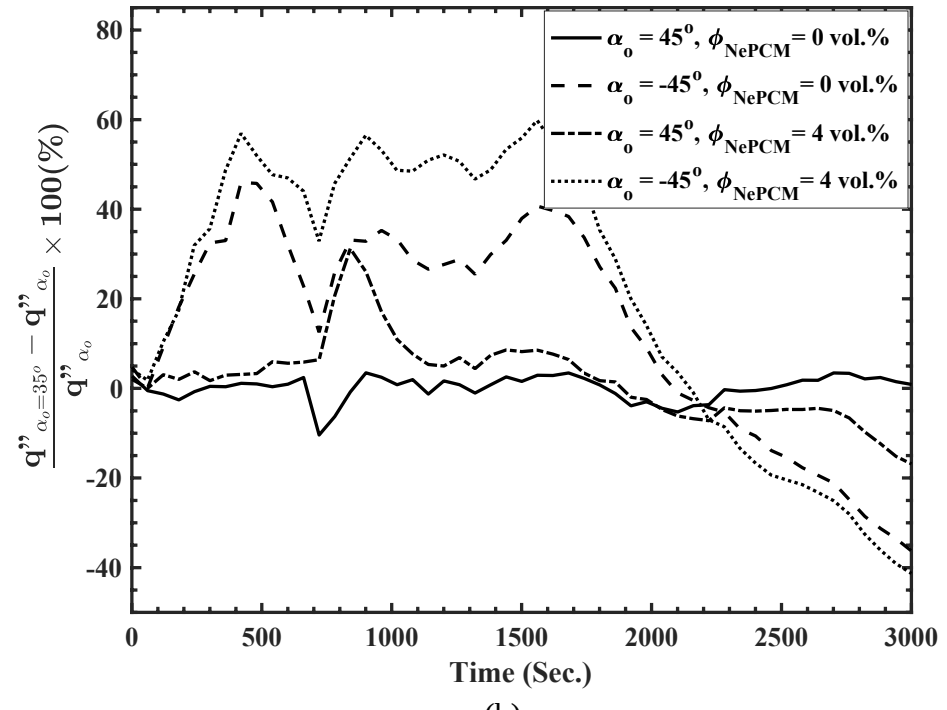

(b)

Fig. 7-15 Heat flux enhancement percentage over time, (a) $p = 45\,mm$ (b) $p = 65\,mm$.

7.5 Discussion of practical applications

Latent heat thermal energy storage system is widely used to store thermal energy from sustainable sources (e.g., solar), recovery of waste heat in industrial processes (Miró, Gasia, & Cabeza, 2016), thermal management (Duan & Naterer, 2010) and home drain water heat recovery (Alimohammadisagvand, Jokisalo, Kilpeläinen, Ali, & Sirén, 2016; Renaldi, Kiprakis, & Friedrich, 2017). The M-TES technology (Shaopeng Guo et al., 2017; H. Li, Wang, Yan, & Dahlquist, 2013) bridges waste heat in industrial processes to end-users and provides required hot water and heat in a cost-effective and efficient way. The recent development of novel hybrid thermal insulation for subsea pipelines also suggests the benefits of latent heat storage with PCMs (Parsazadeh & Duan, 2015, 2016). Optimal design of these systems requires a good understanding of the PCM melting process and the effects of parameters involved in the system. The results from this chapter will be useful in the design of new thermal storage units or improving performance of existing ones, for example by using desirable fin angles or adding more/longer fins on the bottom of a storage tank, etc.

7.6 Summary

A numerical study is performed on the melting of phase change materials with and without nanoparticles in an LHTES unit. A shell-and-tube storage unit is considered with water as HTF flowing inside the tube with plate fins, while the shell is filled with paraffin wax and Al_2O_3 nanoparticles dispersed in the wax. The simulation results are analyzed with the traditional OFAT method and the RSM - specifically a faced-centered central composite design method. The effects of nanoparticle concentration and geometrical parameters of the fins, i.e., fin angle and pitch, on the melting process and charging time are analyzed. The following main conclusions can be obtained:

- In terms of heat exchanger design parameters, a positive fin angle appeared to be favourable. It was found that adverse hot-spots formed below the fins when $\alpha = -45^{o}$ while no hot-spot was observed when $\alpha = 45^{o}$. Furthermore, changing the fin angle from -45^{o} to 45^{o} leads to the formation of larger and stronger vorticities, which are favourable for enhanced convective heat transfer and eventually lead to a significant decrease of total charging time.
- For any fin design and nanoparticle concentration, the simulation results showed that the heat transfer rate in the upper section of the thermal storage unit is much stronger than that in the bottom section. So, increasing the number of fins in the bottom section of an LHTES unit would be able to increase the total heat transfer rate.
- Adding Al_2O_3 nanoparticles into the paraffin wax decreased the total heat transfer rate, leading to longer charging time in all cases studied. The results indicate that thermal conductivity enhancement with nanoparticles may not be able to make up for natural convection reduction when the nanoparticles are added in the finned thermal storage unit.
- Statistical analysis with RSM shows a significant interaction between nanoparticle concentration and fin angle. The charging time considerably increased when the nanoparticles are added at $\alpha = -45^{o}$, however, this effect is less pronounced when $\alpha = 45^{o}$. A nonlinear regression model for the charging time was obtained with two significant parameters, i.e., nanoparticle concentration and fin angle, while the latter is the most significant. Further case evaluation showed the shortest charging time among all studied cases with 35^{o} fin angle, 65 mm pitch, and without nanoparticles in the PCM.

These new findings could be useful in the optimal design of many practical latent heat thermal energy storage systems.

Chapter 8 Conclusions and recommendations for future research

8.1 Conclusions

This thesis presented significant numerical and experimental results regarding the effects of nanoparticles on the phase change rate in different geometries. The following conclusions can be made from these studies:

Scaling analysis in an enclosure heated from the bottom shows that:

- The heat transfer starts with the conduction heat transfer mechanism until the Rayleigh number reaches a critical Rayleigh number (conduction domination regime). Afterwards, the convection heat transfer mechanism becomes dominant (convection domination regime). The parameters that contribute to the melting in each of these regimes were identified and formulated.

Similarly, the numerical part of the study demonstrates that:

- During the conduction domination regime, the solid-liquid interface remained horizontal as the rolls of flow formed in the liquid regimes were small and weak. The rolls became larger and stronger, making the interface curvy by moving the interface upward due to the Rayleigh-Benard convection in the convection domination regime. Depending on the number of rolls, some hot-spots formed over the hot plate (temperature-controlling plate). These hot-spots moved over the hot plate by moving the solid-liquid interface upward.

And, the experimental part of the study illustrates that:

- A relationship exists between the number of waves formed at the solid-liquid interface and the solid-liquid interface location (this point is also visible from the numerical simulations).

- The nanoparticles acted differently in different wall temperatures in terms of the heat transfer rate. This is because the significance of the parameter reported in the scaling analysis is different at different wall temperatures.
- Adding nanoparticles improved the melting rate at the conduction domination regime. This means that nanoparticles improved the melting rate in the short enclosures heated from the bottom. In these enclosures, the Rayleigh-Benard convection never emerges if the Rayleigh number does not reach the critical Rayleigh number due to the smaller height of the enclosure.
- Although the nanoparticles improved the melting rate at low wall temperature (40^oC), no significant melting rate or melting time improvement was observed at the wall temperature of 55^oC. More interestingly, an adverse heat transfer effect was observed in the case of adding nanoparticles at the wall temperature of 70^oC.
- With the previous point in mind, reporting a critical nanoparticle concentration, which leads to a high phase change rate, is only valid at the experimental condition that the value is found, and this value would change at different experimental conditions. This point may not be limited to the type of nanoparticle used in this research. This point can fully be confirmed through experiments as future work.
- Adding nanoparticles improved the thermal conductivity of the NePCM mixture at both solid and liquid phases.
- The higher the temperature (or the lower the viscosity), the stronger the Brownian motion and thermal conductivity in the liquid NePCMs. As expected, the viscosity of the NePCMs increased with an increase in the nanoparticle concentration and with a decrease in the temperature.

- . Also, an empirical correlation was developed to predict the pure coconut oil viscosity.
- Empirical correlations were also developed to predict the melting rate for the PCM and NePCMs for two conduction domination and convection domination conditions in an enclosure heated from the bottom.
- An empirical correlation was developed to evaluate the relationship between the effect of nanoparticles on the melting time, the thermal conductivity enhancement, and the Grashof number reduction. This correlation may not be limited to the type of nanoparticle and the PCM implemented in this research, however, this point is recommended to be evaluated in future research.
- The addition of the nanoparticles reduced the Grashof number approximately by 4500. To compensate for this Grashof number reduction and to improve the melting time with adding nanoparticles, the thermal conductivity enhancement should be over $35\,\%$. This finding may not be limited to the type of nanoparticle and the PCM implemented in this research, however, this finding should be dependent on the geometry and boundary conditions, on which the experiments conducted.
- An empirical correlation was developed to evaluate the melting time variations with the thermal conductivity enhancement and the Grashof number reduction.

The effects of the CuO nanoparticles on the phase change rate in a finless shell-and-tube thermal energy storage revealed the conclusions as follow:

- The nanoparticles enhance the phase change rate up to a critical concentration. Afterwards, the phase change rate may drop. Based on the experimental findings of this thesis, this nanoparticle concentration may change in different experimental conditions, such as higher or lower HTF temperature, etc.

- The obtained regression model for melting of NePCM is nonlinear, and the most and least significant factors were identified. A significant interaction was seen between the HTF temperature and ϕ_{NePCM}. It was found that the effect of nanoparticles on NePCM is less pronounced at higher HTF inlet temperatures. This point has experimentally been indicated in an enclosure heated from the bottom.

The effects of the Al_2O_3 nanoparticles on the phase change rate in a shell-and-tube thermal energy storage mounted with fins illuminated the conclusions as follow:

- Adding Al_2O_3 nanoparticles into paraffin wax did not reduce the charging time in all cases studied, indicating that the thermal conductivity enhancement with nanoparticles may not be able to make up for natural convection reduction, creating due to the local vortex formation. This point clearly shows that nanoparticles are sensitive to the geometry type. This means that we need to know how significant the natural convection mechanism of heat transfer is in the geometry that nanoparticles are dispersed.
- Statistically, a significant interaction was seen between the nanoparticles concentration and the fin angle. A nonlinear regression model for the charging time was obtained with two significant parameters, i.e., nanoparticle concentration and fin angle, while the latter is the most significant. Further case evaluation showed the shortest charging time among all studied cases with 35^o fin angle, 65 mm pitch, and without nanoparticles in the PCM. These new findings could be useful in the optimal design of many practical latent heat thermal energy storage systems.

8.2 Recommendations for future research

The following aspects are recommended for further research on the effects of nanoparticles on the phase change rate:

- The effects of nanoparticles on the phase change rate is recommended to be repeated with different nanoparticle types and/or PCM using a similar methodology to confirm the findings obtained in this thesis for the enclosure heated from the bottom, particularly those findings that may be independent of the type of nanoparticle and PCM.
- It is also recommended that a more accurate thermal conductivity analyzer is implemented than the one used in this study to reduce the thermal conductivity measurement error. This also helps reduce the Rayleigh number error and helps come up with a stronger conclusion.
- The same experiment is suggested to be conducted in other geometries or experimental conditions, such as heating the enclosure from the side and evaluating the melting time as discussed in this thesis. This will help confirm or come up with a better idea regarding the effects of nanoparticles on the phase change rate, rather than introducing another critical nanoparticle concentration, which leads to the highest melting rate in that specific geometry.
- Similar experiments can be conducted with nanofluids to analyze the importance of nanoparticles on the heat transfer rate without phase change in the presence of natural convection. The same approach could be employed to modify the conventional heat transfer correlations such as the Nusselt number with the effect of nanoparticle concentration.

- The same approach can be employed to forced convection but without phase change. With forced convection, this time the flow forcibly moves, and nanoparticles would affect this forced flow movement and thermal conductivity.

References

Abdollahzadeh, M., & Esmaeilpour, M. (2015). Enhancement of phase change material (PCM) based latent heat storage system with nanofluid and wavy surface. *International Journal of Heat and Mass Transfer*, *80*, 376–385. https://doi.org/10.1016/j.ijheatmasstransfer.2014.09.007

Abdou, M. A., & Soliman, A. A. (2005). New applications of variational iteration method. *Physica D*, *211*, 1–8.

Abernethy, R. B., Benedict, R. P., & Dowdell, R. B. (1985). ASME measurment uncertainty. *Journal of Fluids Engineering*, *107*(2), 161–164.

Adomian, G. (1983). Stochastic systems. *Academic Press*.

Adomian, G. (1988). A review of the decomposition method in applied mathematics. *Journal of Mathematical Analysis and Applications*, *135*, 501–544.

Adomian, G. (1994). *Solving frontier problems of physics: The decomposition mthod*. Boston, MA: Kluwer Acadeic Publishers.

Akgün, M., Aydin, O., & Kaygusuz, K. (2007). Experimental study on melting/solidification characteristics of a paraffin as PCM. *Energy Conversion and Management*, *48*(2), 669–678.

Al-Abidi, A., Mat, S., Sopian, K., Sulaiman, Y., & Mohammad, A. (2016). Heat Transfer Enhancement for PCM Thermal Energy Storage in Triplex Tube Heat Exchanger. *Heat Transfer Engineering*, *37*(7–8), 705–712.

Al-Jethelah, M., Tasnim, S. H., Mahmud, S., & Dutta, A. (2018). Nano-PCM filled energy storage system for solar-thermal applications. *Renewable Energy*, *126*, 137–155.

https://doi.org/10.1016/j.renene.2018.02.119

Alexandrov, D. V, Nizovtseva, I. G., Malygin, A. P., Huang, H., & Lee, D. (2008). *Unidirectional solidification of binary melts from a cooled boundary : analytical solutions of a nonlinear diffusion-limited*. https://doi.org/10.1088/0953-8984/20/11/114105

Alexiades, V., & Solomon, A. D. (1993). Mathematical modeling of melting and freezing processes. In *Hemisphere Publishing Corporation*. Washington, DC.

Alimohammadisagvand, B., Jokisalo, J., Kilpeläinen, S., Ali, M., & Sirén, K. (2016). Cost-optimal thermal energy storage system for a residential building with heat pump heating and demand response control. *Applied Energy*, *174*, 275–287. https://doi.org/10.1016/j.apenergy.2016.04.013

Altohamy, A. A., Abd Rabbo, M. F., Sakr, R. Y., & Attia, A. A. A. (2015). Effect of water based Al2O3 nanoparticle PCM on cool storage performance. *Applied Thermal Engineering*, *84*, 331–338.

ANSYS FLUENT. (2013). Ansys Fluent Theory Guide. In *ANSYS Inc., USA*.

Arasu, A. V., & Mujumdar, A. S. (2012). Numerical study on melting of paraffin wax with Al 2O 3 in a square enclosure. *International Communications in Heat and Mass Transfer*, *39*(1), 8–16.

Arasu, A. valan, Sasmito, A. P., & Mujumdar, A. S. (2013). Numerical performance study of paraffin wax dispersed with alumina in a concentric pipe latent heat storage system. *Thermal Science*, *17*(2), 419–430.

Arıcı, M., Tütüncü, E., Kan, M., & Karabay, H. (2017). Melting of nanoparticle-enhanced

paraffin wax in a rectangular enclosure with partially active walls. *International Journal of Heat and Mass Transfer*, *104*, 7–17.

Aydin, O., Akgun, M., & Kaygusuz, K. (2007). An experimental optimization study on a tube-in-shell latent heat storage. *International Journal of Energy Research*, *31*, 274–287.

Azmi, W. H., Sharma, K. V., Sarma, P. K., Mamat, R., Anuar, S., & Dharma Rao, V. (2013). Experimental determination of turbulent forced convection heat transfer and friction factor with SiO2 nanofluid. *Experimental Thermal and Fluid Science*, *51*, 103–111. https://doi.org/10.1016/j.expthermflusci.2013.07.006

Bahiraei, F., Fartaj, A., & Nazri, G. A. (2017). Experimental and numerical investigation on the performance of carbon-based nanoenhanced phase change materials for thermal management applications. *Energy Conversion and Management*, *153*(September), 115–128. https://doi.org/10.1016/j.enconman.2017.09.065

Bejan, A. (2013). *Convective Heat Transfer* (Fourth Edi). https://doi.org/10.1002/9781118671627

Bougoffa, L., Rach, R., Wazwaz, A.-M., & Duan, J.-S. (2015). On the Adomian decomposition method for solving the Stefan problem. *International Journal of Numerical Methods for Heat & Fluid Flow*, *25*(4), 912–928.

Braga, W. F. (2004). Approximate analytical solution for one-dimensional finite ablation problem with constant time heat flux. *AIAA Thermophysics*.

Briozzo, A. C., & Tarzia, D. A. (2002). An explicit solution for an instantaneous two-phase Stefan problem with nonlinear thermal coefficients. *IMA Journal of Applied Mathematics*

(Institute of Mathematics and Its Applications), *67*(3), 249–261.

Caldwell, J., & Kwan, Y. Y. (2003). *On the perturbation method for the Stefan problem with time-dependent boundary conditions*. *46*, 1497–1501.

Calwell, Y. Y., & Ozisk, M. N. (2002). Spherical solidification by the enthalpy method and heat balance integral method. *Advanced Computational Methods in Heat Transfer VII*, 165–174.

Carslaw, H. S., & Jaeger, J. C. (1959). *Conduction of heat in solid*.

Ceretani, A. N., Salva, N. N., & Tarzia, D. A. (2018). An exact solution to a Stefan problem with variable thermal conductivity and a Robin boundary condition. *Nonlinear Analysis: Real World Applications*, *40*, 243–259.

Ceretani, A. N., & Tarzia, D. A. (2016). *Similarity solution for a two-phase one-dimensional Stefan problem with a convective boundary condition and a mushy zone model*. *9*(1990), 201–211. Retrieved from http://arxiv.org/abs/1609.04690

Cho, S. H., & Sunderland, J. E. (1969). Heat conduction problems with melting or freezing. *Journal of Heat Transfer*, *91*, 421–426.

Clapeyron, B. ., & Lame, G. (1831). No Title. *Annual Chemistry Physics*, *47*, 250–256.

Devesse, W., Baere, D., & Guillaume, P. (2014). The isotherm migration method in spherical coordinates with a moving heat source,. *International Journal of Heat and Mass Transfer*, *75*, 726–735.

Devices, D. (2011). *KD2 Pro thermal properties analyzer operator's manual version 4*. Pullman, WA: Decagon Devices,.

Dhaidan, N. S., Khodadadi, J. M., Al-Hattab, T. A., & Al-Mashat, S. M. (2013). Experimental

and numerical investigation of melting of NePCM inside an annular container under a constant heat flux including the effect of eccentricity. *International Journal of Heat and Mass Transfer*, *67*, 455–468.

Doha, E. H., Bhrawy, A. H., & Ezz-Eldien, S. S. (2011). A Chebyshev spectral method based on operational matrix for initial and boundary value problems of fractional order. *Computers & Mathematics with Applications*, *62*(2364–2373).

Doha, E. H., Bhrawy, A. H., & Ezzeldeen, S. s. (2011). Efficient Chebyshev spectral methods for solving multi-term fractional orders differential equations. *Applied Mathematical Modelling*, *35*, 5662–5672.

Duan, X., & Naterer, G. F. (2010). Heat transfer in phase change materials for thermal management of electric vehicle battery modules. *International Journal of Heat and Mass Transfer*, *53*(23–24), 5176–5182.

Dutil, Y., Rousse, D. R., Salah, N. Ben, Lassue, S., & Zalewski, L. (2011). A review on phase-change materials: Mathematical modeling and simulations. *Renewable and Sustainable Energy Reviews*, *15*(1), 112–130.

Ebrahimi, A., & Dadvand, A. (2015). Simulation of melting of a nano-enhanced phase change material (NePCM) in a square cavity with two heat source-sink pairs. *Alexandria Engineering Journal*, *54*(4), 1003–1017. https://doi.org/10.1016/j.aej.2015.09.007

Faghri, A., & Zhang, Y. (2006). 6 – Melting and Solidification. *Transport Phenomena in Multiphase Systems*, 421–530. https://doi.org/10.1016/B978-0-12-370610-2.50011-8

Fan, L., Fang, X., Wang, X., Zeng, Y., Xiao, Y., Yu, Z., … Hu, Y. (2013). Effects of various

carbon nanofillers on the thermal conductivity and energy storage properties of paraffin-based nanocomposite phase change materials. *Applied Energy, 110*, 163–172.

Fan, L. W., Zhu, Z. Q., Zeng, Y., Lu, Q., & Yu, Z. T. (2014). Heat transfer during melting of graphene-based composite phase change materials heated from below. *International Journal of Heat and Mass Transfer, 79*, 94–104. https://doi.org/10.1016/j.ijheatmasstransfer.2014.08.001

Feltham, D. L., & Garside, J. (2001). *Analytical and numerical solutions describing the inward solidification of a binary melt*. *56*, 2357–2370.

Feng, Y., Li, H., Li, L., Bu, L., & Wang, T. (2015). Numerical investigation on the melting of nanoparticle-enhanced phase change materials (NEPCM) in a bottom-heated rectangular cavity using lattice Boltzmann method. *International Journal of Heat and Mass Transfer, 81*, 415–425. https://doi.org/10.1016/j.ijheatmasstransfer.2014.10.048

Foss, S. D., & Fan, S. S. T. (1972). Approximate solution to the freezing of the ice-water system with constant heat flux in the water phase. *Journal of Water Resource Research, 8*, 1083–1086.

Ganji, D. D., & Rajabi, A. (2006). Assessment of homotopy-perturbation and perturbation methods in heat radiation equations. *International Communications in Heat and Mass Transfer, 33*, 391–400.

Ghalambaz, M., Doostani, A., Izadpanahi, E., & Chamkha, A. J. (2017). Phase-change heat transfer in a cavity heated from below: The effect of utilizing single or hybrid nanoparticles as additives. *Journal of the Taiwan Institute of Chemical Engineers, 72*, 104–115. https://doi.org/10.1016/j.jtice.2017.01.010

Ghoreishi, F., & Yazdani, S. (2011). An extension of the spectral Tau method for numerical solution of multi-order fractional differential equations with convergence analysis. *Computers and Mathematics with Applications*, *61*, 30–43.

Goodman, T. (1961). No Title. *Journal of Heat Transfer*, *83C*, 83–86.

Goodman, T. R. (1958). The heat-balance integral and its application to problems involving a change of phase. *Transactions of the American Society of Mechanical Engineers*, *80*, 335–342.

Goodman, T. R. (1964). Application of integral method to transient nonlinear heat transfer. *Advances in Heat Transfer*, *1*, 51–122.

Grzymkowski, Radoslaw, Hetmaniok, E., Pleszczynski, M., & Slota, D. (2013). A Certain analytical method used for solving the stefan problem. *Thermal Science*, *17*(3), 635–642. https://doi.org/10.2298/TSCI120826050G

Grzymkowski, Radosław, & Słota, D. (2005). *Stefan problem solved by Adomian decomposition method*. *82*(7), 851–856.

Guo, S., Zhao, J., Wang, W., Yan, J., Jin, G., Zhang, Z., … Niu, Y. (161AD). Numerical study of the improvement of an indirect contact mobilized thermal energy storage container. *Applied Energy*, *2016*, 476–486.

Guo, Shaopeng, Li, H., Zhao, J., Li, X., & Yan, J. (2013). Numerical simulation study on optimizing charging process of the direct contact mobilized thermal energy storage. *Applied Energy*, *112*, 1416–1423. https://doi.org/10.1016/j.apenergy.2013.01.020

Guo, Shaopeng, Zhao, J., Wang, W., Yan, J., Jin, G., & Wang, X. (2017). Techno-economic

assessment of mobilized thermal energy storage for distributed users: A case study in China. *Applied Energy*, *194*, 481–486. https://doi.org/10.1016/J.APENERGY.2016.08.137

Guo, Shaopeng, Zhao, J., Wang, W., Yan, J., Jin, G., Zhang, Z., … Niu, Y. (2016). Numerical study of the improvement of an indirect contact mobilized thermal energy storage container. *Applied Energy*, *161*, 476–486. https://doi.org/10.1016/j.apenergy.2015.10.032

He, J-H. (2000). Variational iteration method for autonomous ordinary differential systems. *Applied Mathematical Modelling*, *114*(2–3), 115–123.

He, J.-H. (1998a). Approximate analytical solution for seepage flow with fractional derivatives in porous media. *Computer Methods in Applied Mechanics and Engineering*, *167*, 57–68.

He, J.-H. (1998b). Approximate solution of nonlinear differential equations with convolution product nonlinearities. *Computer Methods in Applied Mechanics and Engineering*, *167*, 69–73.

He, J.-H. (1999a). Homotopy perturbation technique. *Computer Methods in Applied Mechanics and Engineering*, *178*, 257–262.

He, J.-H. (1999b). Variational iteration method _ a kind of non-linear analytical technique: some examples. *International Journal of Non-Linear Mechanics*, *34*, 699–708.

He, J.-H. (2000). A coupling method of a homotopy technique and a perturbation technique for non-linear problems. *International Journal of Non-Linear Mechanics*, *35*, 37–43.

He, J.-H. (2004). Comparison of Homotopy perturbation method and homotopy analysis method. *Applied Mathematics and Computation*, *156*, 527–539.

He, J.-H. (2005). Homotopy perturbation method for bifurcation of nonlinear problems.

International Journal of Nonlinear Sciences and Numerical Simulation, *6*(207–208).

He, J.-H. (2006a). Homotopy perturbation method for solving boundary value problems. *Physics Letters A*, *350*, 87–88.

He, J.-H. (2006b). New interpretation of homotopy perturbation method. *International Journal of Modern Physics B*, *20*, 87–88.

He, J.-H. (2006c). Non-perturbative methods for strongly nonlinear problems.

He, J.-H. (2007). Variational iteration method — some recent results and new interpretations. *Journal of Computational and Applied Mathematics*, *207*(1), 3–17.

He, J.-H. (2008). Recent development of the homotopy perturbation method. *Topological Methods i Nonlinear Analysis*, *31*, 205–209.

He, J.-H. (2009). An elementary introduction to the homotopy perturbation method. *Computers & Mathematics with Application*, *57*, 410–412.

Hetmaniok, E, Słota, D., & Zielonka, A. (2009). Solution of the solidification problem by using the variational iteration method. *Achives of Foundary Ngineering*, *9*(4), 63–68.

Hetmaniok, Edyta, Słota, D., Witua, R., & Zielonka, A. (2011). Comparison of the Adomian decomposition method and the variational iteration method in solving the moving boundary problem. *Computers and Mathematics with Applications*, *61*(8), 1931–1934. https://doi.org/10.1016/j.camwa.2010.07.050

Ho, C. J., & Gao, J. Y. (2009). Preparation and thermophysical properties of nanoparticle-in-paraffin emulsion as phase change material. *International Communications in Heat and Mass Transfer*, *36*(5), 467–470. https://doi.org/10.1016/j.icheatmasstransfer.2009.01.015

Ho, C. J., & Gao, J. Y. (2013). An experimental study on melting heat transfer of paraffin dispersed with Al2O3 nanoparticles in a vertical enclosure. *International Journal of Heat and Mass Transfer*, *62*(1), 2–8. https://doi.org/10.1016/j.ijheatmasstransfer.2013.02.065

Hosseini, M., Mustafa, M. T., Jafaryar, M., & Mohammadian, E. (2014). Nanofluid in tilted cavity with partially heated walls. *Journal of Molecular Liquids*, *199*, 545–551. https://doi.org/10.1016/j.molliq.2014.09.051

Hosseini, S. M. J., Ranjbar, A. A., Sedighi, K., & Rahimi, M. (2013). Melting of Nanoprticle-Enhanced Phase Change Material inside Shell and Tube Heat Exchanger. *Journal of Engineering*, *2013*, 1–8. https://doi.org/10.1155/2013/784681

Hosseinizadeh, S. F., Darzi, A. A. R., & Tan, F. L. (2012). Numerical investigations of unconstrained melting of nano-enhanced phase change material (NEPCM) inside a spherical container. *International Journal of Thermal Sciences*, *51*(1), 77–83. https://doi.org/10.1016/j.ijthermalsci.2011.08.006

Hu, H., & Argyropoulos, S. A. (1996). Mathematical modelling of solidification and melting: A review. *Modelling and Simulation in Materials Science and Engineering*, *4*, 371–396. https://doi.org/10.1088/0965-0393/4/4/004

Inokuti, M., Sekine, H., Mura, T., & Nemat-Nasser, S. (1978). General use of the Lagrange multiplier in non-linear mathematical physics. In *Variational Methods in the Mechanics of Solids*.

Jany, P., & Bejan, A. (1988). Scaling theory of melting with natural convection in an enclosure. *International Journal of Heat and Mass Transfer*, *31*(6), 1221–1235. https://doi.org/10.1016/0017-9310(88)90065-8

Jesumathy, S., Udayakumar, M., & Suresh, S. (2012). Experimental study of enhanced heat transfer by addition of CuO nanoparticle. *Heat and Mass Transfer/Waerme- Und Stoffuebertragung*, *48*(6), 965–978. https://doi.org/10.1007/s00231-011-0945-y

Jiji, L. M., & Weimbaum, S. (1974). A nonlinear singular perturbation theory for non-similar melting or freezing problems, conduction Cu-3. *5th International Heat Transfer Conference*. Tokyo.

Kandasamy, R., Wang, X., & Mujumdar, A. S. (2008). Transient cooling of electronics using phase change material (PCM) based heat sinks. *Applied Thermal Engineering*, *28*, 1047–1057.

Kant, K., Shukla, A., Sharma, A., & Henry Biwole, P. (2017). Heat transfer study of phase change materials with graphene nano particle for thermal energy storage. *Solar Energy*, *146*, 453–463. https://doi.org/10.1016/j.solener.2017.03.013

Kartashov, E. M., & Krotov, G. S. (2009). Analytical solution of the single-phase Stefan problem. *Mathematical Models and Computer Simulations*, *1*(2), 180–188. https://doi.org/10.1134/S2070048209020021

Kashani, S., Ranjbar, A. A., Abdollahzadeh, M., & Sebti, S. (2012). Solidification of nano-enhanced phase change material (NEPCM) in a wavy cavity. *Heat and Mass Transfer/Waerme- Und Stoffuebertragung*, *48*(7), 1155–1166. https://doi.org/10.1007/s00231-012-0965-2

Kashani, S., Ranjbar, A. A., Madani, M. M., Mastiani, M., & Jalaly, H. (2013). Numerical study of solidification of a nano-enhanced phase change material (NEPCM) in a thermal storage system. *Journal of Applied Mechanics and Technical Physics*, *54*(5), 702–712.

https://doi.org/10.1134/S0021894413050027

Khalid, M. Z., Zubair, M., & Ali, M. (2017). An analytical method for the solution of two phase Stefan problem in cylindrical geometry. *Applied Mathematics and Computation*, *0*, 1–14. https://doi.org/10.1016/j.amc.2017.09.013

Khodadadi, J. M., & Hosseinizadeh, S. F. (2007). Nanoparticle-enhanced phase change materials (NEPCM) with great potential for improved thermal energy storage. *International Communications in Heat and Mass Transfer*, *34*(5), 534–543. https://doi.org/10.1016/j.icheatmasstransfer.2007.02.005

Kline, S., & Mcclintock, F. (1953). Describing Uncertainties in Single-Sample Experiments. *Mechanical Engineering*, *75*, 3–8.

Kondrashov, E. N. (2007). Influence of the difference in the density of solid and liquid phases on the dynamics of an alloy solidification front at crystallization of a finite volume with a moving boundary t^0.5. *Journal of Engineering Thermophysics*, *16*(2), 88–95. https://doi.org/10.1134/S1810232807020051

Kondrashov, E N. (2009). The analytical solution of the one alloy solidification problem. *International Journal of Heat and Mass Transfer*, *52*, 67–69. https://doi.org/10.1016/j.ijheatmasstransfer.2008.05.027

Kondrashov, Evgeniy N. (2006). *Similarity Solution of the 3-phase Stefan Problem for Alloys with Arbitrary Temperature Dependent Properties*. https://doi.org/10.1103/PhysRevE.68.016612

Kumar, A., Singh, A. K., & Rajeev. (2018). A Stefan problem with temperature and time

dependent thermal conductivity. *Journal of King Saud University - Science*. https://doi.org/10.1016/j.jksus.2018.03.005

Leung, M. (2001). Phase-change heat transfer in laser transformation hardening by moving Gaussian rectangular heat source. *JOurnal of Physics D: Applied Physics*, *34*, 3434–3441.

Li, F., Liu, J., & Yue, K. (2009). *Exact analytical solution to three-dimensional phase change heat transfer problems in biological tissues subject to freezing*. *30*(1), 63–72. https://doi.org/10.1007/s10483-009-0107-x

Li, H., Wang, W., Yan, J., & Dahlquist, E. (2013). Economic assessment of the mobilized thermal energy storage (M-TES) system for distributed heat supply. *Applied Energy*, *104*, 178–186. https://doi.org/10.1016/j.apenergy.2012.11.010

Liao, S. (1998). Homotopy analysis method: a new analytic method for nonlinear problems. *Applied Mathematics and Mechanics*, *19*, 957–962.

Liao, S. (2003). Beyond Perturbation: Introduction to the Homotopy Analysis Method. In *Chapman and Hall–CRC Press, Boca Raton*.

Liao, S. (2004). On the homotopy analysis method for nonlinear problems. *Applied Mathematics and Computation*, *147*, 499–513.

Liao, S. (2009). Notes on the homotopy analysis method: some definitions and theorems. *Communications in Nonlinear Science and Numerical Simulation*, *14*, 983–997.

Liao, S. (2012). Homotopy Analysis Method in Nonlinear Differential Equations. In *Springer/ Higher Education Press*.

Lightfoot, N. (1929). The solidification of molten steel. *London Math. Soc.*, 97–116. London.

Lohrasbi, S., Sheikholeslami, M., & Ganji, D. D. (2016). Discharging process expedition of NEPCM in fin-assisted Latent Heat Thermal Energy Storage System. *Journal of Molecular Liquids*, *221*, 833–841. https://doi.org/10.1016/j.molliq.2016.06.044

Lohrasbi, S., Sheikholeslami, M., & Ganji, D. D. (2017). Multi-objective RSM optimization of fin assisted latent heat thermal energy storage system based on solidification process of phase change Material in presence of copper nanoparticles. *Applied Thermal Engineering*, *118*, 430–447. https://doi.org/10.1016/j.applthermaleng.2017.03.005

Lombardi, A. L., & Tarzia, D. A. (2001). Similarity solutions for thawing processes with a heat flux condition at the fixed boundary. *Meccanica*, *36*(3), 251–264. https://doi.org/10.1023/A:1013963424649

London, A. L., & Seban, R. A. (1943). Rate of ice formation. *Transactions of the American Society of Mechanical Engineers*, *65*, 771–779.

Mahdi, J. M., & Nsofor, E. C. (2017). Melting enhancement in triplex-latent thermal energy storage system using nanoparticle-metal foam combination. *Applied Energy*, *191*, 22–34.

Mahdi, Jasim M., & Nsofor, E. C. (2017). Melting enhancement in triplex-tube latent thermal energy storage system using nanoparticles-fins combination. *International Journal of Heat and Mass Transfer*, *109*, 417–427. https://doi.org/10.1016/j.ijheatmasstransfer.2017.02.016

Mennig, J., & Ozisk, M. N. (1985). Coupled integral equation approach for solving melting or soldificiation. *International Journal of Heat and Mass Transfer*, *28*, 1481–1485.

Michaelides, E. E. (2014). Nanofluidics: Thermodynamic and transport properties. In *Nanofluidics: Thermodynamic and Transport Properties* (Vol. 9783319056).

https://doi.org/10.1007/978-3-319-05621-0

Miró, L., Gasia, J., & Cabeza, L. F. (2016). Thermal energy storage (TES) for industrial waste heat (IWH) recovery: A review. *Applied Energy*, *179*, 284–301. https://doi.org/10.1016/j.apenergy.2016.06.147

Mitchell, S. L. (2012). Applying the combined integral method to one-dimensional ablation. *Applied Mathematical Modelling*, *36*(1), 127–138. https://doi.org/10.1016/j.apm.2011.05.032

Mitchell, S. L. (2015). Applying the combined integral method to two-phase Stefan problems with delayed onset of phase change. *Journal of Computational and Applied Mathematics*, *281*, 58–73. https://doi.org/10.1016/j.cam.2014.11.051

Mitchell, S. L., & Myers, T. G. (2010a). Application of Standard and Refined Heat Balance Integral Methods to One-Dimensional Stefan Problems. *SIAM Review*, *52*(1), 57–86.

Mitchell, S. L., & Myers, T. G. (2010b). Improving the accuracy of heat balance integral methods applied to thermal problems with time dependent boundary conditions. *International Journal of Heat and Mass Transfer*, *53*(17–18), 3540–3551. https://doi.org/10.1016/j.ijheatmasstransfer.2010.04.015

Mitchell, S. L., & Vynnycky, M. (2009). Finite-difference methods with increased accuracy and correct initialization for one-dimensional Stefan problems. *Applied Mathematics and Computation*, *215*, 1609–1621.

Mondal, S. (2008). Phase change materials for smart textiles - An overview. *Applied Thermal Engineering*, *28*(11–12), 1536–1550. https://doi.org/10.1016/j.applthermaleng.2007.08.009

Montgomery, D. C. (2012). *Design and Analysis of Experiment* (8th ed.). New York: John Wiley & Sons Inc.

Mosaffa, A. H., Talati, F., Rosen, M. A., & Tabrizi, H. B. (2012). Approximate analytical model for PCM solidi fi cation in a rectangular fi nned container with convective cooling boundaries ☆. *International Communications in Heat and Mass Transfer*, *39*(2), 318–324. https://doi.org/10.1016/j.icheatmasstransfer.2011.11.015

Myers, T. (2010). Optimal exponent heat balance and refined integral methods applied to Stefan problems. *International Journal of Heat and Mass Transfer*, *53*(5–6), 1119–1127.

Myers, T. G., & Mitchell, S. L. (2011). Application of the combined integral method to Stefan problems. *Applied Mathematical Modelling*, *35*(9), 4281–4294. https://doi.org/10.1016/j.apm.2011.02.049

Myers, T., Mitchell, S., Muchatibva, G., & Myers, M. (2007). A cubic heat balance integral method for one-dmensional melting of a finite theckness layer. *International Journal of Heat and Mass Transfer*, *50*(25–26), 5305–5317.

Natale, M. F., & Tarzia, D. A. (2003). Explicit solutions to the one-phase Stefan problem with temperature-dependent thermal conductivity and a convective term. *International Journal of Engineering Science*, *41*(15), 1685–1698. https://doi.org/10.1016/S0020-7225(03)00067-3

Nayfeh, A. H. (1973). *Perturbation Method*. New York: Wiley.

Neumann, F. (1912). *Die Paruellen Differentialgleichungen der Mathematischen Physik*. *2*, 121.

Nomura, T., Tsubota, M., Oya, T., Okinaka, N., & Akiyama, T. (2013). Heat storage in direct-contact heat exchanger with phase change material. *Applied Thermal Engineering*, *50*(1),

26–34. https://doi.org/10.1016/J.APPLTHERMALENG.2012.04.062

Nourani, M., Hamdami, N., Keramat, J., Moheb, A., & Shahedi, M. (2016). Thermal behavior of paraffin-nano-Al2O3 stabilized by sodium stearoyl lactylate as a stable phase change material with high thermal conductivity. *Renewable Energy*, *88*, 474–482. https://doi.org/10.1016/J.RENENE.2015.11.043

Okada, M. (1984). Analysis of heat transfer during melting from a vertical wall. *International Journal of Heat and Mass Transfer*, *27*(11), 2057–2066. https://doi.org/10.1016/0017-9310(84)90192-3

Oro, E., De Garcia, A., Castell, A., Farid, M. M., & Cabeza, L. F. (2017). Review on phase change material (PCMs) for cold thermal energy storage applications. *Applied Energy*, 281–290.

Ozisk, M., & Necati, M. (1993). *Heat Conduction*. John Wiley & Sons.

Pamuk, S. (2005). An application for linear and nonlinear heat equations by Adomian's decomposition method. *Applied Mathematics and Computation*, *163*, 89–96.

Pan, C., Hoenig, S., Chen, C. H., Neti, S., Romero, C., & Vermaak, N. (2017). Efficient modeling of phase change material solidification with multidimensional fins. *International Journal of Heat and Mass Transfer*, *115*, 897–909. https://doi.org/10.1016/j.ijheatmasstransfer.2017.07.120

Parsazadeh, M., & Duan, X. (2015). Thermal insulation with latent energy storage for flow assurance in subsea pipelines. *34th International Conference on Ocean, Offshore and Arctic Engineering*. St. John's, Canada: ASME.

Parsazadeh, M., & Duan, X. (2016). Numerical study of a hybrid thermal insulation with phase change material for subsea pipelines. *International Mechanical Engineering Congress and Exposition*. Phoenix, USA: ASME.

Parsazadeh, M., & Duan, X. (2017). Numerical and statistical study on melting of nanoparticle enhanced phase change material in a shell-and-tube thermal energy storage system. *Applied Thermal Engineering*, *111*, 950–960. https://doi.org/10.1016/j.applthermaleng.2016.09.133

Parsazadeh, M., & Duan, X. (2018). Numerical study on the effects of fins and nanoparticles in a shell and tube phase change thermal energy storage unit. *Applied Energy*, *216*(February), 142–156. https://doi.org/10.1016/j.apenergy.2018.02.052

Paterson, S. (1952). Propagation of a boundary of fusion. *Proceedings of the Glasgow Mathematical Association*, *1*, 42–47.

Patil, U., Benjakul, S., Prodpran, T., Senphan, T., & Cheetangdee, N. (2016). Characteristics and quality of virgin coconut oil as influenced by maturity stages. *Carpathian Journal of Food Science and Technology*, *8(4)*(February 2018), 103–115. Retrieved from https://www.researchgate.net/publication/313602646

Pedroso, R. I., & Domoto, G. A. (1973). No Title. *Journal of Heat Transfer*, *95*, 42.

Qin, X., Duan, Y., & Yin, M. (2014). *Approximate Analytic Solutions for the Two-Phase Stefan Problem Using the Adomian Decomposition Method*. *2014*.

Rabienataj Darzi, A. A., Jourabian, M., & Farhadi, M. (2016). Melting and solidification of PCM enhanced by radial conductive fins and nanoparticles in cylindrical annulus. *Energy Conversion and Management*, *118*, 253–263.

https://doi.org/10.1016/j.enconman.2016.04.016

Rajeev. (2014). *Homotopy perturbation method for a Stefan problem*. *18*(2), 391–398. https://doi.org/10.2298/TSCI110627008R

Rajeev, & Kushwaha, M. S. (2013). Homotopy perturbation method for a limit case Stefan problem governed by fractional diffusion equation. *Applied Mathematical Modelling*, *37*(5), 3589–3599. https://doi.org/10.1016/j.apm.2012.07.047

Rajeev, Nath, R., & Subir, D. (2009). Solution of one-dimensional moving boundary problem with periodic boundary conditions by variational iteration method. *Thermal Science*, *13*(2), 199–204. https://doi.org/10.2298/TSCI0902199R

Rathjen, K. A., & Jiji, L. M. (1970). Transient heat transfer in fins undergoing phase transformation. *Fourth International Heat Transfer Conference*. Paris.

Reid, R., Prausnitz, J., & Poling, B. (1987). *The Properties of Gases and Liquids*. New York: McGraw-Hill.

Renaldi, R., Kiprakis, A., & Friedrich, D. (2017). An optimisation framework for thermal energy storage integration in a residential heat pump heating system. *Applied Energy*, *186*, 520–529. https://doi.org/10.1016/J.APENERGY.2016.02.067

Sadoun, N., Si-Ahmed, E.-K., & Colinet, P. (2006). *On the refined integral method for the one-phase Stefan problem with time-dependent boundary conditions*. *30*, 531–544. https://doi.org/10.1016/j.apm.2005.06.003

Sasmito, A. P., Kurnia, J. C., & Mujumdar, A. S. (2011). Numerical evaluation of laminar heat transfer enhancement in nanofluid flow in coiled square tubes. *Nanoscale Research Letters*,

6, 1–14. https://doi.org/10.1186/1556-276X-6-376

Sciacovelli, A., Colella, F., & Verda, V. (2013). Melting of PCM in a thermal energy storage unit: Numerical investigation and effect of nanoparticle enhancement. *International Journal of Energy Research*, *37*, 1610–1623.

Sebti, S. S., Mastiani, M., Mirzaei, H., Dadvand, A., Kashani, S., & Hosseini, S. A. (2013). Numerical study of the melting of nano-enhanced phase change material in a square cavity. *Journal of Zhejiang University SCIENCE A*, *14*(5), 307–316. https://doi.org/10.1631/jzus.A1200208

Seniraj, R. V., & Bose, T. K. (1982). Planar solidification of a warm flowing liquid under different boundary conditions. *Warme Stoffubertragung*, *16*, 105–111.

Shang, D. (2006). *Free Convection Film Flows and Heat Transfer*. Berlin Heidelberg: Springer.

Sheikholeslami, M., Lohrasbi, S., & Ganji, D. D. (2016a). Numerical analysis of discharging process acceleration in LHTESS by immersing innovative fin configuration using finite element method. *Applied Thermal Engineering*, *107*, 154–166. https://doi.org/10.1016/j.applthermaleng.2016.06.158

Sheikholeslami, M., Lohrasbi, S., & Ganji, D. D. (2016b). Response surface method optimization of innovative fin structure for expediting discharging process in latent heat thermal energy storage system containing nano-enhanced phase change material. *Journal of the Taiwan Institute of Chemical Engineers*, *67*, 115–125. https://doi.org/10.1016/j.jtice.2016.08.019

Singh, J., Gupta, K., & Rai, N. (2011a). Variational iteration method to solve moving boundary

problem with temperature dependent physical properties. *Thermal Science*, *15*, 229–239. https://doi.org/10.2298/TSCI100226024S

Singh, J., Gupta, P. K., & Rai, K. N. (2011b). Homotopy perturbation method to space – time fractional solidification in a finite slab. *Applied Mathematical Modelling*, *35*(4), 1937–1945. https://doi.org/10.1016/j.apm.2010.11.005

Słota, D. (2007). *Direct and inverse one-phase Stefan problem solved by the variational iteration method*. *54*, 1139–1146. https://doi.org/10.1016/j.camwa.2006.12.061

Słota, D., & Zielonka, A. (2009). A new application of He ' s variational iteration method for the solution of the one-phase Stefan problem. *Computers and Mathematics with Applications*, *58*(11–12), 2489–2494. https://doi.org/10.1016/j.camwa.2009.03.070

Stefan. J. (1891). No Title. *Annual Physics Chemistry*, *42*, 269–286.

Stefan, J. (1889). No Title. *Mat. Natur*, *98*(473–484), 965–983.

Stefanescu, D. M. (2009). Science and engineering of casting solidification, second edition. In *Science and Engineering of Casting Solidification, Second Edition*. https://doi.org/10.1007/978-0-387-74612-8

Stritih, U. (2004). An experimental study of enhanced heat transfer in rectangular PCM thermal storage. *International Journal of Heat and Mass Transfer*, *47*(12–13), 2841–2847. https://doi.org/10.1016/j.ijheatmasstransfer.2004.02.001

Talati, F., Mosaffa, A. H., & Rosen, F. (2011). *Analytical approximation for solidification processes in PCM storage with internal fins : imposed heat flux*. 369–376. https://doi.org/10.1007/s00231-010-0729-9

Tasnim, S. H., Hossain, R., Mahmud, S., & Dutta, A. (2015). Convection effect on the melting process of nano-PCM inside porous enclosure. *International Journal of Heat and Mass Transfer*, *85*, 206–220. https://doi.org/10.1016/j.ijheatmasstransfer.2015.01.073

Tay, N. H. S., Bruno, F., & Belusko, M. (2013). Comparison of pinned and finned tubes in a phase change thermal energy storage system using CFD. *Applied Energy*, *104*, 79–86. https://doi.org/10.1016/j.apenergy.2012.10.040

Tien, R. H., & Geiger, G. E. (1967). A heat transfer analysis of the solidification of a binary eutectic system. *Journal of Heat Transfer*, *89*, 269–286.

Tuan Pham, Q. (2015). *Food Freezing and Thawing calculations*. Springer.

Vajjha, R. S., Das, D. S., & Namburu, P. K. (2010). Numerical study of fluid dynamic and heat transfer performance of Al2O3 and CuO nanofluids in the flat tubes of a radiator. *International Journal of Heat and Fluid Flow*, *31*, 613–621.

Versteeg, H. K., & Malalasekera, W. (2007). *An introduction to computational fluid dynamics: the finite volume method*. Toronto: Harlow, Eng.

Voller, V. R., & Falcini, F. (2013). Two exact solutions of a Stefan problem with varying diffusivity. *International Journal of Heat and Mass Transfer*, *58*(1–2), 80–85. https://doi.org/10.1016/j.ijheatmasstransfer.2012.11.003

Wang, J., Xie, H., Li, Y., & Xin, Z. (2010). based phase change nanocomposites containing γ-Al2O3. *", Journal of Thermal Analysis and Calorimetry*, *102*(2), 709–713.

Wang, W., Guo, S., Li, H., Yan, J., Zhao, J., Li, X., & Ding, J. (2014). Experimental study on the direct/indirect contact energy storage container in mobilized thermal energy system (M-

TES). *Applied Energy*, *119*, 181–189. https://doi.org/10.1016/j.apenergy.2013.12.058

Wang, W., Li, H., Guo, S., He, S., Ding, J., Yan, J., & Yang, J. (2015). Numerical simulation study on discharging process of the direct-contact phase change energy storage system. *Applied Energy*, *150*, 61–68. https://doi.org/10.1016/j.apenergy.2015.03.108

Wazwaz, A. M. (2001). Exact solutions to nonlinear diffusion equations obtained by the decomposition method. *Journal of Applied Mathematics and Computation*, *123*, 109–122.

Wood, A. S. (2001). A new look at the heat balance integral method. *Applied Mathematical Modelling*, *25*, 815–824.

Xu, H., Romagnoli, A., Sze, J. Y., & Py, X. (2017). Application of material assessment methodology in latent heat thermal energy storage for waste heat recovery. *Applied Energy*, *187*, 281–290. https://doi.org/10.1016/j.apenergy.2016.11.070

Xu, Y., Ren, Q., Zheng, Z. J., & He, Y. L. (2017). Evaluation and optimization of melting performance for a latent heat thermal energy storage unit partially filled with porous media. *Applied Energy*, *193*, 84–95. https://doi.org/10.1016/j.apenergy.2017.02.019

Yang, X., Lu, Z., Bai, Q., Zhang, Q., Jin, L., & Yan, J. (2017). Thermal performance of a shell-and-tube latent heat thermal energy storage unit: Role of annular fins. *Applied Energy*, *202*, 558–570. https://doi.org/10.1016/j.apenergy.2017.05.007

Yao, L., & Cherney, W. (1981). Transient phase-change around a horizontal cylinder. *International Journal of Heat and Mass Transfer*, *24*(12), 1971–1981.

Zauner, C., Hengstberger, F., Etzel, M., Lager, D., Hofmann, R., & Walter, H. (2016). Experimental characterization and simulation of a fin-tube latent heat storage using high

density polyethylene as PCM. *Applied Energy*, *179*, 237–246. https://doi.org/10.1016/j.apenergy.2016.06.138

Zeng, Y., FAN, L., Xiao, Y., Yu, Z., & Cen, K. (2013). An experimental investigation of melting of nanoparticle-enhanced phase change materials (NePCMs) in a bottom-heated vertical cylindrical cavity. , *International Journal of Heat and Mass Transfer*, *66*, 111–117.

Zhang, Y., & Faghri, A. (1996). Semi-analytical solution of thermal energy storage system with conjugate laminar forced convection. *International Journal of Heat and Mass Transfer*, *39*, 717–724.

Zhou, D., & Zhao, C. Y. (2011). Experimental investigations on heat transfer in phase change materials (PCMs) embedded in porous materials. *Applied Thermal Engineering*, *31*(5), 970–977. https://doi.org/10.1016/J.APPLTHERMALENG.2010.11.022

Zhou, D., Zhao, C. Y., & Tian, Y. (2012). Review on thermal energy storage with phase change materials (PCMs) in building applications. *Applied Energy*, *92*, 593–605. https://doi.org/10.1016/j.apenergy.2011.08.025

Zhou, Y., Wang, Y., & Bu, W. (2014). Exact solution for a Stefan problem with latent heat a power function of position We have. *International Journal of Heat and Mass Transfer*, *69*, 451–454. https://doi.org/10.1016/j.ijheatmasstransfer.2013.10.043

Appendix

Appendix 1: List of publications from this research

Published

- M. Parsazadeh, X. Duan, Numerical and statistical study on melting of nanoparticle enhanced phase change material in a shell-and-tube thermal energy storage system, *Applied Thermal Engineering*, 111(2017) 950-960.
- M. Parsazadeh, X. Duan, Numerical study on the effects of fins and nanoparticles in a shell and tube phase change thermal energy storage unit, *Applied Energy*, 216 (2018) 142-156.
- V. Saydam, M. Parsazadeh, M. Radeef, X. Duan, Design and experimental analysis of a helical coil phase change heat exchanger for thermal energy storage, *Journal of Energy Storage*, 21(2019) 9-17.

Submitted and/or in progress

- M. Parsazadeh, X. Duan, An improved layered thermal resistance model for solidification time estimation, *Journal of Thermophysics and Heat Transfer* (2019).
- M. Parsazadeh, X. Duan, Numerical and experimental investigation of phase change heat transfer in the presence of Rayleigh-Benard convection (2019).
- M. Parsazadeh, X. Duan, Effects of nanoparticles on phase change heat transfer rate in the presence of Rayleigh-Benard convection (2019)**.**

Conference presentations

- Mohammad Parsazadeh, Xili Duan, Numerical study of a hybrid thermal insulation with phase change material for subsea pipelines, *Proceedings of the ASME 2016 International Mechanical Engineering Congress and Exposition IMECE2016,* November 11-17, 2016, Phoenix, Arizona, USA.

- Mohammad Parsazadeh, Xili Duan, Numerical study of nanoparticle enhanced heat transfer in a solar thermal energy storage unit, *Proceedings of the 2nd Thermal and Fluid Engineering Conference, TFEC2017 4th*, 2-5th April 2017, Las Vegas, NV, USA.
- Mohammad Parsazadeh, Xili Duan, Thermal insulation with Latent energy storage for flow assurance in subsea pipelines, *Proceedings of* the ASME 2015 *34th International Conference on Ocean, Offshore and Arctic Engineering, OMAE2015*, May 31-June 5, 2015, St. John's, Newfoundland, Canada**.**

Posters

- M. Parsazadeh, X. Duan, V. Saydam "Analysis of advanced phase change materials for thermal energy applications" (Presentation and poster, Best Poster Award), *26th Canadian Thermal Analysis Society Workshop and Exhibition*, May, 3-4, 2016 Toronto Canada.
- M. Parsazadeh, X. Duan, V. Saydam, Thermal management with Latent Energy Storage", *Memorial University Engineering Research Day*, March 2016.

Appendix 2: Design of the enclosure

The following figures (**Fig. A-1**) show the detailed design of the enclosure implemented in this study. In **Fig. A-1** (a)-(c), the cross-sectional view of the enclosure, while **Fig. A-1** (d)- represents 2-D and 3-D view of the enclosure's walls.

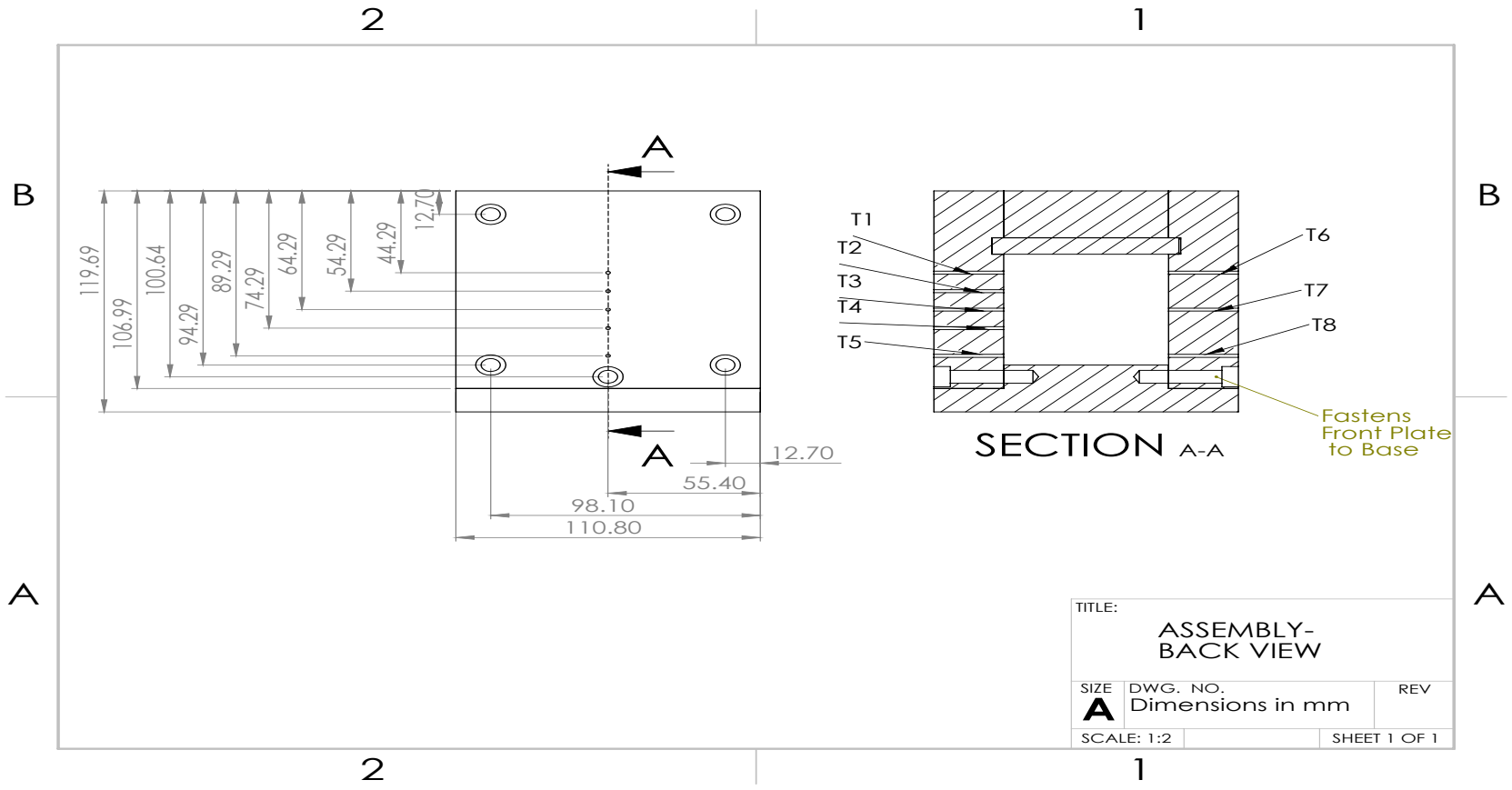

(a)

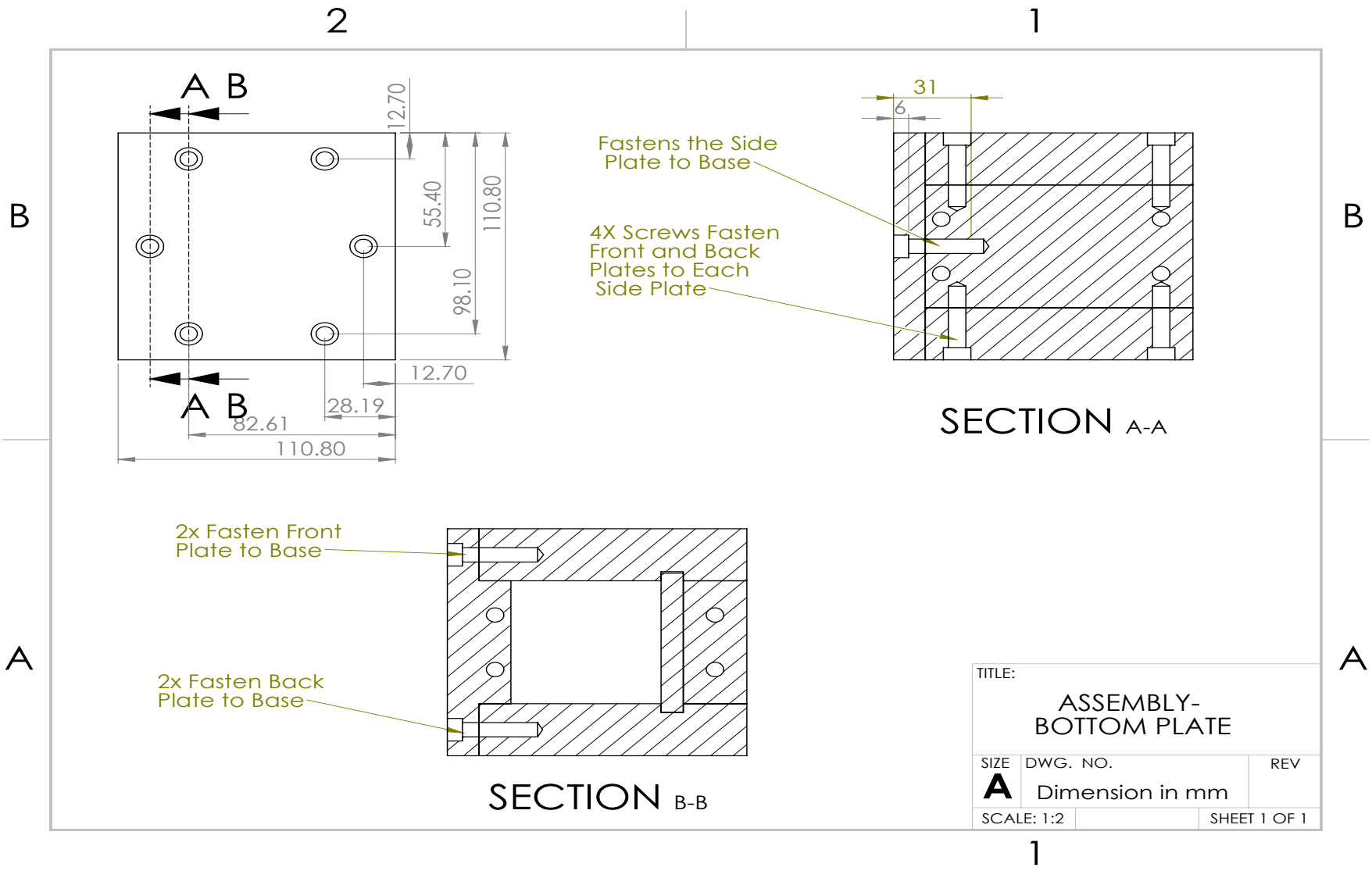
2
1
B
A
A B
12.70
55.40
110.80
98.10
12.70
A B
28.19
82.61
110.80
31
6
Fastens the Side Plate to Base
4X Screws Fasten Front and Back Plates to Each Side Plate
SECTION A-A
2x Fasten Front Plate to Base
2x Fasten Back Plate to Base
SECTION B-B
TITLE:
ASSEMBLY-
BOTTOM PLATE
SIZE
A
DWG. NO.
Dimension in mm
REV
SCALE: 1:2
SHEET 1 OF 1

(b)

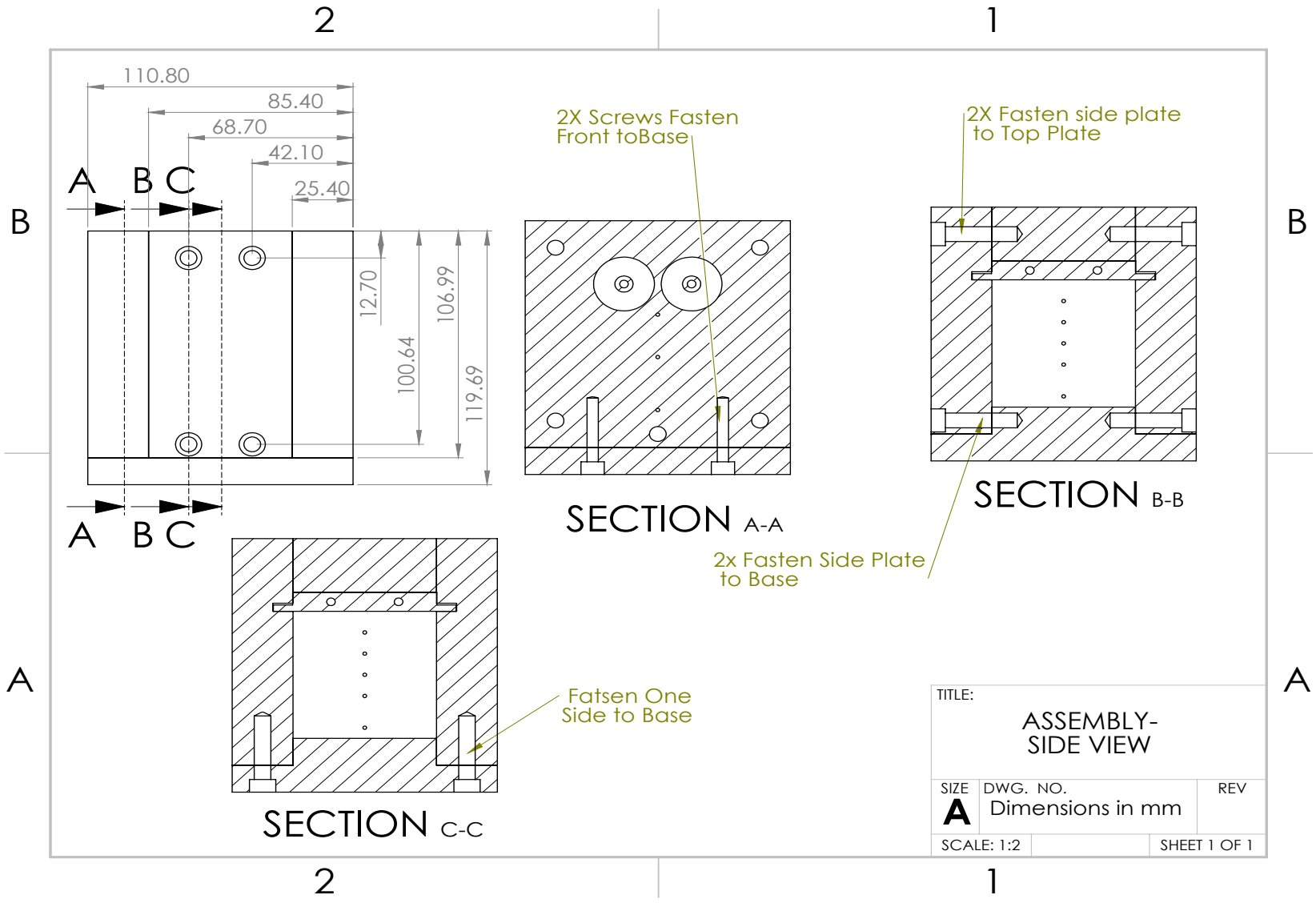
2
1
B
A
110.80
85.40
68.70
42.10
25.40
A B C
A B C
12.70
100.64
106.99
119.69
2X Screws Fasten
Front toBase
SECTION A-A
2X Fasten side plate
to Top Plate
SECTION B-B
2x Fasten Side Plate
to Base
Fatsen One
Side to Base
SECTION C-C
TITLE:
ASSEMBLY-
SIDE VIEW
SIZE
A
DWG. NO.
Dimensions in mm
REV
SCALE: 1:2
SHEET 1 OF 1

(c)

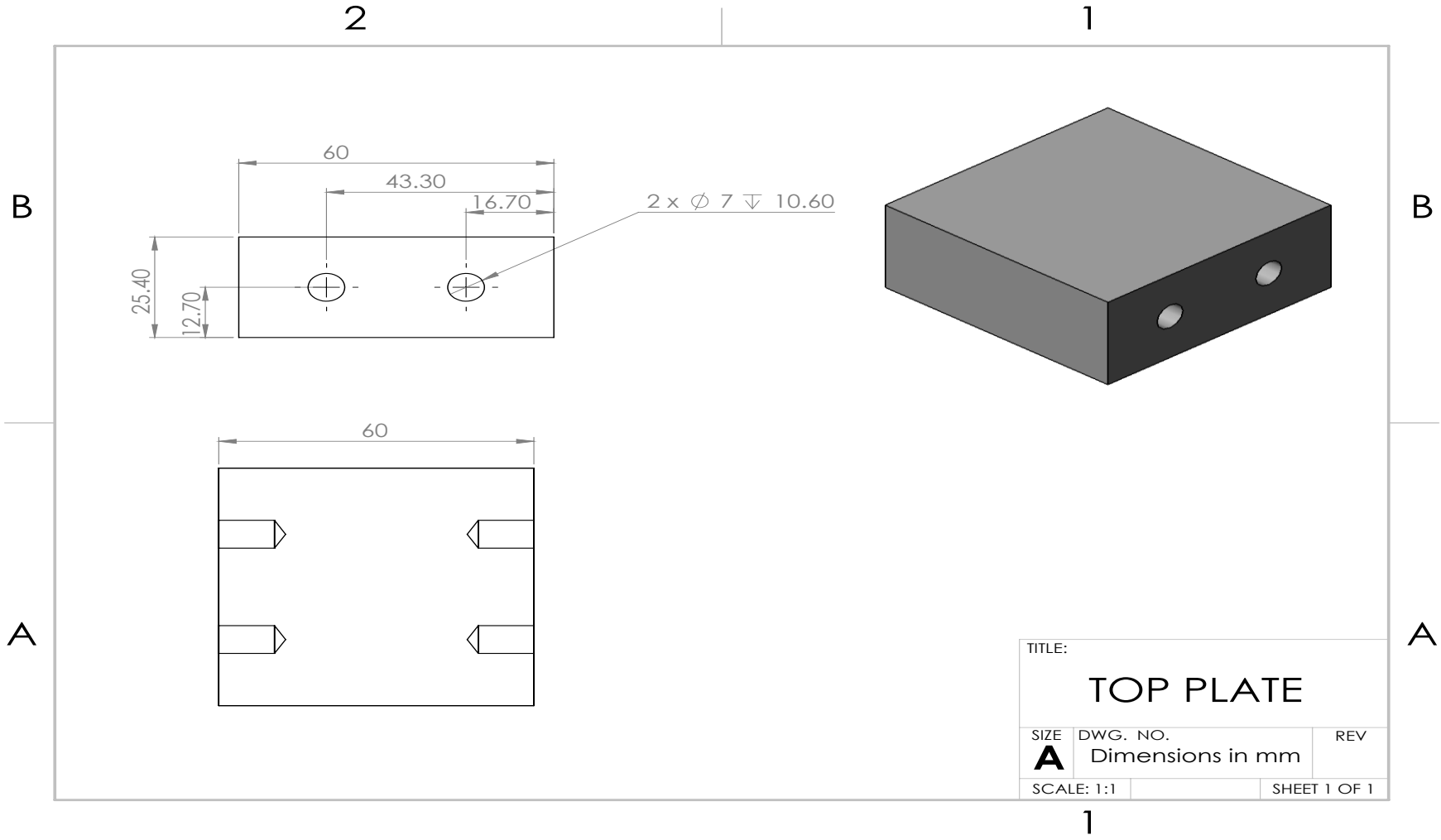
2
1
B
A
60
43.30
16.70
2 x ∅ 7 ↧ 10.60
25.40
12.70
60
TITLE:
TOP PLATE
SIZE
A
DWG. NO.
Dimensions in mm
REV
SCALE: 1:1
SHEET 1 OF 1

(d)

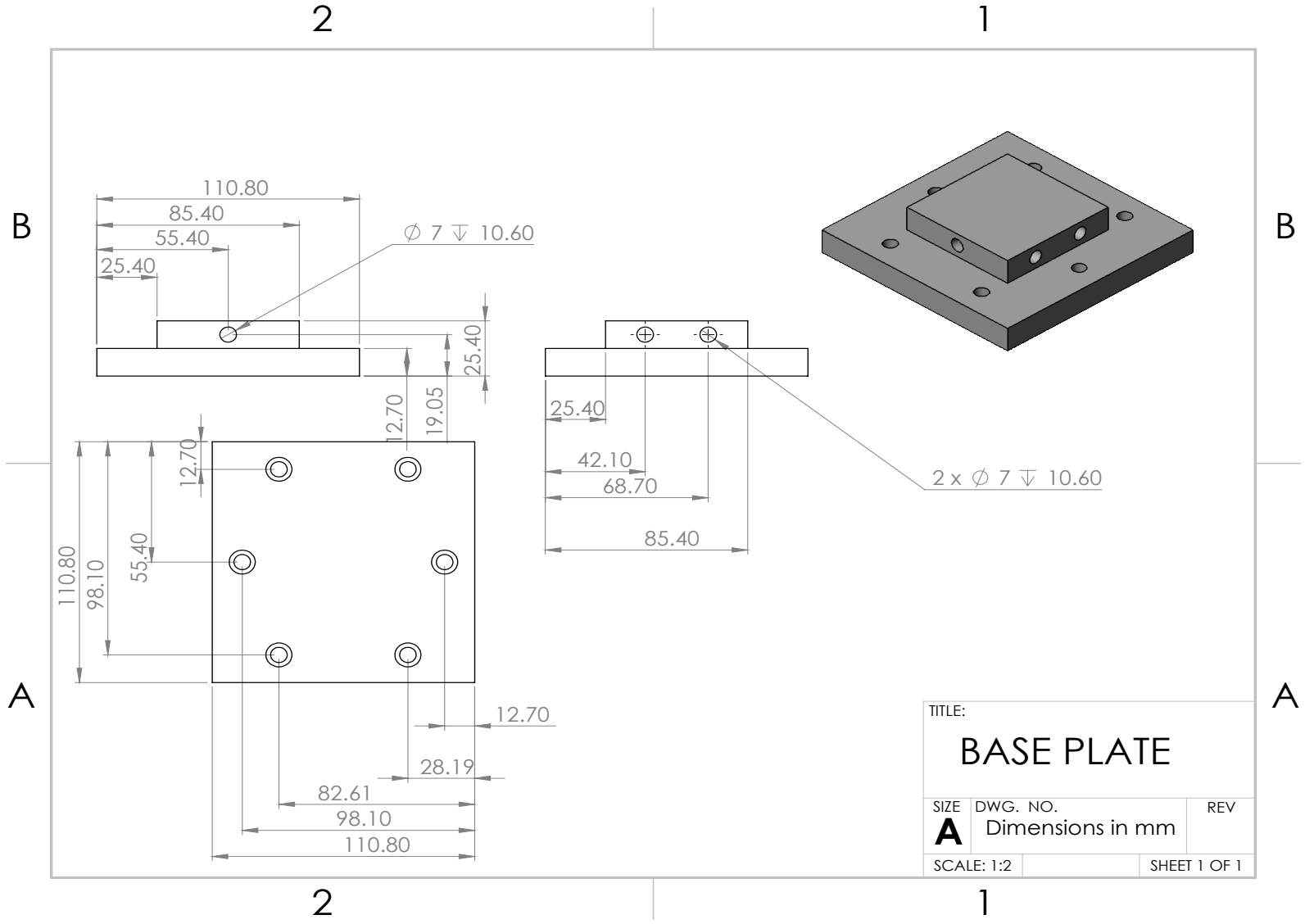
2
1
B
A
110.80
85.40
55.40
25.40
∅ 7 ↧ 10.60
25.40
12.70
19.05
12.70
55.40
98.10
110.80
12.70
28.19
82.61
98.10
110.80
25.40
42.10
68.70
85.40
2 x ∅ 7 ↧ 10.60
TITLE:
BASE PLATE
SIZE
A
DWG. NO.
Dimensions in mm
REV
SCALE: 1:2
SHEET 1 OF 1

(e)

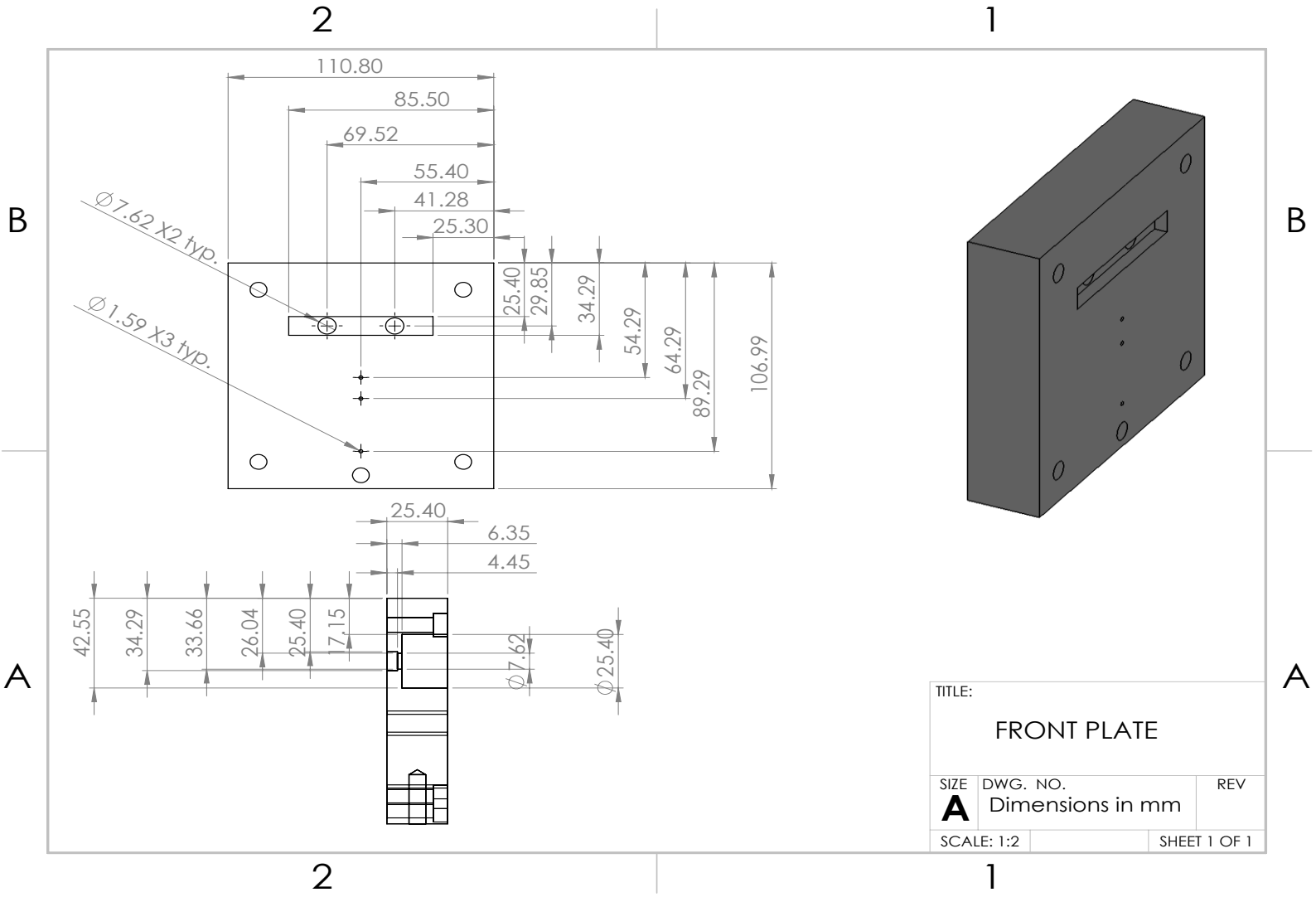
2
1
B
A
110.80
85.50
69.52
55.40
41.28
25.30
Ø7.62 X2 typ.
Ø1.59 X3 typ.
25.40
29.85
34.29
54.29
64.29
89.29
106.99
25.40
6.35
4.45
42.55
34.29
33.66
26.04
25.40
17.15
Ø7.62
Ø25.40
TITLE:
FRONT PLATE
SIZE
A
DWG. NO.
Dimensions in mm
REV
SCALE: 1:2
SHEET 1 OF 1

(f)

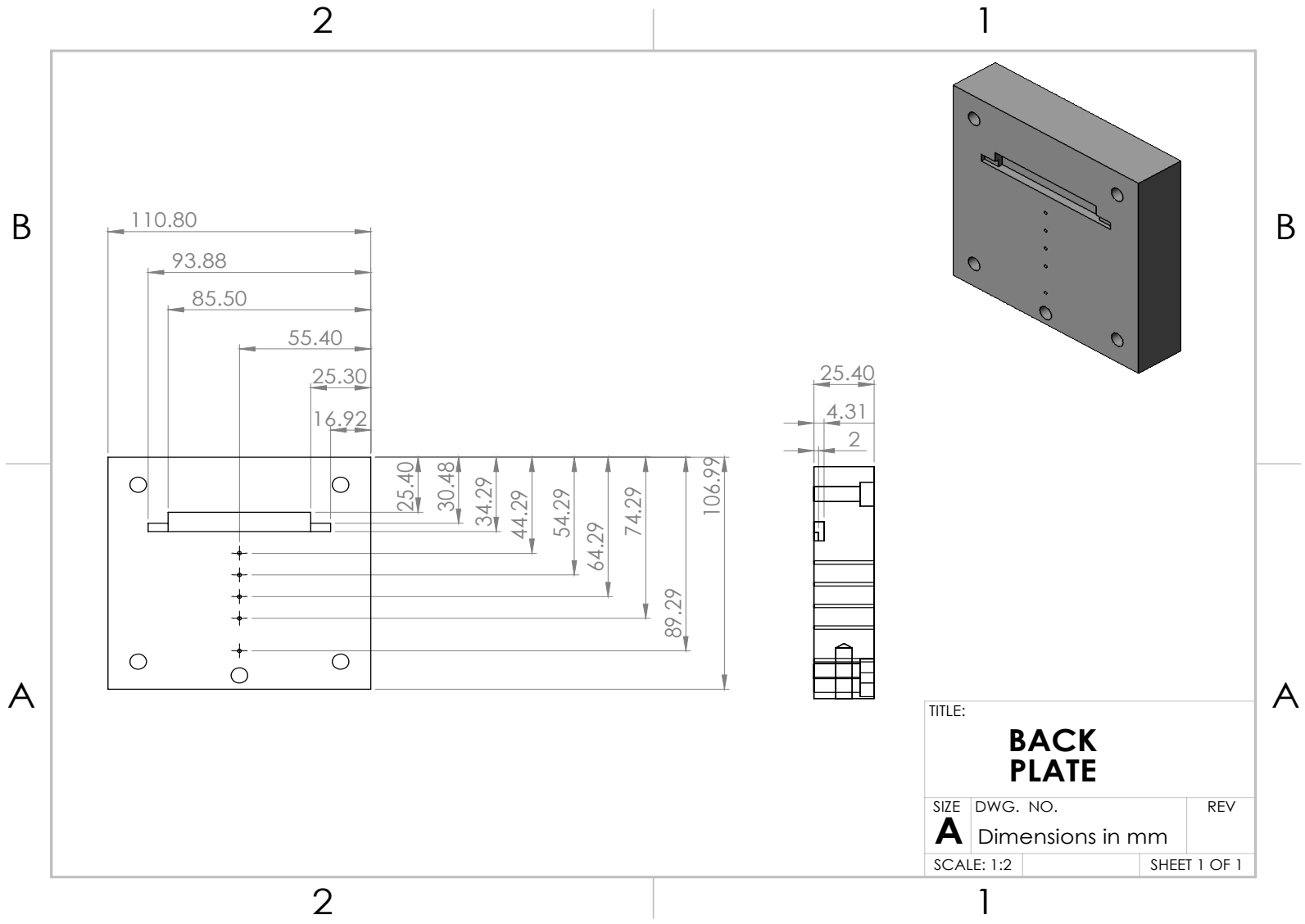
2
1
B
A
110.80
93.88
85.50
55.40
25.30
16.92
25.40
30.48
34.29
44.29
54.29
64.29
74.29
89.29
106.99
25.40
4.31
2
TITLE:
BACK PLATE
SIZE
A
DWG. NO.
Dimensions in mm
REV
SCALE: 1:2
SHEET 1 OF 1

(g)

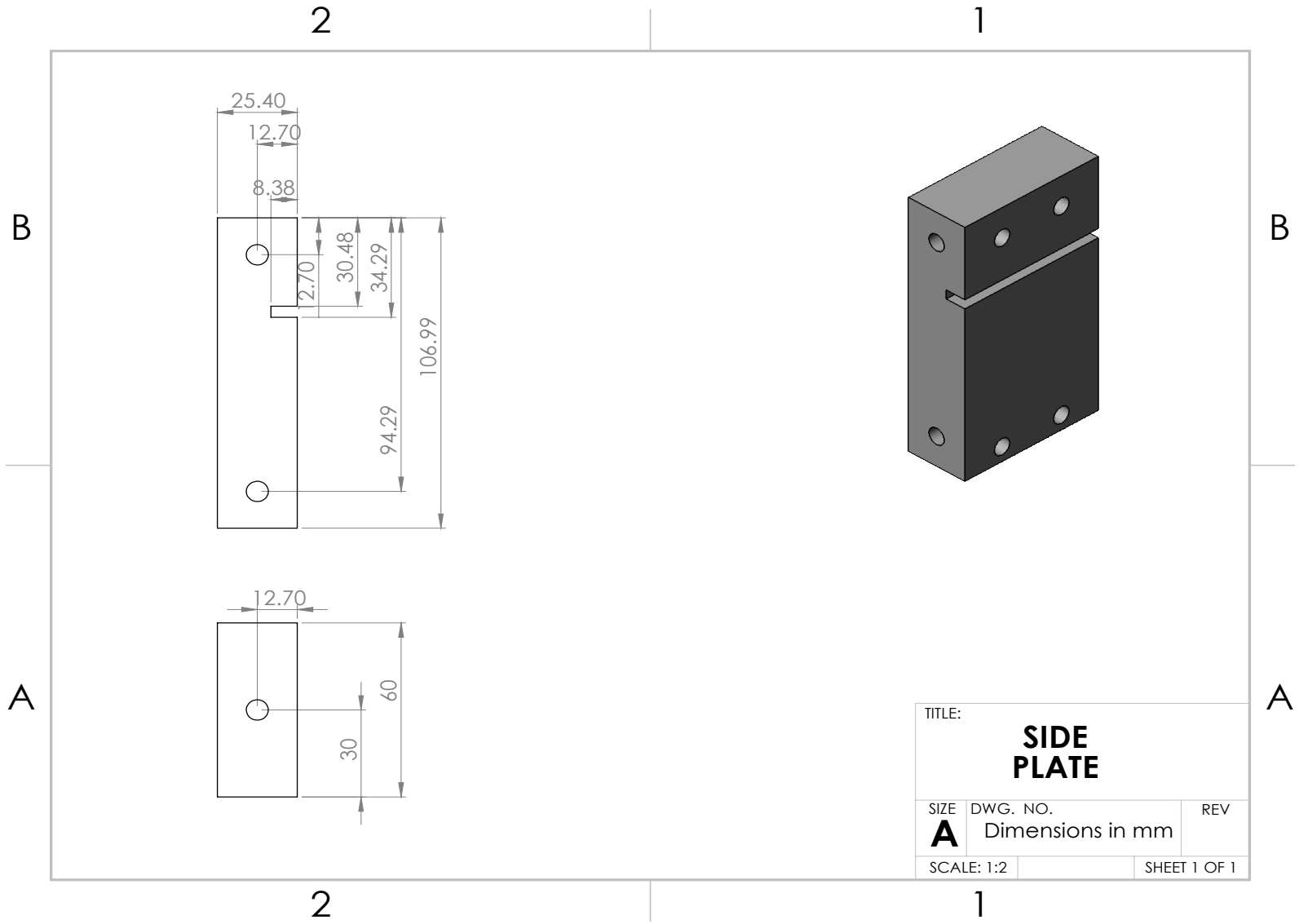
2
1
B
A
25.40
12.70
8.38
2.70
30.48
34.29
94.29
106.99
12.70
30
60
TITLE:
SIDE PLATE
SIZE
A
DWG. NO.
Dimensions in mm
REV
SCALE: 1:2
SHEET 1 OF 1

(h)

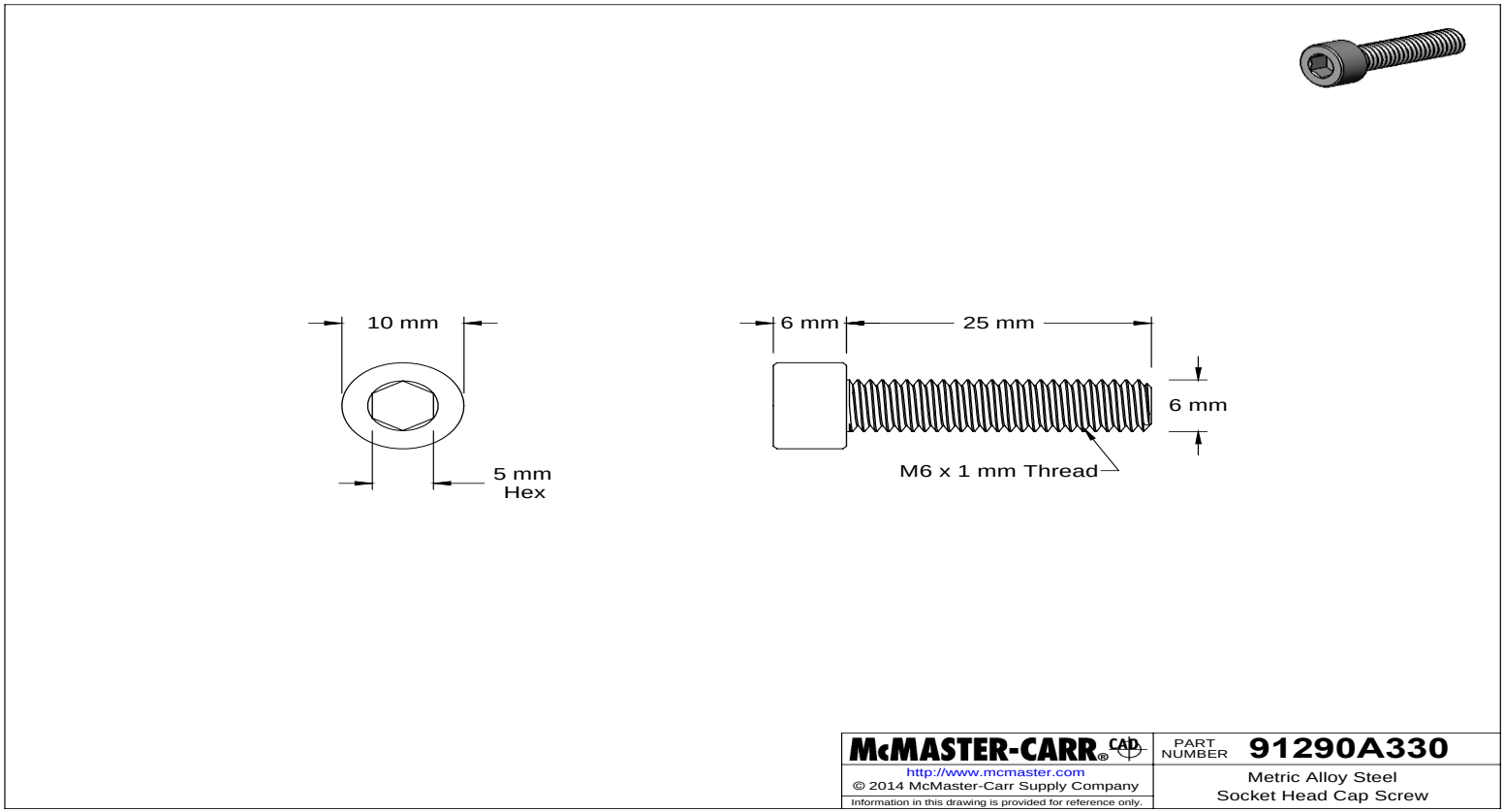

(I)

Fig. A-1 The enclosure's drawing (a) back view (b) bottom view (c) side view (d) top plate (e) base plate (f) front plate (g) back plate (h) side plate (I) socket head cap screw.